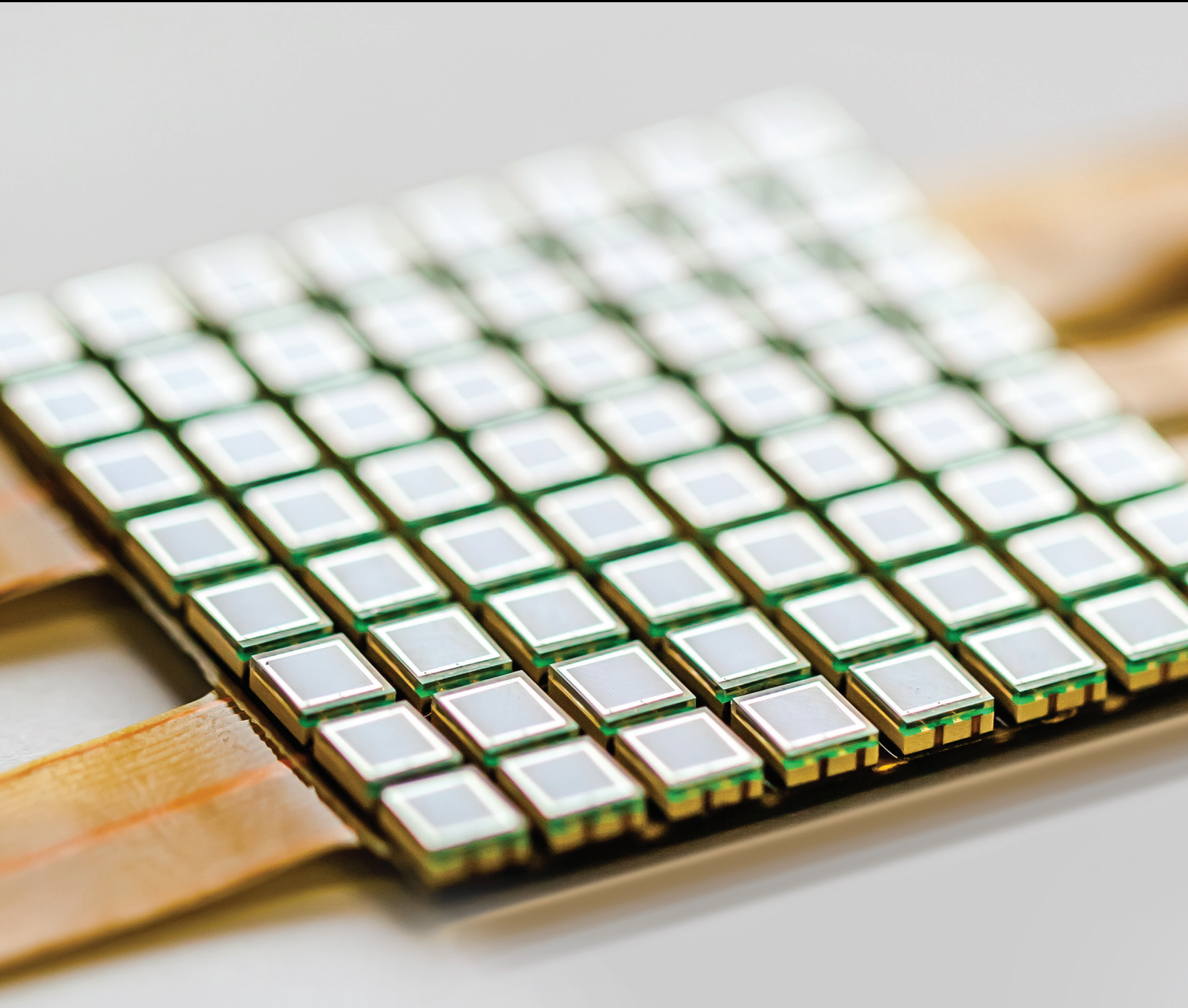


Sensors for Structural Health Monitoring in Civil Infrastructure

Lead Guest Editor: Yinan Zhang

Guest Editors: Zhou Zhi, Lei Yuan, and Amardeep Kaur





Sensors for Structural Health Monitoring in Civil Infrastructure

Journal of Sensors

Sensors for Structural Health Monitoring in Civil Infrastructure

Lead Guest Editor: Yinan Zhang

Guest Editors: Zhou Zhi, Lei Yuan, and Amardeep Kaur



Copyright © 2018 Hindawi. All rights reserved.

This is a special issue published in "Journal of Sensors." All articles are open access articles distributed under the Creative Commons Attribution License, which permits unrestricted use, distribution, and reproduction in any medium, provided the original work is properly cited.

Editorial Board

- Harith Ahmad, Malaysia
M. İlhan Akbaş, USA
Manuel Aleixandre, Spain
Bruno Andò, Italy
Constantin Apetrei, Romania
Marko Beko, Portugal
Fernando Benito-Lopez, Spain
Romeo Bernini, Italy
Shekhar Bhansali, USA
Wojtek J. Bock, Canada
Matthew Brodie, Australia
Paolo Bruschi, Italy
Belén Calvo, Spain
Stefania Campopiano, Italy
Domenico Caputo, Italy
Sara Casciati, Italy
Gabriele Cazzulani, Italy
Chi Chiu Chan, Singapore
Edmon Chehura, UK
Marvin H Cheng, USA
Nicola Cioffi, Italy
Mario Collotta, Italy
Marco Consales, Italy
Jesus Corres, Spain
Andrea Cusano, Italy
Antonello Cutolo, Italy
Dzung Dao, Australia
Luca De Stefano, Italy
Manel del Valle, Spain
Francesco Dell'Olio, Italy
Franz L. Dickert, Austria
Giovanni Diraco, Italy
Nicola Donato, Italy
Mauro Epifani, Italy
Abdelhamid Errachid, France
Stephane Evoy, Canada
Vittorio Ferrari, Italy
Luca Francioso, Italy
Manel Gasulla, Spain
Carmine Granata, Italy
Alfredo Guemes, Spain
Banshi D. Gupta, India
Mohammad Haider, USA
- Clemens Heitzinger, Austria
María del Carmen Horrillo, Spain
Evangelos Hristoforou, Greece
Syed K. Islam, USA
Stephen James, UK
Bruno C. Janegitz, Brazil
Hai-Feng Ji, USA
Sang Sub Kim, Republic of Korea
Antonio Lazaro, Spain
Laura M. Lechuga, Spain
Chengkuo Lee, Singapore
Chenzong Li, USA
Xinyu Liu, Canada
Eduard Llobet, Spain
Jaime Lloret, Spain
Yu-Lung Lo, Taiwan
Jesús Lozano, Spain
Oleg Lupan, Moldova
Frederick Mailly, France
Pawel Malinowski, Poland
Santiago Marco, Spain
Vincenzo Marletta, Italy
Carlos Marques, Portugal
Eugenio Martinelli, Italy
Antonio Martínez Olmos, Spain
Jose R. Martinez-De-Dios, Spain
Giuseppe Maruccio, Italy
Yasuko Y. Maruo, Japan
Mike McShane, USA
Fanli Meng, China
Stephen. J. Mihailov, Canada
Heinz C. Neitzert, Italy
Calogero M. Oddo, Italy
Keat Ghee Ong, USA
Marimuthu Palaniswami, Australia
Alberto J. Palma, Spain
Lucio Pancheri, Italy
Roberto Paolesse, Italy
Giovanni Pau, Italy
Alain Pauly, France
Giorgio Pennazza, Italy
Michele Penza, Italy
Salvatore Pirozzi, Italy
- Antonina Pirrotta, Italy
Stavros Pissadakis, Greece
Stelios M. Potirakis, Greece
Biswajeet Pradhan, Malaysia
Valerie Renaudin, France
Armando Ricciardi, Italy
Christos Riziotis, Greece
Maria Luz Rodriguez-Mendez, Spain
Jerome Rossignol, France
Carlos Ruiz, Spain
Ylias Sabri, Australia
Josep Samitier, Spain
José P. Santos, Spain
Isabel Sayago, Spain
Giorgio Sberveglieri, Italy
Andreas Schütze, Germany
Praveen K. Sekhar, USA
Sandra Sendra, Spain
Woosuck Shin, Japan
Pietro Siciliano, Italy
Vincenzo Spagnolo, Italy
Sachin K. Srivastava, India
Stefano Stassi, Italy
Vincenzo Stornelli, Italy
Weilian Su, USA
Tong Sun, UK
Salvatore Surdo, Italy
Raymond Swartz, USA
Hidekuni Takao, Japan
Guiyun Tian, UK
Suna Timur, Turkey
Vijay Tomer, USA
Abdellah Touhafi, Belgium
H. Vaisocherova-Lisalova, Czech Republic
Everardo Vargas-Rodriguez, Mexico
Xavier Vilanova, Spain
Luca Vollero, Italy
Tomasz Wandowski, Poland
Qihao Weng, USA
Qiang Wu, UK
Hai Xiao, USA
Chouki Zerrouki, France

Contents

Sensors for Structural Health Monitoring in Civil Infrastructure

Yinan Zhang , Lei Yuan , Zhi Zhou , and Amardeep Kaur 
Editorial (2 pages), Article ID 6023059, Volume 2018 (2018)

Feasibility Study of Interlayer Slide Monitoring Using Postembedded Piezoceramic Smart Aggregates

Jianchao Wu , Qingzhao Kong , Ing Lim, and Gangbing Song 
Research Article (10 pages), Article ID 1953528, Volume 2018 (2018)

Dielectric Characteristics of Unsaturated Loess and the Safety Detection of the Road Subgrade Based on GPR

Gao Lv , Jie Yang, Ning Li, Dexiu Hu, Yan Zhang, and Feng Zhao
Research Article (8 pages), Article ID 5185460, Volume 2018 (2018)

Performance Deterioration of Heavy-Haul Railway Bridges under Fatigue Loading Monitored by a Multisensor System

Zhiwu Yu, Zhi Shan , Ju Yuan, and Xiao Li
Research Article (14 pages), Article ID 5465391, Volume 2018 (2018)

Water Level Sensing in a Steel Vessel Using A_0 and Quasi-Scholte Waves

Peng Guo, Bo Deng, Xiang Lan, Kaili Zhang, Hongyuan Li, Zhenhua Tian, and Hong Xu
Research Article (11 pages), Article ID 2596291, Volume 2017 (2018)

Mechanism of Subordinate Peak Skewing of FBG Sensor during Cracks Propagation Monitoring on Aluminum Alloy Structure

Bo Jin, Weifang Zhang, Feifei Ren, Meng Zhang, Wei Dai, and Yanrong Wang
Research Article (7 pages), Article ID 2857693, Volume 2017 (2018)

Decision Matrix Analysis of Impact Sounding Test Method to Determine Interlayer Condition of Concrete Bridge Deck

Cristina Amor Rosales, Hyun Jong Lee, Wonjae Kim, and Chang kyu Park
Research Article (11 pages), Article ID 8516319, Volume 2017 (2018)

A Highly Sensitive Intensity-Modulated Optical Fiber Magnetic Field Sensor Based on the Magnetic Fluid and Multimode Interference

Yi Huang, Tingyun Wang, Chuanlu Deng, Xiaobei Zhang, Fufei Pang, Xuekun Bai, Weilong Dong, Liangjiang Wang, and Zhenyi Chen
Research Article (7 pages), Article ID 9573061, Volume 2017 (2018)

Experimental Verification for Cable Force Estimation Using Handheld Shooting of Smartphones

Xuefeng Zhao, Kwang Ri, and Niannian Wang
Research Article (13 pages), Article ID 5625396, Volume 2017 (2018)

A Study for Optimum Survey Method of Underwater Structure Using the Dual Sonar Sensor

Youngseok Kim, Heungsu Lee, Chul Park, and Sangsik Choi
Research Article (10 pages), Article ID 9206898, Volume 2017 (2018)

Editorial

Sensors for Structural Health Monitoring in Civil Infrastructure

Yinan Zhang ¹, Lei Yuan ², Zhi Zhou ³, and Amardeep Kaur ¹

¹Department of Electrical and Computer Engineering, Missouri University of Science and Technology, Rolla, MO 65409, USA

²Department of Electrical and Computer Engineering, Clemson University, Clemson, SC 29634, USA

³Department of Civil Engineering, Dalian University of Technology, Dalian, China

Correspondence should be addressed to Yinan Zhang; yzfyc@mst.edu

Received 13 March 2018; Accepted 13 March 2018; Published 3 June 2018

Copyright © 2018 Yinan Zhang et al. This is an open access article distributed under the Creative Commons Attribution License, which permits unrestricted use, distribution, and reproduction in any medium, provided the original work is properly cited.

Our lives rely heavily on the civil infrastructure such as bridges, buildings, tunnels, power plants, and dams. Maintenance and monitoring of civil infrastructure for an accurate estimation of infrastructure age, usability, and also the probable causes of concern are of great importance. Malfunctioning and reckless, negligence, and unconscious human actions over civil infrastructure have caused tremendous economic loss and claimed numerous human lives. The development of effective structural health monitoring (SHM) methods has gained traction amongst the research community in recent years. A typical health monitoring system is composed of a network of sensors that measure the parameters relevant to the state of the structure and its environment, such as temperature, stress, delamination, strain, vibration, and humidity. Accurate, robust, fast response, and long-term reliable sensors are necessary for in situ structural health monitoring. Although many types of sensors have been developed and demonstrated, the potential for innovative high-performance in situ sensors is increasingly evident.

This special issue seeks to attract researchers to contribute their original articles and review articles on sensor development and application for structural health monitoring. The special issue consists of 9 papers whose brief summaries are listed below.

“Dielectric Characteristics of Unsaturated Loess and the Safety Detection of the Road Subgrade Based on GPR” by G. Lv et al. presents a moisture content and permittivity model to simultaneously detect and estimate defects in loess subgrade. The model can be applied in the engineering

practices to provide guidance for determining the qualitative research of defects in the roadbed.

“Performance Deterioration of Heavy-Haul Railway Bridges under Fatigue Loading Monitored by a Multisensor System” by Z. Yu et al. studied the performance deterioration of the scale models of a typical heavy-haul railway bridge under fatigue loading based on a multisensor system including the fiber-reinforced polymer optical fiber Bragg grating and electrical resistance strain gauges, linear variable displacement transducer, and accelerometer.

“Water Level Sensing in a Steel Vessel Using A_0 and Quasi-Scholte Waves” by P. Guo et al. presents a water level sensing method using guided waves of A_0 and quasi-Scholte modes. A laboratory experiment using a pitch-catch configuration with two piezoelectric transducers is designed for sensing the water level in a steel vessel. The experimental results show that the travelling time between the two transducers linearly increases with the increase of the water level and agree well with the theoretical predictions.

“Mechanism of Subordinate Peak Skewing of FBG Sensor during Cracks Propagation Monitoring on Aluminum Alloy Structure” by B. Jin et al. investigates the variety of the spectrum features of fiber Bragg grating (FBG) around the crack tip during fatigue crack propagation.

“Decision Matrix Analysis of Impact Sounding Test Method to Determine Interlayer Condition of Concrete Bridge Deck” by C. A. Rosales et al. focused on analysis of the frequency spectra of the impact sounding test performed on composite slabs with different interlayer conditions.

The proposed analysis was capable of detecting intermediate condition interlayer, which emphasized the transition of damage in the interlayer section.

“A Highly Sensitive Intensity-Modulated Optical Fiber Magnetic Field Sensor Based on the Magnetic Fluid and Multimode Interference” by Y. Huang et al. demonstrated an optical fiber magnetic field sensor based on a single-mode-multimode-single-mode (SMS) structure immersed into the magnetic fluid (MF). This optical fiber sensor possesses advantages of low cost, ease of fabrication, high sensitivity, simple structure, and compact size, with great potential applications in measuring the magnetic field.

“Experimental Verification for Cable Force Estimation Using Handheld Shooting of Smartphones” by X. Zhao et al. proposed a vision-based approach for cable force estimation using handheld shooting of a smartphone camera. This study demonstrates the feasibility of cable force measurement using handheld shooting of a smartphone camera.

“A Study for Optimum Survey Method of Underwater Structure Using the Dual Sonar Sensor” by Y. Kim et al. developed the equipment to investigate damage of underwater structures effectively using the dual sonar and studied the operation method to improve the resolution of sonar data.

“Feasibility Study of Interlayer Slide Monitoring Using Postembedded Piezoceramic Smart Aggregates” by J. Wu et al. demonstrated that the postembedded smart aggregate-based technique for interlayer slide monitoring was feasible and effective in detecting a slide damage. Experimental results demonstrated that SAs installed through a postembedding process are an innovative yet effective approach to monitor the interlayer slide.

Acknowledgments

Introducing this special issue to this journal, we would like to thank all the researchers for their contributions and reviewers for their help in achieving a high technical quality of papers in this special issue. The Lead Guest Editor Yinan Zhang would like to thank all the Guest Editors for their valuable contribution to this special issue. We hope all the readers can enjoy the papers in the special issue as we do.

*Yinan Zhang
Lei Yuan
Zhi Zhou
Amardeep Kaur*

Research Article

Feasibility Study of Interlayer Slide Monitoring Using Postembedded Piezoceramic Smart Aggregates

Jianchao Wu ^{1,2}, Qingzhao Kong ², Ing Lim,³ and Gangbing Song ^{2,3}

¹Key Laboratory of Earthquake Geodesy, Institute of Seismology, China Earthquake Administration, Wuhan 430071, China

²Department of Mechanical Engineering, University of Houston, Houston, TX 77204, USA

³Department of Civil and Environmental Engineering, University of Houston, Houston, TX 77204, USA

Correspondence should be addressed to Gangbing Song; gsong@uh.edu

Received 10 August 2017; Accepted 3 January 2018; Published 25 March 2018

Academic Editor: Yinan Zhang

Copyright © 2018 Jianchao Wu et al. This is an open access article distributed under the Creative Commons Attribution License, which permits unrestricted use, distribution, and reproduction in any medium, provided the original work is properly cited.

Utilizing embedded transducers is an effective approach to monitor a landslide. However, for existing structures, sensors can only be postembedded, which involves drilling and grouting, and may change the original state of the structure, which calls for the need to study the effectiveness of postembedded transducers. The main focus of this paper is the feasibility study of the interlayer slide detection using postembedded piezoceramic smart aggregates (SAs). In this study, a small landslide structure that involves a weak layer is studied and two pairs of SAs were embedded in predetermined positions inside the structure. To study the difference, one pair of transducer was preembedded and the other pair was postembedded. Within each pair, one SA was employed as an actuator to generate stress waves, and another SA used as a sensor to detect wave responses. Active-sensing approach was developed to perform continuous monitoring during structural loading that was used to induce an interlayer slide. The occurrence of interlayer slide attenuates wave energy and decreases signal intensity. A wavelet-packed index was proposed to detect the occurrence and development of interlayer slide. Experimental results demonstrated that SA installation through postembedding process is an innovative yet effective approach to monitor interlayer slide.

1. Introduction

Landslides may cause immense property damage and even loss of life. Landslides are usually triggered by environmental changes, such as earthquake, heavy rainfall, or rise of ground water levels. These factors can amplify the inherent weakness inside a landslide body, which is defined as a weak layer [1]. Landslides occur due to interlayer slide along the weak layer. The interface between the weak layer and the surrounding medium transfers internal stress when the slope mass is subjected to vertical loading compression. Before a slide, the friction between these two regions accumulates until the accumulated stress is suddenly released and the mass slips along the weak sliding surface. It is essential to develop an effective detection technique to monitor and study interlayer slide damage to provide early warning.

Continuous and in situ monitoring of landslide is essential for the identification of potential landslide and predicting the behavior of active landslide, and its importance has been recognized by the scientific community since adequate monitoring is an effective measure for understanding kinematic aspects of landslide movement. In the past decades, different types of instruments and techniques have been utilized for landslide monitoring. These techniques can be classified as remote sensing or satellite technique [2–4], photogrammetric technique [5, 6], ground-based geodetic or observational technique [7–9], satellite-based geodetic technique [10–13], and geotechnical technique [14, 15]. The selection of techniques for natural landslide monitoring depends on the different types of deformations that will affect the stability analysis. Each monitoring technique has its advantages but retains limitations. For example, the ground-based geodetic technique requires an unobstructed line of sight between

the instrument and the targeting prism; the detection range of the remote sensing or satellite technique is costly limited to a small scale of satellite imagery; as for the photogrammetric technique, the temporal coverage is relatively poor; the geotechnical technique may lose the data if transfer media is not operating and internal storage is not activated [1].

Piezoceramic materials, with the unique advantages of wide bandwidth, low cost, small size, embeddability, and dual actuation/sensing function, have been actively researched in structural health monitoring (SHM) for many years [16–28]. The unique properties of piezoceramic materials have led to a wide variety of research, including material modeling [29–31], sensor development [32–35], energy harvesting [36–41], actuation, and sensing mechanisms [42, 43], among others. One particular piezoceramic material, lead zirconate titanate (PZT), has a strong piezoelectric effect and is commonly used. For example, a pair of PZT patches was used in smart aggregate (SA), which offers protection to the fragile PZT patches. Smart aggregates have found a wide range of active sensing enabled research, where at least two SAs are used with one as an actuator to generate stress waves and the other one as a sensor to detect the propagated waves. By interrogating the signals detected by the sensor, the changes along the wave propagating path between the actuator and the sensor can be monitored. Examples of active sensing with embedded SAs include crack and damage detection of concrete structures [44–48], water seepage monitoring of cement [49–51], soil freeze-thaw status monitoring [52], and cure-state monitoring [53]. In addition, the concept of active sensing using PZT transducers is extended to bolt looseness monitoring [54, 55]. In a preliminary study, we demonstrated that an interlayer slide can be effectively monitored using preembedded smart aggregates with the active sensing approach [56]. In addition, this technology is a low-cost method and can determine the interface slide in real time. However, for an existing structure or landslide body, transducers, such as the smart aggregates, have to be installed through the postembedding procedure. In addition, to enable the active sensing approach, at least two SAs have to be installed with one on each side of the interlayer. The installation of postembedded smart aggregates involves drilling, embedding the smart aggregates, and grouting, and obviously the postembedding procedure changes the original conditions of the landslide body, which calls for experimental study to verify the effectiveness of the active sensing approach using embedded SAs through the postembedding procedure.

Currently, there is no study on interlayer slide monitoring with postembedded piezoceramic transducers, to the author's best knowledge. In this study, the active sensing approach using postembedded SAs was adopted as transducers for interlayer slide monitoring of a specimen with a weak layer under compressive loading. Two pairs of SAs were utilized for the excitation and detection of the sine sweep signals. For comparison, one pair of SAs was preembedded and the other pair was postembedded. The wavelet packet-based energy index of the continuous signals was employed

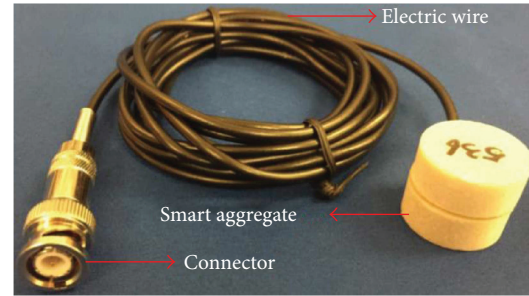


FIGURE 1: A fabricated smart aggregate.

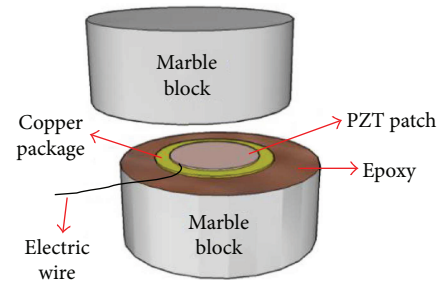


FIGURE 2: Components of a smart aggregate.

to quantitatively indicate the occurrence and development of the interlayer slide. Experimental results verified the feasibility and effectiveness of postembedded SAs for in situ interlayer slide detection for landslide monitoring through a comparative study.

2. Detection Principle

2.1. Smart Aggregate. Smart aggregates (SAs) are piezoceramic-based multifunctional transducers (Figure 1) and have been researched in structural health monitoring. SA was first proposed by Song et al. [57, 58] and can be embedded and fixed at a designated position within a concrete structure before casting. Due to the direct and converse piezoelectric effect of the PZT patch, SAs can satisfy the dual functions of actuation and sensing. In this paper, an SA was fabricated by sandwiching two PZT patches between a pair of cylindrical marble blocks with epoxy and proper electric shielding, as shown in Figure 2.

2.2. Principle of the Active Sensing Method. In this study, a smart aggregate-based active sensing approach is used to detect the interlayer slide damage. Active sensing method takes advantage of the dual actuation/sensing capability of piezoelectric transducers. Figure 3 demonstrates the SA-based active sensing approach for interlayer slide detection. Two pairs of SAs are used, and each pair is installed in opposite sides of a weak interlayer. Between them, one pair of SAs was preembedded before the casting, and the other pair was postembedded after curing of the concrete. For each pair, one SA functions as an actuator to generate stress waves which propagate along the structure and across the

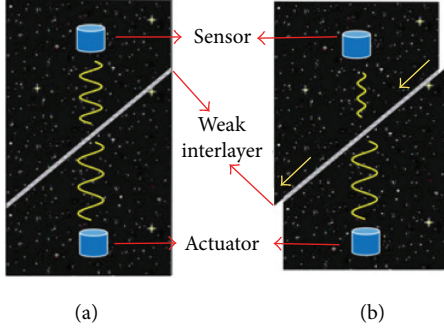


FIGURE 3: Schematic diagram of smart aggregate-based active sensing approach for interlayer slide detection. (a) Before slide. (b) After slide.

interlayer, and the other one acts as a sensor to detect the wave response. The energy attenuation of the propagating wave crossing the interlayer is heavily influenced by the interlayer condition. If an interlayer slide occurs, which weakens the interlayer, the energy attenuation of the stress wave will increase. Analysis of the sensor signal can reveal the occurrence of the interlayer slide when compared with a baseline or initial condition.

2.3. Interlayer Slide Index. Wavelet packet analysis was used as a signal-processing tool to analyze the detected signal. A wavelet is a waveform of effective limited duration with an average value of zero. Wavelet packet analyses enable the inspection of narrow frequency bands over a relatively short time window [59]. Based on wavelet packet analysis, an interlayer slide index, which represents the transmission energy loss caused by the development of slide failure, can be established as follows:

The sensor signal X , which represents the detected wave response, is first filtered by a Butterworth filter and then decomposed by an n -level wavelet packet decomposition into 2^n signal sets $\{X_1, X_2, \dots, X_j, \dots, X_{2^n}\}$. X_j is the decomposed sensor signal and can be represented as

$$X_j = [X_{j,1}, X_{j,2}, \dots, X_{j,m}], \quad (1)$$

where m is the number of the sampling data and j is the frequency band number ($j = 1, 2, \dots, 2^n$).

The energy of each decomposed signal E_j is defined as

$$E_j = X_{j,1}^2 + X_{j,2}^2 + \dots + X_{j,m}^2. \quad (2)$$

The energy vector of the signal X_i at the i th measurement is given by

$$\mathbf{E}_{i,i} = [E_{i,1}, E_{i,2}, \dots, E_{i,2^n}]. \quad (3)$$

The interlayer slide index, using root-mean-square deviation (RMSD) [60–62], indicates the severity of damage between the chosen actuator-sensor systems. Specifically, the index can be developed by calculating the RMSD between the energy vectors of the initial state and subsequent states

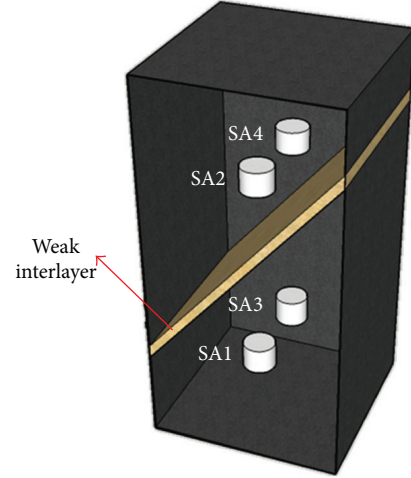


FIGURE 4: Schematics of the specimen. SA1 and SA2 are preembedded. SA3 and SA4 are postembedded.

during the test. The proposed wavelet-based interlayer slide index at the i th time index is defined as

$$I = \sqrt{\frac{\sum_{j=1}^{2^n} (E_{i,j} - E_{h,j})^2}{\sum_{j=1}^{2^n} (E_{h,j})^2}}, \quad (4)$$

where $E_{h,j}$ is the energy at the j th frequency band ($j = 1, 2, \dots, 2^n$) in the initial or the healthy state and $E_{i,j}$ is the energy in the i th time index. As an example, for a laboratory test of the structure with an interlayer, the structure is considered in a healthy state without the slide before the compressive loading, and the interlayer slide index value is zero at this situation. As the loading progresses, a slide happens and the index value will eventually approach one. Therefore, the values of the interlayer slide index can be used to monitor the interlayer slide, since the interlayer slide index was computed based on the baseline data which was recorded when the structure is in health status. The method has the capability to tolerate small degrees of misalignment when the smart aggregate pairs were postembedded in the structure.

3. Experimental Setup

The specimen and SAs were fabricated in the Smart Material and Structure Laboratory, University of Houston. To verify the feasibility and reliability of our proposed approach, we chose mortar to simulate the environmental medium due to its uniform and relative isotropic properties so that the experimental results will not be strongly affected by the non-linear and nonisotropic material properties of the medium. In addition, to implement the active sensing approach, two pairs of smart aggregates are embedded into the specimen at prearranged locations on each side of the interlayer. The size of the specimen was $150 \times 150 \times 300 \text{ mm}^3$, and the location of SAs is shown in Figure 4. The size was selected to avoid mechanical damage to the surrounding medium. Considering that the natural landslide usually occurs in high inclination, the angle between the weak interlayer and

TABLE 1: Composition of the surrounding specimen and weak interlayer under study.

| Material | Constituent | Content (kg) |
|-----------------|-------------|--------------|
| Weak interlayer | Mortar | 0.25 |
| | Clay | 0.075 |
| | Sand | 0.075 |
| | Water | 0.1 |
| Specimen | Mortar | 3.85 |
| | Water | 0.65 |

horizontal surface was set to 40°. In this research, a compression test was designed to simulate the interfacial slide of the specimen. It should be noted that the thickness of the weak interlayer was 15 mm. The weak interlayer was simulated by a mixture of mortar, clay, sand, and water, and the mixing ratio was mortar : clay : sand : water = 5 : 1.5 : 1.5 : 2. Its quantitative composition is listed in Table 1. The dimensional details are shown in Figure 5.

The preembedded SAs were labeled SA1 and SA2, while the postembedded SAs were labeled SA3 and SA4. Postembedded SAs were installed by drilling a 30 mm diameter and 35 mm deep hole in the side face of the specimen, as shown in Figure 6. The SAs were embedded into the hole and refilled by nonshrinkage mortar. Both preembedded and postembedded SAs were located symmetrically at the same level with a horizontal distance of about 75 mm. To ensure the position and orientation of the smart aggregates, the first smart aggregate was installed after the mortar was poured at the designed height where the first smart aggregate should be located. With a 5-minute hold for the mortar drying and a careful check of the position and orientation of the smart aggregate, more mortar was filled until the second smart aggregate was placed. Finally, the mortar was poured to completely fill the drilled hole. After the curing of the mortar, the two SAs became an integrated part of the landslide body. The SA1 and SA3 were used as the actuators to generate repeated swept sine wave. SA2 and SA4 were adopted as the sensors to detect the wave response.

Instrumentation includes two power amplifiers (Trek 2100HF), data acquisition system (NI USB6353), and a Shore Western universal hydraulic testing machine, as shown in Figure 7. The loading test was conducted by employing the hydraulic testing machine with a separate acquisition system. During the test, a swept sine wave was generated by the NI USB6353 system and then amplified by the power amplifier with a gain of 50. The frequency range of the swept sine wave is from 100 Hz to 150 kHz. The amplitude and period of the signal are 150 V and 1 second, respectively. The sampling rate of the data acquisition system is 1.25 MS/s.

Loading on the specimen was achieved with an 1112 KN capacity Shore Western universal hydraulic testing machine. The specimen was subjected to an axial pressure loading, with a loading rate of 0.033 mm/min. Every 10 minutes, SA1 and SA3 generated repeated swept sine waves, and the corresponding sensors (SA2 and SA4) detected the wave signal that propagated through the weak interlayer.

4. Experimental Results and Discussions

4.1. Pressure Loading History. The loading test lasted 310 minutes, and the loading history curve is shown in Figure 8. The entire loading history can be divided into three stages. During the first stage (0–60 minutes), the loading history curve displayed a linear increase which indicated that the structure experienced elastic deformation and becomes denser. During the second stage (61–290 minutes), the loading history curve increased linearly. With an increasing load, the friction between the weak interlayer and the surrounding medium accumulated and increased. During the last stage (291–310 minutes), the loading stress suddenly decreased, which indicated the occurrence of the interlayer slide. In this stage, a relative displacement was observed between the upper specimen and the lower specimen.

4.2. Time Domain Analysis. The detected signals before and after the interlayer slide in time domain by SA2 and SA4 are shown in Figure 9. In each figure, the red and blue curves represented the signal received at 290 and 300 minutes, respectively. The entire signals corresponded to one period of the excitation signal. Due to the differences of the location, interface, wave propagation medium, and orientation between the preembedded SA pair and the postembedded SA pair, the received signals of these two pairs present similar amplitude levels but still retain unique details. Both of the received signal amplitudes experienced obvious decreases after slide damage occurs due to the attenuation of the stress wave that propagated through the sliding interlayer. From the experimental results of the time domain signal response, the postembedded SAs show potentials to be used for the detection of the interface slide.

4.3. Wavelet Packet-Based Analysis. According to the wavelet decomposition, a signal can be decomposed into several frequency bands. As shown in Figures 10 and 11, energy vectors (level 5 decomposition) of the time domain signal given in Figure 9 are formed by calculating the energy of each subset (frequency band) to present the energy distribution along the frequency bands. When the interlayer slide occurred, the propagating stress wave energy attenuates at the sliding interface so that to reduce the energy of the signal received by SA sensors. Compared with the energy vector before and after the slide as shown in Figures 10 and 11, obvious energies' drop can be found at different frequency bands. It can be seen that the wavelet-based analysis helps to provide quantitative attenuation values of the signal corresponding to each frequency band before and after the interlayer slide. To further determine the occurrence of the interface slide, the wavelet packet-based interlayer slide damage index is computed, as shown in the next section.

4.4. Wavelet Packet-Based Interlayer Slide Damage Indices. To provide quantitative analysis of the entire loading process, the energy of the detected signal was computed by employing the wavelet packet-based energy analysis. The computed interlayer slide damage indices are shown in Figures 12 and 13. Both figures depict the energy levels throughout the entire loading process. Both indices show a similar overall

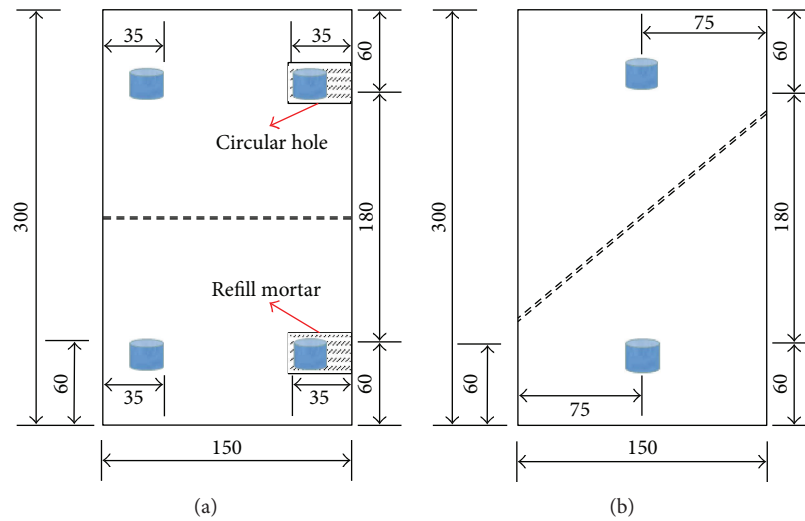


FIGURE 5: Locations of smart aggregates in the specimen (unit: mm). (a) Lateral view. (b) Front view.

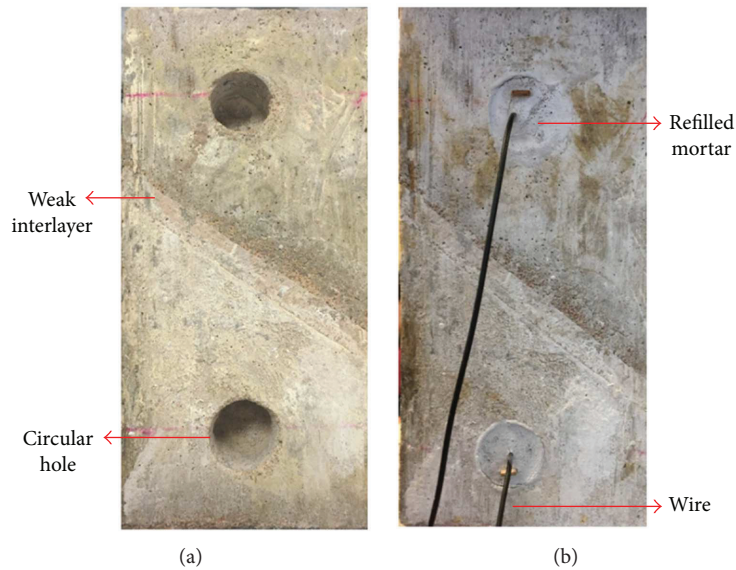


FIGURE 6: Installation of postembedded smart aggregates in the specimen. (a) Circular hole before installation of SA. (b) Refilled mortar after the installation of SAs.

increasing trend, and a sharp increase was observed near the 300th minute, due to the occurrence of interlayer slide damage that resulted in a sudden release of stress wave energy. Correspondingly, the damage indices increased suddenly when the slide occurred near the 300th minute. Both pre- and postembedded SAs effectively detected the interlayer slide.

We monitored the occurrence of the interlayer slide in real time by detecting the sensors' responses and the associated energy levels. Compared to the time domain analysis, wavelet packet-based energy analysis shows an abrupt energy change that corresponded to the interlayer slide. Therefore, wavelet packet-based energy analysis using the data from the postembedded transducers has the capacity to determine the occurrence of an interlayer slide.

4.5. Discussions. Through the experiment, the occurrence of the interlayer slide was successfully detected in real time by employing the active sensing-based approach with post-embedded smart aggregates. It should be noted that the deformation of the specimen with a weak interlayer under loading compression is complex. The structure is a heterogeneous material and exhibits a complex elastic behavior related to the presence of microcracks. Due to the complexity of the interlayer slide, there is lack of real-time-based technologies to monitor the interlayer slide, especially at its early age. This research proposes a piezoceramic-based active sensing approach which could have a potential to provide an early warning of the interlayer slide in real time. Due to the principle of the proposed method, the energy of the propagating stress wave between SAs attenuates (a sudden drop of

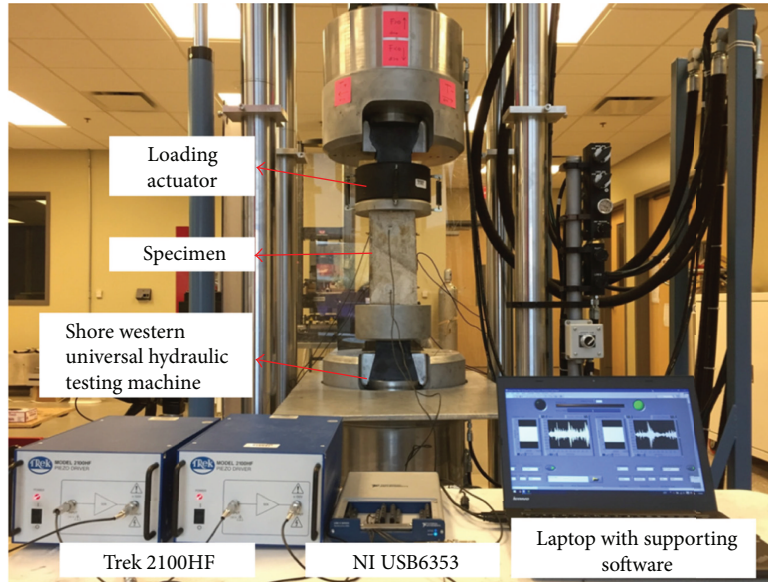


FIGURE 7: Experimental setup.

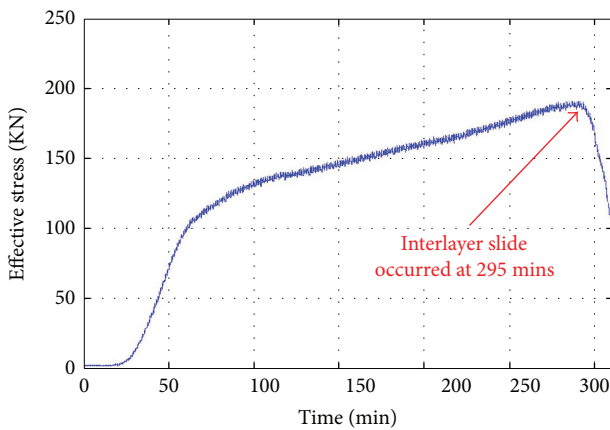


FIGURE 8: Loading history.

the received energy) when the slide occurs. By using the developed sliding interlayer index, the slide event can be immediately determined when a “sharp” increase value is presented in the index. However, many factors including the distance of SAs, wave propagation medium property, and excitation signal parameters, may influence the threshold values. A comparative study of the results of preembedded smart aggregates and postembedded smart aggregates reveals that the differences between the two are very limited, demonstrating the effectiveness of interlayer slide detection by using the postembedded smart aggregates. Since the proposed method is limited to detecting a local slide near the sliding surface, a number of actuator-and-sensor pairs should be deployed to monitor the slide in an actual landslide body. Compared with other landslide monitoring techniques, the proposed active sensing approach based on SAs is a low-cost, robust, and real-time approach and can provide a localized damage information. Due to these advantages, the smart aggregates can be easily postembedded into the existing landslide body. Currently, the

proposed technique is still a qualitative method, which can hardly provide accurate parameters of the landslide.

According to the acoustoelastic theory, the velocity of the propagating ultrasonic waves varies in the concrete body subjected to a high level of stress [63]. The differences of the wave velocities will affect the wave propagation in concrete. In this research, the acoustoelastic effect during the loading test is not considered. Further analysis of the results considering the acoustoelastic effect will be investigated. In addition, more tests will be conducted to further verify the validity, reliability, and accuracy of the proposed approach. The accuracy of the proposed approach on the detection of the interlayer slide damage of a structure due to bending force will also be considered.

5. Conclusions

This research, through experimental means, demonstrated that postembedded smart aggregate-based technique for interlayer slide monitoring was feasible and effective in detecting a slide damage. This technique adopts a stress wave-based active sensing approach with piezoceramic transducers. Since a slide event weakened the interface between the two layers and reduced the energy carried by the stress wave crossing the interlayer, the occurrence of the interlayer slide was detected when a significant drop in the detected signal was observed. It was found that both pre- and postembedded SAs effectively detected interlayer slide damage with minimum differences. In addition, the proposed wavelet packet-based interlayer slide indices can qualitatively determine the initiation and development of a slide damage. The index values provided by postembedded SAs reflect the occurrence of the interlayer slide and are consistent with time domain results. In conclusion, the postembedded smart aggregate-based method has the potential for implementation to monitor and detect landslide; however, the determination of the threshold value of the developed sliding

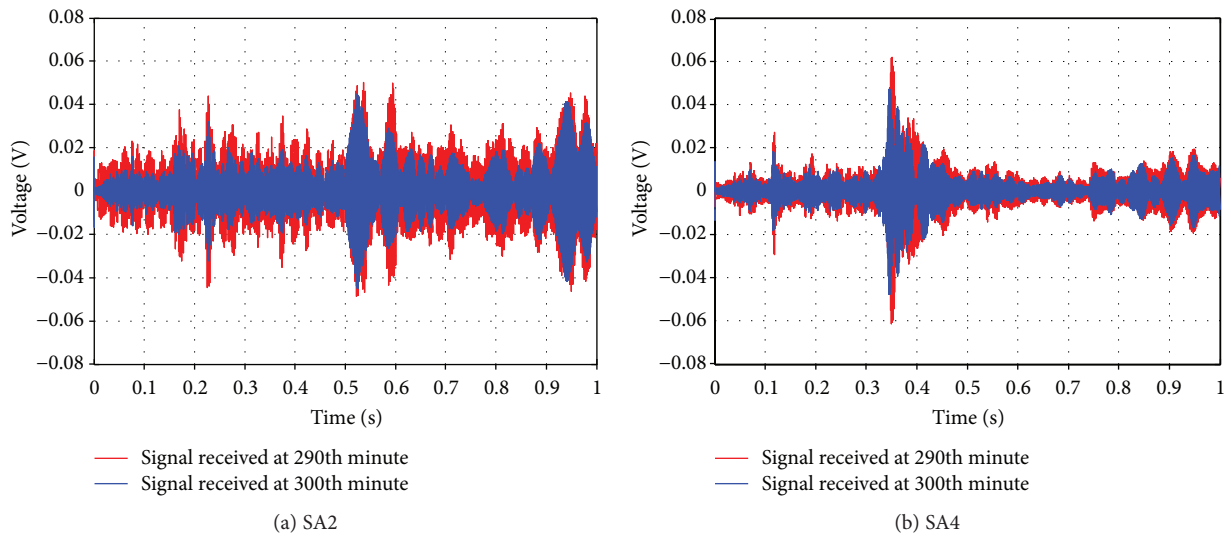


FIGURE 9: Signal received by preembedded SAs before and after slide.

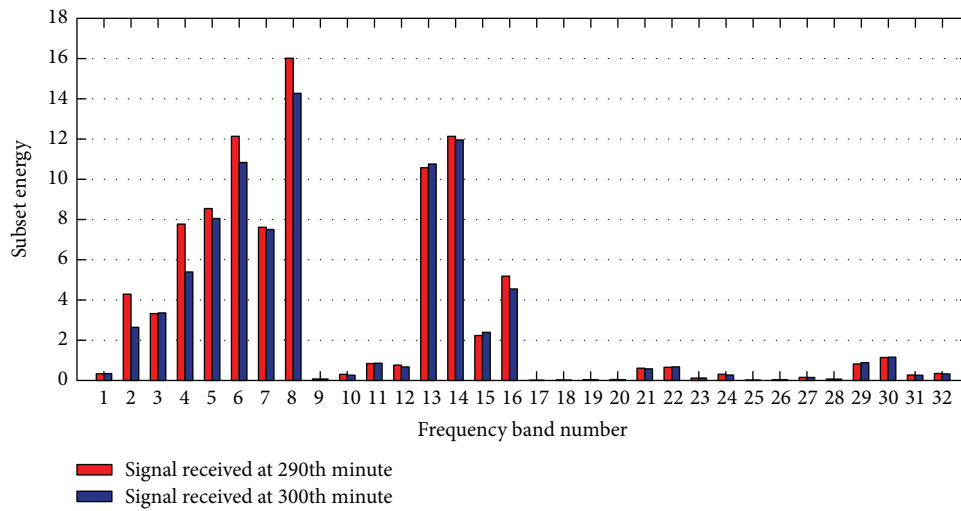


FIGURE 10: Energy vector of the signals received by postembedded SA2 before and after slide.

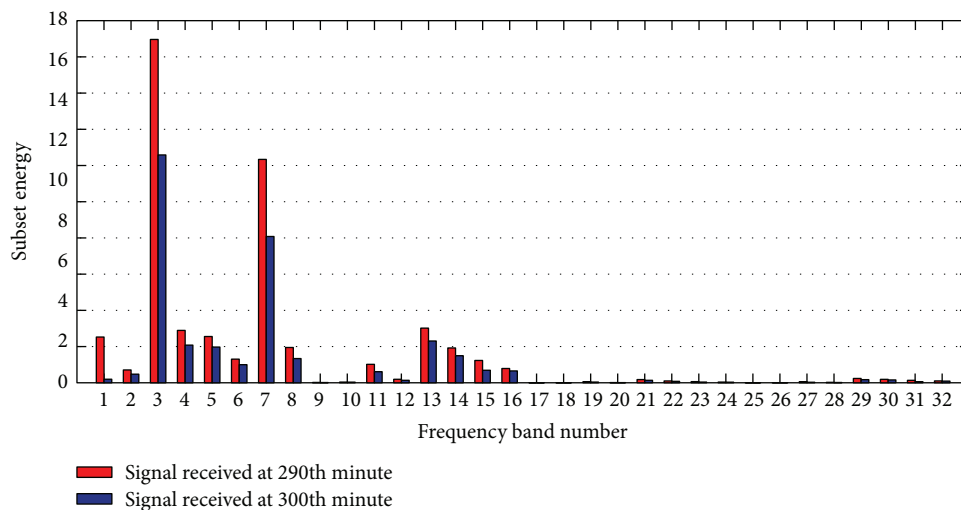


FIGURE 11: Energy vector of the signals received by postembedded SA2 before and after slide.

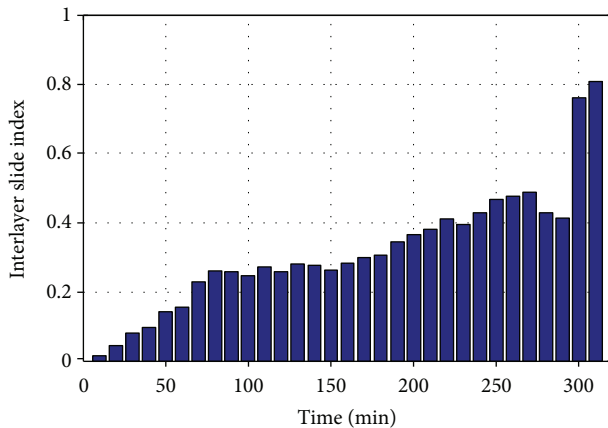


FIGURE 12: Interlayer slide indices of preembedded SA2 throughout the test.

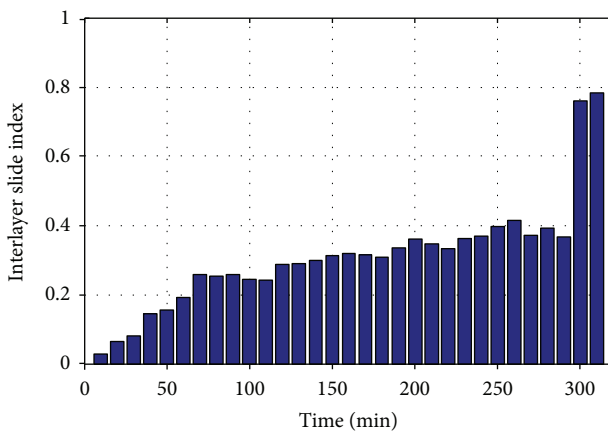


FIGURE 13: Interlayer slide index of postembedded SA4 throughout the test.

interlayer index requires further theoretical and experimental investigation, which will be considered in the authors' future work.

Conflicts of Interest

The authors declare no conflict of interest.

Authors' Contributions

Jianchao Wu and Gangbing Song developed the idea, designed the experiments, and wrote the paper. Qingzhao Kong helped design the experiment and write the paper. Ing Lim helped perform the experiments. Gangbing Song made critical comments to the paper. Jianchao Wu and Qingzhao Kong contributed equally to this work.

Acknowledgments

This work is supported by the Director Foundation of the Institute of Seismology, China Earthquake Administration (IS201726163).

References

- [1] P. Savvaidis, "Existing landslide monitoring systems and techniques," in *From Stars to Earth and Culture. In Honor of the Memory of Professor Alexandros Tsioumis*, pp. 242–258, The Aristotle University of Thessaloniki, Greece, 2003.
- [2] D. Tarchi, N. Casagli, R. Fanti et al., "Landslide monitoring by using ground-based SAR interferometry: an example of application to the Tessina landslide in Italy," *Engineering Geology*, vol. 68, no. 1-2, pp. 15–30, 2003.
- [3] X. Ye, H. Kaufmann, and X. F. Guo, "Landslide monitoring in the Three Gorges area using D-InSAR and corner reflectors," *Photogrammetric Engineering & Remote Sensing*, vol. 70, no. 10, pp. 1167–1172, 2004.
- [4] C. Colesanti and J. Wasowski, "Investigating landslides with space-borne synthetic aperture radar (SAR) interferometry," *Engineering Geology*, vol. 88, no. 3-4, pp. 173–199, 2006.
- [5] G. Bitelli, M. Dubbini, and A. Zanutta, "Terrestrial laser scanning and digital photogrammetry techniques to monitor landslide bodies," *International Archives of Photogrammetry, Remote Sensing and Spatial Information Sciences*, vol. 35, no. B5, pp. 246–251, 2004.
- [6] E. Brückl, F. K. Brunner, and K. Kraus, "Kinematics of a deep-seated landslide derived from photogrammetric, GPS and geophysical data," *Engineering Geology*, vol. 88, no. 3-4, pp. 149–159, 2006.
- [7] S. C. Stiros, C. Vichas, and C. Skourtis, "Landslide monitoring based on geodetically derived distance changes," *Journal of Surveying Engineering*, vol. 130, no. 4, pp. 156–162, 2004.
- [8] M. Haberler-Weber, "Analysis and interpretation of geodetic landslide monitoring data based on fuzzy systems," *Natural Hazards and Earth System Science*, vol. 5, no. 5, pp. 755–760, 2005.
- [9] G. Barla, F. Antolini, M. Barla, E. Mensi, and G. Piovano, "Monitoring of the Beauregard landslide (Aosta Valley, Italy) using advanced and conventional techniques," *Engineering Geology*, vol. 116, no. 3-4, pp. 218–235, 2010.
- [10] J. A. Gili, J. Corominas, and J. Rius, "Using Global Positioning System techniques in landslide monitoring," *Engineering Geology*, vol. 55, no. 3, pp. 167–192, 2000.
- [11] C. Squarzoni, C. Delacourt, and P. Allemand, "Differential single-frequency GPS monitoring of the La Valette landslide (French Alps)," *Engineering Geology*, vol. 79, no. 3-4, pp. 215–229, 2005.
- [12] G. Wang, "Millimeter-accuracy GPS landslide monitoring using precise point positioning with single receiver phase ambiguity (PPP-SRPA) resolution: a case study in Puerto Rico," *Journal of Geodetic Science*, vol. 3, no. 1, pp. 22–31, 2013.
- [13] L. Gui, K. Yin, and T. Glade, "Landslide displacement analysis based on fractal theory, in Wanzhou District, Three Gorges Reservoir, China," *Geomatics, Natural Hazards and Risk*, vol. 7, no. 5, pp. 1707–1725, 2016.
- [14] J. Corominas, J. Moya, A. Lloret et al., "Measurement of landslide displacements using a wire extensometer," *Engineering Geology*, vol. 55, no. 3, pp. 149–166, 2000.
- [15] L. Simeoni and L. Mongioli, "Inclinometer monitoring of the Castelrotto landslide in Italy," *Journal of Geotechnical and Geoenvironmental Engineering*, vol. 133, no. 6, pp. 653–666, 2007.

- [16] B. Sabet Divsholi and Y. Yang, "Combined embedded and surface-bonded piezoelectric transducers for monitoring of concrete structures," *NDT & E International*, vol. 65, pp. 28–34, 2014.
- [17] C. Dumoulin, G. Karaiskos, J. Carette, S. Staquet, and A. Deraemaeker, "Monitoring of the ultrasonic P-wave velocity in early-age concrete with embedded piezoelectric transducers," *Smart Materials and Structures*, vol. 21, no. 4, article 047001, 2012.
- [18] Z. Shi and T. Zhang, "Bending analysis of a piezoelectric curved actuator with a generally graded property for the piezoelectric parameter," *Smart Materials and Structures*, vol. 17, no. 4, article 045018, 2008.
- [19] V. P. Venugopal and G. Wang, "Modeling and analysis of Lamb wave propagation in a beam under lead zirconate titanate actuation and sensing," *Journal of Intelligent Material Systems and Structures*, vol. 26, no. 13, pp. 1679–1698, 2015.
- [20] Y. Yang, V. G. M. Annamdas, C. Wang, and Y. Zhou, "Application of multiplexed FBG and PZT impedance sensors for health monitoring of rocks," *Sensors*, vol. 8, no. 1, pp. 271–289, 2008.
- [21] W. Dansheng, L. Zhi, and Z. Hongping, "A new three-dimensional electromechanical impedance model for an embedded dual-PZT transducer," *Smart Materials and Structures*, vol. 25, no. 7, article 075002, 2016.
- [22] D. Wang, Q. Wang, H. Wang, and H. Zhu, "Experimental study on damage detection in timber specimens based on an electromechanical impedance technique and RMSD-based Mahalanobis distance," *Sensors*, vol. 16, no. 10, p. 1765, 2016.
- [23] C. Dumoulin and A. Deraemaeker, "Design optimization of embedded ultrasonic transducers for concrete structures assessment," *Ultrasonics*, vol. 79, pp. 18–33, 2017.
- [24] Z. F. Shi, H. J. Xiang, and B. F. Spencer Jr, "Exact analysis of multi-layer piezoelectric/composite cantilevers," *Smart Materials and Structures*, vol. 15, no. 5, pp. 1447–1458, 2006.
- [25] G. Song, H. Li, B. Gajic, W. Zhou, P. Chen, and H. Gu, "Wind turbine blade health monitoring with piezoceramic-based wireless sensor network," *International Journal of Smart and Nano Materials*, vol. 4, no. 3, pp. 150–166, 2013.
- [26] Z. Wu and M. Abe, "Structural health monitoring and intelligent infrastructure," in *Proceedings of the First International Conference on Structural Health Monitoring and Intelligent Infrastructure, 13-15 November 2003*, Tokyo, Japan, Taylor & Francis, 2003.
- [27] S. V. Gopinathan, V. V. Varadan, and V. K. Varadan, "A review and critique of theories for piezoelectric laminates," *Smart Materials and Structures*, vol. 9, no. 1, pp. 24–48, 2000.
- [28] X. Wang, L. Ye, Y.-W. Mai, and S. C. Galea, "Designing for piezoelectric ceramic wafers bonded on structures using force transfer criteria," *Smart Materials and Structures*, vol. 9, no. 2, pp. 157–162, 2000.
- [29] M. Kamlah and Q. Jiang, "A constitutive model for ferroelectric PZT ceramics under uniaxial loading," *Smart Materials and Structures*, vol. 8, no. 4, pp. 441–459, 1999.
- [30] S. C. Hwang, C. S. Lynch, and R. M. McMeeking, "Ferroelectric/ferroelastic interactions and a polarization switching model," *Acta Metallurgica et Materialia*, vol. 43, no. 5, pp. 2073–2084, 1995.
- [31] M. Kamlah, "Ferroelectric and ferroelastic piezoceramics – modeling of electromechanical hysteresis phenomena," *Continuum Mechanics and Thermodynamics*, vol. 13, no. 4, pp. 219–268, 2001.
- [32] X.-F. Li, X.-L. Peng, and K. Y. Lee, "The static response of functionally graded radially polarized piezoelectric spherical shells as sensors and actuators," *Smart Materials and Structures*, vol. 19, no. 3, article 035010, 2010.
- [33] H. Miao, S. Dong, and F. Li, "Excitation of fundamental shear horizontal wave by using face-shear (d36) piezoelectric ceramics," *Journal of Applied Physics*, vol. 119, no. 17, article 174101, 2016.
- [34] J. Kim and J.-H. Lee, "Self-moving cell linear motor using piezoelectric stack actuators," *Smart Materials and Structures*, vol. 14, no. 5, pp. 934–940, 2005.
- [35] T. T. Zhang, Z. F. Shi, and B. F. Spencer Jr, "Vibration analysis of a functionally graded piezoelectric cylindrical actuator," *Smart Materials and Structures*, vol. 17, no. 2, article 025018, 2008.
- [36] H. S. Kim, J.-H. Kim, and J. Kim, "A review of piezoelectric energy harvesting based on vibration," *International Journal of Precision Engineering and Manufacturing*, vol. 12, no. 6, pp. 1129–1141, 2011.
- [37] J. Liang and W.-H. Liao, "Energy flow in piezoelectric energy harvesting systems," *Smart Materials and Structures*, vol. 20, no. 1, article 015005, 2010.
- [38] Y. C. Shu, I. C. Lien, and W. J. Wu, "An improved analysis of the SSHI interface in piezoelectric energy harvesting," *Smart Materials and Structures*, vol. 16, no. 6, pp. 2253–2264, 2007.
- [39] H. J. Song, Y. T. Choi, G. Wang, and N. M. Wereley, "Energy harvesting utilizing single crystal PMN-PT material and application to a self-powered accelerometer," *Journal of Mechanical Design*, vol. 131, no. 9, article 091008, 2009.
- [40] F. Ewere, G. Wang, and B. Cain, "Experimental investigation of galloping piezoelectric energy harvesters with square bluff bodies," *Smart Materials and Structures*, vol. 23, no. 10, article 104012, 2014.
- [41] H. A. Sodano, A. Erturk, J. M. Renno, and D. J. Inman, "Modeling of piezoelectric energy harvesting from an L-shaped beam-mass structure with an application to UAVs," *Journal of Intelligent Material Systems and Structures*, vol. 20, no. 5, pp. 529–544, 2009.
- [42] Y.-H. Hsu and C.-K. Lee, "Targeted origin placement for the autonomous gain-phase tailoring of piezoelectric sensors," *Smart Materials and Structures*, vol. 11, no. 3, pp. 444–458, 2002.
- [43] W. J. Staszewski, "Structural health monitoring using guided ultrasonic waves," in *Advances in Smart Technologies in Structural Engineering. Computational Methods in Applied Sciences, vol 1*, J. Holnicki-Szulc and C. M. Soares, Eds., pp. 117–162, Springer, Berlin, Heidelberg, 2004.
- [44] Q. Kong, R. Robert, P. Silva, and Y. Mo, "Cyclic crack monitoring of a reinforced concrete column under simulated pseudo-dynamic loading using piezoceramic-based smart aggregates," *Applied Sciences*, vol. 6, no. 11, p. 341, 2016.
- [45] L. F. Li, B. Xu, and J. M. Chen, "Damage monitoring for a Rc shear wall under rapid cyclic loading with embedded smart aggregates," *Proceedings of the Eleventh International Symposium on Structural Engineering*, vol. I and II, pp. 1432–1437, 2010.
- [46] S. Gupta, J. Gonzalez, and K. J. Loh, "Damage detection using smart concrete engineered with nanocomposite cement-aggregate interfaces," *Structural Health Monitoring 2015:*

- System Reliability for Verification and Implementation, Vols. 1 and 2*, pp. 3033–3040, 2015, <http://www.dpi-proceedings.com/index.php/SHM2015/article/view/1037>.
- [47] C. Zhang, X. Yu, L. Alexander, Y. Zhang, R. Rajamani, and N. Garg, “Piezoelectric active sensing system for crack detection in concrete structure,” *Journal of Civil Structural Health Monitoring*, vol. 6, no. 1, pp. 129–139, 2016.
- [48] Q. Kong, Q. Feng, and G. Song, “Water presence detection in a concrete crack using smart aggregates,” *International Journal of Smart and Nano Materials*, vol. 6, no. 3, pp. 149–161, 2015.
- [49] D. Zou, T. Liu, Y. Huang, F. Zhang, C. Du, and B. Li, “Feasibility of water seepage monitoring in concrete with embedded smart aggregates by P-wave travel time measurement,” *Smart Materials and Structures*, vol. 23, no. 6, article 067003, 2014.
- [50] Q. Feng, Q. Kong, L. Huo, and G. Song, “Crack detection and leakage monitoring on reinforced concrete pipe,” *Smart Materials and Structures*, vol. 24, no. 11, article 115020, 2015.
- [51] T. Liu, Y. Huang, D. Zou, J. Teng, and B. Li, “Exploratory study on water seepage monitoring of concrete structures using piezoceramic based smart aggregates,” *Smart Materials and Structures*, vol. 22, no. 6, article 065002, 2013.
- [52] Q. Kong, R. Wang, G. Song, Z. J. Yang, and B. Still, “Monitoring the soil freeze-thaw process using piezoceramic-based smart aggregate,” *Journal of Cold Regions Engineering*, vol. 28, no. 2, article 06014001, 2014.
- [53] K. Chung, S. Kharkovsky, Q. Kong, and G. Song, “Cure-state monitoring of concrete and mortar specimens using smart aggregates,” in *2014 IEEE International Instrumentation and Measurement Technology Conference (I2MTC) Proceedings*, pp. 304–308, Montevideo, Uruguay, May 2014.
- [54] H. Yin, T. Wang, D. Yang, S. Liu, J. Shao, and Y. Li, “A smart washer for bolt looseness monitoring based on piezoelectric active sensing method,” *Applied Sciences*, vol. 6, no. 11, p. 320, 2016.
- [55] J. Shao, T. Wang, H. Yin, D. Yang, and Y. Li, “Bolt looseness detection based on piezoelectric impedance frequency shift,” *Applied Sciences*, vol. 6, no. 10, p. 298, 2016.
- [56] J. Wu, Q. Kong, W. Li, I. Lim, and G. Song, “Interlayer slide detection using piezoceramic smart aggregates based on active sensing approach,” *IEEE Sensors Journal*, vol. 17, no. 19, pp. 6160–6166, 2017.
- [57] G. Song, H. Gu, and Y.-L. Mo, “Smart aggregates: multifunctional sensors for concrete structures—a tutorial and a review,” *Smart Materials and Structures*, vol. 17, no. 3, article 033001, 2008.
- [58] G. Song, H. Gu, and Y. L. Mo, “Smart aggregates: a distributed intelligent multi-purpose sensor network (DIMSN) for civil structures,” in *2007 IEEE International Conference on Networking, Sensing and Control*, pp. 775–780, London, UK, April 2007.
- [59] B. Xu, T. Zhang, G. Song, and H. Gu, “Active interface debonding detection of a concrete-filled steel tube with piezoelectric technologies using wavelet packet analysis,” *Mechanical Systems and Signal Processing*, vol. 36, no. 1, pp. 7–17, 2013.
- [60] G. Song, H. Gu, Y. L. Mo, T. T. C. Hsu, and H. Dhonde, “Concrete structural health monitoring using embedded piezoceramic transducers,” *Smart Materials and Structures*, vol. 16, no. 4, pp. 959–968, 2007.
- [61] L. Yabin, L. Dongsheng, P. Seyed Mohammad, K. Qingzhao, L. Ing, and S. Gangbing, “Bond-slip detection of concrete-encased composite structure using electro-mechanical impedance technique,” *Smart Materials and Structures*, vol. 25, no. 9, article 095003, 2016.
- [62] T. Jiang, Q. Kong, W. Wang, L. Huo, and G. Song, “Monitoring of grouting compactness in a post-tensioning tendon duct using piezoceramic transducers,” *Sensors*, vol. 16, no. 8, p. 1343, 2016.
- [63] I. Lillamand, J.-F. Chaix, M.-A. Ploix, and V. Garnier, “Acoustoelastic effect in concrete material under uni-axial compressive loading,” *NDT & E International*, vol. 43, no. 8, pp. 655–660, 2010.

Research Article

Dielectric Characteristics of Unsaturated Loess and the Safety Detection of the Road Subgrade Based on GPR

Gao Lv ¹, Jie Yang,¹ Ning Li,¹ Dexiu Hu,¹ Yan Zhang,² and Feng Zhao³

¹School of Water Resources and Hydro-Electric Engineering, Xi'an University of Technology, Xi'an 710048, China

²School of Architecture and Civil Engineering, Xi'an University of Science and Technology, Xi'an 710054, China

³Geochemical Exploration Team of Shaanxi Geological Mineral Survey Group, Xingfu Road No. 7, Xincheng District, Xi'an 710043, China

Correspondence should be addressed to Gao Lv; lvgao116@xaut.edu.cn

Received 28 July 2017; Revised 16 November 2017; Accepted 26 November 2017; Published 31 January 2018

Academic Editor: Lei Yuan

Copyright © 2018 Gao Lv et al. This is an open access article distributed under the Creative Commons Attribution License, which permits unrestricted use, distribution, and reproduction in any medium, provided the original work is properly cited.

We present a moisture content and permittivity model to simultaneously detect and estimate defects in loess subgrade. Based on the ground-penetrating radar (GPR) method, the dielectric properties of loess in the northwest of China and the imaging feature of the moisture content of different strata were studied. The relative permittivity of loess with different moisture contents was experimented in the laboratory. It was found that the relative permittivity of unsaturated loess was positively related to moisture content. The relationship between relative permittivity and moisture content in different antenna frequencies of GPR was analyzed. Electromagnetic wave reflection rules in the loess interface were studied using the numerical method with different moisture contents. With the increase in moisture content, the amplitude of GPR was increased. When the above conclusions were applied in the engineering practices, there are good effects to detect the defects of the road subgrade. It is a significant guidance for determining the qualitative research of defects in the roadbed.

1. Introduction

Loess subgrade in the area of northwestern China often appears to collapse, to settle, and to have other problems [1, 2].

So it is necessary to earlier detect the defects and cavities in the road subgrade. Then, targeted prevention and treatment will be applied, and the potential losses caused by roadbed subsidence will be avoided. At present, there are many kinds of nondestructive testing (NDT) technologies of subgrade defect, for example, ground-penetrating radar (GPR), hammer sounding, acoustic tomography, falling weight deflectometer (FWD), and time-domain reflectometry (TDR) [3]. Hereinto, GPR is a kind of geophysical detection technology based on electromagnetic wave, which is nondestructive, low-cost, portable, effective, fast, and accurate [4]. The detection principle of GPR is as follows: When the emitted electromagnetic waves (frequency range is 10–2200 MHz) transmit in the underground, the electromagnetic waves, arriving at

the interface of inhomogeneous permittivity, will produce the phenomenon of reflection and refraction. And then, the signals of reflected waves, that is, echo, can reflect the characteristics of underground medium [5, 6]. As a nondestructive testing technology, GPR has received more and more attention [7–9].

The main wave characteristics of GPR data received by sounding road pavement deformations were revealed by the theoretical and experimental studies of subgrade soils of roads [10]. In order to achieve the best methodology for subgrade cracking detection, different GPR systems, both antenna configuration and frequencies, were tested [11]. Experimental results from field and laboratory investigations using a ground-coupled GPR, dielectric measurement, magnetic imaging tomography (MIT), and DCP tests were presented [12]. Several GPR methods and analysis techniques were used to nondestructively investigate the electromagnetic behavior of subasphalt compacted clayey layers and subgrade soils in unsaturated conditions [13].

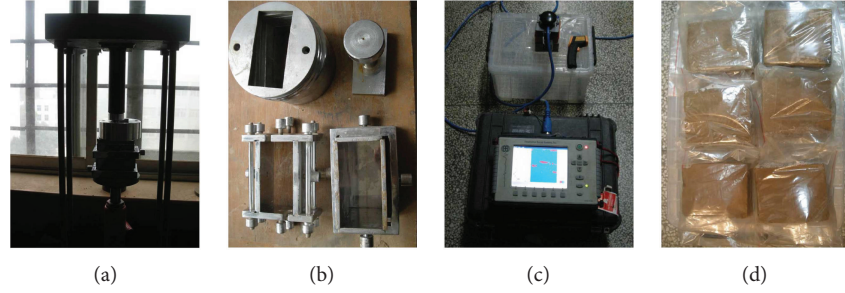


FIGURE 1: (a) Compacted equipment, (b) sample moulds, (c) GPR device, and (d) the prepared loess samples.

At present, the study of permittivity of unsaturated loess is few, and the direct measurement of the permittivity of unsaturated loess by GPR has little result in this field. In this paper, the empirical relationship between permittivity and unsaturated loess moisture content was obtained by the direct test with the different frequencies of the GPR antenna. The mechanism and law of the GPR wave reflection imaging in the unsaturated loess interface have been studied. The above results were directly applied to detect defects in an engineering project.

2. Dielectric Property of the Loess

2.1. Experimental Procedures and Test Parameters. In this paper, loess is the object of the study. The GPR (SIR-3000 series, Geophysical Survey Systems Inc.) was employed to measure the permittivity of loess in laboratory experiment. The experimental procedures are the following:

- (1) The soil samples were collected from a construction site and sealed for later use.
- (2) The soil samples were manually screened in order to obtain the fine powder.
- (3) The samples in which the moisture content was from 10% to 37% were prepared.
- (4) The plane strain test apparatus was utilized for the sample preparation. The size was 5 cm by 10 cm by 10 cm. The reaction frame was utilized for pressuring samples. After 48-hour standing, the reaction frame was used to compact samples. Then, the soil samples were sealed in plastic bags.
- (5) According to the sizes of the samples, the selected antenna frequencies were 400 MHz, 900 MHz, and 2 GHz, respectively. The soil samples were scanned, and the data was collected.
- (6) The measured data postprocessing was done by the RADAN5 Software.

The devices in the experiment and the prepared soil samples are shown in Figure 1, and the antenna parameters of GPR are shown in Table 1.

2.2. Test Principle of the Loess Permittivity. The calculation model is shown in Figure 2. The travel time of the GPR wave

TABLE 1: The antenna parameters of GPR.

| Frequency | 2 GHz | 900 MHz | 400 MHz |
|-------------------------|---------|---------|---------|
| Emissivity | 350 kHz | 100 kHz | 100 kHz |
| Ranges (ns) | 12 | 20 | 40 |
| Scanning speed (scan/s) | 300 | 50 | 50 |
| Gain | 1 | 2 | 5 |

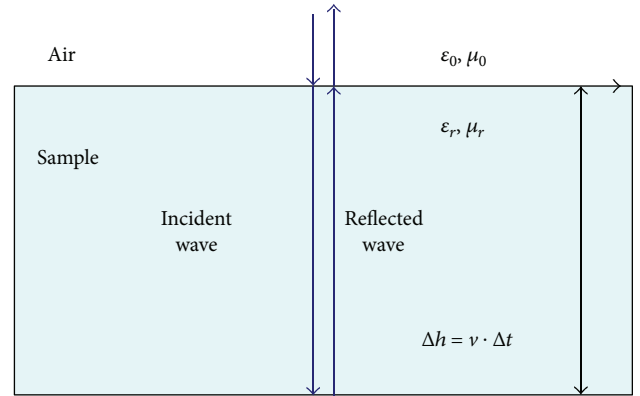


FIGURE 2: Wave velocity calculation model of GPR.

in the medium is also the object of the study. The reflection positions of electromagnetic wave in the sample interfaces are analyzed. Meanwhile, according to the travel time, the actual wave velocity of the GPR wave can be calculated.

The electromagnetic waves propagate in the loess samples and reach the bottom of the sample after the travel time Δt . Then, the reflected part of the electromagnetic waves will propagate to the surface of the loess samples after the travel time Δt and will be received by GPR equipment. The value of the travel time Δt can be read from the scanning data of the GPR. Meanwhile, the travel length of the electromagnetic wave Δh can be directly measured by the size of the sample. Therefore, the actual wave velocity of the electromagnetic waves propagating in the loess samples can be calculated by the formula $v = \Delta h / \Delta t$. The relative permittivity of the loess samples can be calculated as follows:

$$\sqrt{\epsilon_r} = c \frac{\Delta h}{\Delta t}. \quad (1)$$

2.3. Calculation of the Permittivity. The soil samples were scanned by the GPR antenna. The antenna frequencies were

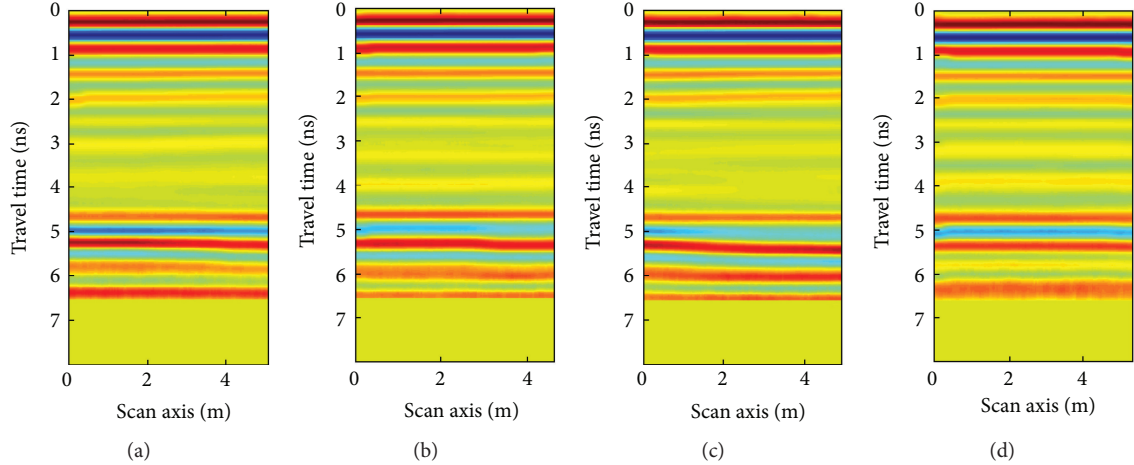


FIGURE 3: (a–d) The GPR images of loess with the moisture contents 10%, 19%, 28%, and 37%, respectively.

TABLE 2: Loess permittivity with different moisture contents under different frequencies.

| Moisture content (%) | $\epsilon_{\text{RADAN900}}$ | $\epsilon_{\text{RADAN400}}$ | $\epsilon_{\text{RADAN2G}}$ |
|----------------------|------------------------------|------------------------------|-----------------------------|
| 10 | 4.06 | 3.96 | 5.21 |
| 13 | 4.82 | 4.26 | 6.01 |
| 16 | 5.98 | 5.78 | 7.12 |
| 19 | 6.99 | 6.65 | 8.93 |
| 22 | 8.98 | 8.37 | 10.98 |
| 25 | 11.43 | 10.86 | 12.88 |
| 28 | 13.21 | 12.56 | 14.98 |
| 31 | 15.43 | 14.77 | 17.12 |
| 34 | 18.12 | 17.36 | 19.57 |
| 37 | 20.98 | 20.32 | 22.23 |

400 MHz, 900 MHz, and 2 GHz, respectively. The measured data was processed by the RADAN5 Software through filtering the wave and removing the background noise. The data of 2 GHz as an example are shown in Figure 3.

The different imaging features in the process of the electromagnetic wave propagation are shown in Figures 3(a)–3(d). The reflected waves from 1 ns to 3 ns are obvious, due to the surface reflection of loess samples and self-deconvolution of GPR wavelets. The propagation range of the electromagnetic waves in the samples is mainly from 3 ns to 6 ns. In this range, there is no obvious reflection of electromagnetic wave. The electromagnetic waves keep good damping characteristics. It is indicated that the samples are relatively homogeneous. The reflected waves from 6 ns to 8 ns are due to the reflection of the bottom surface of the samples. Because the change of soil moisture content directly affects the soil permittivity, there must be differences in the GPR images. Therefore, GPR reflection amplitudes increase with the increase in moisture content of soil samples from 10% to 37%.

The permittivity of the samples with different moisture contents via applying different frequencies can be calculated by (1). The values of the permittivity are shown in Table 2.

For the same sample, different frequencies can induce the different values of permittivity. The reason is that the electromagnetic waves of different frequencies have differently impacted the intrinsic nature of loess permittivity. Therefore, the same sample exhibits different test values of the permittivity under different frequencies, which is considered a standard and an important basis of the influence on antenna frequency.

3. The Relationship of Permittivity and Moisture Content under Different Frequencies

3.1. Experience Curves of Permittivity and Moisture Content.

(1) Topp formula [14], obtained by experiment fitting the empirical cubic formula

$$\epsilon_r = 3.03 + 9.3\theta_v + 146.0\theta_v^2 - 76.6\theta_v^3, \quad (2)$$

$$\theta_v = -5.3 \times 10^{-2} + 2.92 \times 10^{-2}\epsilon_r - 5.5 \times 10^{-4}\epsilon_r^2 + 4.3 \times 10^{-6}\epsilon_r^3, \quad (3)$$

where ϵ_r is the permittivity and θ_v is the volume of moisture content. In (2), the moisture content is used to calculate the permittivity. On the contrary, the permittivity is used to calculate the moisture content in (3).

(2) CRIM (complex reflective index model) [15] formula, an arithmetic square root model

$$\sqrt{\epsilon} = (1 - \phi)\sqrt{\epsilon_s} + S_w\phi\sqrt{\epsilon_w} + (1 - S_w)\phi\sqrt{\epsilon_a}. \quad (4)$$

The subscripts s , w , and a represent the soil, water, and air, respectively. ϕ represents the moisture content, and S_w is on behalf of the moisture saturation. On the condition that the water permittivity is 81 and the loess permittivity is 5, so (4) can be simplified as

$$\sqrt{\epsilon} = \phi\sqrt{\epsilon_m} + (1 - \phi)\sqrt{\epsilon_w}. \quad (5)$$

(3) Dobson [16] formula

$$\epsilon_{\text{soil}}^\alpha = 1 + \frac{\rho_b}{\rho_{ss}}(1 - \epsilon_{ss}^\alpha) + m_v^\beta(\epsilon_{fw}^\alpha - 1). \quad (6)$$

ϵ_{soil} refers to the soil permittivity. ρ_b and ρ_{ss} refer to the densities of dry soil and soil skeleton, respectively. E_{ss} refers to the solid permittivity. m_v refers to the solid quality. Empirical coefficient α is 0.65 and β is 1.0~1.17 (from sandy soil to clay).

3.2. The Measured Permittivity Results under Different Frequencies. The samples with different moisture contents were tested by the antenna of 400 MHz, 900 MHz, and 2 GHz. The scatter diagrams of the permittivity and moisture content were fitted. The optimum fitting curves are shown in Figure 4.

As shown in Figure 4, the experimental results are near to the experiential fitting curves. It demonstrates the correctness of the experimental results. Under the same frequency of the GPR antenna, sample permittivity is increased with the increase in moisture content. At the same time, the permittivity of the sample with the same moisture content is also increased with the increase in frequency. The antenna frequencies applied in the experiment are 400 MHz, 900 MHz, and 2 GHz, respectively. So the permittivity of the antenna frequency of 400 MHz is minimal, and that of 2 GHz is maximal.

There is a distance between the blue points and the formula lines (black). It could be briefly analyzed as the following. First, the GPR method is a nondestructive method. So it is always less accurate than an empirical formula established by an invasive method. Next, the GPR method is easily subject to external disturbances.

The conjugate gradient method is used to describe the mathematical relationship between the moisture content and permittivity. Meanwhile, the linear models are established according to the former testing data.

$$\begin{aligned} \epsilon_r &= 0.61 \cdot \theta_v + 1.58, f = 400 \text{ MHz}, \\ \epsilon_r &= 0.63 \cdot \theta_v + 1.81, f = 900 \text{ MHz}, \\ \epsilon_r &= 0.64 \cdot \theta_v + 3.18, f = 2 \text{ GHz}. \end{aligned} \quad (7)$$

The fitting calculation results show that the conjugate gradient method can solve the correction factors well in one dimensional model. And the model can be applied directly to the practice and is a reliable tool for moisture content of similar projects.

4. Numerical Simulation of the Interface Reflection Mechanism of Unsaturated Loess

Compared with the experimental method, an ideal effect of wave propagation can be received by the numerical simulation method. The numerical method can avoid the defects of the test method, such as inhomogeneous medium, uneven compaction degree of large-scale samples, and measurement error. In this section, imaging features of different permittivity values were comparatively analyzed. Further, the influence of the dielectric constant on radar echo waveform was studied.

4.1. Geoelectric Model of Interface Reflection of Unsaturated Loess. GprMax2.0 software is used for numerical simulation

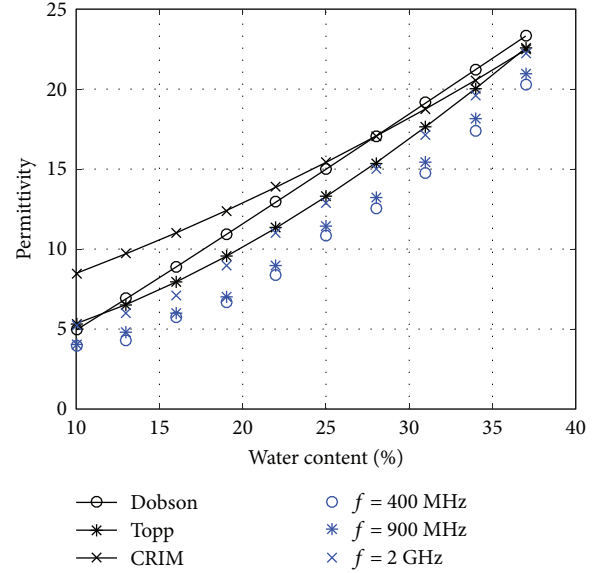


FIGURE 4: The experiential fitting curves and experimental results of the loess with different moisture contents under different frequencies (the black symbols represent the experiential results, and the blue symbols represent the experimental results).

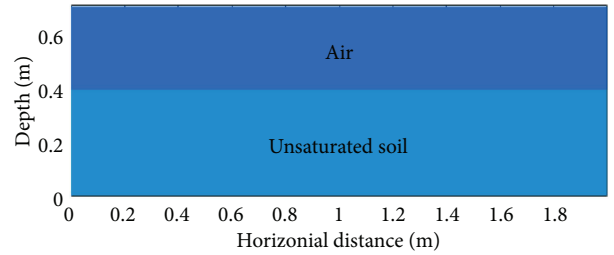


FIGURE 5: The schematic diagram of the numerical model of unsaturated loess.

in this article. GprMax is open-source software that simulates electromagnetic wave propagation. It solves Maxwell's equations in 3D using the finite-difference time-domain (FDTD) method. GprMax was designed for modelling GPR [17–19].

The geoelectric model of shallow loess was designed according to the waveform comparison. Keeping the other parameters held, the influence of permittivity on GPR imaging was investigated and the quantification of the echo waveform was deeply analyzed. The schematic diagram of the specific geoelectric model is shown in Figure 5.

The horizontal distance of this model is 2.0 m. The depth is 0.7 m. The cell size is 0.0025 m by 0.0025 m. The time depth is 20 ns. The parameters of the first layer are as follows. The permittivity is 0. The electrical conductivity is 0.00 S/m. The thickness of the first layer is 30 cm. The permittivity values of the second layers are 5, 10, 20, 30, 40, and 50, respectively. The electrical conductivity is 0.00001 S/m. The thickness of the second layer is 0.4 m. The wavelet frequency is set as 900 MHz. The excitation source is the Ricker wavelet. In the numerical simulation, there are 180 step calculations and each step calculation contains 3391 times.

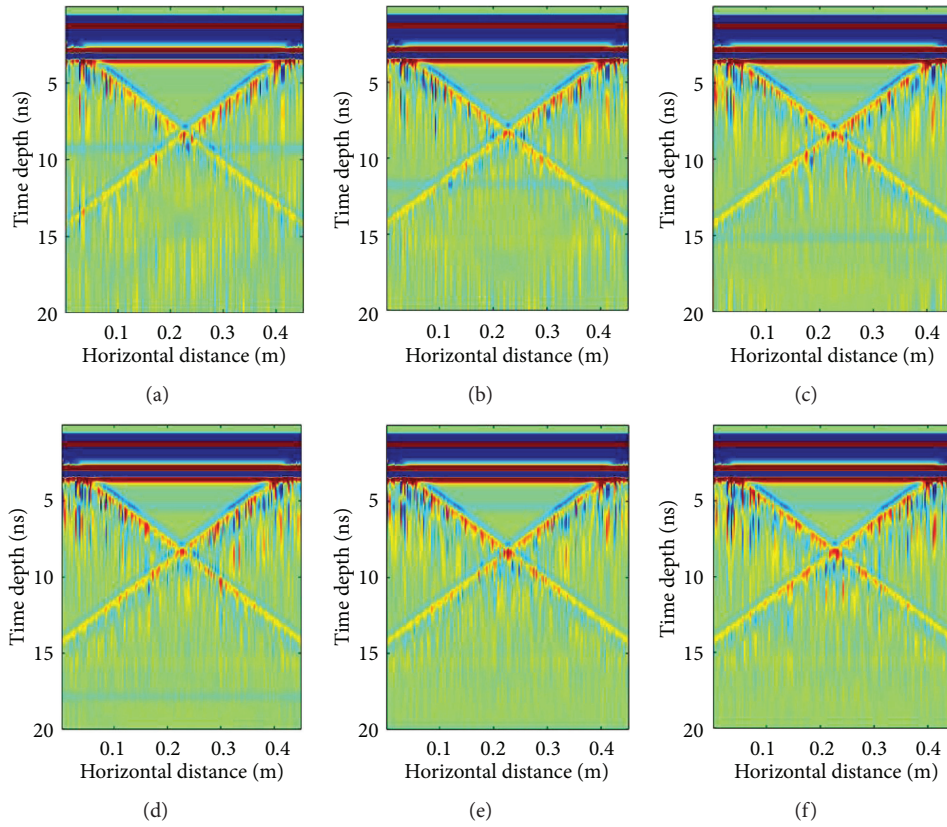


FIGURE 6: (a–f) The GPR imaging of the subgrade of unsaturated loess when ϵ_r are 5, 10, 20, 30, 40, and 50, respectively.

4.2. *The Amplitude Rule of Reflected Wave on Different Permittivity Layers.* According to the above numerical calculation, the reflected characteristics of the GPR waves in different moisture content interfaces can be observed. The permittivity values of the grassroot level of unsaturated loess were set as 5, 10, 20, 30, 40, and 50, respectively. Then, the simulate calculation was done. The stratigraphic sections were obtained and shown in Figure 6.

In Figure 6, the interface reflection trend of permittivity is obvious. The reflection amplitude shows an increasing trend at the position of 3 ns. It is indicated that the interface inflection obviously increases with the increase in the moisture content. But it cannot give quantitative descriptions only from the stratigraphic sections. So it is necessary to comparatively analyze the amplitude value.

The method extracts the single wave in the forward modeling data. Obviously, the interface reflection interval is presented as the characteristics of “positive-negative-positive.” This dissertation applies the data of peaks and troughs, as shown in Figure 7.

In Figure 7, the first crest of the echo curves of interface reflection appears when STEPS = 490. The wave trough appears when STEPS = 545, and the absolute value of the wave valley is the maximum point of the reflection amplitude. With the increases in moisture content on the interface, the reflection amplitudes of GPR are enlarged accordingly. There is a clear mathematical relationship between the maximum reflection amplitude and permittivity of medium.

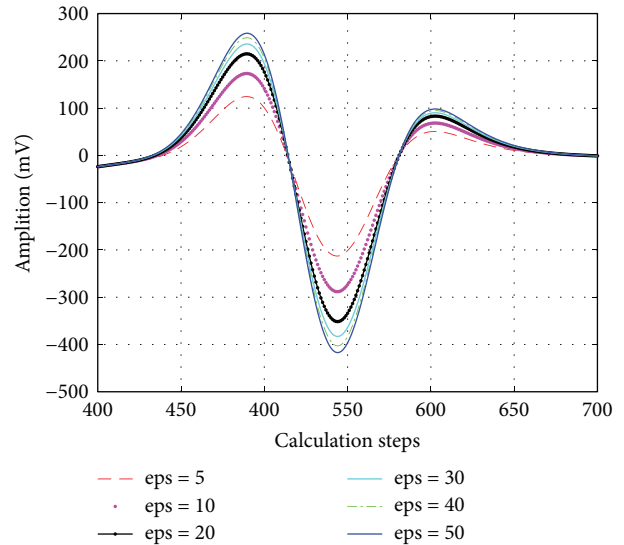


FIGURE 7: Single waves of unsaturated loess interface echoes.

The amplitude values of interface reflection are shown in Table 3.

From the wave amplitudes in Table 3, it can be clearly seen that the absolute values of the maximum amplitude and minimum amplitude are increased, respectively, with the increase in the permittivity of the loess.

TABLE 3: Reflection amplitude under different moisture contents on the loess interface.

| | $\epsilon_r = 5$ | $\epsilon_r = 10$ | $\epsilon_r = 20$ | $\epsilon_r = 30$ | $\epsilon_r = 40$ | $\epsilon_r = 50$ |
|-------------------|------------------|-------------------|-------------------|-------------------|-------------------|-------------------|
| Amplitude maximum | 124.37 | 173.19 | 214.77 | 235.61 | 248.89 | 258.37 |
| Amplitude minimum | -212.89 | -288.34 | -351.61 | -383.03 | -402.97 | -417.21 |

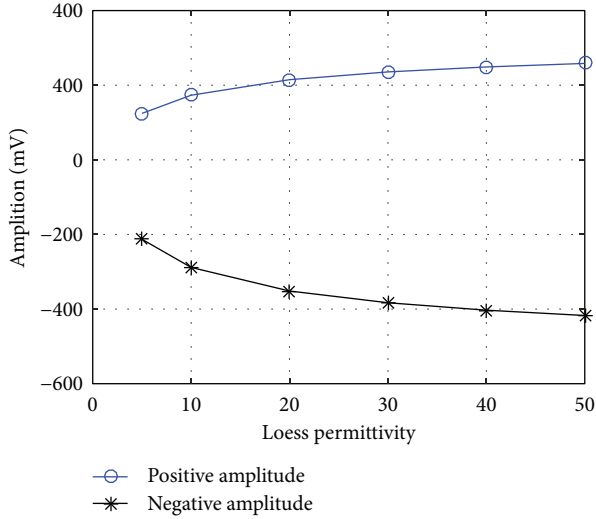


FIGURE 8: Amplitudes of unsaturated loess interface echoes.

Therefore, the mathematical relation between the reflection amplitude of loess interfaces and permittivity is obtained and shown as follows.

$$\text{Peak: } A_{\text{peak}} = -0.08\epsilon_r^2 - 7.04\epsilon_r + 100.42, \quad (8)$$

$$\text{Trough: } A_{\text{trough}} = 0.12\epsilon_r^2 - 10.79\epsilon_r - 176.5.$$

Based on the result of numerical calculation, the empirical correlation of the reflection amplitude and permittivity is shown in Figure 8.

5. Actual Measurements and Analysis of Loess Roadbed Diseases

5.1. Project Overview. The Bin He Road built in 2013 is isolated on the south of Wei He River in Baoji city, China. The road was established on the site of the river bed post, and the foundation is roller-compacted loess. In 2016, sewage pipes were laid at the depth of 10 meters below the surface using the straight push method. And then, poor geological disasters arise, such as surface collapse and surface subsidence. The specific positions are pinpointed in Figure 9.

5.2. The GPR Sections of the Subgrade before and after Road Maintenance. According to the practical situation in the spot, the pavements above the sewage pipe were scanned directly using the 200 MHz and 400 MHz antenna, respectively. The testing purpose is to identify the subgrade of the abnormal area which is located between the road surfaces and pipes. Furthermore, the hidden area of risk will be repaired early, and the sinking or void of the road will be avoided.

The geological sections of 40 m length at the horizontal distance between point 360 and point 380 of the Bin He Road were extracted. The GPR grams of the subgrade before and after road maintenance are shown in Figures 10 and 11, respectively.

These comparison sections show the profile of before and after maintenance using the GPR antenna of 200 MHz. Figure 10(a) shows the obvious points, such as D1, D2, D3, D4, D5, and D6. Hereinto, D2 and D5 are near-surface reflection anomalies. Both of them belong to very serious potential hazards. The reflection signal intensity curves of D1 were inferred as water-rich drawbacks (refer to the laws of Section 4.2).

To avert disasters, the test results were immediately sent to the administration. The measured locations were repaired. And then, the former areas were measured again. The geological sections are shown in Figure 10(b). The consolidated methods were timely taken, and the dangerous situation of D2 and D5 disappeared. In the meantime, the foundation of D1 and D4 was also consolidated and compacted.

These comparison sections show the profile of before and after maintenance using the GPR antenna of 400 MHz. Figure 11(a) shows the obvious points such as d1, d2, and d3. Hereinto, d2 and d3 are near-surface reflection anomalies corresponding to the D2 and D5 in Figure 10(a). In the similar way, d1 corresponds to D1. Apparently, there are certain differences in estimating depth and radius of the targets by different frequency antennas.

According to the specific points to find out the defect and repaired, there is no remarkable abnormality as shown in Figure 11(b). Timely detection and maintenance of the roadbed are effective ways to enhance the integrity and stability of the subgrade. The hidden trouble of the structure can be detected in time, and accident can be avoided by the damage detection and diagnosis.

The antenna of GPR has a constraint condition they must simultaneously satisfy: detecting depth and detecting precision. In general, the bigger the value of the principal frequency, the smaller the detecting depth. By comparing the quantity of the target exposed in Figures 10 and 11, it can be seen that the measurements using the 200 MHz GPR antenna are more accurate. And the antenna frequency change plays a vital role in the precision, which reflected the general rule.

The field excavation of the D1 point is shown in Figure 12.

The point D1 excavation verifies that the anomaly characteristics of the GPR imaging accord with the true position of the subterranean cavitation. The horizontal position about 360 meters has a cylindrical hole about 1 m in diameter and 1 m deep. This shows that geophysical methods have prompt, high-precision, and nondevastating advantages in environmental protection.



FIGURE 9: Location of the project.

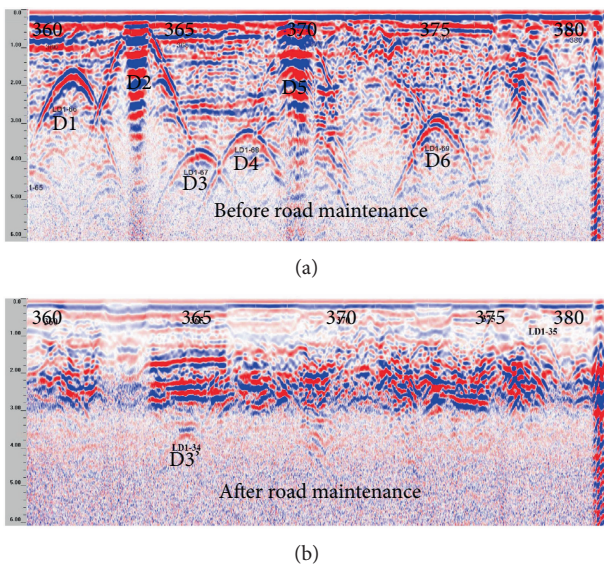


FIGURE 10: (a) GPR sections by the 200 MHz antenna before road maintenance. (b) GPR sections by the 200 MHz antenna after road maintenance.

6. Conclusions

Through the research on the loess permittivity at different moisture contents and the influence of the antenna frequency on the loess permittivity, the conclusions are as follows:

- (1) The experiment and comparison results show that the loess permittivity increases along with the broadening of moisture content in the loess soil. In addition, the same sample produces different permittivity values under different frequencies, and the

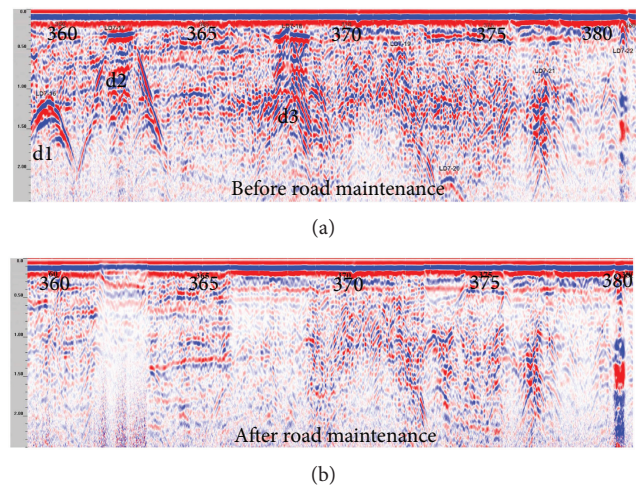


FIGURE 11: (a) GPR sections by the 400 MHz antenna before road maintenance. (b) GPR sections by the 400 MHz antenna before road maintenance.

loess permittivity increases when the frequencies are increased.

- (2) With the increase in the moisture content in unsaturated loess, the permittivity and the interface reflection amplitudes markedly improved. There is a corresponding increase in the absolute value of the maximum amplitude and the minimum amplitude of the reflection amplitudes with increasing permittivity. And then, this law is established.
- (3) From the study of characteristics of the loess permittivity and the interfacial reflection, we can gain some understanding of actual detection. Systemic discusses with the geology flaw recognition and flaw measurements have been made.



FIGURE 12: The verification of excavation.

Conflicts of Interest

The authors declare that they have no conflicts of interest.

Acknowledgments

The authors gratefully acknowledge the financial supports by the China Postdoctoral Science Foundation (Grant no. 2017M613175). And the work was supported by the National Science Foundation of China (Grant nos. 41301597, 11572246, and 51509200) and the Open Foundation of State Key Laboratory Base of Eco-Hydraulic Engineering in Arid Area (Grant no. 2016ZZKT-8).

References

- [1] E. Forte and M. Pipan, "Review of multi-offset GPR applications: data acquisition, processing and analysis," *Signal Processing*, vol. 132, pp. 210–220, 2017.
- [2] P. Dobriyal, A. Qureshi, R. Badola, and S. A. Hussain, "A review of the methods available for estimating soil moisture and its implications for water resource management," *Journal of Hydrology*, vol. 458–459, pp. 110–117, 2012.
- [3] S. K. Verma, S. S. Bhadauria, and S. Akhtar, "Review of nondestructive testing methods for condition monitoring of concrete structures," *Journal of Construction Engineering*, vol. 2013, Article ID 834572, 11 pages, 2013.
- [4] A. Sadoun, M. Broutin, and J. M. Simonin, "Assessment of HWD ability to detect debonding of pavement layer interfaces," in *8th International Conference on Mechanisms of Cracking and Debonding in Pavements*, pp. 763–769, Springer, Dordrecht, 2016.
- [5] F. Tosti and A. Umiliaco, "FDTD simulation of the GPR signal for preventing the risk of accidents due to pavement damages," *International Journal of Interdisciplinary Telecommunications and Networking*, vol. 6, no. 1, pp. 1–9, 2014.
- [6] T. Inazaki, S. Imamura, H. Kisanuki, and K. Hayashi, "Combined GPR and non-contact surface wave measurements for the investigation of pavement structure," in *Symposium on the application of geophysics to engineering and environmental problems*, pp. 308–313, Society of Exploration Geophysicists and Environment and Engineering Geophysical Society, Austin, TX, USA, 2015.
- [7] K. T. Rudahl and S. E. Goldin, "A Smart Geofabric for Detecting Transportation Substructure Damage," in *DEStech Transactions on Engineering and Technology Research, 1st International Conference on Transportation Infrastructure and Materials (ICTIM 2016)*, pp. 767–773, University of Chang'an Press, Xi'an, 2016.
- [8] T. Saarenketo, *Electrical Properties of Road Materials and Subgrade Soils and the Use of Ground Penetrating Radar in Traffic Infrastructure Surveys*, Oulu university press, Finland, 2006.
- [9] A. Benedetto, "Water content evaluation in unsaturated soil using GPR signal analysis in the frequency domain," *Journal of Applied Geophysics*, vol. 71, no. 1, pp. 26–35, 2010.
- [10] R. E. Smith, D. T. Anderson, J. E. Ball, A. Zare, and B. Alvey, "Aggregation of Choquet integrals in GPR and EMI for handheld platform-based explosive hazard detection," in *Proceeding Volume 10182, Detection and sensing of mines, explosive objects, and obscured targets XXII*, p. 1018217, Anaheim, CA, USA, 2017.
- [11] J. Xiao and L. Liu, "Permafrost subgrade condition assessment using extrapolation by deterministic deconvolution on multi-frequency GPR data acquired along the Qinghai-Tibet Railway," *IEEE Journal of Selected Topics in Applied Earth Observations and Remote Sensing*, vol. 9, no. 1, pp. 83–90, 2016.
- [12] L. L. Fedorova, D. V. Savvin, M. P. Fedorov, and A. S. Struchkov, "GPR monitoring of cryogenic processes in subgrade soils," in *2016 16th International Conference on Ground penetrating radar (GPR)*, Hong Kong, 2016, IEEE.
- [13] V. Marecos, M. Solla, S. Fontul, and V. Antunes, "Assessing the pavement subgrade by combining different non-destructive methods," *Construction and Building Materials*, vol. 135, pp. 76–85, 2017.
- [14] G. C. Topp, J. L. Davis, and A. P. Annan, "Electromagnetic determination of soil water content: measurements in coaxial transmission lines," *Water Resources Research*, vol. 16, no. 3, pp. 574–582, 1980.
- [15] S. Laurens, J. P. Balayssac, J. Rhazi, G. Klysz, and G. Arliguie, "Non-destructive evaluation of concrete moisture by GPR: experimental study and direct modeling," *Materials and Structures*, vol. 38, no. 9, pp. 827–832, 2005.
- [16] M. C. Dobson, F. T. Ulaby, M. T. Hallikainen, and M. A. El-Rayes, "Microwave dielectric behaviour of wet soil part II: dielectric mixing models," *IEEE Transactions on Geoscience and Remote Sensing*, vol. GE-23, no. 1, pp. 35–46, 1985.
- [17] C. Warren, A. Giannopoulos, and I. Giannakis, "gprMax: open source software to simulate electromagnetic wave propagation for ground penetrating radar," *Computer Physics Communications*, vol. 209, pp. 163–170, 2016.
- [18] I. Giannakis, A. Giannopoulos, and C. Warren, "A realistic FDTD numerical modeling framework of ground penetrating radar for landmine detection," *IEEE Journal of Selected Topics in Applied Earth Observations and Remote Sensing*, vol. 9, no. 1, pp. 37–51, 2016.
- [19] I. Giannakis and A. Giannopoulos, "A novel piecewise linear recursive convolution approach for dispersive media using the finite-difference time-domain method," *IEEE Transactions on Antennas and Propagation*, vol. 62, no. 5, pp. 2669–2678, 2014.

Research Article

Performance Deterioration of Heavy-Haul Railway Bridges under Fatigue Loading Monitored by a Multisensor System

Zhiwu Yu,^{1,2} Zhi Shan ,^{1,2} Ju Yuan,^{1,2} and Xiao Li^{1,2}

¹School of Civil Engineering, Central South University, 68 South Shaoshan Road, Changsha 410004, China

²National Engineering Laboratory for High-Speed Railway Construction, Central South University, Changsha 410004, China

Correspondence should be addressed to Zhi Shan; zhishan@csu.edu.cn

Received 24 August 2017; Accepted 8 November 2017; Published 9 January 2018

Academic Editor: Yinan Zhang

Copyright © 2018 Zhiwu Yu et al. This is an open access article distributed under the Creative Commons Attribution License, which permits unrestricted use, distribution, and reproduction in any medium, provided the original work is properly cited.

Heavy-haul railway bridges play an increasingly essential role in the transportation in China due to the increasing transport volume. The performance deterioration of the scale models of a typical heavy-haul railway bridge under fatigue loading is monitored in this work, based on a multisensor system including the fiber-reinforced polymer optical fiber Bragg grating and electrical resistance strain gauges, linear variable displacement transducer, and accelerometer. Specifically, by monitoring/observing on the failure mode, fatigue life, load-midspan deflection response, material strain development, and so forth, this work develops an *S-N* model by comparing the relationship between fatigue life and rebar stress range with that between fatigue life and load level and proposes a damage evolution model considering the coupling of the stiffness degradation and inelastic deformation of specimens. It is found that the fatigue life of specimens is determined by the fatigue life of the rebar at the bottom and it may be lower than 2.0 million cycles with a 30-ton axle weight when environmental factors are taken into account. The predictions of the models agree well with experimental results. Therefore, this work furthers the understanding of the fatigue performance deterioration of the bridges by using a multisensor system.

1. Introduction

It is required to observe on the performance deterioration of heavy-haul railway bridges under fatigue loading due to the increasing transport volume and train axle weight of trains in China [1–3]. Specifically, the train axle weight is being increased from 23 tons to 30 tons and the transport volume is also being developed with the growing traffic requirement. Further, it may result in the serious performance deterioration of the bridges, such that the designed prestressed beam may be changed into a partially prestressed beam, the performance may be degraded in a short time, consequently, the fatigue life may be reduced obviously, and so forth.

As an essential method, the experimental investigations in the literature are generally able to be concluded in the following three aspects: the investigation on the fatigue performance deterioration of the reinforced concrete (RC) beams or strengthened RC beams [4–7], the investigation on that of the partially prestressed concrete (PC) beams [8–14], and the investigation on that of the heavy-haul railway

bridges [15–17]. For example, Zhang et al. [8] observed on the partially PC beams with corroded rebars and found out that the fatigue life of the beams decreases and the rate of the stiffness degradation and the midspan deflection development grows with the corrosion ratio increasing. Additionally, the researchers conducted other investigations on the partially PC beams and drew some conclusions such that [9–14] the fatigue failure of the beams begins from the fatigue fracture of the rebar at the bottom, which determines the fatigue life of the beams and the maximum midspan deflection increased by 10%~20% to failure than that in the initial case and so forth. Furthermore, according to the investigation on the fatigue performance deterioration of the heavy-haul railway bridges, firstly, an *S-N* model [15] is developed considering the rebar stress range—fatigue life relationship and stress ratio (the ratio of initial stress range to stress range to failure)—and fatigue life relationship, by observing the scale model of bridges under fatigue loading. Secondly, Luo et al. [16] investigated on the variation of the midspan deflection, the stiffness, and the material strain during the fatigue life and

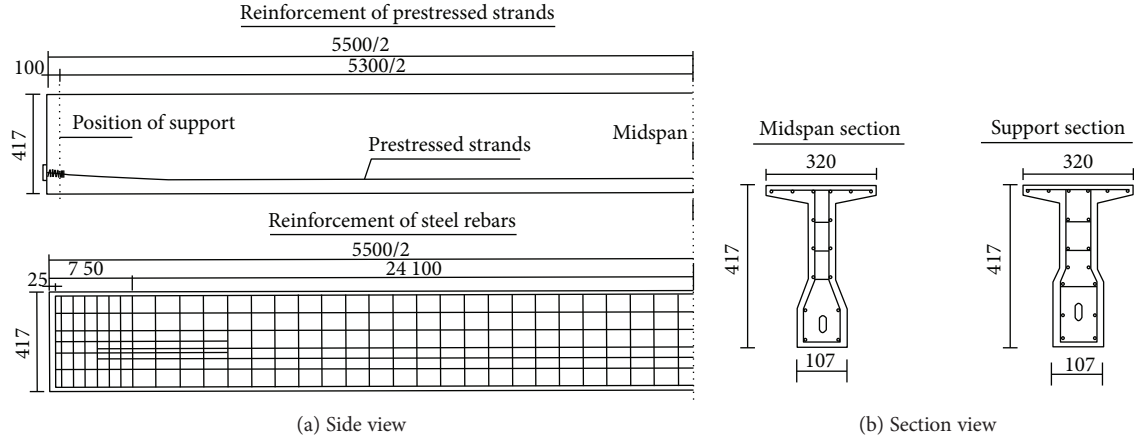


FIGURE 1: Details of specimens (unit : mm).

TABLE 1: Parameters of specimens.

| Length l (mm) | Span l_0 (mm) | Depth h (mm) | Web width w (mm) | f_{cm} (MPa) | Prestressed steel strand (7 ϕ 5) | | |
|-----------------|-----------------|----------------|--------------------|----------------|---------------------------------------|--------|--------------------|
| | | | | | f_{pk} (MPa) | Bundle | Strands per bundle |
| 5500 | 5300 | 417 | 80 | 53.6 | 1860 | 1 | 2 |

developed a simplified analysis method on the variation, based on the scale model experiments; literature [15] developed a stiffness degradation model and a related damage evolution model.

However, initially, the investigation results in literature [4–14, 16] are generally not applicable to the performance deterioration of the heavy-haul railway bridges (i.e., PC beams), due to the different material/structural parameters or fatigue loading. For example, literature [4–7] observed on the performance deterioration of the RC beams but not PC beams, literature [8–14] focused on that of PC beams with rectangular sections [8–10, 12, 14] or different dimension T-type sections [11, 13] compared with the typical heavy-haul railway bridges of T-type sections, and literature [16] analyzed that of unbonded PC beams rather than the bonded bridges. Additionally, for the $S-N$ model in literature [15], no explanations for the relationship between the stress ratio and the fatigue life were given, which caused approximately 20% relative errors for the resulted predictions in nearly half cases. Furthermore, the predictions of the performance deterioration models in literature [15] are not accurate enough (the relative error of 40% approximately of the predictions is higher than 20%), and the damage evolution [15] did not consider the coupling of the stiffness degradation and the residual/inelastic deformation development, which are two essential mechanical behaviors of the bridges.

Therefore, the aim of this work is to develop a comprehensive and accurate $S-N$ model by comparing the relationship between the fatigue life and the rebar stress range with that of the fatigue life and the load level and to propose a damage evolution model considering the coupling of the stiffness degradation and inelastic deformation, by monitoring/observing on the failure mode, the fatigue life, the load-

midspan deflection response, the material strain development, and so forth, using a multisensor system. Specifically, the comparison will be conducted to analyze the influence of the key factors on the fatigue life of the bridges. With this methodology, the developed $S-N$ model is more considerable than that in literature [15–17]. Additionally, the coupling of the stiffness degradation and inelastic deformation will be taken into account to better understand the performance deterioration of the bridge and to characterize the fatigue behaviors more accurately than that in literature [15–17].

This work monitors the performance deterioration of the scale models of a typical heavy-haul railway bridge in China under fatigue loading based on a multisensor system, analyzes the results of the failure mode, the fatigue life, the load-midspan deflection response, the material strain development, and so forth, and further develops an $S-N$ model and a damage evolution model to better understand the fatigue performance deterioration of the bridge.

2. Materials and Methods

2.1. Specimen Details. The specimen is designed based on a typical heavy-haul railway bridge, the simply supported PC beam with T-type section and 32 m span, which follows the design standard of 2059F [1–3, 15]. And it satisfies the requirement of the mechanical similarity between the specimen and the standard beam. Therefore, 12 specimens (the 1:6 scale models) are designed and made considering the similarity, the manufacture scale accuracy, and the experimental practicability (see details in Figure 1 and Table 1).

Additionally, the details of the materials are as follows. The mixture ratio of concrete is such that cement:water:sand:

TABLE 2: Mechanical property of reinforced steel.

| Steel type | Nominal diameter d (mm) | Yield strength f_y (MPa) | Strength f_u (MPa) | Elastic modulus $E_{s\&p}$ (GPa) |
|-------------------|------------------------------|-------------------------------|-------------------------|-------------------------------------|
| Q235 | 8 | 310.0 | 455.0 | 211.0 |
| HRB335 | 10 | 405.0 | 575.0 | 203.0 |
| Steel strand 1860 | 15.24 | 1795.0 | 1929.0 | 196.0 |

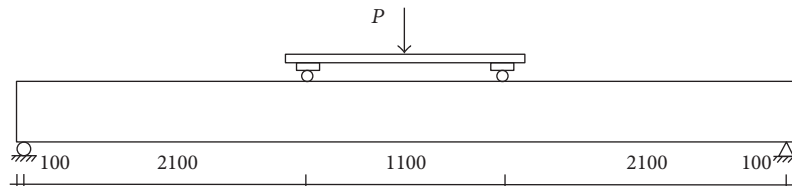


FIGURE 2: Experimental setup (unit : mm).

TABLE 3: Details of specimens and loading conditions.

| Specimen | Loading (kN) | | ΔP | P_u | $L = P_{\max}/P_u$ (-) | FRP-OFBG | Fatigue life (10^6) | |
|-----------|--------------|------------|------------|-------|------------------------|----------|-------------------------|-----------|
| | P_{\min} | P_{\max} | | | | | N_f | $N_{0.2}$ |
| Number 1 | — | — | — | 158.6 | — | Yes | — | — |
| Number 2 | — | — | — | 180.0 | — | No | — | — |
| Number 3 | 27.2 | 90.6 | 63.4 | — | 0.60 | Yes | 0.917 | 0.480 |
| Number 4 | 27.2 | 82.7 | 55.5 | — | 0.55 | Yes | 1.405 | 0.951 |
| Number 5 | 27.2 | 74.7 | 47.5 | — | 0.50 | Yes | 1.769 | 1.100 |
| Number 6 | 27.2 | 66.8 | 39.6 | — | 0.45 | Yes | 2.162 | 1.252 |
| Number 7 | 27.2 | 62.2 | 35.0 | — | 0.35 | Yes | 2.107 | 1.830 |
| Number 8 | 27.2 | 85.4 | 58.2 | — | 0.50 | No | 2.690 | 2.077 |
| Number 9 | 27.2 | 76.4 | 49.2 | — | 0.45 | No | 3.676 | 3.251 |
| Number 10 | 27.2 | 62.2 | 35.0 | — | 0.35 | No | 4.646 | 3.256 |
| Number 11 | 27.2 | 62.2 | 35.0 | — | 0.35 | No | 3.497 | 2.876 |
| Number 12 | 27.2 | 62.2 | 35.0 | — | 0.35 | No | 2.954 | 2.751 |

aggregate : admixture = 380 : 155 : 720 : 1084 : 120 (unit : kg/m^3). The cement is Portland cement of P.II 42.5 R, the water is tap water, the aggregates are crushed limestone with diameters of approximately 5~20 mm, the sands are middle grain sands, the mineral admixtures are mineral powder of S95 and fly ash, and the water-reducing agent is named as NoF-II with admixture quantity of $5.15 \text{ kg}/\text{m}^3$. The concrete strength is in the range of 44.0–66.0 MPa, and its mean value is 53.6 MPa. The mechanical property of the reinforced steel is tested following the Chinese standard [18] and listed in Table 2.

Furthermore, the prestressed steel strands are tensioned on both beam ends after a curing of 28 days, anchored at the ends, and sealed with the cement grouting. To reduce the influence of shrinkage and creep of concrete, all specimens have been stored in the laboratory for more than six months.

2.2. Experimental Setup. The four-point bending loading method is applied in the experiment (Figure 2), with the

loading points calculated by the wheelbase of the train [1–3]. Two specimens are employed to test the static ultra-load P_u and make sure the specimens are designed as the reinforced beams, and the other 10 specimens are used to be investigated on the fatigue performance deterioration (see Table 3).

The fatigue loads are calculated as follows. Initially, the minimum load P_{\min} is estimated by the equivalent bending moment of the scale model compared with the standard beam under static load, considered an increasing 20% of the load due to the replacement of the former lighter sleepers by new heavier ones (Table 3). Furthermore, the maximum load P_{\max} is estimated by the equivalent bending moment under both static and live loads, that is, the basic maximum load is $P_{\max} = 62.2 \text{ kN}$ with the load level $L = P_{\max}/P_u = 0.35$ in Table 3. The other maximum loads are $P_{\max} = 0.40P_u$, $0.45P_u$, $0.50P_u$, $0.55P_u$, and $0.60P_u$, with load levels $L = 0.40$, 0.45 , 0.50 , 0.55 , and 0.60 in Table 3, taking into account a higher quality of the specimens compared with the standard beams on site.

2.3. Multisensor System. The multisensor system consisted of the strain sensors, the static and dynamic deflection/displacement sensors, and the corresponding data acquisition systems, in order to monitor the performance deterioration of the bridges under fatigue loading. The details of the system are as follows.

Initially, the strains of the concrete, rebar, and prestressed strand on the midspan were monitored by using the smart fiber-reinforced polymer (FRP) and electrical resistance strain gauges. The smart FRP is named as the FRP optical fiber Bragg grating (FRP-OFBG, Table 3) and it was used as a reinforcement and strain sensor with a resolution of $1 \mu\epsilon$ in this work. In detail, it is one of the new smart optical-fiber-sensor-based structures combined with FRP (e.g., FRP-OFBG composite rebar, boards, tubes, and sheets), and it is developed by the research groups of fiber sensors for structural-health monitoring in Dalian University of Technology and Harbin Institute of Technology. The FRP-OFBGs generally can act simultaneously as strain sensors and reinforcing components and can detect slips and cracks in RC structures. They are characterized by small dimensions, good resolution and accuracy, excellent durability, a wide range of operating temperature, and good signal transmission over long distances. For the purpose of strain monitoring, the force transferred from the host material to the grating region of the fiber core causes the length of the grating region to change and the refractive index of the core section to vary accordingly. When the light is illuminated from the broadband source via the coupler, part of this light is reflected back to the coupler and the reflected wavelength is detected by the optical spectrum analyzer. The strain variation in the grating region is then simply determined by measuring the change in the reflected wavelength from the FRP-OFBG sensor. These sensors have been shown to possess a linear relationship between the strain and the reflected wavelength shift, provided that the elastic deformation limit of the fiber is not exceeded.

Additionally, the linear variable displacement transducer (LVDT) and the accelerometer of type 891-II were used to monitor the static and dynamic deflections, respectively, on the midspan, the points on 1/4 span from the supports, and two supports. The resolution of the accelerometer is 1×10^{-7} mm, the measurement range is 0–70 mm, and the effective frequency range is 1–100 Hz.

Therefore, the multisensor system used in the test is characterized by good resolution and accuracy and excellent durability for monitoring the performance deterioration of heavy-haul railway bridges under fatigue loading. By using this system, it is able to monitor the performance deterioration in the aspect of both structural response and material degradation and further to better understand the mechanism of the deterioration.

3. Experimental Results

3.1. Static Experimental Results. The static experiments were conducted after the standard for test method of concrete structures (GB50152-92) [19]. The experimental results verified that the designed beams were reinforced beams with a

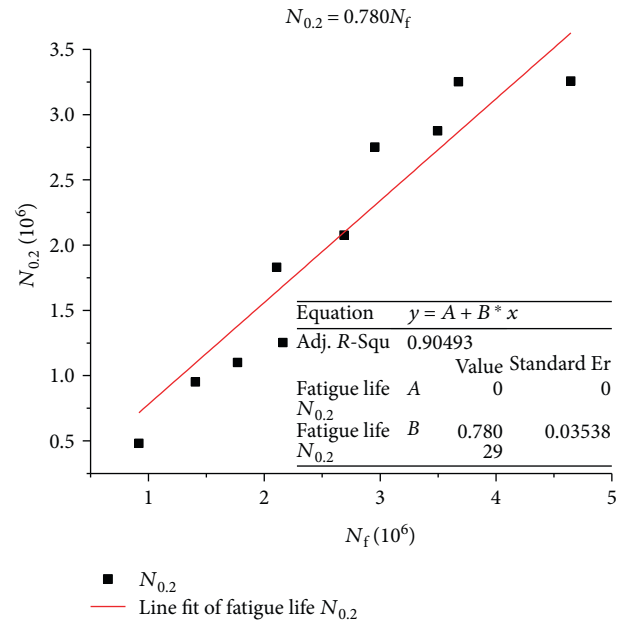


FIGURE 3: $N_{0.2}$ versus N_f .

typical bending failure mode. Additionally, the static ultraload P_u of the specimen numbers 1 and 2 is listed in Table 3. Since the FRP-OFBG in specimen number 1 has a lower mechanical property than that of the steel strands in specimen number 2, the specimen number 1 obtains a lower scalar of P_u . Therefore, the load level of the specimens in the fatigue experiments is calculated by the static ultraloads with/without FRP-OFBG (Table 3).

3.2. Fatigue Experimental Results

3.2.1. Failure Mode. All specimens under fatigue loading obtained the same failure mode such that the failure of the rebars at the bottom started the specimen failure. Furthermore, the dominant cracks are located at two positions approximately the midspan and the loading point for specimen numbers 3, 4, 6, 9, and other specimens.

3.2.2. Fatigue Life. Since the bridge is estimated to be under serviceability limit state when there is a crack with a width of 0.2 mm, after the code TB10002.3-2005 [20], the allowable fatigue life ($N_{0.2}$) is defined as the cycle number when the width of a crack reaches 0.2 mm of the specimen. Furthermore, the fatigue life (N_f) is defined as the cycle number relating to the first failure of the rebar.

Therefore, $N_{0.2}$ and N_f are listed in Table 3. And the linear relationship between $N_{0.2}$ and N_f is proposed such that (Figure 3)

$$N_{0.2} = 0.780N_f. \quad (1)$$

3.2.3. Midspan Deflection. The variation of midspan deflection depending on the cycle number is obtained and the typical results are plotted in Figures 4(a) and 4(b). It is found that the response of load-midspan deflection is almost linear and the slope of the response varies depending on the cycle

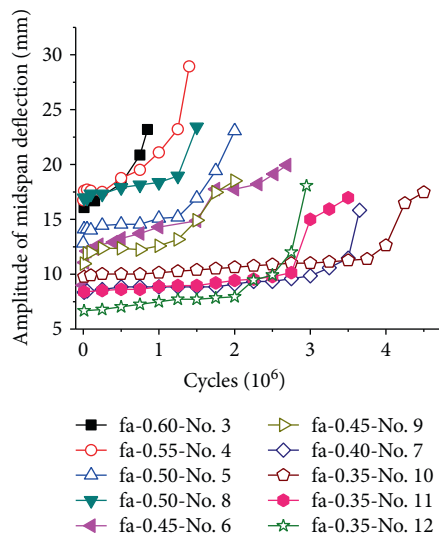
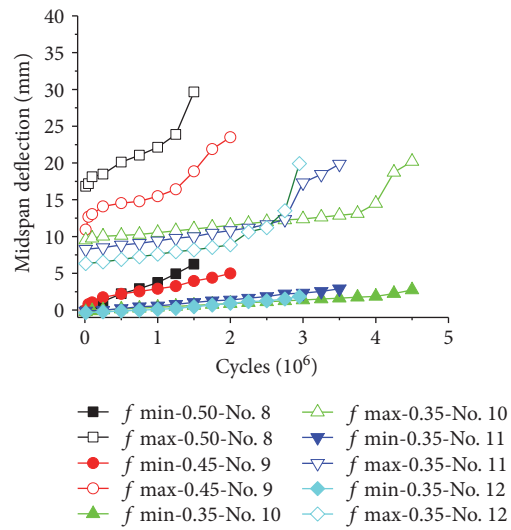
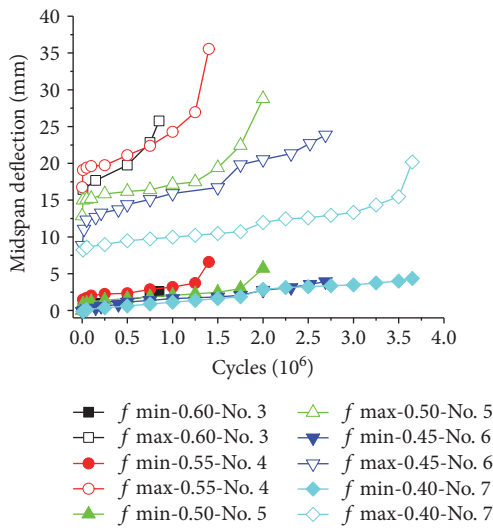
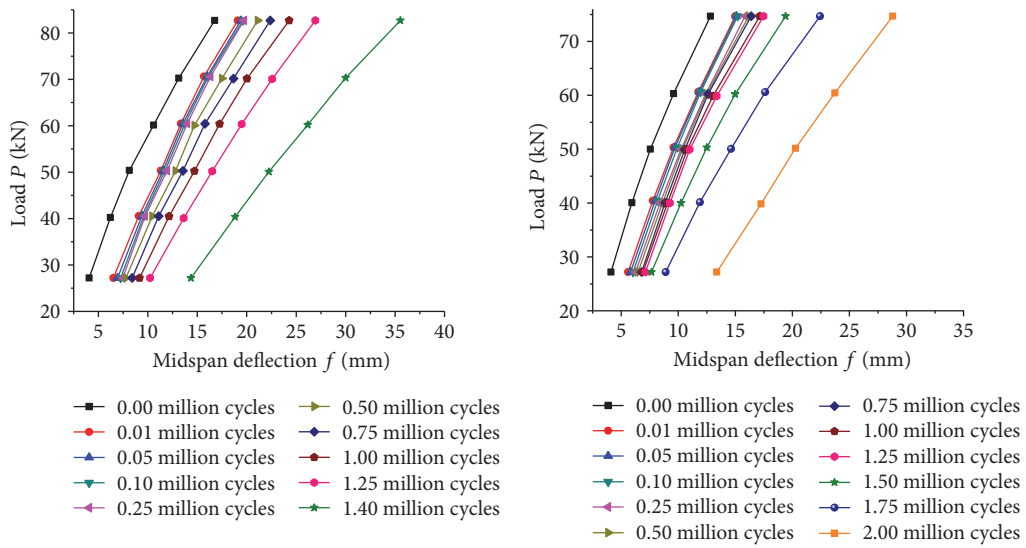
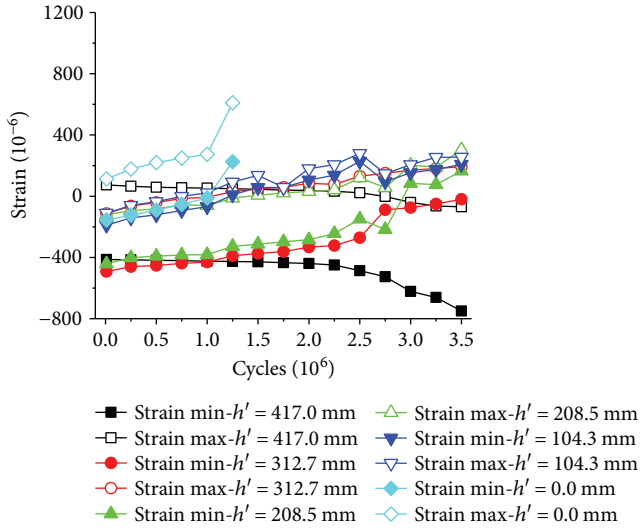
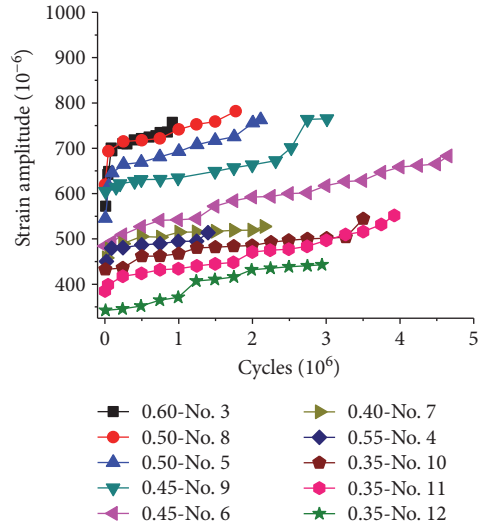


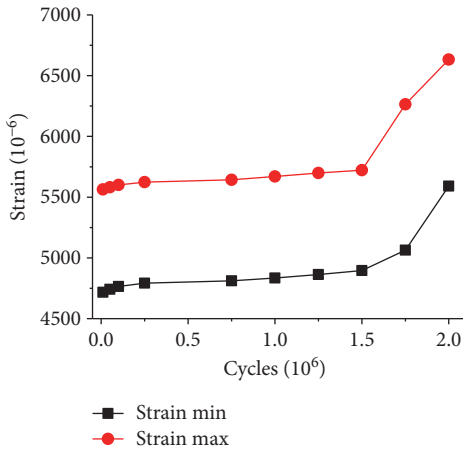
FIGURE 4: Relationships of P - f , f - N , and Δf - N .



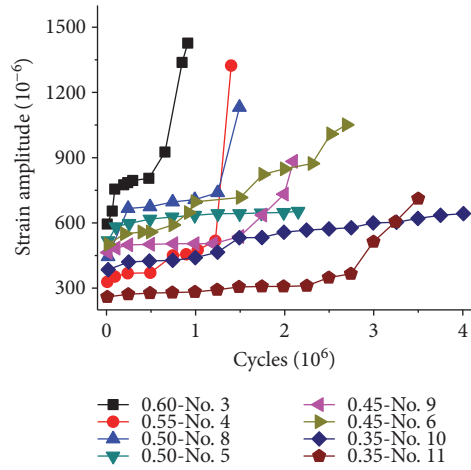
(a) ϵ_c-N (concrete strain for specimen number 11)



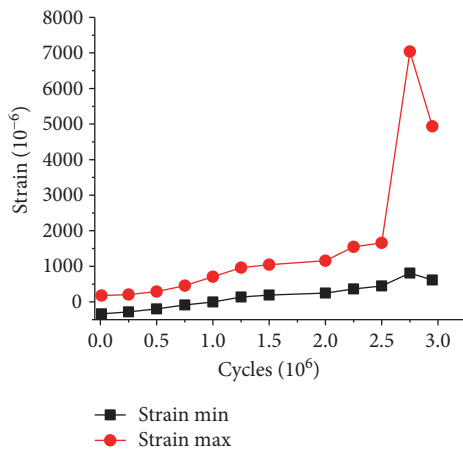
(b) $\Delta\epsilon_c-N$ ($h' = 417.0$ mm)



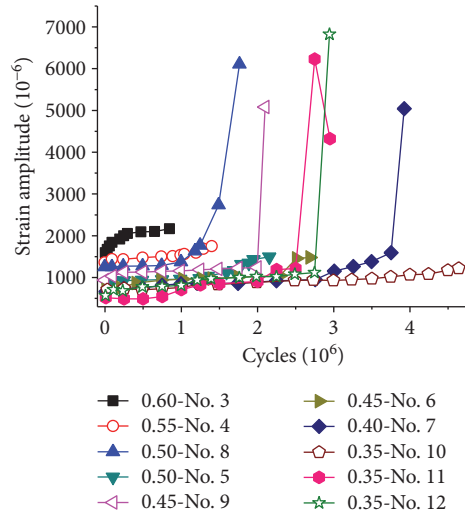
(c) ϵ_p-N (prestressed strand strain for specimen number 11)



(d) $\Delta\epsilon_p-N$

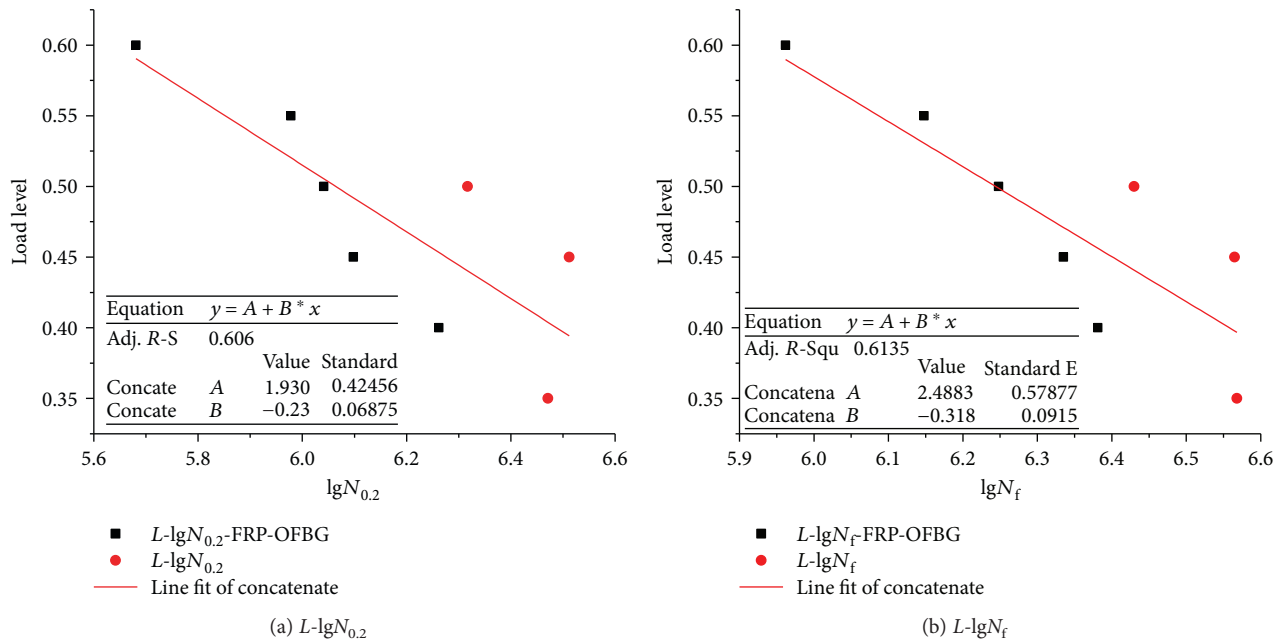


(e) ϵ_s-N (steel rebar strain for specimen number 11)



(f) $\Delta\epsilon_s-N$

FIGURE 5: Variation of material strain and its amplitude on the midspan during fatigue life (h' denotes the depth of the sensor on the midspan section).

FIGURE 6: Relationships of $L\text{-}\lg N_{0.2}$ and $L\text{-}\lg N_f$.

number in three stages: quickly reducing, slowly reducing, and quickly reducing again.

Furthermore, the variation of the maximum, minimum, and amplitude of the midspan deflection depending on the cycle number also experiences a three-stage process (Figures 4(c)–4(e)).

3.2.4. Material Strain Development. Observing on the variation of material strain development and its amplitude depending on the cycle number in Figure 5, it is found that they experience the three-stage process. Specifically, the material strain development and its amplitude on the midspan develop in a three-stage process of the increasing rate: quickly increasing, slowly increasing, and quickly increasing again.

4. Discussion

4.1. S-N Model. The relationship between load level and fatigue life ($L\text{-}N$) and the relationship between load range and fatigue life ($\Delta P\text{-}N$) are plotted in Figures 6 and 7, respectively, based on the results listed in Table 3. And the results of ΔP obtain a better linear dependence on N in Figure 7 than that on L in Figure 6, which may be due to the initial elastic response of the rebar at the bottom $\Delta\sigma$ caused by the load range ΔP (see the linear relationship of $\Delta\sigma\text{-}\Delta P$ in Figure 7(c)).

Additionally, observing on the typical $S\text{-}N$ relationship, that is, the relationship between the stress range (or its denary logarithm) of the rebar at the bottom and the cycle number in Figures 8(a) and 8(b), the $S\text{-}N$ model by fitting the experimental results is obtained such that

$$\Delta\sigma_r = 2149.32 - 308.69 \lg N_f, \quad (2)$$

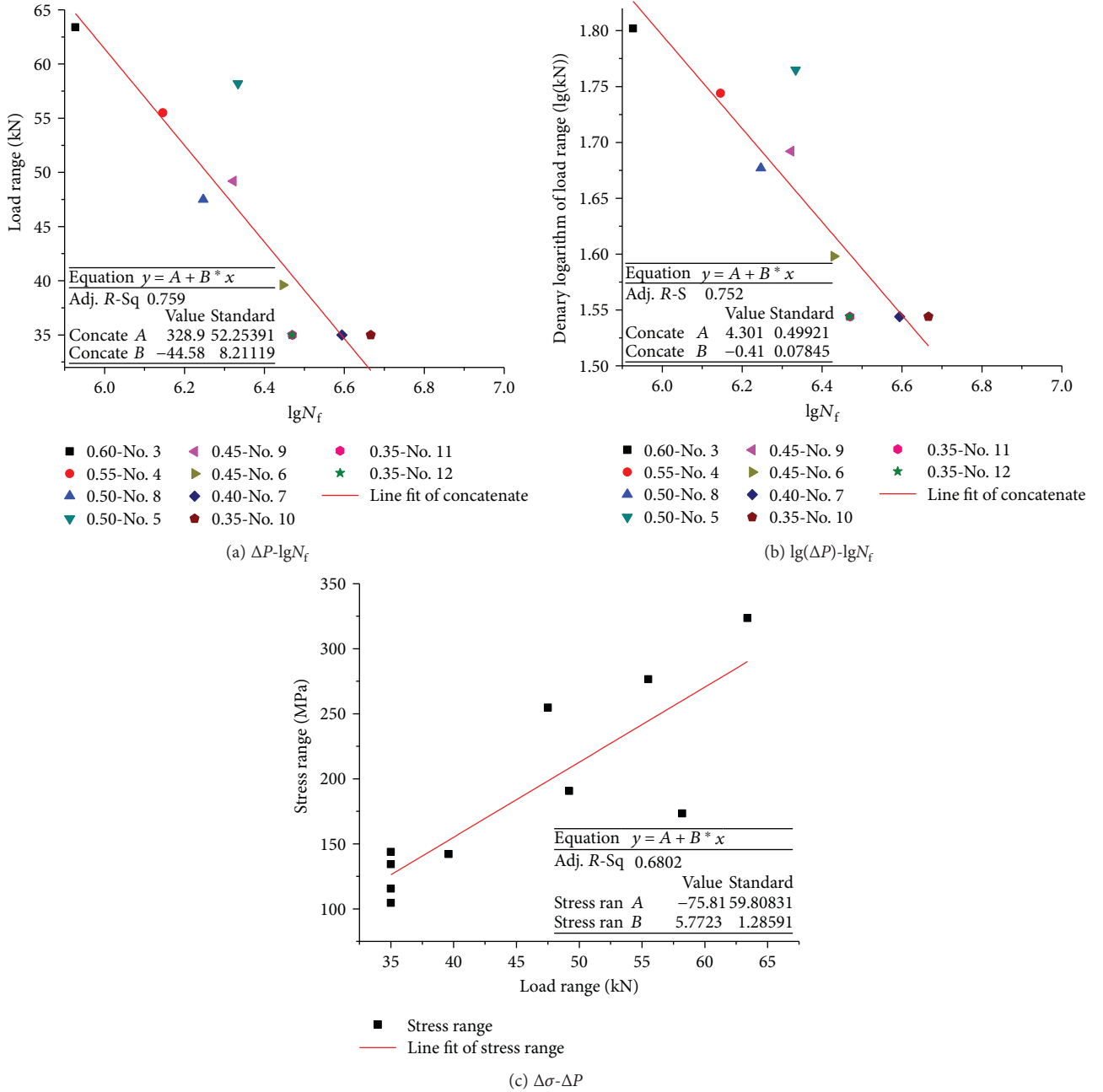
$$\lg(\Delta\sigma_r) = 6.446 - 0.661 \lg N_f. \quad (3)$$

Equations (2) and (3) show that the fatigue life of specimens is determined by the fatigue life of the rebar at the bottom, which agrees with the experimental results in literature [8–15]. The fatigue life of specimens decreases when the stress range (or its denary logarithm) of the rebar increases.

Furthermore, the $S\text{-}N$ model in (2) or (3) is able to be used to predict the specimen fatigue life considering the stress range of the rebar. The predictions are plotted in Figure 8(c), comparing with the predictions of other $S\text{-}N$ models [10, 21, 22].

Figure 8(c) illustrates that, firstly, the predictions of the model in this work are more agreeable with the experimental results than those of other models [10, 21, 22]. Secondly, though the models [10, 22] predict a close fatigue life ($N_f \approx 200 \times 10^6$) when the stress range of the rebar $\sigma_r \approx 200$ MPa, the model proposed in this work predicts a lower fatigue life when $\Delta\sigma_r < 200$ MPa, and a higher fatigue life when $\Delta\sigma_r > 200$ MPa, compared with that of the other models [10, 22]. The reason can be concluded that the performance deterioration of the specimens supplies a specific stress state variation for the rebar at the bottom in this work which is different from that in literature [10, 22], due to the different processes of material degradation (e.g., the concrete degradation caused by fatigue cracks [10, 23–26], the prestressed strand degradation resulted from fatigue plasticity [27]), specimen stiffness degradation and curvature variation [8–14], and so forth. Thirdly, the corrosion of the rebar generally results in an obvious reduction of specimen fatigue life [4, 6, 8, 21]. It causes an obviously lower fatigue life predicted by the model [21] compared with that by the other models (Figure 8(c)); therefore, the corrosion of rebar influences the fatigue life of the bridge.

4.2. Damage Evolution Model. It is found that the slope of the $P\text{-}f$ response (i.e., the specimen stiffness) decreases and the

FIGURE 7: Relationships of ΔP - $\lg N_f$, $\lg(\Delta P)$ - $\lg N_f$, and $\Delta\sigma$ - ΔP .

residual midspan deflection (i.e., the specimen residual/inelastic deformation) develops with the increasing of the cycle number, by observing on the P - f response in Figures 4(a) and 4(b). Therefore, an elastic damage variable D_e according to specimen stiffness degradation and an inelastic damage variable D_i responding to specimen inelastic deformation are defined, respectively, in this work, such that

$$D_e = \frac{P_{de}}{P_0} = \frac{f_{de}}{f}, \quad (4)$$

$$D_i = \frac{P_{di}}{P_0} = \frac{f_{di}}{f}, \quad (5)$$

where P_{de} and P_{di} denote the elastic and inelastic damage-caused load reductions, respectively (similar to the elastic and inelastic damage-caused stress reduction, respectively in literature [24, 25]); f_{de} and f_{di} denote the elastic and inelastic damage-caused midspan deflections, respectively; P_0 denotes the idealized load without damage in the specimen (similar to the effective stress [24, 25]); f denotes the total midspan deflection.

Further, a (total) damage variable D is defined as follows:

$$D = D_e + D_i = \frac{(P_{de} + P_{di})}{P_0} = \frac{(f_{de} + f_{di})}{f}, \quad (6)$$

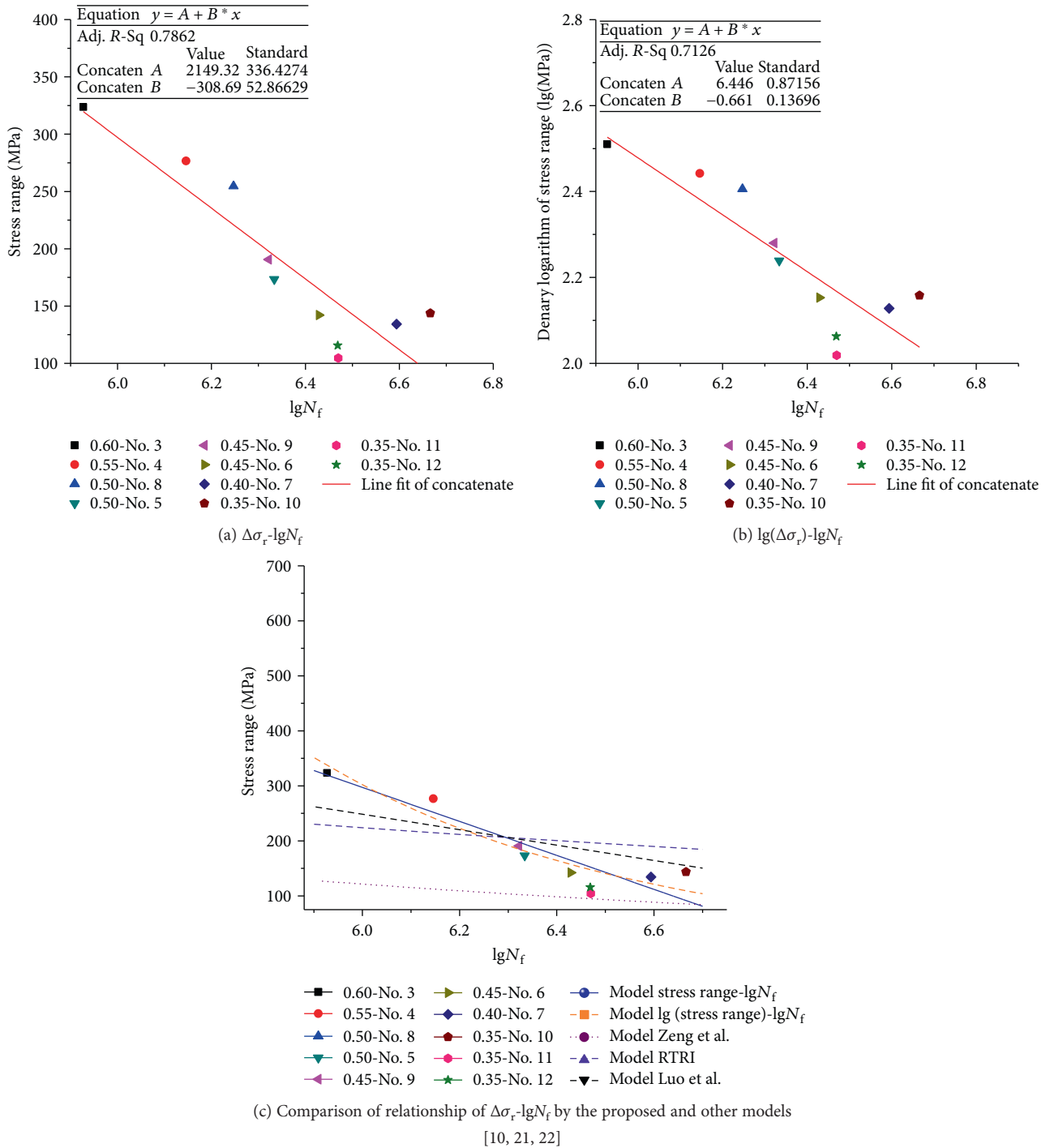


FIGURE 8: S-N model.

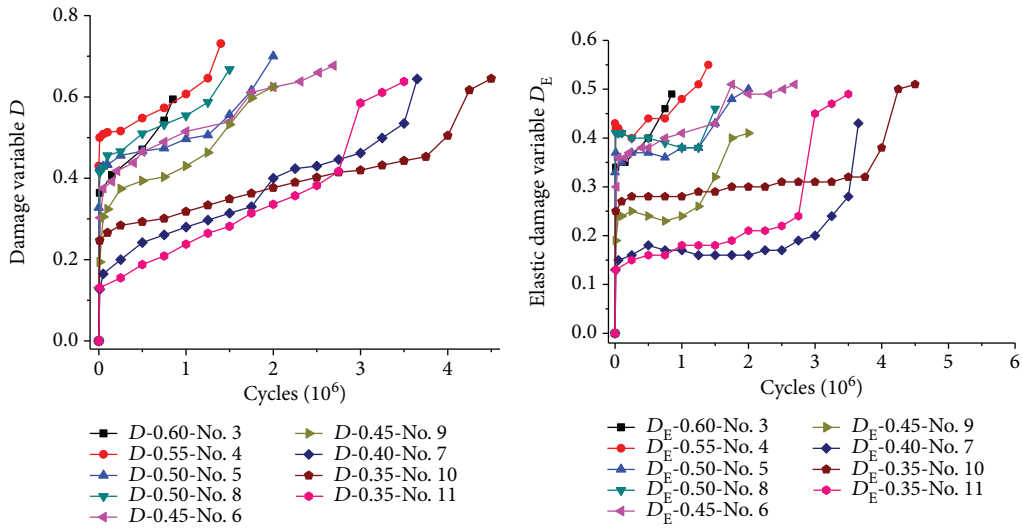
where the relationship between D_e and the current specimen stiffness E is expressed such that

$$E = D_e(1 - D_i)E_0 = D_e E_0, \quad (7)$$

where D_e denotes the elastic damage variable in the total midspan deflection space, D_e denotes the elastic damage variable in the elastic midspan deflection space f_E ($f_E = f - f_{di}$). Comparing with the damage variable D_E based on the

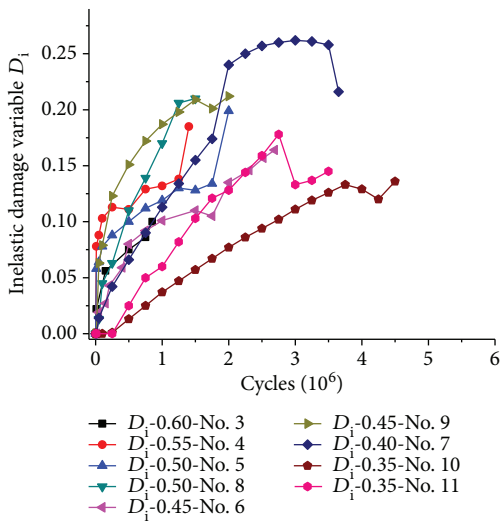
specimen stiffness degradation in literature [9, 15], the damage variable D in this work is more considerable for its characterization of the coupling of stiffness degradation and inelastic deformation.

Thus, the damage evolution is obtained in Figures 9(a)–9(c). Figures 9(a)–9(c) illustrate that the damage evolution and elastic damage evolution (i.e., $D-N$ and D_e-N) experience a three-stage process; however, the inelastic damage evolution D_i-N experiences only a two-stage process: the initial



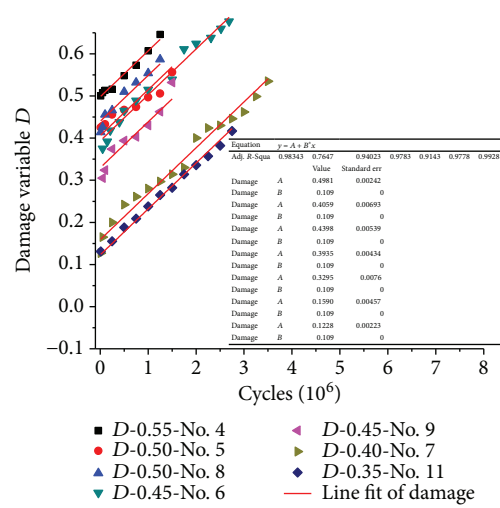
(a) $D-N$ (specimen numbers 3–11)

(b) D_E-N (specimen numbers 3–11)

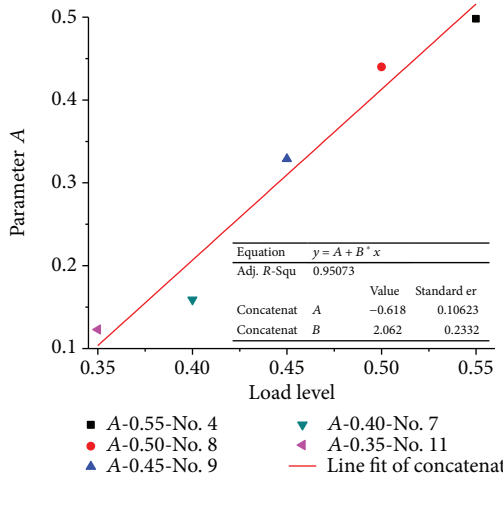


(c) D_i-N (specimen numbers 3–11)

(d) D_c-N (specimen numbers 3–11)

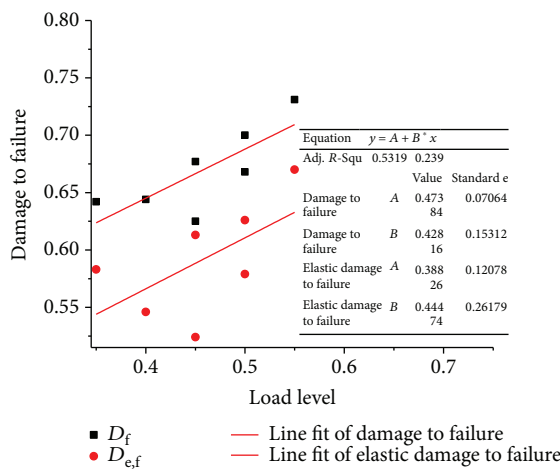


(e) $D-N$ during the second stage

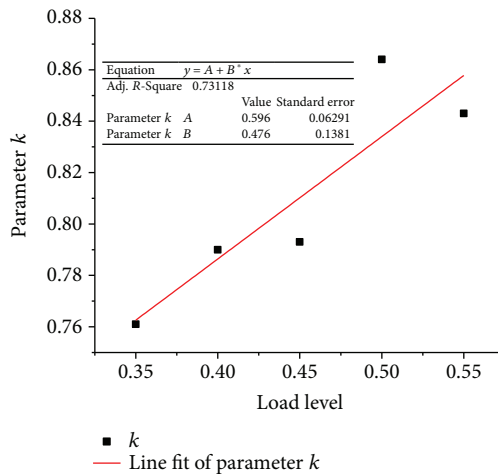


(f) $A-L$ (second stage)

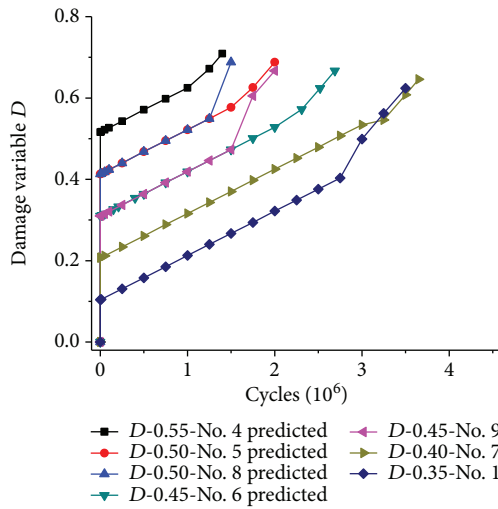
FIGURE 9: Continued.



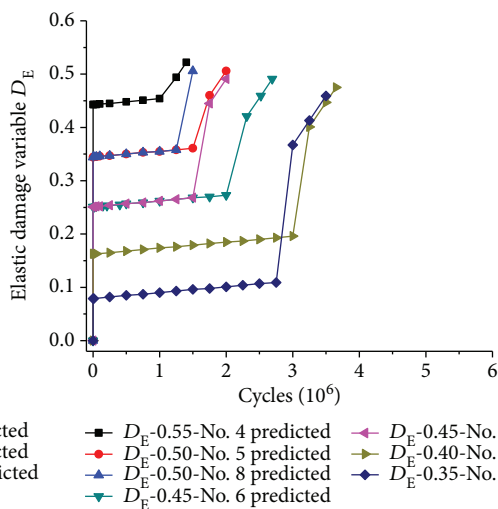
(g) D_f and $D_{e,f}$ -L (specimen numbers 4–11)



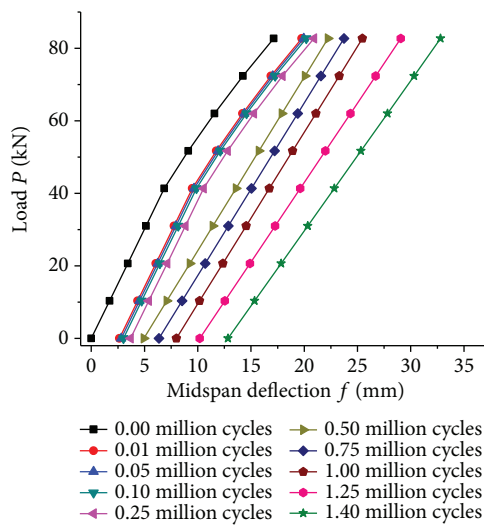
(h) k -L (specimen numbers 4, 5, 8, 9, and 11)



(i) D -N predicted



(j) D_E -N predicted



(k) P - f (load level $L = 0.50$) predicted

FIGURE 9: Damage evolution, its related parameters (e.g., D_f , $D_{e,f}$, A , and k), and predictions.

linearly increasing and the subsequent increasing with a reduced rate.

The damage variable and the elastic damage variable to the fatigue failure are defined as D_f and $D_{e,p}$ respectively. The stochastic damage evolution of materials [21, 24] generally caused the existence of the stochastic damage evolution of the bridges; hence, considering the shortage of statistical experimental results and the unavailability of stochastic analysis methods of the bridges, for simplicity, the variables (D_f and $D_{e,f}$) are assumed to be linearly dependent on the load level L (Figure 9(g)), as follows:

$$D_f = 0.474 + 0.428L, \quad (8)$$

$$D_{e,f} = 0.388 + 0.445L. \quad (9)$$

This assumed that the linear relationship will be verified or improved in the future with the help of further experimental results and stochastic analysis methods.

Additionally, by investigating on the damage evolution in Figure 9(a), it is concluded that the relationship of D - N during the second stage is linear with an equal slope (Figure 9(e)), such that

$$D = A + B \cdot N, \quad (10)$$

where A denotes the damage variable D_1 after the first cycle, that is, $D_1 = A$ (see Figures 9(a), 9(e), and 9(f)), and B denotes the slope of the D - N relationship. In this work, A is proposed to follow the equation such that

$$A = -0.618 + 2.062L. \quad (11)$$

And it is assumed that $B = 0.109$ (Figure 9(e)).

Furthermore, since it is found that the elastic damage variable $D_{E,1}$ after the first cycle is approximately proportional to the damage variable D_1 (see Figures 9(a) and 9(b)); it is proposed that $D_{E,1}$ follows the equation such that

$$D_{E,1} = kD_1 = kA. \quad (12)$$

And the slope of D_E - N relationship during the second stage is assumed to be $B_E = 0.1 * B = 0.0109 \approx 0.011$ (Figure 9(j)), by investigating on the elastic damage evolution in Figure 9(b).

Therefore, the damage evolution (i.e., D - N , $D_{E\&e}$ - N , and D_i - N) is able to be predicted by the proposed models in (8), (9), (10), (11), and (12) in Figures 9(i), 9(g), and 9(j); further, the P - f response of the specimen is also able to be predicted in Figure 9(k). Figures 9(i), 9(g), 9(j), and 9(k) illustrate that the proposed damage evolution model is verified to be effective to characterize the damage evolution and mechanical response of the specimen, by comparing the predictions with the experimental results.

4.3. Performance Deterioration of Heavy-Haul Railway Bridges under Fatigue Loading. Based on the above investigation and analysis, it is concluded as follows.

Initially, according to the fatigue life, it is necessary to strengthen the heavy-haul railway bridge with a consideration of the environmental effects. In detail, Figure 8 and (2) show that the bridge subjected to the train loading with a 30-ton axle weight (i.e., $\Delta\sigma_r \approx 120$ MPa) satisfies

the fatigue life requirement of the Chinese standard [20] (i.e., $N_f \approx 10^{6.57} \approx 3.7 \times 10^6 > 2.0 \times 10^6$). However, considering the environmental effects, such as the corrosion of rebar/prestressed strand, especially taking into account the negative effects of the low quality of concrete casting, and so forth, the coupling of train loads and environmental effects generally highly reduces the fatigue life of the bridge compared with that only of train loading [4, 6, 8, 21] (see Figure 8(c)).

Furthermore, relating to performance deterioration, the conclusion is obtained from Figures 9(a)–9(c), 9(i), and 9(j) as follows. Firstly, the damage evolves linearly to $D \approx 0.4$ during the second stage (i.e., $10\%N_f \sim 80\%N_f$), when the coupling of stiffness degradation and inelastic deformation is taken into account. Secondly, the stiffness reduces slowly and linearly to 80% of the initial stiffness (according to the elastic damage variable $D_E \approx 0.2$, see Figures 9(b) and 9(j)), and the residual midspan deflection reaches to 2.0 mm (relating to the inelastic damage variable $D_i \approx 0.2$, see Figures 4 and 9(c)), when the bridge is subjected to the train loading with a 30-ton axle weight. Thirdly, the ratio of the specimen maximum midspan deflection of $N \approx 3.0 \times 10^6$ to the initial maximum deflection is 150% (f_{\max} is 12.0 mm and 8.0 mm, resp.), and it is 250% to fatigue failure (f_{\max} is 20.0 mm and 8.0 mm, resp.), when the bridge is subjected to the train loading with a 30-ton axle weight. Fourthly, by applying the mechanical similarity mentioned in the specimen design section, it is speculated that the residual midspan deflection for the bridge on site is $f_r \approx 2.0 \times 6 = 12.0$ mm, when the bridge is subjected to the train loading with a 30-ton axle weight experiencing cycle number $N \approx 3.0 \times 10^6$. Therefore, the performance deterioration of the bridge may cause serious traffic safety problems, especially considering the dynamic coupling of the train and the bridge [28, 29].

5. Conclusions

This work monitored the performance deterioration of the scale models of a typical heavy-haul railway bridge under fatigue loading, analyzed the results of the failure mode, the fatigue life, the loads–midspan deflection response and the materials strain development, and so forth, by using a multisensor system, and further developed the comprehensive S - N model and the damage evolution model considering the coupling of stiffness degradation and inelastic deformation. The conclusions are able to be drawn as follows:

- (1) By comparing the relationship between the fatigue life and the rebar stress range with that of the fatigue life and the load level, the S - N model was developed in this work obtaining more comprehensive and accurate predictions. The fatigue life of the specimens is determined by the fatigue life of the rebar at the bottom. The fatigue life of the bridge subjected to the train loading with a 30-ton axle weight may be lower than 2.0×10^6 cycles when the environmental factors are taken into account.

- (2) The damage evolution model considered the coupling of the stiffness degradation and the inelastic deformation development is more reasonable than not. The predictions agree with the experimental results. The damage evolution obtained a three-stage process with a constantly sloped linear developing during the second stage.

Therefore, this work furthers the understanding of the performance deterioration of the heavy-haul railway bridge under fatigue loading. And it may also be able to help maintain and monitor the other partially prestressed concrete beams.

Conflicts of Interest

The authors declare that they have no competing interests.

Acknowledgments

The studies presented here were developed within the research projects U1434204, 51378506, and 51278496 funded by the National Natural Science Foundation of China, whose assistance is gratefully acknowledged.

References

- [1] W. Hou, "Construction of Datong-Qinhuangdao heavy-haul railway and operation management technique," *China Railway Science*, vol. 22, no. 6, pp. 135–136, 2001.
- [2] J. Zuo, "Influence on the upper-structure of the existing bridges from the 20000-ton heavy-haul trains running in Datong-Qinhuangdao railway," *Railway Standard Design*, vol. 1, pp. 43–44, 2006.
- [3] Z. Geng, *Heavy-Haul Transportation Technologies on Datong-Qinhuangdao Railway*, China Railway Publishing House, Beijing, 2009.
- [4] J. Sun, Q. Huang, and Y. Ren, "Performance deterioration of corroded RC beams and reinforcing bars under repeated loading," *Construction and Building Materials*, vol. 96, pp. 404–415, 2015.
- [5] F. Liu and J. Zhou, "Fatigue strain and damage analysis of concrete in reinforced concrete beams under constant amplitude fatigue loading," *Shock and Vibration*, vol. 2016, Article ID 3950140, 7 pages, 2016.
- [6] L. Song and Z. Yu, "Fatigue performance of corroded reinforced concrete beams strengthened with CFRP sheets," *Construction and Building Materials*, vol. 90, pp. 99–109, 2015.
- [7] S. Parniani and H. Toutanji, "Monotonic and fatigue performance of RC beams strengthened with a polyurea coating system," *Construction and Building Materials*, vol. 101, pp. 22–29, 2015.
- [8] W. Zhang, X. Liu, and X. Gu, "Fatigue behavior of corroded prestressed concrete beams," *Construction and Building Materials*, vol. 106, pp. 198–208, 2016.
- [9] J. H. Xie, P. Y. Huang, and Y. C. Guo, "Fatigue behavior of reinforced concrete beams strengthened with prestressed fiber reinforced polymer," *Construction and Building Materials*, vol. 27, no. 1, pp. 149–157, 2012.
- [10] X. Luo, Z. Yu, J. Nie, and X. Liu, "Experimental study on fatigue properties of self compacting prestressed concrete beams," *Journal of Building Structures*, vol. 24, no. 3, pp. 76–81, 2003.
- [11] J. Han, Y. Song, and J. Chang, "Analysis model of crack width of partially prestressed concrete beams under fatigue loading," *Journal of Central South University (Science and Technology)*, vol. 45, no. 11, pp. 3977–3985, 2014.
- [12] M. H. Harajli, "Static and fatigue tests on partially prestressed beams," *Journal of Structural Engineering*, vol. 111, no. 7, pp. 1602–1618, 1985.
- [13] M. El Shahawi, "Fatigue of partially prestressed concrete," *Journal of Structural Engineering*, vol. 112, no. 3, pp. 524–537, 1986.
- [14] A. E. Naaman and M. Founas, "Partially prestressed beams under random-amplitude fatigue loading," *Journal of Structural Engineering*, vol. 117, no. 12, pp. 3742–3761, 1991.
- [15] Z. Yu, J. Li, and L. Song, "Experimental study on fatigue behaviors of heavy-haul railway bridges," *China Civil Engineering Journal*, vol. 45, no. 12, pp. 115–126, 2012.
- [16] X. Luo and G. Dai, "Study on computational method of fatigue damages of unbonded prestressed high performance fly ash concrete bridges," *Journal of the China Railway Society*, vol. 31, no. 6, pp. 76–82, 2009.
- [17] J. Li, Z. Yu, and L. Song, "Law of neutral axis variations of heavy-haul railway bridges under repeated fatigue loading," *Journal of the China Railway Society*, vol. 35, no. 6, pp. 96–103, 2013.
- [18] General Administration of Quality Supervision and Inspection and Quarantine of the People's Republic of China, *Metallic Materials-Tensile Testing at Ambient Temperature*, Chinese Standard, Standards Press of China, Beijing, 2002.
- [19] Ministry of Housing and Urban-Rural Development of the People's Republic of China, *Standard for Test Method of Concrete Structures*, Chinese Standard, China Architecture & Building Press, Beijing, 1992.
- [20] Ministry of Railways of the People's Republic of China, *Code for Design on Reinforced and Prestressed Concrete Structure of Railway Bridge and Culvert*, Chinese Standard, China Railway Press, Beijing, 2005.
- [21] Z. Zeng and Z. Li, "Research on fatigue S-N curves of reinforcing bars in common reinforced concrete beams," *China Civil Engineering Journal*, vol. 32, no. 5, pp. 10–14, 1999.
- [22] Railway Technical Research Institute (RTRI), *Design Code for Railway Structures and Its Explanation. Japanese Standard*, 2000.
- [23] C. Jiang, X. Gu, Q. Huang, and W. Zhang, "Deformation of concrete under high-cycle fatigue loads in uniaxial and eccentric compression," *Construction and Building Materials*, vol. 141, pp. 379–392, 2017.
- [24] Z. Shan and Z. Yu, "A fiber bundle-plastic chain model for quasi-brittle materials under uniaxial loading," *Journal of Statistical Mechanics: Theory and Experiment*, article P11010, 2015.
- [25] Z. Yu, Z. Shan, Z. Ouyang, and F. Guo, "A simple damage model for concrete considering irreversible mode-II microcracks," *Fatigue & Fracture of Engineering Materials & Structure*, vol. 39, no. 11, pp. 1419–1432, 2016.
- [26] Z. Yu, S. Tan, Z. Shan, and X. Tian, "X-ray computed tomography quantification of damage in concrete under compression considering irreversible mode-II microcracks," *Fatigue & Fracture of Engineering Materials & Structures*, vol. 40, no. 12, pp. 1960–1972, 2017.

- [27] B. Qin, G. Sheng, and S. Gong, "Analysis on high strain low cycle fatigue properties of 20MnSiVHRB400 reinforced steel bars," *Journal of Chongqing University*, vol. 26, no. 7, pp. 93–96, 2003.
- [28] Z.-w. Yu, J.-f. Mao, F.-q. Guo, and W. Guo, "Non-stationary random vibration analysis of a 3D train-bridge system using the probability density evolution method," *Journal of Sound and Vibration*, vol. 366, pp. 173–189, 2016.
- [29] J. Mao, Z. Yu, Y. Xiao, C. Jin, and Y. Bai, "Random dynamic analysis of a train-bridge coupled system involving random system parameters based on probability density evolution method," *Probabilistic Engineering Mechanics*, vol. 46, pp. 48–61, 2016.

Research Article

Water Level Sensing in a Steel Vessel Using A_0 and Quasi-Scholte Waves

Peng Guo,¹ Bo Deng,¹ Xiang Lan,¹ Kaili Zhang,¹ Hongyuan Li,¹ Zhenhua Tian,²
and Hong Xu¹

¹Key Laboratory of Condition Monitoring and Control for Power Plant Equipment of Ministry of Education, School of Energy, Power and Mechanical Engineering, North China Electric Power University, Beijing 102206, China

²Department of Mechanical Engineering and Material Science, Duke University, Durham, NC 27708, USA

Correspondence should be addressed to Zhenhua Tian; zhenhua.tian@duke.edu

Received 15 July 2017; Accepted 25 October 2017; Published 20 December 2017

Academic Editor: Amardeep Kaur

Copyright © 2017 Peng Guo et al. This is an open access article distributed under the Creative Commons Attribution License, which permits unrestricted use, distribution, and reproduction in any medium, provided the original work is properly cited.

This paper presents a water level sensing method using guided waves of A_0 and quasi-Scholte modes. Theoretical, numerical, and experimental studies are performed to investigate the properties of both the A_0 and quasi-Scholte modes. The comparative study of dispersion curves reveals that the plate with one side in water supports a quasi-Scholte mode besides Lamb modes. In addition, group velocities of A_0 and quasi-Scholte modes are different. It is also found that the low-frequency A_0 mode propagating in a free plate can convert to the quasi-Scholte mode when the plate has one side in water. Based on the velocity difference and mode conversion, a water level sensing method is developed. For the proof of concept, a laboratory experiment using a pitch-catch configuration with two piezoelectric transducers is designed for sensing water level in a steel vessel. The experimental results show that the travelling time between the two transducers linearly increases with the increase of water level and agree well with the theoretical predictions.

1. Introduction

In power plants, monitoring the water levels in core facilities, such as the boiler steam drum, condensers, and cooling pipes, is critical for the safety and economical operation of power plants. Hence, there is a need to develop nondestructive technologies for high-precision, high-reliability, real-time monitoring of water levels in steel vessels. Ultrasonic guided waves have opened new opportunities for cost-effective non-destructive evaluation (NDE), because they can reveal small features related to the interaction between guided waves and structures and provide considerable information about the structures [1–4]. When a solid waveguide is immersed in water, the traction-free boundary condition changes and the wave propagation in the solid will change accordingly. When a free plate is immersed in water, the out-of-plane displacement in the plate can transmit into the water through the plate-water interface [1]. Worlton [5] extended the Lamb theory by using experimental observations and derived

the dispersion curves for aluminum and zirconium plates. Bingham et al. [6] used ultrasonic guided waves to identify the mass loading on ship hulls. Na and Kundu [7] detected gouges and dents in an underwater pipeline using guided waves. Chen et al. [8] developed a damage identification approach using the A_0 mode for evaluating corrosion damage in submerged structures. Koduru and Rose [9] utilized an array of permanently mounted transducers to detect defects and avoid the influences from external environmental conditions, for example, water loading and temperature change. Pistone et al. [10] performed experimental studies using a pulsed laser for structural health monitoring of immersed aluminum plates. Yapura and Kinra [11] derived dispersion equations for a fluid-solid bilayer and then presented a numerical result for a water-aluminum bilayer. Baron and Naili [12] studied the fluid-loaded anisotropic and homogeneous plane waveguide with two different fluids on each side using an analytical approach. Yu and Tian [13] used a scanning laser Doppler vibrometer for measuring quasi-

Scholte waves in one-side water-immersed plates. Banerjee and Kundu [14] developed the distributed point source method (DPSM) to simulate the ultrasonic wavefields at the fluid and solid interface; their method can also be used to calculate the pressure, velocity, and displacement fields in the fluid.

For power plants, the frequently used water level measurement methods include the differential pressure gauge [15], ultrasonic level meter [16, 17], and radar level gauge [18]. For the differential pressure gauge, the water level is determined from the static pressure change induced by the water level change. Usually, there is a delay for determining the water level after the water level changes. In addition, the pressure condition might change due to the changes of temperature and other operation conditions. These factors could cause large errors in water level sensing. The ultrasonic level meter uses ultrasonic pulses reflected from the liquid-gas interface to determine the water level. In this method, ultrasonic pulses are generated by a transducer placed on the bottom of the container. Based on the travelling time of reflection waves, the water level is determined. However, large errors can be induced by poor reflection from the water surface and complex scattering waves in the container. The principle of radar level gauge is similar to the ultrasonic level meter, while the radar level gauge uses microwave pulses. In this method, the sensors need to be installed in the container, and thus the sensor installation may influence the integrity of the container and cause leakage. In addition, the water vapor on the waveguide tube might influence the signal quality.

In this paper, we present a water level sensing method for steel vessels by using guided waves of A_0 and quasi-Scholte modes. For water level sensing, two piezoelectric transducers (PZTs) are bonded on the out surface of the vessel in the pitch-catch configuration to generate and measure guided waves. The generated guided waves propagate in the wall of the vessel. The mode conversion between A_0 and quasi-Scholte modes at the water interface is observed. Based on the velocity difference between A_0 and quasi-Scholte modes, a quantitative method for detecting the water level is developed. Through proof-of-concept experiments, it has been found that the travelling time of guided waves in the vessel linearly increases with the increase of water level. Moreover,

the experimental results agree well with theoretical predictions. The developed method provides several advantages. The method has a small error less than 3.7 mm, and sensors can be easily installed on the outer surface of the container without influencing the structural integrity. In addition, since the sensors are not in the container, the sensors can be easily maintained. Moreover, compared to the ultrasonic level meter, our method does not rely on the poor reflection from the water boundary and is less influenced by the scattering waves inside the container.

The rest of this paper is organized as follows. Section 2 presents the guided wave fundamentals, such as characteristic equations and dispersion curves for the free plate and the plate with one side in water. Section 3 presents the verifications of A_0 mode in the free plate and quasi-Scholte mode in the plate with one side in water through finite element simulations and experiments. Section 4 presents the water level sensing method with a proof-of-concept experiment. Section 5 concludes the paper with findings and future work.

2. Theoretical Fundamentals

2.1. Free Plates. Considerable research exists on the dispersion characteristics of guided waves in free isotropic plates [1, 2, 13, 19]. In this section, the dispersion characteristics of guided waves in a free plate with traction-free boundary conditions are given. For a free plate (in Figure 1(a)), the boundary conditions for the top and bottom surfaces of the plate can be described as follows:

$$\begin{aligned}\sigma_{xx}^{p-t} &= 0, \\ \sigma_{xz}^{p-t} &= 0, \\ \sigma_{xx}^{p-b} &= 0, \\ \sigma_{xz}^{p-b} &= 0,\end{aligned}\quad (1)$$

where σ_{xx}^{p-t} and σ_{xz}^{p-t} are the normal and shear stresses on the top surface of the plate, respectively. σ_{xx}^{p-b} and σ_{xz}^{p-b} are the normal and shear stresses on the bottom surface of the plate, respectively. The characteristic equation of Lamb waves in a free plate can be expressed as follows:

$$\begin{vmatrix} k_{sx}^2 - k_z^2 & k_{sx}^2 - k_z^2 & -2k_{sx}k_z & 2k_{sx}k_z \\ 2k_{lx}k_z & -2k_{lx}k_z & k_{sx}^2 - k_z^2 & k_{sx}^2 - k_z^2 \\ (k_{sx}^2 - k_z^2)e^{ik_{lx}d} & (k_{sx}^2 - k_z^2)e^{-ik_{lx}d} & -2k_{sx}k_z e^{ik_{sx}d} & 2k_{sx}k_z e^{-ik_{sx}d} \\ 2k_{lx}k_z e^{ik_{lx}d} & -2k_{lx}k_z e^{-ik_{lx}d} & (k_{sx}^2 - k_z^2)e^{ik_{sx}d} & (k_{sx}^2 - k_z^2)e^{-ik_{sx}d} \end{vmatrix} = 0, \quad (2)$$

where $k_{lx}^2 = \omega^2/c_L^2 - k_z^2$, $k_{sx}^2 = \omega^2/c_S^2 - k_z^2$, $k_z = 2\pi/\lambda_{\text{wave}}$, $c_L = \sqrt{[2\mu(1-\nu)]/[\rho(1-2\nu)]}$, and $c_S = \sqrt{\mu/\rho}$. k_z is the wavenumber of Lamb waves. d is the plate thickness. ω and

λ_{wave} are the circular frequency and wavelength, respectively. c_L and c_S are the velocities of longitudinal and shear waves, respectively. ρ , μ , and ν are the density, shear modulus, and

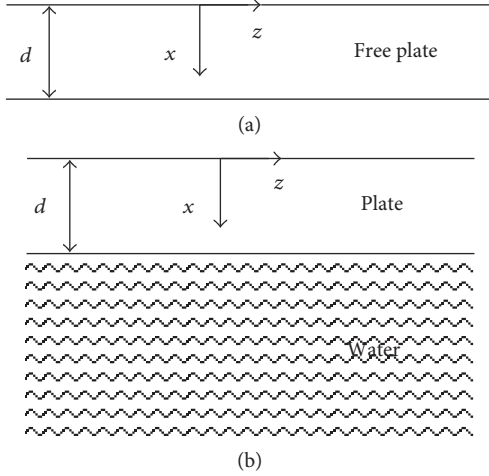


FIGURE 1: Sketches of (a) a free plate and (b) a plate with one side in water.

Poisson's ratio of the plate, respectively. By solving (2), the dispersion curves for a steel plate (the material properties of the steel plate are listed in Table 1) are obtained, as shown in Figures 2(a) and 2(b). In the low-frequency region, the group velocity of S_0 mode is relatively high. In contrast, the group velocity of A_0 mode is relatively low and changes greatly with respect to frequency.

TABLE 1: Material properties for a steel plate and water.

| | | |
|-----------------------|-----------------------------|-------|
| Stainless steel plate | Density (kg/m^3) | 8000 |
| | Young's modulus (GPa) | 196.5 |
| | Poisson's ratio | 0.29 |
| | Thickness (mm) | 1.2 |
| Water | Density (kg/m^3) | 1000 |
| | Bulk wave velocity (m/s) | 1500 |

2.2. *Plates with One Side in Water.* As shown in Figure 1(b), when the bottom surface of a free plate is in water, its boundary conditions change compared to a free plate. Under the nonviscosity assumption, the boundary conditions for the bottom surface become

$$\begin{aligned} \sigma_{xx}^{\text{p-b}} &= \sigma_{xx}^{\text{water}}, \\ \sigma_{xz}^{\text{p-b}} &= 0, \\ u_{xx}^{\text{p-b}} &= u_{xx}^{\text{water}}, \end{aligned} \quad (3)$$

where $u_{xx}^{\text{p-b}}$ is the normal displacement on the bottom surface of the plate. u_{xx}^{water} and $\sigma_{xx}^{\text{water}}$ are the normal displacement and stress at the plate-water interface, respectively. The characteristic equation for the plate with one side in water can be assembled and expressed as follows:

$$\begin{bmatrix} k_{sx}^2 - k_z^2 & k_{sx}^2 - k_z^2 & -2k_{sx}k_z & 2k_{sx}k_z & 0 \\ 2k_{lx}k_z & -2k_{lx}k_z & k_{sx}^2 - k_z^2 & k_{sx}^2 - k_z^2 & 0 \\ (k_{sx}^2 - k_z^2)e^{ik_{lx}d} & (k_{sx}^2 - k_z^2)e^{-ik_{lx}d} & -2k_{sx}k_z e^{ik_{sx}d} & 2k_{sx}k_z e^{-ik_{sx}d} & \frac{\omega^2 \rho_w}{\mu} \\ 2k_{lx}k_z e^{ik_{lx}d} & -2k_{lx}k_z e^{-ik_{lx}d} & (k_{sx}^2 - k_z^2)e^{ik_{sx}d} & (k_{sx}^2 - k_z^2)e^{-ik_{sx}d} & 0 \\ k_{lx}e^{ik_{lx}d} & -k_{lx}e^{-ik_{lx}d} & -k_z e^{ik_{sx}d} & -k_z e^{-ik_{sx}d} & \gamma \end{bmatrix} = 0, \quad (4)$$

where $\gamma^2 = \omega^2/c_{Lw}^2 - k_z^2$ and $c_{Lw} = \sqrt{\lambda_w/\rho_w}$. c_{Lw} is the bulk velocity in water; λ_w and ρ_w are the bulk stiffness and density of water, respectively. By solving (4), the dispersion curves of a 1.2 mm thick steel plate with one side in water are obtained. As shown in Figures 2(c) and 2(d), the fundamental antisymmetric and symmetric modes are denoted as A_{0w} and S_{0w} . Compared to dispersion curves for a free plate (Figure 2(a)), dispersion curves for a plate with one side in water (Figure 2(c)) clearly show another mode, the quasi-Scholte mode, in addition to the fundamental antisymmetric and symmetric modes. The dispersive behavior of the quasi-Scholte mode in the plate with one side in water is the same as the mode discovered in a two-side water-immersed plate in [20]. The quasi-Scholte mode is dispersive in the low-frequency region; however, with the increase of the frequency,

the mode gradually approaches the nondispersive Scholte mode (interface wave at solid and liquid interface) [20, 21].

3. Simulation and Experimental Studies

In the previous section, the dispersion curves of guided waves in a free plate and a plate with one side in water are theoretically studied. In this section, the quasi-Scholte and A_0 modes are further investigated through finite element simulations and experiments.

3.1. *Verification of the A_0 Mode in a Free Plate.* Finite element simulations are performed using the commercial software ANSYS to analyze the propagation of A_0 mode in a free plate. The finite element model of a plate's cross section is built using 2D elements (8-node PLANE82). Table 1 gives the

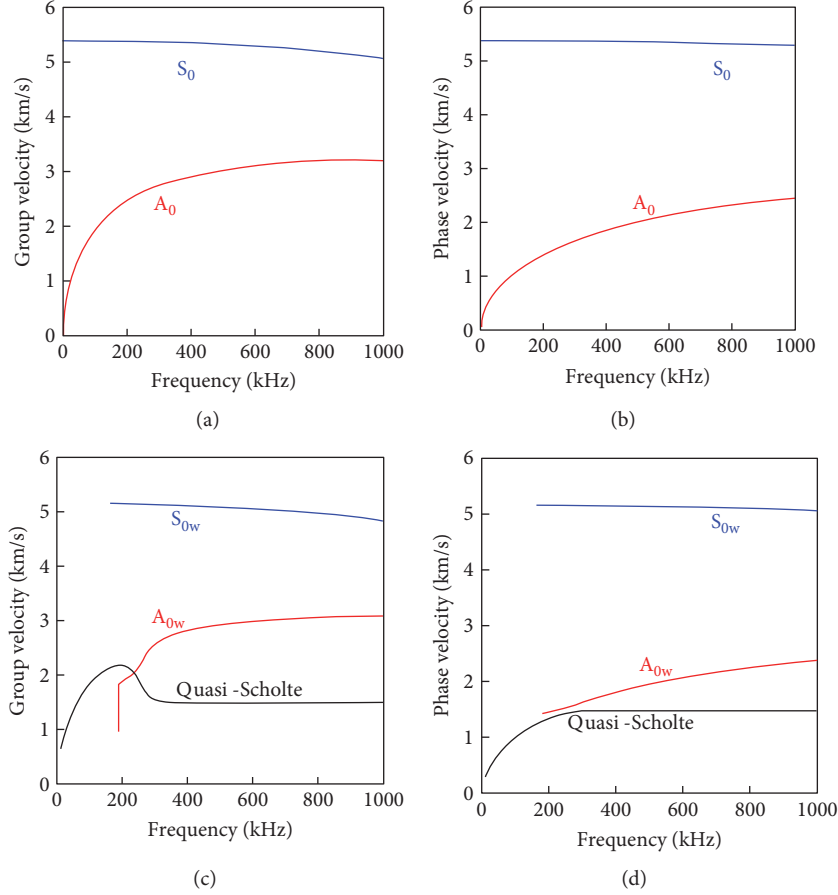


FIGURE 2: Theoretical dispersion curves: (a) and (b) are group and phase velocities for a 1.2 mm thick steel plate; (c) and (d) are group and phase velocities for a 1.2 mm thick steel plate with one side in water.

material parameters of the plate. The thickness and length of the plate are 1.2 mm and 100 mm, respectively. For simulating elastic waves in solids using finite element method (FEM), the transient analysis in ANSYS is adopted. To ensure the accuracy of the simulation, the grid size and the integral time step satisfy the following:

$$L_{\max} < \frac{\lambda_{\min}}{n_{\min}} = \frac{c_{\min}}{n_{\min}f}, \quad (5)$$

$$\Delta t \leq \frac{L_{\min}}{c_s},$$

where L_{\max} and L_{\min} are the maximum and minimum grid size, respectively; λ_{\min} is the minimum wavelength; n_{\min} is the minimum number of elements within one wavelength (usually n_{\min} is in the range of 8~10); c_s denotes the velocity of shear waves; and c_{\min} is the minimum group velocity of elastic waves. Vertical loads are applied on the nodes at $X=0$ on top and bottom surfaces, for generating a pure A_0 mode.

Figure 3 shows the simulation result (a vector field of displacement) for the A_0 mode, when the excitation is 5-count tone bursts at 100 kHz. From the result, it can be seen that the A_0 mode is antisymmetric. In addition, the

vertical displacement is much stronger than the horizontal displacement. The displacement signals at four different locations ($X=20, 40, 60,$ and 80 mm on the bottom surface of the plate) are plotted in Figure 4. Using the traveling time and propagation distance, we can calculate the group velocity of A_0 mode, $1.92 \text{ mm}/\mu\text{s}$, which agrees well with the theoretical velocity $1.925 \text{ mm}/\mu\text{s}$.

An experiment is performed using the setup in Figure 5(a), for wave mode verification. Two PZT transducers (with dimensions of $7 \times 7 \times 0.2$ mm) in a pitch-catch configuration are adopted. The distance between two transducers is 150 mm. The excitation signal is 2.5-cycle tone bursts at 100 kHz. Figure 6 plots a received signal with its Hilbert envelope. Using the travelling time obtained from the received signal and the distance between two transducers, the group velocity of A_0 mode is calculated, which is $1.89 \text{ mm}/\mu\text{s}$. Figure 7 compares the A_0 mode's group velocities obtained from the theory, simulation, and experiment at 50, 100, and 150 kHz. The results of the theory, simulation, and experiment agree well with each other.

3.2. Verification of the Quasi-Scholte Mode in a Plate with One Side in Water. Finite element simulations are performed to analyze the propagation of quasi-Scholte mode in a plate with one side in water. Figure 8(a) plots a schematic of the

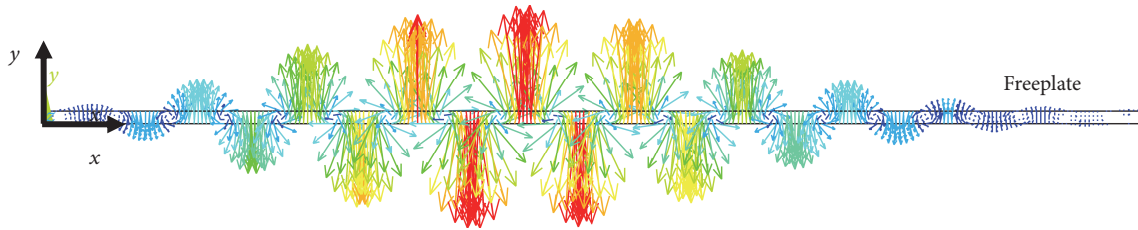


FIGURE 3: The FEM simulation result (displacement vector field) of the excited A_0 mode in a free plate at 100 kHz.

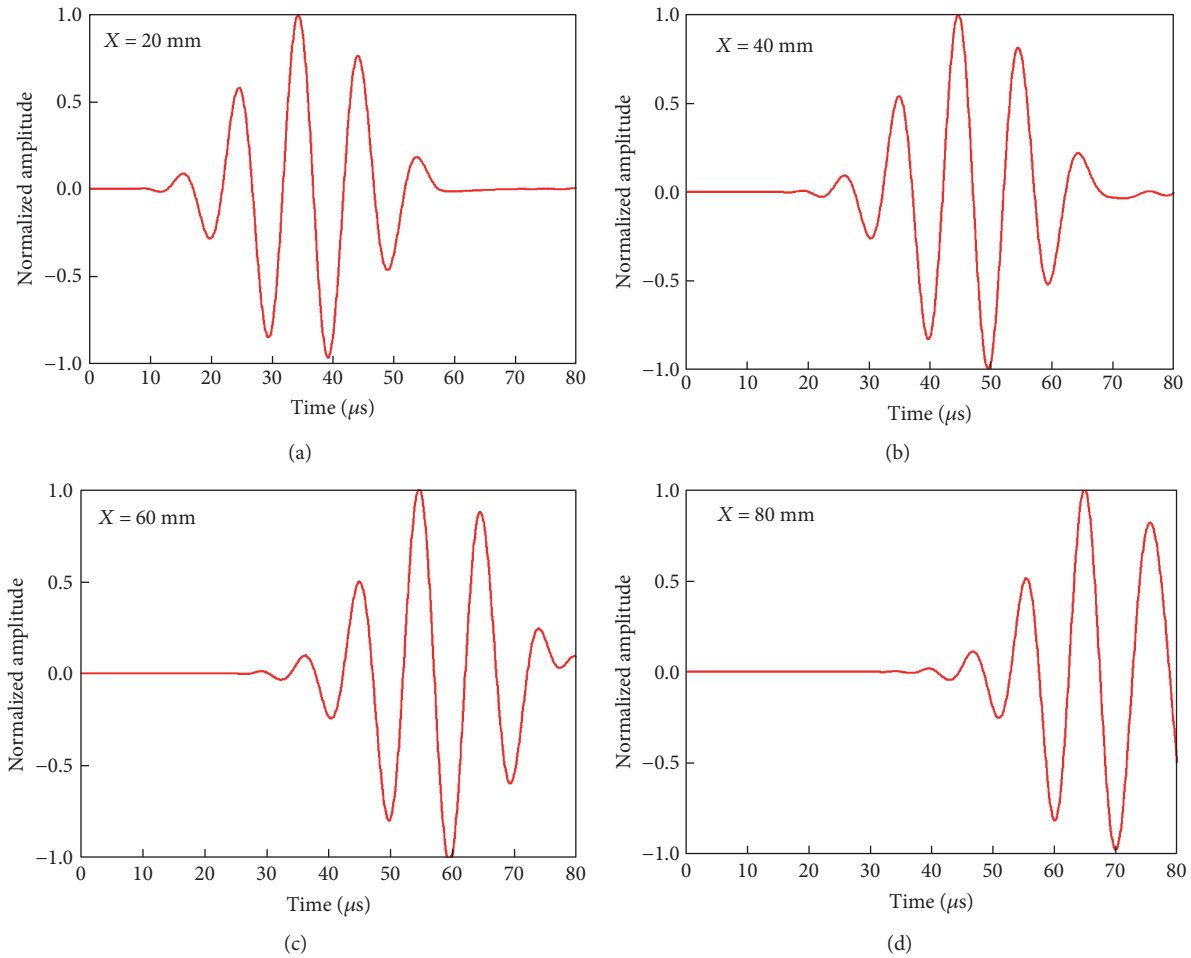


FIGURE 4: Out-of-plate displacement signals (simulation results) at different locations in the free plate. (a), (b), (c), and (d) are for $X = 20$, 40, 60, and 80 mm, respectively, on the bottom surface of the plate.

simulation setup. The top layer is a 1.2 mm thick steel plate. The bottom layer is water with the depth of 40 mm. In the finite element model, the water layer is created using the coupling field element (FLUID29).

Figure 8(b) shows the simulation result (pressure field) when the excitation is 5-count tone bursts at 100 kHz. In the water layer, it can be seen that there are two types of waves, the quasi-Scholte waves and pressure waves (P waves). The quasi-Scholte mode propagates along the interface between the plate and the water, while the P waves only propagate in water. The displacement signals at four different locations ($X = 20$, 40, 60, and 80 mm on the bottom surface

of the plate) are plotted in Figure 9. Using the traveling time and propagation distance, we find the group velocity of the quasi-Scholte mode, $1.86 \text{ mm}/\mu\text{s}$ at 100 kHz, which agrees well with the theoretical velocity $1.84 \text{ mm}/\mu\text{s}$.

An experiment is also performed using the setup in Figure 5(b), for wave mode verification. Two PZT transducers (with dimensions of $7 \times 7 \times 0.2 \text{ mm}$) in a pitch-catch configuration are adopted. The distance between the two transducers is 150 mm. The excitation signal is 2.5-cycle tone bursts 100 kHz. Figure 10 plots a received signal with its Hilbert envelope, when the excitation frequency is 100 kHz. Using the received signal and the distance between two

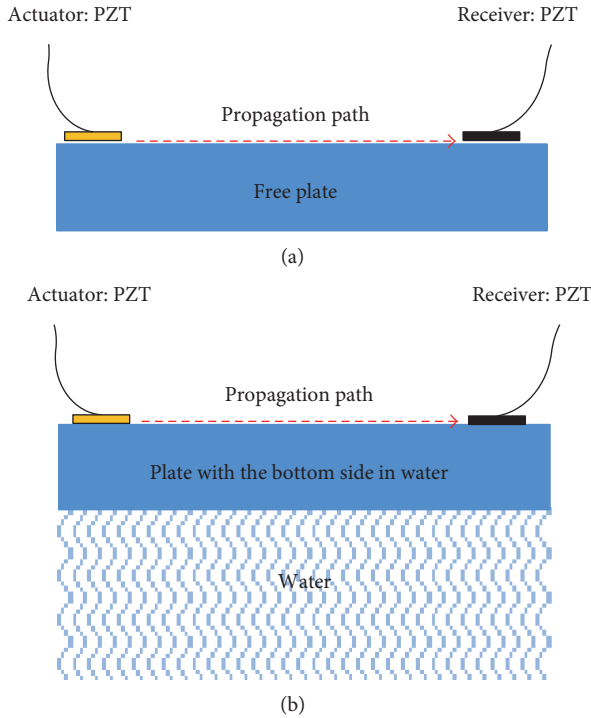


FIGURE 5: The experimental setup for guided wave sensing and mode identification: (a) in a free plate; (b) in a plate with one side in water.

transducers, the group velocity of A_0 mode is obtained, which is $1.85 \text{ mm}/\mu\text{s}$. Figure 11 compares the quasi-Scholte mode's group velocities obtained from the theory, simulation, and experiment at 50, 100, and 150 kHz. The results of theory, simulation, and experiment agree well with each other.

4. Water Level Sensing Using A_0 and Quasi-Scholte Modes

This section presents a water level sensing method by using both A_0 and quasi-Scholte modes. A pitch-catch sensing configuration with two PZT transducers is employed. For this configuration, a theoretical prediction of the relation between water level and wave travelling time is derived. For the proof of concept, a laboratory experiment is performed. The experimental results agree well with the theoretical predictions and show that the travelling time linearly increases with the increase of water level.

4.1. Theoretical Predictions. Figure 12 plots a proposed pitch-catch configuration with two PZT transducers for water level sensing. The full wave propagation path (d_{T-R}) consists of two parts: the water path d_W and the dry path $d_{T-R} - d_W$. In the water path d_W , the quasi-Scholte mode propagates in the plate with one side in water; in the dry path $d_{T-R} - d_W$, the A_0 mode propagates in the free plate. When the water level changes, it will directly change the portions of dry path $d_{T-R} - d_W$ and water path d_W . The guided waves leave the excitation PZT as the quasi-Scholte mode in the water path d_W and then are converted to the A_0 mode in the dry

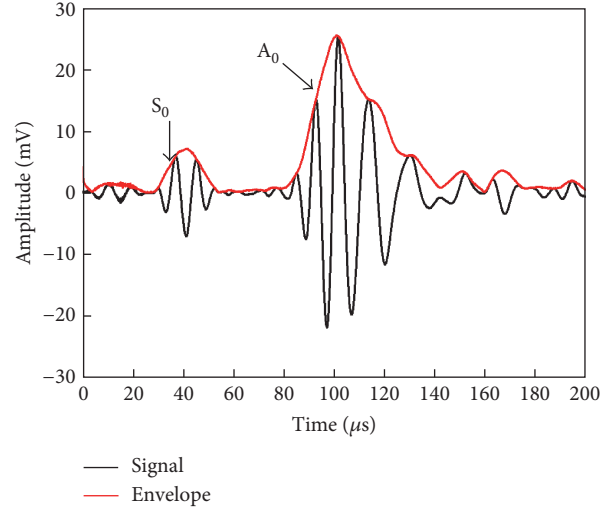


FIGURE 6: Experimental signal of guided waves in a free steel plate at 100 kHz.

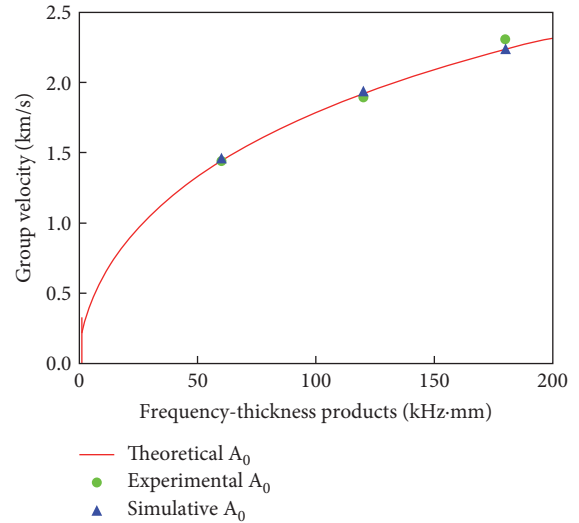


FIGURE 7: Comparison of A_0 mode's group velocities obtained from theory, simulation, and experiment.

path $d_{T-R} - d_W$. Therefore, the propagation time over the entire path d_{T-R} is given by the following:

$$t_{T-R} = \frac{d_W}{c_{QS}} + \frac{d_{T-R} - d_W}{c_{A_0}}, \quad (6)$$

where c_{QS} is the quasi-Scholte mode group velocity, c_{A_0} is the A_0 mode group velocity, and t_{T-R} is the propagation time over the entire propagation path d_{T-R} . If $d_W = 0$ is the baseline, when the water level d_W changes, the relation between time difference Δt_{T-R} on the entire propagation path d_{T-R} is given by the following expression:

$$\Delta t_{T-R} = d_W \left(\frac{1}{c_{QS}} - \frac{1}{c_{A_0}} \right). \quad (7)$$

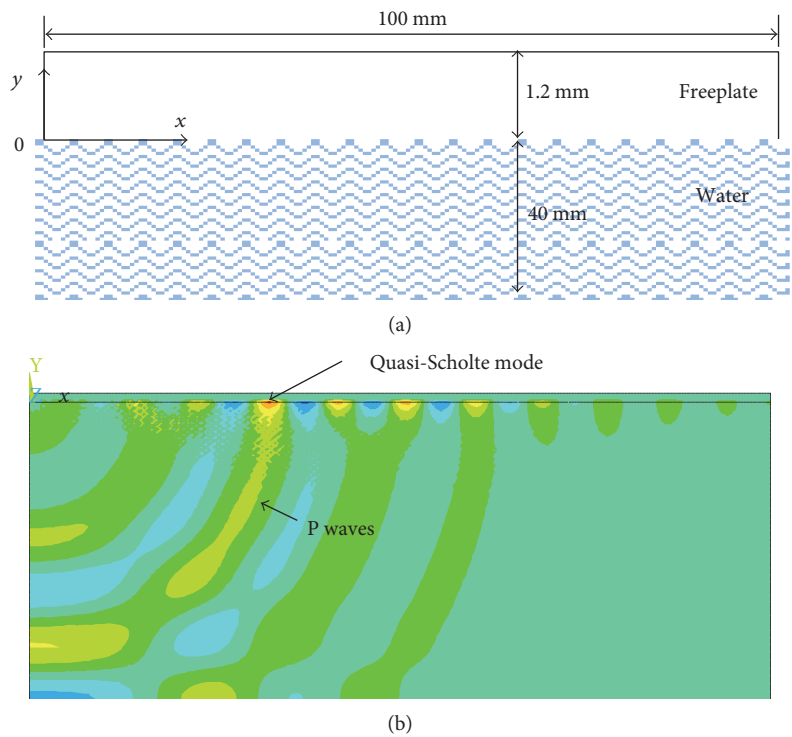


FIGURE 8: FEM simulation of the quasi-Scholte mode in a plate with one side in water at 100 kHz: (a) a schematic of the FEM model and (b) the simulation result (pressure field).

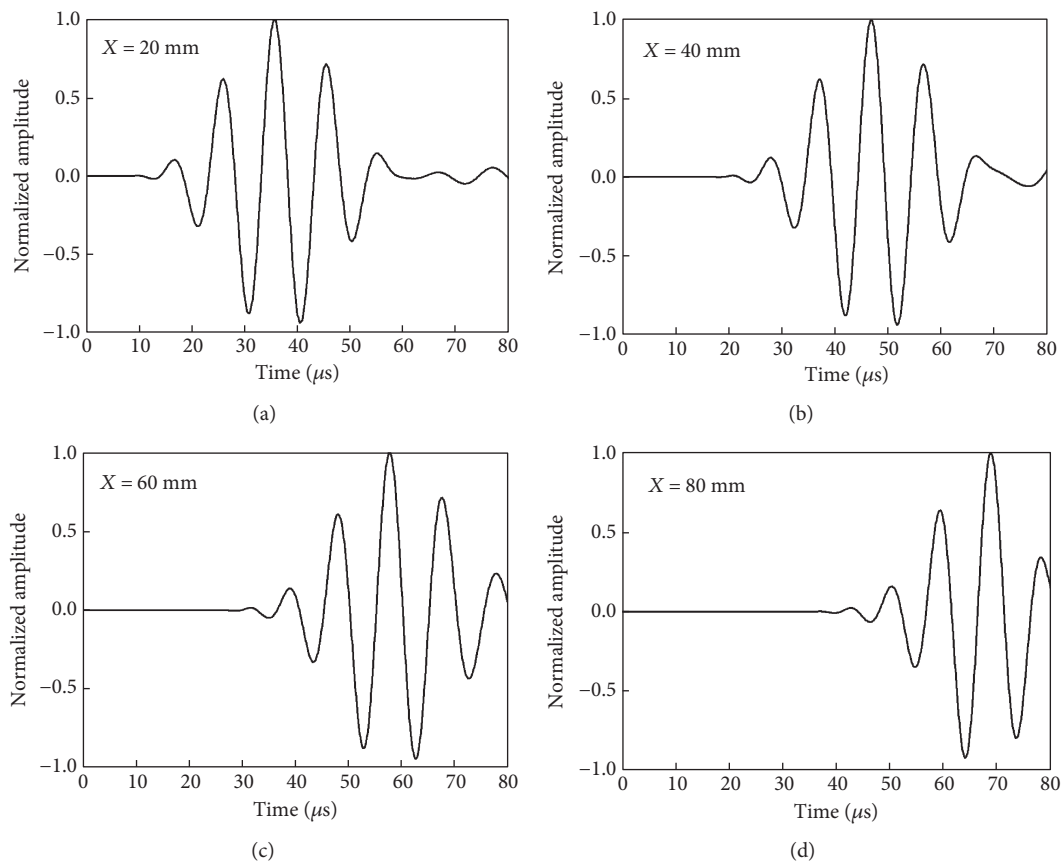


FIGURE 9: Out-of-plate displacement signals (simulation results) at different locations in the plate with one side in water: (a), (b), (c), and (d) are for $X = 20, 40, 60,$ and 80 mm, respectively, on the bottom surface of the plate.

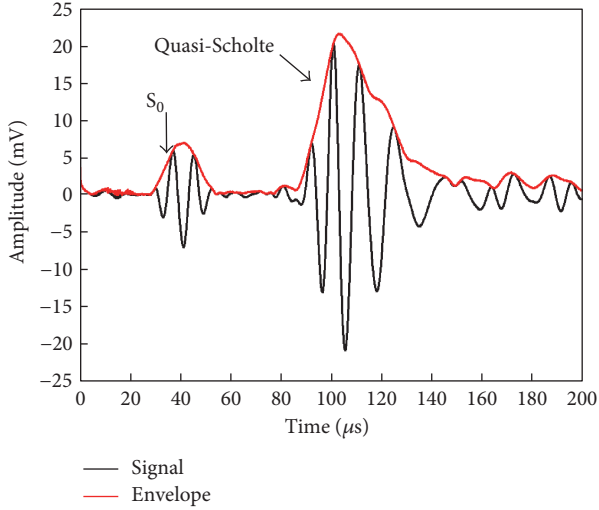


FIGURE 10: Experimental signal of guided waves in the plate with one side in water at 100 kHz.

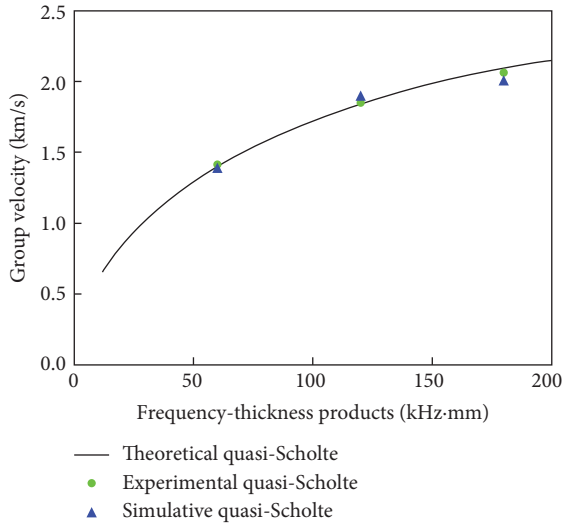


FIGURE 11: Comparison of quasi-Scholte mode's group velocities obtained from theory, simulation, and experiment.

As seen in (7), the water level d_W is linearly related to the time difference Δt_{T-R} .

4.2. Experimental Setup for Water Level Sensing. An experiment is performed using the configuration in Figure 12. The plate is a 1.2 mm thick steel with material properties given in Table 1. Two PZT transducers (with dimensions of $7 \times 7 \times 0.2$ mm) are bonded on the plate in a pitch-catch configuration with the distance of 100 mm. The excitation signal has 2.5-cycle tone bursts, generated by an arbitrary function generator (model: Tektronix AFG 3022). The amplitude of the excitation signal is 10 V, which is the maximum output of our function generator. With this amplitude, we can achieve the optimal signal-to-noise ratio within the capability of our current equipment. In this water level sensing test, the

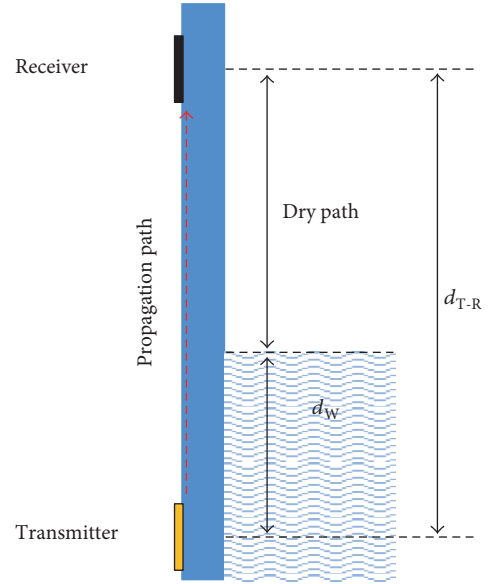


FIGURE 12: A pitch-catch configuration with two PZT transducers for water level sensing.

excitation frequency is selected at 130 kHz for the proof of concept. The guided waves excited by the actuator propagate along the plate. At the receiver, waves are measured by an oscilloscope (Tektronix TDS 2022B).

4.3. Data Analysis Using Pseudo Wigner-Vile Distribution (PWVD). Time-frequency analysis is a description of a signal in the time and frequency domain, indicating the energy distribution of the signal in the time-frequency space [22–27]. For signal analysis, this study employs PWVD. The measured experimental signal at the 50 mm water level is used as an example. The received waveform at the 50 mm water level is given in Figure 13(a). The travelling time of the second wave packet is contributions of both the A_0 and quasi-Scholte modes. Since the low-frequency A_0 and quasi-Scholte modes are highly dispersive, this dispersive effect may influence the measurement of travelling time of a wave packet. To precisely determine the travelling time at a certain frequency, time-frequency analysis is needed. Figure 13(b) plots a 2D time-frequency distribution of the PWVD. Figure 13(c) plots an extracted PWVD result at 130 kHz. Hence, the travelling time of the second wave package at 130 kHz can be determined.

4.4. Experimental Results. To investigate the relationship between the water level and the received signal, signals at the receiver are collected at a series of water levels from 0 mm to 100 mm with a step of 10 mm. Figure 14(a) plots four representative signals when the water levels are 0, 30, 60, and 100 mm. As shown in Figure 14(a), with the increase of water level, the wave packet gradually shifts to the right, which means the travelling time gradually increases. Using the PWVD method, the traveling time and time difference Δt_{T-R} at 130 kHz are obtained. Figure 14(b) plots the derived time difference Δt_{T-R} with respect to water level d_W . A linear fitting is applied to the experimental data. The fitting result is

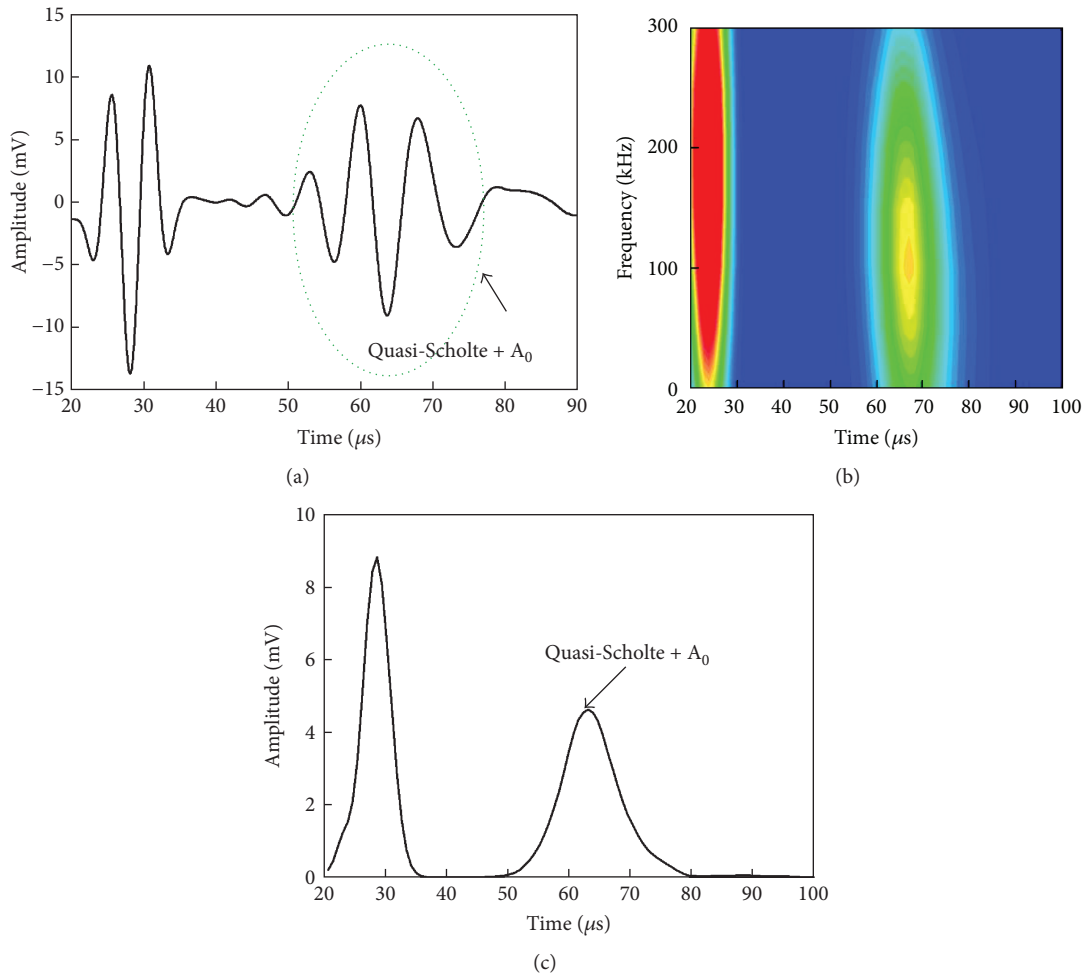


FIGURE 13: Analysis of a received signal using the PWVD: (a) received signal at the water level of 50 mm, (b) the PWVD result in time-frequency domain, and (c) the result of PWVD at 130 kHz.

$\Delta t_{T-R} = 0.034d_W$ with the R^2 value of 0.998, which is close to 1. This means that the experimental results are in a linear relationship. The theoretical prediction derived from (7) is $\Delta t_{T-R} = 0.035d_W$, which is also plotted in Figure 14(b). The coefficient of the linear fitting is very close to that of the theoretical prediction with an error of 2.9%. In addition, it can be seen that the experimental result agrees well with the theoretical prediction. The error for water level sensing is less than 3.7 mm. The precision of our method could be influenced by several factors including sensor installation errors, structural damage (corrosion, rust, and crack), environmental conditions, errors of wave speeds, and errors of the time differences. The measuring range depends on the distance between the actuator and the receiver. In the current setup, the distance is 100 mm, and thus the measuring range is 0~100 mm.

5. Conclusions

This paper presents a water level sensing method by using the A_0 and quasi-Scholte modes. The water level sensing method adopts a pitch-catch sensing configuration with a pair of PZT transducers bonded on a steel vessel. The travelling time of

guided waves between the two transducers is influenced by the water level. Hence, by measuring the travelling time, the water level in the vessel can be found.

This study investigates the difference between guided waves in a free plate and a plate with one side. Through theoretical, numerical, and experimental studies, it is confirmed that the A_0 mode presents in a free plate and the quasi-Scholte mode presents in a plate with one side in water at low frequencies. Moreover, the A_0 mode can convert to the quasi-Scholte mode and vice versa. Lastly, the group velocity of the quasi-Scholte mode is smaller than that of the A_0 mode. Based on these findings, a water level sensing method is developed, which takes the advantage of the group velocity difference between the quasi-Scholte and A_0 modes.

The water level sensing method adopts a pair of PZT transducers in the pitch-catch configuration bonded on the out surface of the vessel. When the water level is between the two transducers, the entire travelling path can be divided into two portions, the dry path (with A_0 mode) and the water path (with quasi-Scholte mode). If the water level changes, the lengths of dry path and water path change; hence, the total travelling time changes. Based on this principle, the water level can be predicted by using

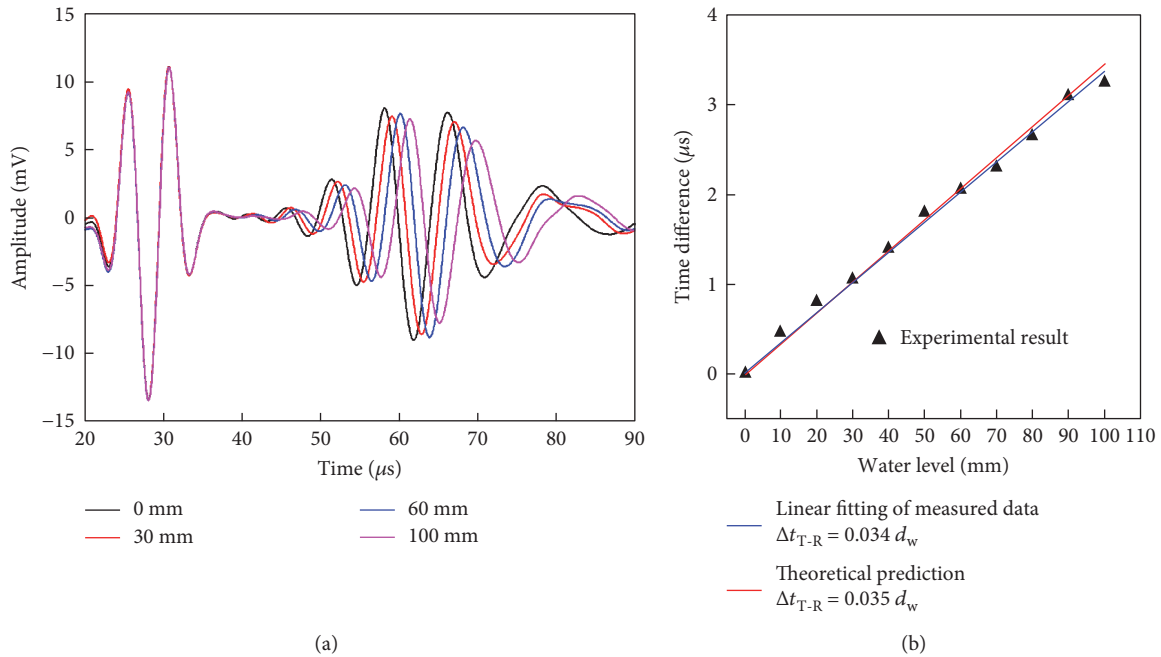


FIGURE 14: Experimental results. (a) Received waveforms at different water levels. (b) Water level sensing results. The linear fitting result shows that the water level d_w is in a linear relationship with the time difference Δt_{T-R} . In addition, experimental results agree well with the theoretical predictions.

the travelling time. For the proof of concept, we experimentally demonstrate water level sensing using guided waves. The experimental results show that wave travelling time linearly increases with the increase of water level and agree well with theoretical predictions.

For our method, the sensing resolution could be influenced by the wave speed, sampling rate of the data acquisition equipment, and the smallest time difference that can be determined. The sensitivity could be influenced by the wave speed difference between the A_0 mode and the quasi-Scholte mode. In the future, we will perform detailed parametric studies with both theoretical analysis and experiments, in order to characterize the sensing resolution and sensitivity, as well as identify the optimum frequency that can provide the best sensing resolution and sensitivity. For real-world applications, there are still some challenges. Our method could be influenced by structural damage (corrosion, rust, and crack), temperature fluctuation, and sensor degradation under harsh environmental conditions. In the future, we aim to develop a more robust system with these challenges considered for practical applications in power plants.

Conflicts of Interest

The authors declare that there is no conflict of interest regarding the publication of this paper.

Acknowledgments

The authors would like to acknowledge and thank (1) National Natural Science Foundation of China (51134016, 11074073) and (2) the Fundamental Research Funds for the Central Universities (2016XS25).

References

- [1] J. L. Rose, *Ultrasonic Waves in Solid Media*, Cambridge University Press, Cambridge, 1999.
- [2] V. Giurgiutiu, *Structural Health Monitoring with Piezoelectric Wafer Active Sensors*, Academic Press, Boston, MA, USA, 2008.
- [3] D. C. Worlton, *Ultrasonic Testing with Lamb Waves*, General Electric Co., Hanford Atomic Products Operation, Richland, Washington, 1956.
- [4] D. N. Alleyne and P. Cawley, "The interaction of lamb waves with defects," *IEEE Transactions on Ultrasonics, Ferroelectrics, and Frequency Control*, vol. 39, no. 3, pp. 381–397, 1992.
- [5] D. C. Worlton, "Experimental confirmation of lamb waves at megacycle frequencies," *Journal of Applied Physics*, vol. 32, no. 6, pp. 967–971, 1961.
- [6] J. Bingham, M. Hinders, and A. Friedman, "Lamb wave detection of limpet mines on ship hulls," *Ultrasonics*, vol. 49, no. 8, pp. 706–722, 2009.
- [7] W. B. Na and T. Kundu, "Underwater pipeline inspection using guided waves," *Transactions-American Society of Mechanical Engineers Journal of Pressure Vessel Technology*, vol. 124, no. 2, pp. 196–200, 2002.
- [8] J. Chen, Z. Su, and L. Cheng, "Identification of corrosion damage in submerged structures using fundamental anti-symmetric lamb waves," *Smart Materials and Structures*, vol. 19, no. 1, article 015004, 2009.
- [9] J. P. Koduru and J. L. Rose, "Mode controlled guided wave tomography using annular array transducers for SHM of water loaded plate like structures," *Smart Materials and Structures*, vol. 22, no. 12, article 125021, 2013.
- [10] E. Pistone, K. Li, and P. Rizzo, "Noncontact monitoring of immersed plates by means of laser-induced ultrasounds," *Structural Health Monitoring*, vol. 12, no. 5-6, pp. 549–565, 2013.

- [11] C. L. Yapura and V. K. Kinra, "Guided waves in a fluid-solid bilayer," *Wave Motion*, vol. 21, no. 1, pp. 35–46, 1995.
- [12] C. Baron and S. Naili, "Propagation of elastic waves in a fluid-loaded anisotropic functionally graded waveguide: application to ultrasound characterization," *The Journal of the Acoustical Society of America*, vol. 127, no. 3, pp. 1307–1317, 2010.
- [13] L. Yu and Z. Tian, "Case study of guided wave propagation in a one-side water-immersed steel plate," *Case Studies in Nondestructive Testing and Evaluation*, vol. 3, pp. 1–8, 2015.
- [14] S. Banerjee and T. Kundu, "Ultrasonic field modeling in plates immersed in fluid," *International Journal of Solids and Structures*, vol. 44, no. 18-19, pp. 6013–6029, 2007.
- [15] M. Cui, F. Tian, Y. Li, and J. Wang, "Research on uncertainty evaluation of the compensated differential pressure level measurement," *Chinese Journal of Mechanical Engineering*, vol. 37, no. 7, pp. 1524–1531, 2016.
- [16] V. E. Sakharov, S. A. Kuznetsov, B. D. Zaitsev, I. E. Kuznetsova, and S. G. Joshi, "Liquid level sensor using ultrasonic lamb waves," *Ultrasonics*, vol. 41, no. 4, pp. 319–322, 2003.
- [17] H. H. Hao and J. Q. Xiong, "A method of liquid level measurement based on ultrasonic echo characteristics," in *2010 International Conference on Computer Application and System Modeling (ICCASM 2010)*, pp. V11–682–V11–684, Taiyuan, China, October 2010.
- [18] Z. Qingqing, "Study on measurement of guided wave radar level gauge technology," *Electronic Instrumentation Customers*, vol. 24, no. 3, pp. 23–27, 2017.
- [19] H. Lamb, "On waves in an elastic plate," *Proceedings of the Royal Society of London A: Mathematical, Physical and Engineering Sciences*, vol. 93, no. 648, pp. 114–128, 1917.
- [20] F. B. Cegla, P. Cawley, and M. J. S. Lowe, "Material property measurement using the quasi-Scholte mode—a waveguide sensor," *The Journal of the Acoustical Society of America*, vol. 117, no. 3, pp. 1098–1107, 2005.
- [21] F. B. Cegla, P. Cawley, and M. J. S. Lowe, "Fluid bulk velocity and attenuation measurements in non-Newtonian liquids using a dipstick sensor," *Measurement Science and Technology*, vol. 17, no. 2, p. 264, 2005.
- [22] L. Cohen, "Time-frequency distributions: a review," *Proceedings of the IEEE*, vol. 77, no. 7, pp. 941–981, 1989.
- [23] W. J. Williams, "Cross Hilbert time-frequency distributions," in *Proceedings SPIE 3461, Advanced Signal Processing Algorithms, Architectures, and Implementations VIII*, pp. 120–129, San Diego, CA, USA, October 1998.
- [24] L. B. White and B. Boashash, "Cross spectral analysis of nonstationary processes," *IEEE Transactions on Information Theory*, vol. 36, no. 4, pp. 830–835, 1990.
- [25] B. Boashash and P. O'shea, "Use of the cross Wigner-Ville distribution for estimation of instantaneous frequency," *IEEE Transactions on Signal Processing*, vol. 41, no. 3, pp. 1439–1445, 1993.
- [26] L. Yu, Y. Shin, J. Wang, and Y. Shen, "An ultrasonic guided wave sensor for gas accumulation detection in nuclear emergency core cooling systems," *8th International Workshop on Structural Health Monitoring*, DEStech Publications, Inc., Lancaster, PA, USA, 2011.
- [27] L. Yu, B. Lin, Y. J. Shin, J. Wang, and Z. Tian, "Ultrasonic gas accumulation detection and evaluation in nuclear cooling pipes," in *Proceedings SPIE 8345, Sensors and Smart Structures Technologies for Civil, Mechanical, and Aerospace Systems 2012*, p. 83454U, San Diego, CA, USA, April 2012.

Research Article

Mechanism of Subordinate Peak Skewing of FBG Sensor during Cracks Propagation Monitoring on Aluminum Alloy Structure

Bo Jin,^{1,2} Weifang Zhang,³ Feifei Ren,³ Meng Zhang,³ Wei Dai,³ and Yanrong Wang¹

¹School of Energy and Power Engineering, Beihang University, 37 Xueyuan Rd., Haidian District, Beijing 100191, China

²Collaborative Innovation Center for Advanced Aero-Engine, Beihang University, 37 Xueyuan Rd., Haidian District, Beijing 100191, China

³School of Reliability and Systems Engineering, Beihang University, 37 Xueyuan Rd., Haidian District, Beijing 100191, China

Correspondence should be addressed to Wei Dai; dw@buaa.edu.cn

Received 7 August 2017; Revised 30 September 2017; Accepted 9 October 2017; Published 20 November 2017

Academic Editor: Lei Yuan

Copyright © 2017 Bo Jin et al. This is an open access article distributed under the Creative Commons Attribution License, which permits unrestricted use, distribution, and reproduction in any medium, provided the original work is properly cited.

This study investigates the variety of the spectra features of fiber Bragg grating (FBG) around the crack tip during fatigue crack propagation. The study results reveal that the turning of the subordinate peak is significantly associated with crack lengths and corresponds to strain gradient along the FBG. Meanwhile, the strain distribution sensed by the FBG changes with the sensing section of the grating. FBG sensors could observe the monotonic plastic zone ahead of the fatigue crack tip. The cubic strain is distributed along the grating, with monotonic plastic zone propagation at the initial and terminal part of the grating, at approximately a 30% ratio of the entire grating. However, the monotonic plastic zone is sensed by the FBG, at $\pm 15\%$ bias of the grating center, with the quadratic strain gradient pattern along the grating. In particular, when the initial and terminal parts of the grating experience highly inhomogeneous strain distribution, the spectrum distortion occurs.

1. Introduction

The structural damage of aircraft constructions cannot be avoided over the course of long-term service. Such damage can include fatigue, material aging, corrosion, and cracking problems [1]. Furthermore, structural damage can be identified in synchronous real-time monitoring of the aluminum alloy crack propagation [2]. FBG sensors are recognized and are applicable to structural health monitoring (SHM), such as in the concrete structure of bridges, nuclear power stations, and large dams [3]. This is due to the specific benefits of FBG sensors, such as erosion resistance, small size, and multiplexing [4]. It is argued to be one of the most promising sensors in crack propagation prediction [5].

Several researchers have made contributions to mechanical interpretations of spectral characteristics, changes with crack propagation, and the health monitoring of composite materials. Reference [6] found that the FBG spectrum was sensitive to the delamination propagation behavior of composite materials. The spectrum was split into two peaks dependent on the strain gradient which was caused by

edge delamination. The light intensity of the primary peak increases with the extent of edge delamination. In addition, further interpretation of spectral features changed with the extension of delamination [7]. Regarding predictions of delamination size in composites, an indicator of the light intensity ratio of the primary peak to the subordinate peak was proposed by [8]. In addition, [9] states that the two peaks at lower and higher wavelengths in the reflection spectra correspond to the various forms of strain distribution, with the increment of delaminated area of composites.

Regarding strain distribution analysis around the crack tip, many numerical approaches are developed to investigate the strain distribution, such as FEM and the Local-Global method. Reference [10] states that the plastic zone is divided into three regions: the monotonic plastic zone, the cyclic plastic zone, and the process zone. Meanwhile, several experimental advancements have already improved the strain distribution calculation of aluminum, such as digital image correlation (DIC), the laser speckle method, and laser speckle imaging (LSI). These improvements are also accompanied by increased instrument precision and accuracy. Strain sensing

sensors include eddy current measurement sensors, strain gauge, and the coupling fiber-optic strain sensor [11] for the strain sensitivity of FBG. The latter is used for strain monitoring; however, it is costly and is used for the monitoring of structural deformation. Therefore, the method is unsuitable for the local stress concentration, such as the strain concentration around the crack tip. Consequently, the FBG is considered as a potential sensor for the monitoring of aluminum crack concentration.

However, there has been little research focused on the mechanism of subordinate peak skewing of the FBG on aluminum crack propagation. Peters et al. [12] discussed the spectra of the FBG as a possible basis for the resolution of an arbitrary applied strain distribution. Jin et al. [13] discussed the subordinate peak of the reflection spectrum in crack propagation monitoring of aluminum alloys. The FBG was placed parallel to the external loading direction. However, in this paper, the FBG was applied perpendicular to the axial direction of the external load in this study. Subordinate peak variation which shows a strong correlation to the strain region size with crack propagation was demonstrated in this research.

2. Experiment

The core principle was to investigate the mechanism on various physical characteristics, extracted from the spectrum intensity during crack propagation. The mechanism of subordinate wavelength variation during the crack propagation demonstrated practical significance regarding quantifiable crack identification. Thus, the structure is equipped with sensors and interacts with the crack propagation, which presents the evolution of the state and physical parameters.

2.1. Specimen. The objective system established in this paper is a plate made of aluminum alloy 7075-T6, with the dimension of 300 mm × 100 mm × 2 mm as shown in Figure 1. A 10 mm diameter hole was drilled into the center of the plate. A 3 mm precrack is introduced by electrical discharge machining to activate fatigue crack propagation. The top frontier is fastened and a uniform tensile load of 65 MPa is implemented from the bottom, as indicated in Figure 1. Table 1 shows specimen properties. To sense the strain in various shapes distributed along the grating caused by the crack tip, the FBG sensor is adhered parallel to the precrack direction. The horizontal distance from the initial grating to the hole edge is 7 mm, and the perpendicular distance to the horizontal line is 1 mm. The FBG sensor length is 10.1 mm. A liquid cyanoacrylate adhesive is used to glue the FBG sensor onto the specimen surface. Young's modulus of the adhesive is 1.75 MPa.

2.2. Experiment Setup. A fatigue crack damage recognition test platform is developed and FBG sensors are utilized to abstract the damage indicator. Figure 2 illustrates the hole-edge crack experimental setup which is composed of three main segments: fatigue loading equipment, the optical modulation analyzer, and a fatigue crack detection device.

TABLE 1: Mechanical properties of 7075-T6 aluminum alloy.

| Material | Tensile strength (MPa) | Yield strength (MPa) | Poisson's ratio (MPa) | Elastic modulus (MPa) |
|-----------|------------------------|----------------------|-----------------------|-----------------------|
| AL7075-T6 | 572 | 503 | 0.33 | 73100 |

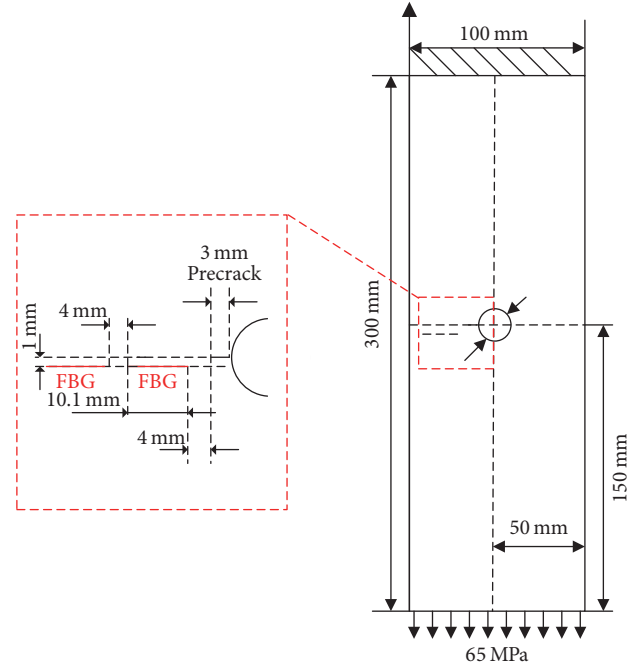


FIGURE 1: Schematic of the aluminum specimen.

The reflected spectrum of the FBG is obtained by an optical demodulator (SM125, Micro Optics Inc.), which possesses high wavelength accuracy. An optical microscope oversees the fatigue crack propagation with a Charge Coupled Device (CCD) camera during the loading progression. Fatigue testing is undertaken using a hydraulic MTS machine with continuous fatigue loading along the axial direction as shown in Figure 2. The spectra data and crack length were collected with the increase of crack length of about 1.0 mm visually, in which the fatigue loading machine was shut down and modulated at the maximum load value. The constant amplitude loading spectra used in this study have a maximum value of loading set at 65 MPa and a cycling frequency of 10 Hz. The FBG sensor number is FSSR5025.

3. Results

The natural crack in the plate was initiated and propagated through the use of a cyclic fatigue test. The FBG sensor was used to measure strain distribution along the axial grating at differential strain profiles with the crack propagation. The data was obtained using the FBG sensing demodulation system throughout cyclic fatigue. Initially, the reflection spectra are symmetrical and had a primary reflection spectrum. Subsequently, the peak simply moves backwards or

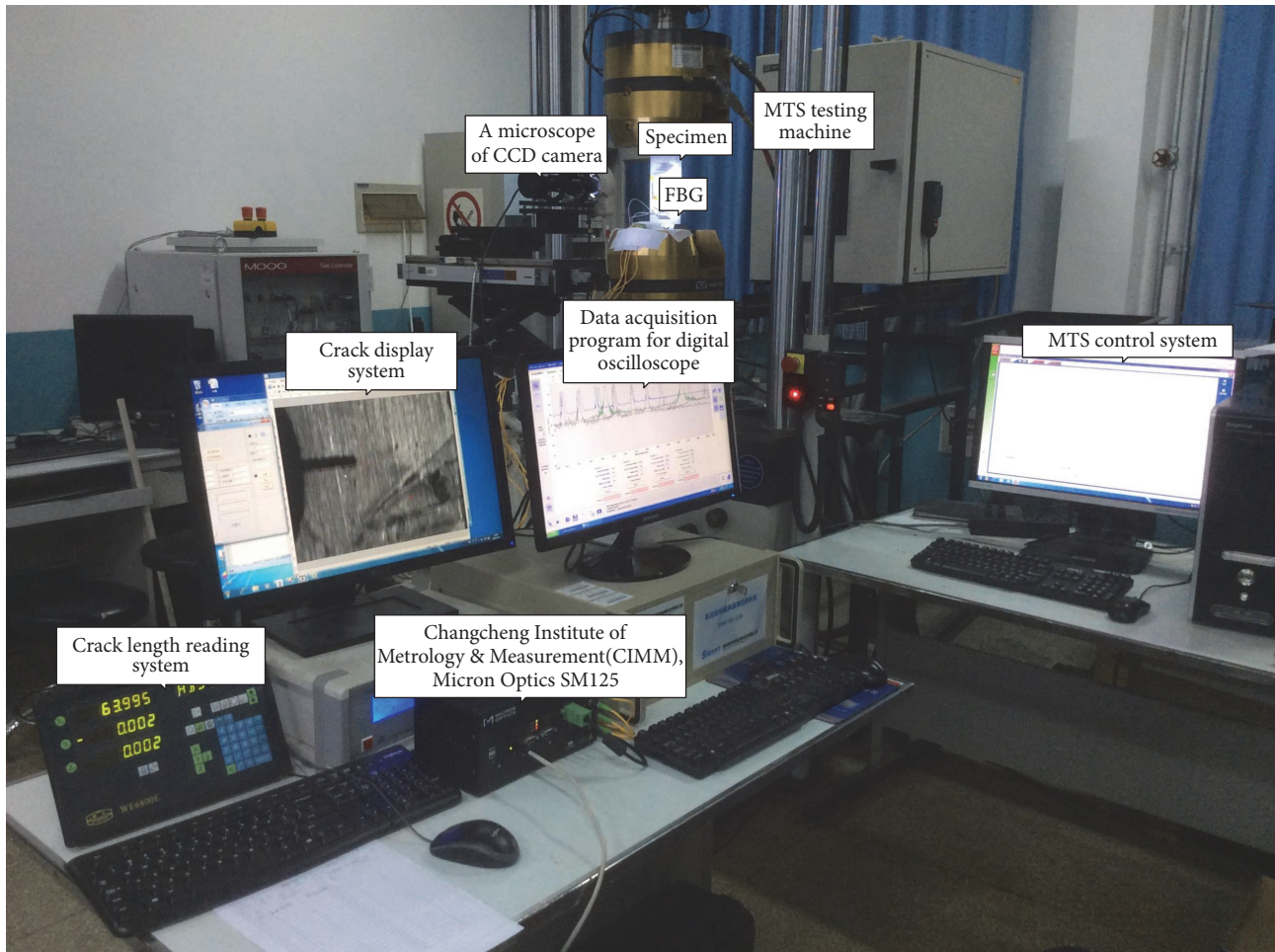


FIGURE 2: Experiment setup for the crack detection in aluminum structure.

forwards when the grating sensed uniformity strain profile. Concurrently, the pitch changes accordingly with the internal periodic modulation and all grating periods experience changes synchronously. This results in a shift of the Bragg wavelength without modification of the spectrum shape, and consequently the spectrum becomes symmetric and smooth due to the uniformity of the strain distribution along the grating (Figure 3). However, regarding crack propagation, the spectral wavelength shifts gradually and the reflection spectrum showed a significant change in shape. This is represented as subordinate peaks as shown in Figures 5(a), 6(a), and 7(a). Meanwhile, the FWHM also displayed an obvious correlation with the crack length until a saturation crack length is reached. The spectrum bandwidth is also directly related to strain distribution and hence has been previously applied [14, 15]. A shift of the measured central wavelength of less than 0.1 nm is observed during the process. The reason is that there is a small offset between the center of the FBG and the intersection point between the FBG and the neutral line.

It is clearly demonstrated that the strain patterns are distributed around the crack tip according to perfect nonuniformity. Thus, nonuniform strain is distributed along the entire length of the FBG with the crack propagation. Meanwhile, the

subordinate peaks vary with the complex strain distribution along the grating. In addition, the relationship between the subordinate peak and the strain distribution pattern has been discussed and simulated in previous research [13]. The turning subordination peaks coincide with the crack length, which is represented in the comparison between Figures 5(a) and 6(a) with Figure 7(a). The presence of crack propagation introduced three regions (Zones A, B, and C) of uniform grating strain, creating two primary peaks in the reflected spectrum as shown in Figure 4.

The distribution of strain patterns along the grating is mainly due to the ratio of crack length lying in the grating with the entire grating (Figure 4). Additionally, the crack propagation rate is a major factor in determining the monotonic plastic zone propagation rate. Regarding the cracks, the propagation rate affects the ratio of crack length lying in the grating with the entire grating. Reference [16] shows that crack propagation rate changes with external applied stress and this ratio could be changed with external loading stress.

And when the crack approaches initial grating, approximately 30% of the entire grating ratio, positioning at -0.2 – 3.2 mm to initial grating (Zone A), the reflection spectra appear to have subordinate peaks located to the left side of the primary peak. However, the subordinate peak appears at

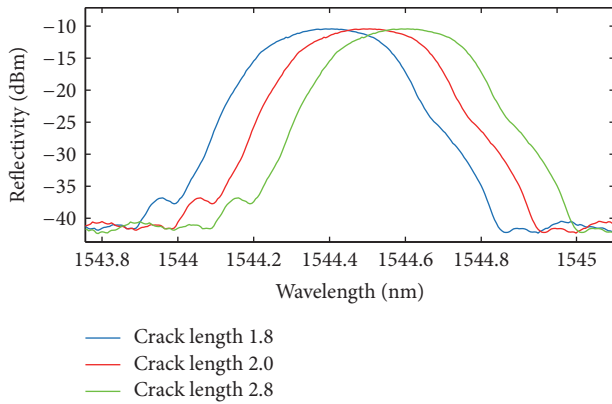


FIGURE 3: Reflection spectrum of FBG in uniform strain distribution.

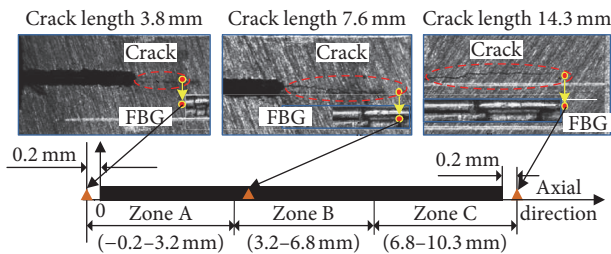


FIGURE 4: Three sensing regions of the grating.

higher wavelengths when the crack approaches $\pm 15\%$ bias of the central grating, positioned at 3.2–6.8 mm to the initial grating (Zone B). When the crack propagates to the terminal grating, at approximately 30% ratio of the entire grating, positioning at 6.8–10.3 mm to initial grating (Zone C), the reflection spectra appear to have subordinate peaks located to the left side of the major peak.

3.1. Analysis of Spectra in Zone A Sensing Grating. When the crack propagates close to observation Zone A, the subordinate peak is initially presented in the lower wavelength and drifts towards the same orientation. Moreover, the peak broadens and the subordinate peak energy increases as shown in Figure 5(a). Typically, the reflected spectra broaden and multiple peaks appear. The spectrum modifications may be due to polarization-induced lateral strains and/or nonhomogeneous strains parallel to the fiber axis.

If the FBG is submitted to different strain patterns along the grating, different lower peaks distort the reflected peak, as shown by curve A in Figure 5(a), and more details are shown in Figure 5(b). The slitting of the spectra occurred and the spectra shape was distorted. Afterwards, the spectra enlarged and the spectra distortion is critical, which corresponds to the outcomes by Ussorio [17]. The reflection spectra are evenly slit into several peaks at the initial and eventual break of the grating. The form of reflection spectra depends on the strain distribution along the grating [18]. Thus, the serve nonuniform strain pattern along the grating is assumed to be the principal reason for the spectra oscillation [19].

Figure 5(a) also shows a spectral wavelength shift towards a lower wavelength, with crack propagation in Zone A. These indicate a decrease of tensile strain in the grating. Thus, the central wavelengths diminished from 1544.7 nm to 1544.6 nm.

The deformity of the reflection spectra is generally related to the strain distribution along the FBGs [20]. In fact, the distribution of strain patterns along the grating corresponds to crack propagation. Regarding crack propagation, the spectrum bandwidth and full width at half maximum (FWHM) [21] broadened, accompanied by a sudden broadening of the spectrum that occurs at a 5.4 mm crack length, in comparison with curve A in Figure 5(a). Meanwhile, the bandwidth of FWHM broadens from 0.3 nm to 0.4 nm, and the FWHM increases from 0.3 nm to 0.7 nm, with the crack propagating in Zone A.

3.2. Analysis of Spectra in Zone B Sensing Grating. As the crack propagates to Zone B with a crack length of 7.6 mm, the number of subordinate peaks increases, as shown in Figure 6(b). Meanwhile, the reflection spectra appear to have multiple peaks located at the right side of the primary peak. Figure 6(a) also shows that the spectral intensity shifts towards a lower wavelength, with the crack propagation in Zone B. This indicates a decrease in tensile strain at the grating. Thus, the central wavelengths diminish from 1544.2 nm to 1544.1 nm.

The crack in the aluminum material can produce a strain concentration or gradient zone, which contains complex strain patterns. If differential strain patterns are applied to the grating, it will suffer from a nonuniform strain distribution pattern. This causes a sensor response that is more complicated than uniform cases [22, 23]. The nonuniform strain along the grating will change the periodicity of the grating pattern. The grating pattern is modified from a uniform to a chirped configuration [24], as shown in Figure 6(a). Thus, the width of FWHM broadened from 0.6 nm to 1.0 nm. Simultaneously, longer wavelength subordinate peaks appear and drift to naturally similar orientations.

3.3. Analysis of Spectra in Zone C Sensing Grating. For crack propagation towards Zone C terminal with a crack length of 14.3 mm, the distortion of the spectrum occurs as shown in Figure 7(b). Meanwhile, the reflection spectra are slit into multiple peaks located on the left side of the primary peak. Thus, it is confirmed that the spectrum oscillation can be related to the nonuniform strain distribution along the grating caused by transverse crack.

Figure 7(a) also shows that the spectral intensity shifts towards a lower wavelength, with crack propagation in Zone C. Thus, the central wavelength diminishes from 1544.7 nm to 1544.6 nm, and the width of FWHM broadens from 0.5 nm to 1.0 nm.

4. Discussion

4.1. Mechanism of the Skewing of the Subordinate Wavelength. Generally, when the compressional strain is sensed by the

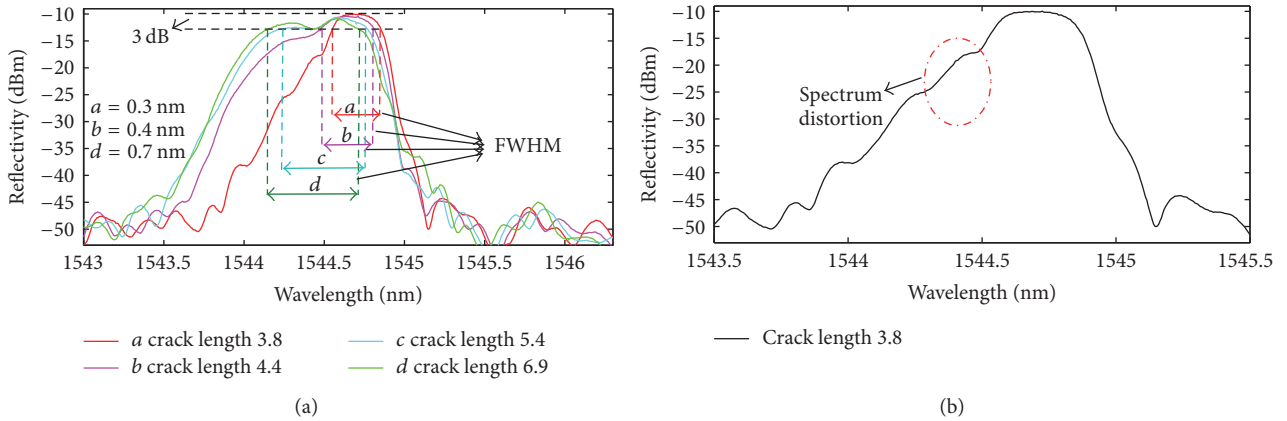


FIGURE 5: Reflection spectra of FBG in Zone A sensing grating. (a) The global curves; (b) the distortion of spectrum.

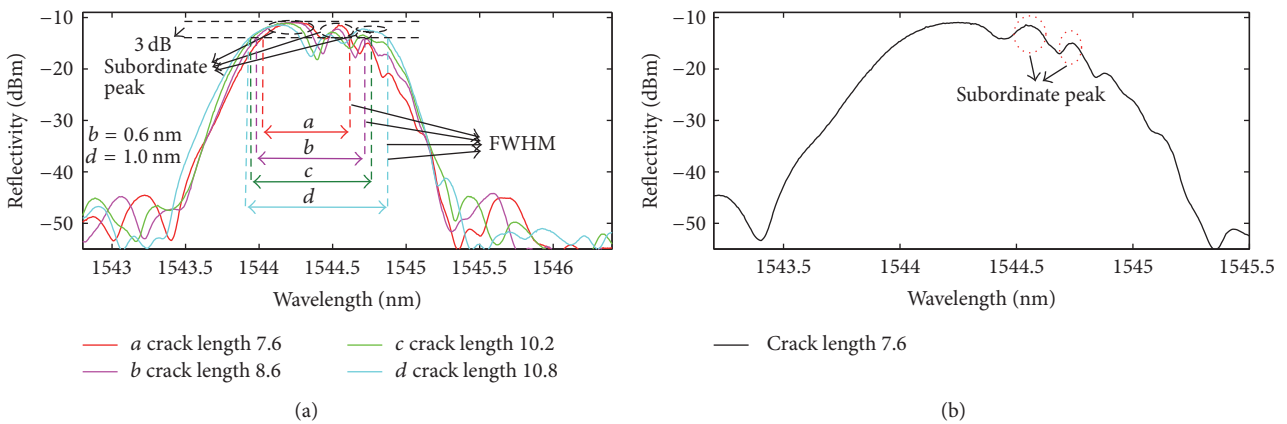


FIGURE 6: Reflection spectra of FBG in Zone B sensing grating. (a) The global curve; (b) subordinate peaks of the intensity spectra.

FBG, the reflection spectra move towards a lower wavelength. While tensile strain is sensed by FBG, the reflection spectra will shift to a higher wavelength [25]. There is a high order of the strain distribution around the crack of the test specimen. Thus, the strain distribution along the grating is nonuniform and the width of the spectra broadens. As the FWHM of reflection spectra increases, reflectance decreases and the subordinate peaks appear initially, and even spectra distortion occurs.

Reference [13] investigates the subordinate peak located in the lower wavelength, with quadratic strain distribution being employed along the grating of the fiber. When the cubic strain gradient is employed along the grating of the fiber, the subordinate peak is located at a higher wavelength. Meanwhile, the strain distribution along the grating corresponds to the plastic zone ratio ahead of the crack tip to the entire grating. When the crack propagates to the initial or terminal part of grating, at approximately 30% ratio of the entire grating, the cubic strain is distributed along the grating. However, the monotonic plastic zone is sensed by the FBG, at $\pm 15\%$ bias of the grating center, with the quadratic strain gradient pattern along the grating.

Results conclude that the FWHM and location skewing of the subordinate peak are related to the change of strain

distribution along the grating, with the crack propagation. The FWHM and the subordinate peak skewing are proved to be good indicators for real-time crack propagation evaluation.

4.2. Analysis of the Spectrum Distortion. Crack progression causes a nonuniform strain field around the crack tip to reach the grating area. This modifies the FBG response by significant variations with the subordinate reflected peak. As previously discussed, a severe strain distribution pattern, such as linear, quadratic, and cubic strain distributions, is sensed by the grating and can be attributed to the complex strain distribution around the crack tip. Previous research reveals that the linear and quadratic strain can be perceived by the FBG, which can be obtained by experiment and simulation. Meanwhile, Peters et al. [26] stated that the cubic strain gradient can be perceived by FBG, through the development of an experiment to calibrate the strain distribution pattern along the grating.

Meanwhile, [27] proposes that axial and transverse strain can both be sensed by the FBG, especially when the grating is adhered perpendicular to the loading direction. However, it is still a challenge to identify whether the distortion is promoted

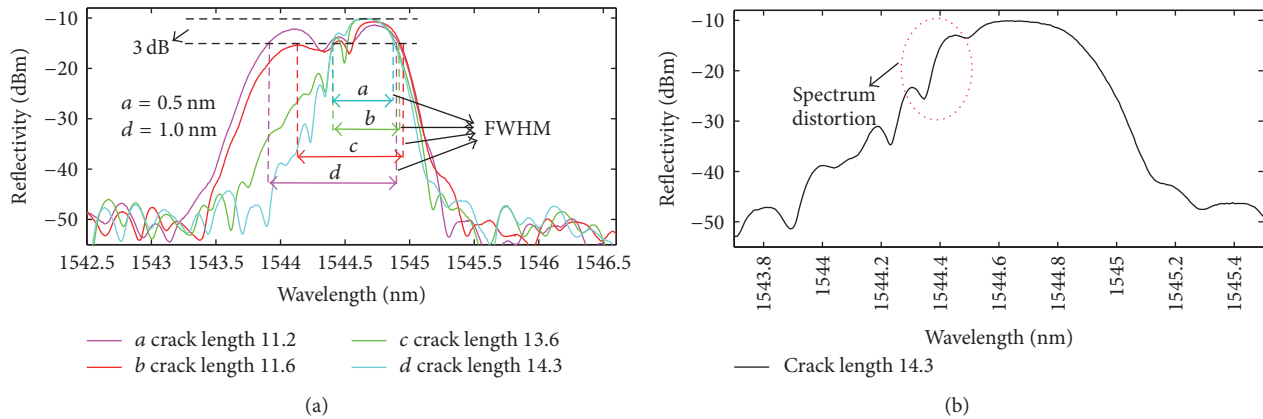


FIGURE 7: Reflection spectra of FBG in Zone C sensing grating. (a) The global curve; (b) the distortion of spectrum.

by a nonuniform longitudinal strain or by transverse stress splitting.

Thus, it is concluded that the complex strain distribution pattern sensed by FBG could be the major reason of spectrum distortion, which correlates with the distance of crack tip from the initial grating.

5. Conclusion

To determine the presence and development of the crack, FBGs show significant changes in the strain due to crack propagation in the specimen. In this study, the experimental data from fatigue testing is used to analyze the characteristic parameters for different crack lengths, in combination with the variable strain distribution. The spectrum became deformed with crack propagation, such as the number of subordinate peaks, and subordinate peak skewing. The change of strain distribution pattern sensed by the grating is assumed to cause the subordinate peak skewing, with the crack propagation. The monotonic plastic zone ahead of the crack tip is sensed by the grating, and the strain distribution pattern is closely related to ratio of sensed subgrating to the entire grating. When the crack propagates to approximately 30% of the initial or terminal grating, the cubic strain distribution is sensed by the FBG.

Furthermore, the FBG-based demodulation method can be used as a novel and alternative technique to real-time detection of the transverse cracks within the complex structure of aluminum alloy.

Conflicts of Interest

The authors declare no conflicts of interest.

Authors' Contributions

Bo Jin and Wei Dai conceived the key idea and designed the experiments. Weifang Zhang provided the academic support and checked the manuscript. Feifei Ren and Meng Zhang performed the experiment. And Yanrong Wang contributed

to optical measurement tools. All authors made contributions to the writing and revising of the manuscript.

Acknowledgments

This work was supported by the Technical Foundation Program (Grant no. KG06002201) from the Ministry of Industry and Information Technology of China.

References

- [1] D. Kinet, P. Mégret, K. W. Goossen, L. Qiu, D. Heider, and C. Caucheteur, "Fiber bragg grating sensors toward structural health monitoring in composite materials: challenges and solutions," *Sensors*, vol. 14, no. 4, pp. 7394–7419, 2014.
- [2] J. P. Ou, "Some recent advance of intelligent monitoring system for civil infrastructures in mainland China," in *Proceedings of the First International Conference on Structural Health Monitoring and Intelligent Infrastructures*, pp. 131–144, Tokyo, Japan, 2003.
- [3] K. Manfred, *Strain Measurement with Fiber Bragg Grating Sensors*, HBM, 2006.
- [4] S. Cieszyk and P. Kisała, "Inverse problem of determining periodic surface profile oscillation defects of steel materials with a fiber Bragg grating sensor," *Applied Optics*, vol. 55, no. 6, pp. 1412–1420, 2016.
- [5] L. C. Hollaway, "A review of the present and future utilisation of FRP composites in the civil infrastructure with reference to their important in-service properties," *Construction and Building Materials*, vol. 24, no. 12, pp. 2419–2445, 2010.
- [6] N. Takeda, Y. Okabe, and T. Mizutani, "Damage detection in composites using optical fibre sensors," in *Proceedings of the Institution of Mechanical Engineers Part G Journal of Aerospace Engineering*, vol. 221, pp. 497–508.
- [7] S. Takeda, Y. Okabe, and N. Takeda, "Monitoring of delamination growth in CFRP laminates using chirped FBG sensors," *Journal of Intelligent Material Systems and Structures*, vol. 19, no. 4, pp. 437–444, 2008.
- [8] N. Takeda, Y. Okabe, J. Kuwahara, S. Kojima, and T. Ogisu, "Development of smart composite structures with small-diameter fiber Bragg grating sensors for damage detection:

- quantitative evaluation of delamination length in CFRP laminates using Lamb wave sensing,” *Composites Science and Technology*, vol. 65, no. 15-16, pp. 2575–2587, 2005.
- [9] R. Ramly, W. Kuntjoro, and M. K. Abd Rahman, “Embedded FBG sensor in aircraft smart composite materials for structural monitoring,” *Applied Mechanics and Materials*, vol. 393, pp. 311–316, 2013.
- [10] K. M. Lal, “On the evaluation of monotonic and cyclic plastic zones,” *Engineering Fracture Mechanics*, vol. 9, no. 2, pp. 433–442, 1977.
- [11] B. Ma, “Research of coupling single-mode fiber-optic vibration sensor and experimental test,” *Applied Mechanics and Materials*, vol. 405-408, pp. 3318–3322, 2013.
- [12] K. Peters, P. Pattis, J. Botsis, and P. Giaccari, “Experimental verification of response of embedded optical fiber Bragg grating sensors in non-homogeneous strain fields,” *Optics and Lasers in Engineering*, vol. 33, no. 2, pp. 107–119, 2000.
- [13] B. Jin, W. Zhang, M. Zhang, F. Ren, W. Dai, and Y. Wang, “Investigation on characteristic variation of the FBG spectrum with crack propagation in aluminum plate structures,” *Materials*, vol. 10, no. 6, p. 588, 2017.
- [14] Y. Okabe, S. Yashiro, T. Kosaka, and N. Takeda, “Detection of transverse cracks in CFRP composites using embedded fiber Bragg grating sensors,” *Smart Materials and Structures*, vol. 9, no. 6, pp. 832–838, 2000.
- [15] P. Childs, A. C. L. Wong, W. Terry, and G. D. Peng, “Measurement of crack formation in concrete using embedded optical fibre sensors and differential strain analysis,” *Measurement Science and Technology*, vol. 19, no. 6, Article ID 065301, 2008.
- [16] G. Forman Royce and J. P. Hudson, “Digital computer program for the analysis of crack propagation in cyclic loaded structures,” 1967.
- [17] M. Ussorio, “Modifications to FBG sensor spectra due to matrix cracking in a GFRP composite,” *Construction and Building Materials*, vol. 1, pp. 111–118, 2006.
- [18] R. Di Sante, “Fibre optic sensors for structural health monitoring of aircraft composite structures: recent advances and applications,” *Sensors*, vol. 15, no. 8, pp. 18666–18713, 2015.
- [19] K. Peters, M. Studer, J. Botsis, A. Iocco, H. Limberger, and R. Salathé, “Embedded optical fiber bragg grating sensor in a nonuniform strain field: measurements and simulations,” *Experimental Mechanics*, vol. 41, no. 1, pp. 19–28, 2001.
- [20] S. Huang, M. Leblanc, M. M. Ohn, and R. M. Measures, “Bragg intragrating structural sensing,” *Applied Optics*, vol. 34, no. 22, pp. 5003–5009, 1995.
- [21] H. Ahmad, M. Z. Zulkifli, K. Thambiratnam, S. F. Latif, and S. W. Harun, “High power and compact switchable bismuth based multiwavelength fiber laser,” *Laser Physics Letters*, vol. 6, no. 5, pp. 380–383, 2009.
- [22] J. Zhou, Z. Zhou, and D. Zhang, “Study on strain transfer characteristics of fiber bragg grating sensors,” *Journal of Intelligent Material Systems and Structures*, vol. 21, no. 11, pp. 1117–1122, 2010.
- [23] J. F. Botero-Cadavid, J. D. Causado-Buelvas, and P. Torres, “Spectral properties of locally pressed fiber bragg gratings written in polarization maintaining fibers,” *American Institute of Physics*, pp. 248–253, 2008.
- [24] O. Andreas and K. Kalli, “Fiber bragg gratings: fundamentals and applications in telecommunications and sensing,” *APS Meeting Abstracts*, p. 61, 2004.
- [25] K. Peters, “Networking of optical fiber sensors for extreme environments,” in *Proceedings of the Sensors and Smart Structures Technologies for Civil, Mechanical, and Aerospace Systems 2016*, usa, March 2016.
- [26] K. J. Peters, M. Studer, J. Botsis et al., “Measurement of stress concentrations using embedded optical fiber Bragg grating sensors,” in *Proceedings of the 1999 Symposium on Smart Structures and Materials*, pp. 195–206, Newport Beach, Calif, USA.
- [27] D. Balageas, *Structural Health and Monitoring*, Great Britain, Antony power Ltd, London, UK.

Research Article

Decision Matrix Analysis of Impact Sounding Test Method to Determine Interlayer Condition of Concrete Bridge Deck

Cristina Amor Rosales,^{1,2} Hyun Jong Lee,¹ Wonjae Kim,¹ and Chang kyu Park¹

¹Department of Civil and Environmental Engineering, Sejong University, Chungmu-gwan, 98 Gunja-dong, Gwangjin-gu, Seoul 143-747, Republic of Korea

²Department of Civil and Environmental Engineering, Batangas State University, Batangas City, Philippines

Correspondence should be addressed to Hyun Jong Lee; hlee@sejong.ac.kr

Received 25 May 2017; Accepted 13 August 2017; Published 1 November 2017

Academic Editor: Zhou Zhi

Copyright © 2017 Cristina Amor Rosales et al. This is an open access article distributed under the Creative Commons Attribution License, which permits unrestricted use, distribution, and reproduction in any medium, provided the original work is properly cited.

This study focused on the analysis of the frequency spectra of impact sounding test performed on composite slabs with different interlayer condition. Distinct and consistent characteristics of the frequency spectra were observed from the impact signals. The consistency of results for bonding condition at varying temperature was also investigated. Results of laboratory tests were compared to different bonding condition observed in the field. Finally, a proposed decision matrix analysis was presented and successfully identified the interface bonding condition. The proposed decision matrix is composed of four zones characterizing each interlayer condition based on the features of impact signals. Field and laboratory assessment conform to decision matrix result.

1. Introduction

Bonding between pavement layers is an important factor for long term performance of asphalt concrete (AC) pavements and for the durability of bridge deck slabs. A decrease in the bonding strength at the interface between the AC deck pavement and Portland cement concrete (PCC) deck plate and increase in pavement deflection caused by traffic loading may result in accelerated fatigue damage in the pavement [1–3]. In addition, debonding between a water proofing layer and bridge deck may cause more serious problems to the bridge deck. Water and/or deicing salt could easily penetrate into the concrete deck resulting in deterioration of concrete slab and corrosion of reinforcements [3, 4]. Therefore, appropriate interlayer bonding is essential to achieve the long term durability of the AC-PCC bridge deck pavement.

Evaluating the amount of debonding area developed in the bridge deck is very important to determine proper timing and methods for repair or rehabilitation. However it is not an easy task because debonding cannot be determined by visual inspection of the pavement, especially at the early stages of deterioration. Therefore, nondestructive

tests (NDTs) such as impact echo (IE), ground penetrating radar (GPR), and sounding methods have been applied to determine the condition of bridge deck pavements. American Society for Testing and Materials (ASTM) released guidelines and methods for detecting delamination using sounding (ASTM 4580), infrared thermograph (ASTM 4788), and GPR (ASTM D6087) [5–7]. These approaches focused on concrete bridge deck condition but not on the interlayer debonding problems. The second Strategic Highway Research Program (SHRP-2) was recently conducted to evaluate the efficiency of available NDTs in determining delamination and debonding of pavement infrastructures [8]. GPR methods displayed limitations on determining delamination in shallow depth or on wet conditions and detailed boundaries of damaged area at fast survey [9]. Previous study indicated that GPR tests succeeded in detecting 33% of simulated debonded sections and could only qualitatively identify severely debonded areas with presence of moisture [10]. The limitation of IE/SASW tests is greatly affected by the temperature of AC pavements and the slow-walking speed limits [8]. The IE method was also found to be limited to certain deterioration size and shallow delamination which generates vibration frequency [11].

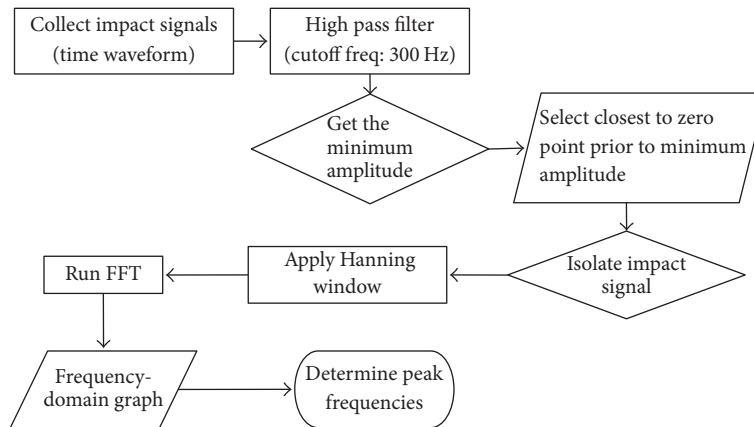


FIGURE 1: Impact sounding preprocessing algorithm.

In addition to the GPR and IE methods, impact sounding has long been used to detect deterioration and debonding problems of AC covered PCC bridge deck plate. Impact sounding involves tapping of hammer and dragging chains on pavement surface and interpreting the sound produced. Ringing sound corresponds to bonded section whereas the dull or hollow sound corresponds to debonded section. The impact sounding approach is relatively simple and has been practically used in the field. The major deficiencies of the impact sounding are time consuming for large area survey and inspector-dependent interpretations to testing results. Different studies using signal processing techniques interpret impact sounds of damaged and deteriorated structures [12–15]. The damaged portion of structures using the impact sound method was determined by analyzing the frequency-domain spectra of impact sound data at sensitive ranges [14]. Despite accurate results obtained from these studies, none of these studies focused on the interlayer condition of composite pavement but on overall assessment of the bridge. In addition, the analysis time and cost in performing the tests are relatively expensive and impractical for small projects needing assessment. Therefore, this study proposed a simple and direct sounding signal analysis of determining interlayer condition of pavement system.

The major objective of this study was to perform comparative analysis of impact sounding parameters between deteriorated and nondeteriorated interlayer of composite slab. The specific objective was to establish mathematical expression of impact sounding parameters which will identify the interlayer condition of composite slab with AC surface. Following a traditional impact sounding method, impact sounds were collected and transformed in frequency domain and the whole spectra were analyzed to differentiate normal from deteriorated conditions. Finally a quantitative approach of evaluating the interlayer condition was proposed.

2. Impact Sound Analysis

Impact sounding test involves hammer hitting or chain dragging in which the sounds produced are analyzed by inspectors during the testing or after sound recording.

Real-time evaluation of impact sounds is subjected to human-error and perception of the sound if the bridge deck produces ringing or hollow sound. In ASTM 4580-12, the standard method for measuring delamination in concrete bridge decks by sounding, impact sounding samples are taken within 3 milliseconds after the tap. The hollowness or defective sound can be detected at significant component frequency range of 300 to 1,200 Hz.

Michigan Department of Transportation [16] designed a delamination detection device which records the impact sounds and the signal is recorded. The recorded signal is passed through a band-pass filter with cutoff frequencies 300 and 1200 Hz and played back to the inspector for delamination determination. The method eliminates the traffic noise but the inspector still performs subjective identification of damage.

Henderson et al. [12] developed an automatic chain dragging system (ACDS) which can record, analyze, and evaluate the concrete bridge deck condition. The system records chain drag sound using microphone and filter it based on linear prediction coefficients (LPC). The filter process is done by inverting the LPC of the signal from solid concrete. This study also showed that, between delaminated and sound concrete, significant difference is observed at 1 kHz to 6 kHz of frequency spectra. If the tested concrete is solid and sound, the output will be clear or “white” whereas if delamination occurs, it would change. This study found that the frequency range of defects on concrete bridge deck extends up to 5 kHz.

From these studies, two significant points were noted: (1) frequencies below 5,000 Hz characterize hollow sound and (2) characterization of frequency band provides training parameters to quantify the degree of damage. Thus, in this study, these two findings served as fundamental basis for feature extraction of impact sounds to determine the interlayer debonding of concrete decks.

The data analysis process used in this study is presented in Figure 1. Impact sound signals were filtered using high pass with cutoff frequency of 300 Hz to eliminate the frequency caused by traffic noise. To further eliminate noise from original signal, 10-millisecond length impact signals were isolated manually by selecting the closest zero-amplitude

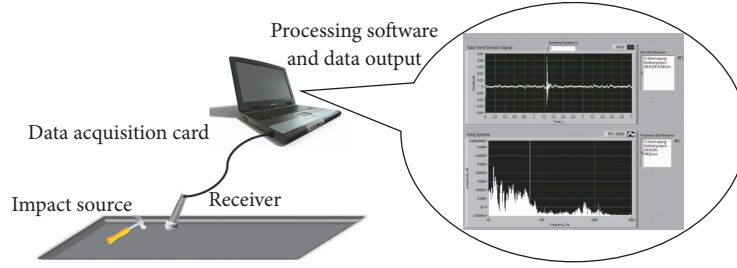


FIGURE 2: Sounding signal acquisition process.

point prior to the minimum amplitude. The sliced length of 10 milliseconds was based on the decay rate of the impact sound signals observed in the initial test and previous studies on impact sound duration [17, 18]. This signal is isolated and Hanning window is applied prior to FFT conversion. As commonly employed in sound signal analysis, fast Fourier transform was performed to convert waveform data to frequency spectra [15, 19].

3. Feature Extraction

Contrary to impact echo, ultrasonic wave, and surface wave analysis, sounding test analysis considers broad frequency characteristics of impact sound. It is noted that impact signal classified as transient signals is a nonstationary signal in which the whole duration is analyzed as a whole entity with no regard of how they vary with time. Hence, it is considered to have a finite amount of “energy” (amplitude squared integrated over time) and the spectrum is most readily expressed in terms of “energy spectral density” [20]. Simply put, the analysis of impact signals considers the whole range of frequency spectra.

Previous sounding studies [5, 12, 16] mentioned that identification of hollow sound relies on the features of frequency spectra. Sets of impact sounding data are “trained” to identify damaged condition which is similar to human’s logic-based identification. Several studies successfully applied this method specifically in tunnel linings [14] and tile [21, 22] as these studies focus on bonding quality of materials. Based on impact sounding studies mentioned, two features, sound pressure level and frequency spectra range of 300 Hz to 5000 Hz, are common features that identify damage using impact sounding.

In this study, preliminary investigation was performed in the laboratory to confirm how sound pressure level differs with debonded and bonded concrete bridge deck layer. Features of these data are further investigated to extract the most appropriate parameter for quantifying interlayer conditions.

4. Sounding Signal Acquisition Process

The signal acquisition process consists of signal source, receiver collecting signal data, processing software for interpretation, and display of the signal data in time and frequency domain. Figure 2 shows the components of signal acquisition process used in this research. The impact device such as a

hammer hits a specimen and then the receiver picks up the impact signals. The data acquisition system (DAQ) transfers the signal to the processing software in the computer.

4.1. Impact Sounding Device. In general, an impact device having shorter contact time and smaller contact area is more desirable to produce better accurate sound. In addition, to detect delamination using acoustic sensors, impact source should have high force amplitude, relatively low frequency content, and minimal production of ancillary sound [23]. Depending on the diameter of the impact device, the contact time, t_C in μs , can be computed given the equation of the American Concrete Institute (ACI):

$$t_C = 4.3D, \quad (1)$$

where D is the diameter of the impact equipment in mm. Contact time, t_C , is the reciprocal of the maximum frequency, f_{max} , the impact equipment can induce as stress wave in the material. It was found from the study of Sansalone and Streett [24] that the amplitudes of stress waves at frequencies below $1.25/t_C$ are sufficient for impact-echo testing. Thus, the maximum frequency, f_{max} (kHz), that the impact equipment can induce as stress wave in the material can be computed using

$$f_{max} = \frac{1.25}{t_C}. \quad (2)$$

This maximum frequency can detect a smallest flaw depth, D_{min} , using

$$D_{min} = \frac{0.96C_p}{2f_{max}}, \quad (3)$$

where C_p is the P-wave speed. The typical value of C_p from previous studies [24, 25] for concrete ranges from 3,600 to 4,000 m/s whereas asphalt is 2,640 m/s. In the study of Sansalone and Carino [25], impact echo was modified to remove the effect of overlaid material by allowing the small spherical balls (4–12 mm) to hit 12.5 mm diameter steel plate with 4 mm thickness. In the study, they proposed

$$T_d = 0.5 \left[\frac{C_{pc}}{f_d} + \frac{C_{pa} - C_{pc}}{f_a} \right], \quad (4)$$

where T_d is the depth of delamination, C_{pc} is the P-wave speed in cement concrete, C_{pa} is the P-wave speed in the asphalt

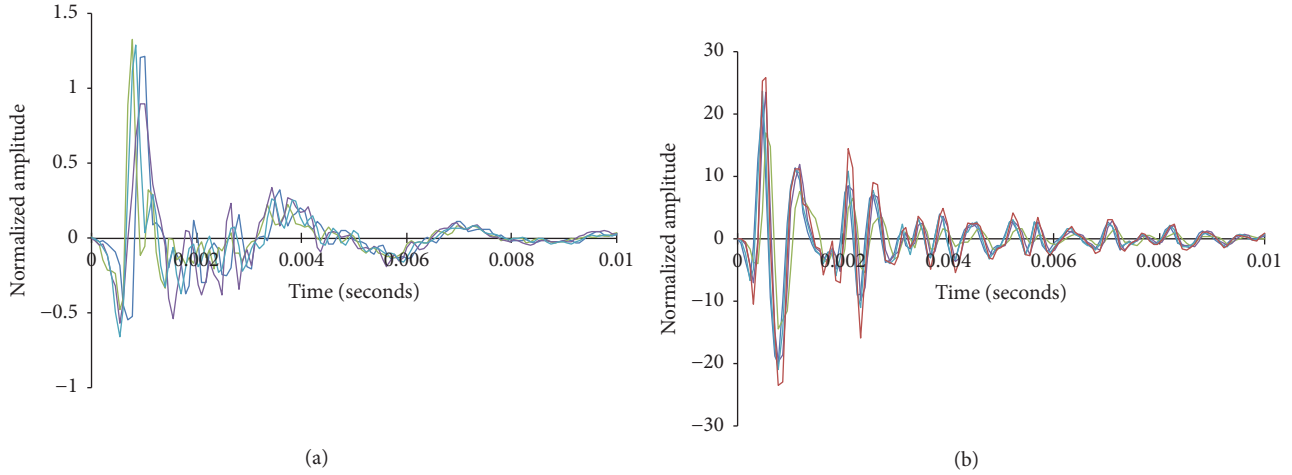


FIGURE 3: Time waveform of hand-held hammer: (a) 23.45 mm diameter; (b) 21.5 mm diameter.

overlay, f_d is the corresponding frequency of the depth of the delamination, and f_a is the corresponding thickness frequency of the asphalt overlay. In this study, the concerned location is equivalent to the depth of the asphalt overlay; $f_d = f_a$; thus (3) is applicable to interlayer condition.

Spherical steel ball is the most common device used in impact testing and its diameter dictates the depth of flaw it can analyze. As one of the goals of this research is to provide an economical mobile device, commercially available devices for impact sounding source were used in order to determine the appropriate impact height. Hammers are the most common and economically available tool in the field for sounding; thus different impact head size was selected and evaluated. To obtain the acceptable diameter of impact device, (1), (2), and (3) are combined resulting in the following:

$$D = \frac{6056 \times D_{\min}}{C_p}, \quad (5)$$

where D is the acceptable impact diameter in mm; C_p is the P-wave speed in m/s and the typical value of 2640 m/s was used; and D_{\min} is the smallest flaw depth (cm) it can detect.

Two commercial hand-held hammers with spherical tip and diameters 23.45 mm and 21.50 mm were tested. Figure 3 displayed the time waveform of the two hammers showing that the smaller diameter hammer displays smoothed and consistent data compared with the big one. Also, it can give a minimum contact time of 92.45 μ s resulting in maximum frequency 10,817 Hz. The computed minimum depth it can detect based on (3) is 117 mm which is slightly higher than desired 80 mm typical thickness of asphalt concrete overlaid in concrete bridge decks. Since the study focused on the interlayer of composite pavement, the 37 mm difference provides good flexibility in investigating the interlayer surface of composite pavement. Therefore, in this study, 21.5 mm diameter of impacting device was used.

4.2. Sound Receiver. In this study, several types of receivers were evaluated to select the most appropriate device for

receiving and logging sounding data. Accelerometers typically used for IE tests were excluded in this study because they can be operated only on contact with the surface of pavements. For mobility, a pressure field microphone with a preamplifier (model PCB 378B11) with frequency response of 6.3 Hz to 125 kHz was selected. In addition to its durability on impact pressure, this microphone sound acquisition is unidirectional, thus reducing the effect of noise in the acquisition process.

The microphone was placed as close to a hitting point as possible to receive desired impact sound signals by minimizing external noise from the environment. From several initial trials, the appropriate vertical and horizontal distances of the microphone from the hitting point were determined as 50 mm and 5 mm, respectively. The microphone was connected to a National Instruments DAQ (model DAQ 9234) with maximum sampling rate of 51.2 kHz. A simple data acquisition and analysis program based on LabView 2013 was developed.

Different sampling frequencies were evaluated to determine the optimal size including the length of samples. Three sampling rates were evaluated: 12.8 kHz, 25.6 kHz, and 51.2 kHz. Figure 4 presented the frequency spectra of different sampling frequency and it showed that the spectrum is concentrated on frequencies lower than 5,000 Hz. The sampling frequency of 12.8 kHz providing significant frequency values for the acoustic sounding test without compromising the accuracy of the acquired signal, hence, was used in this study.

5. Laboratory Tests

5.1. Specimen Preparation. The three slab specimens, consisting of an AC upper layer and PCC bottom layer, were prepared as shown in Figure 5. The PCC slabs were 60 cm long, 60 cm wide, and 20 cm thick. The first and second PCC slabs had single and double steel reinforcement in the middle of the slab, respectively; the third PCC slab had no reinforcement. These slabs were overlaid with a 5 cm thick AC layer. Before placing the AC layer, tack coat was applied

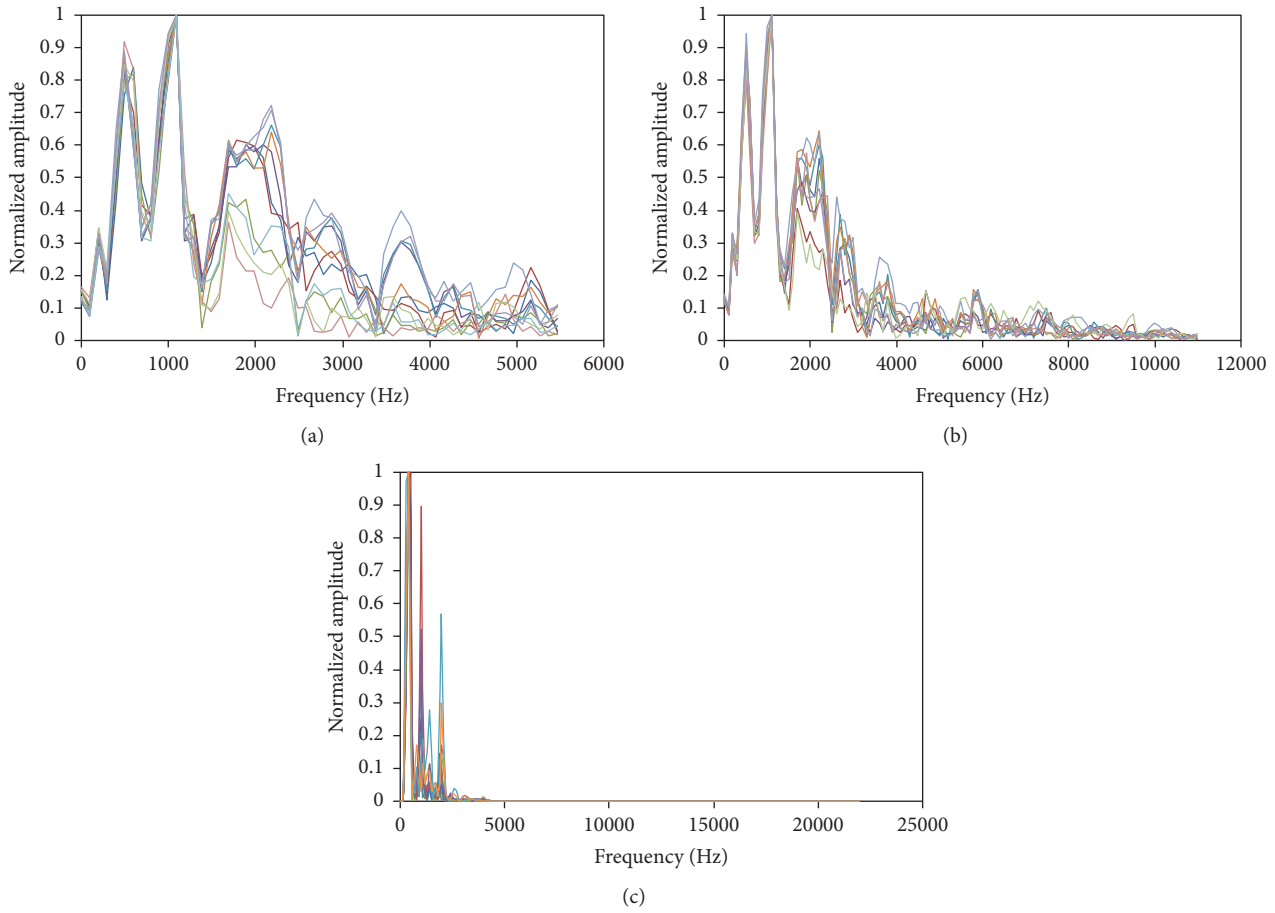


FIGURE 4: Effect of different sampling rate on frequency spectra: (a) 12,800 Hz; (b) 25,200 Hz; (c) 51,200 Hz.

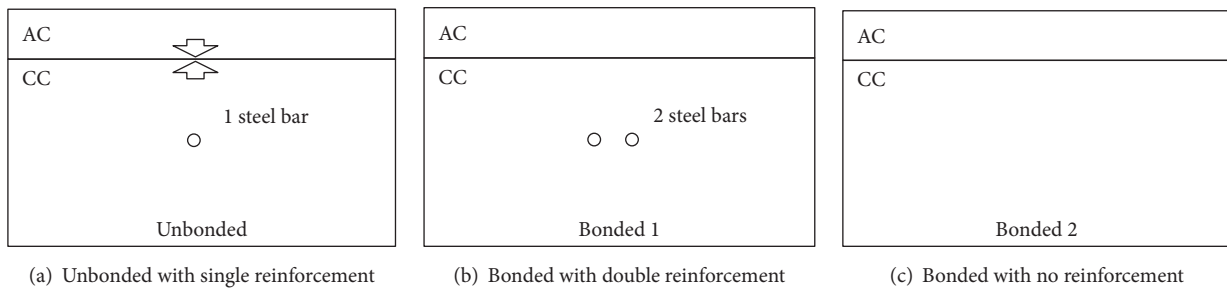


FIGURE 5: Configuration of the slab specimens.

on the surface of the PCC slabs for better bonding. On the other hand, to simulate a completely debonded interlayer condition, plastic tape was covered onto the concrete surface before pouring of asphalt mixtures. Then, the AC layer was carefully torn off from the PCC slab after one week and placed right before the test to keep the interlayer debonded.

5.2. Sounding Test Setup and Procedure. An impact sound test device was used for the slab specimens as shown in Figure 6. A commercially available hammer (612 grams, 21.5 mm spherical hammer head) was connected to a stable stand and allowed to have a free fall impact on the surface

of the asphalt concrete layer. The energy or height of the hammer was controlled by the angle of the hammer on the top. The impact hammer was dropped three times.

6. Results and Discussion

6.1. Effect of Interface Condition. The frequency spectra of interlayer condition distinctively showed significant differences in the peak frequency and spectral pattern. In Figure 7, bonding condition showed that the highest amplitude of peak frequency is at 1700 Hz whereas the unbonded condition highest amplitude peak frequency is at 1100 Hz. The peak

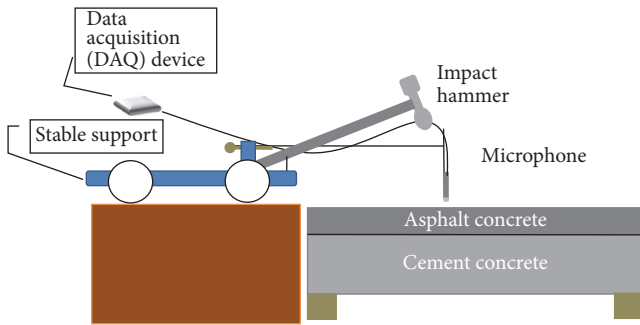


FIGURE 6: Supported slab sounding test setup.

TABLE 1: Observed peaks at frequency spectra for different bonding condition (frequency, Hz).

| Bonded with double reinforcement | Bonded with no reinforcement | Unbonded with single reinforcement |
|----------------------------------|------------------------------|------------------------------------|
| 307 ± 27 | 331 ± 90 | |
| 493 ± 10 | 491 ± 10 | 455 ± 29 |
| 1166 ± 32 | 1168 ± 31 | 1087 ± 25* |
| 1724 ± 34* | 1722 ± 34* | 1724 ± 35 |
| 2311 ± 113 | 2358 ± 40 | 2359 ± 39 |
| 2924 ± 294 | | |

* Highest peak frequency for each bonding condition.

amplitude of the unreinforced bonded slab specimen is 20% higher than the peak amplitudes of reinforced bonded slab. The amplitude difference between unbonded and bonded slab specimens can be attributed to energy dissipation in the interlayer [20, 26, 27] resulting in high pressure amplitude measured in the frequency spectra of the unbonded slab specimen.

Table 1 showed the observed average peaks at frequency spectra detected at any bonding condition where the peaks of at least 10% of the highest peak frequency were identified. Since the bandwidth of the frequency spectra is 100 Hz, it can be generalized that the peaks occurred at similar value and differed where each peak amplitude value was detected. Of the three bonding conditions, only unbonded condition displayed a high amplitude peak greater than 50% of the highest peak at frequency 455 ± 2 Hz. This peak became the highest frequency peak of unbonded condition at higher temperature. The effect of temperature is being discussed in the next section.

6.2. Effect of Temperature. Since asphalt concrete is a viscoelastic material, the elastic modulus varies with temperature. Therefore, when considering the parameters, it is very important to determine if the material properties have an effect. Figure 8 showed the frequency spectra of different bonding conditions at different temperature. It was observed that the frequency spectra of bonded sections consistently displayed high multiple peak frequencies above 1,000 Hz. Unbonded section, on the other hand, displayed peak frequencies below 1,100 Hz.

The amplitude at peak in the frequency spectra at the various temperatures, for all slab specimens, was presented in Figure 9. It was observed that the peak amplitude of unbonded condition was always higher than that of the bonded condition. In addition, the amplitude of the peak frequency of the unbonded condition decreased as temperature was increased. It could be mainly due to the fact that asphalt concrete at higher temperature demonstrates more viscous behavior where the material is capable of absorbing more energy.

The frequency peaks of the unbonded slab specimen in Figure 10 showed that the peaks of unbonded condition depend on temperature. At temperature 5°C and below, the highest peak was observed at 1,100 Hz, whereas at temperature above 5°C , the highest peak was at 400 Hz. With regard to bonded condition, frequency peaks remained high above 1,500 Hz.

Although the amplitudes and peak frequencies showed temperature dependence in the unbonded condition, the difference in amplitude and peak frequency between interlayer conditions was significantly high. From these observations, the amplitude and peak frequency were used as features to differentiate between bonded and unbonded conditions.

7. Field Observations

Field sounding tests were also performed using similar setup to validate the laboratory results. Yanggok Bridge in Muju, South Korea, will undergo asphalt concrete overlay rehabilitation and hence was selected as suitable area for field validation. The field test was performed before the actual rehabilitation while the other lane of the bridge was operational. Consequently, because of the limited access to the whole concrete bridge deck, only several sections of the bridge identified to have varying condition were selected.

Hitting points were laid at 30 cm distance along the width of the road starting from point closest to the concrete barrier. Impact sounding samples were also collected near the concrete barrier section with heaved surface. This section was considered to have completely debonded interface. A total of 103 data points were collected from the field observation.

Figure 11 shows that sounding test was performed before removal of asphalt concrete and visual inspection for each point was performed after water jet process was applied. Water jet process was done to completely remove the damaged parts of the concrete deck. By taking its deterioration depth and surface condition, three condition levels were identified for field evaluation as summarized in Table 2. Heaved section was also considered as separate condition since the damage was remarkable from the asphalt surface.

Similar to laboratory test, frequency spectra for the hitting points were plotted and compared with each other according to their condition. Figure 12 presented the combined frequency spectra of points depending on their condition level. It was observed that there was an increase in amplitude value as condition reached deterioration level. In addition, peak frequencies of good and minor conditions occurred at frequencies higher than 1,500 Hz whereas severe

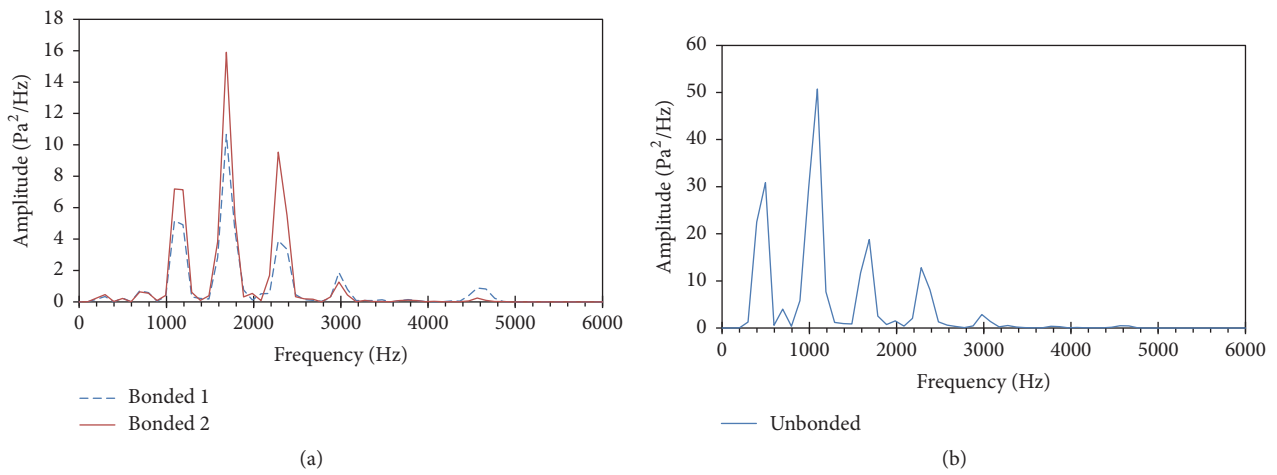


FIGURE 7: Frequency spectra of slab specimen with different bonding condition: (a) bonded slab specimen; (b) unbonded slab specimens.

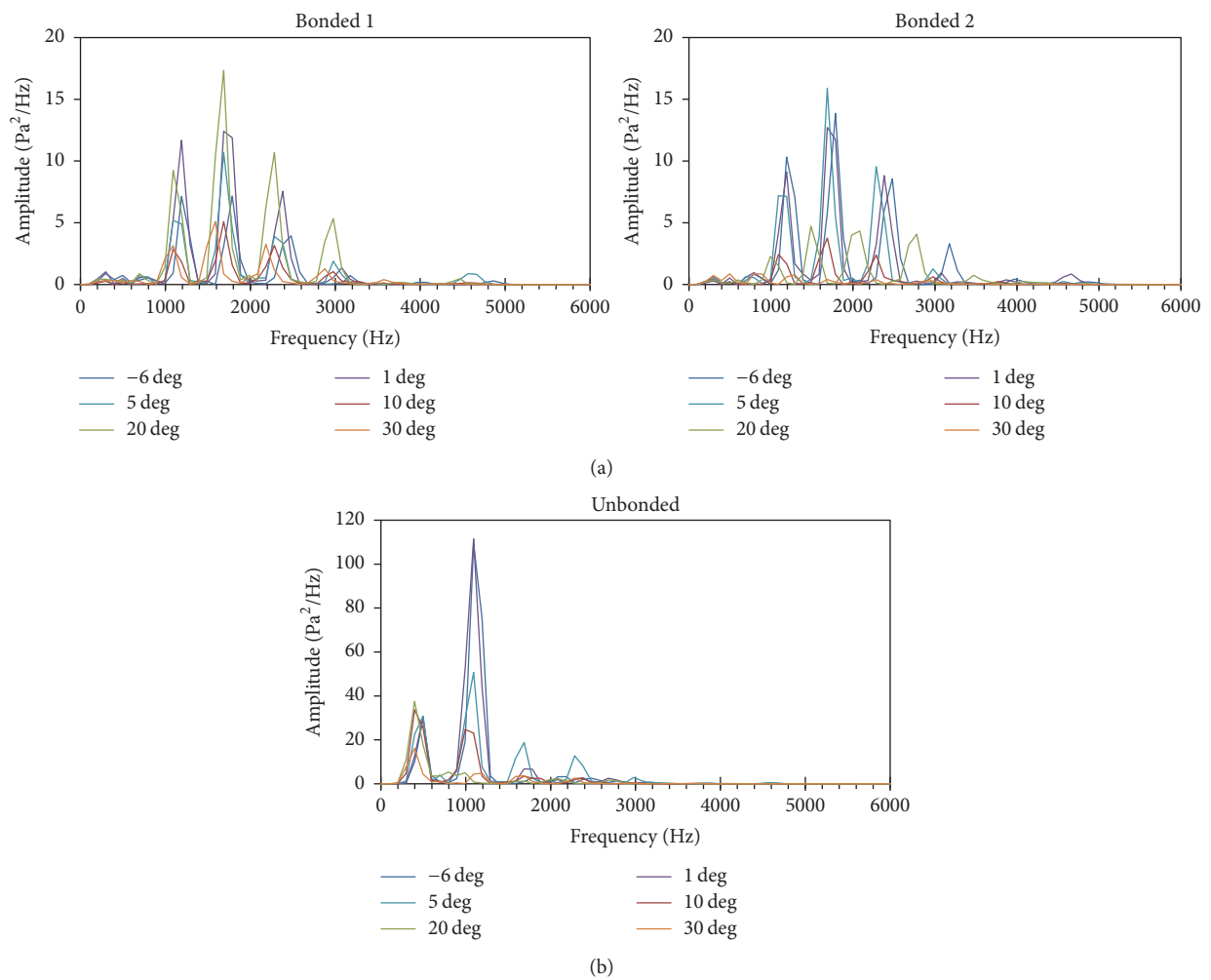


FIGURE 8: Frequency spectra of different bonding conditions at different temperatures: (a) bonded sections; (b) unbonded section.

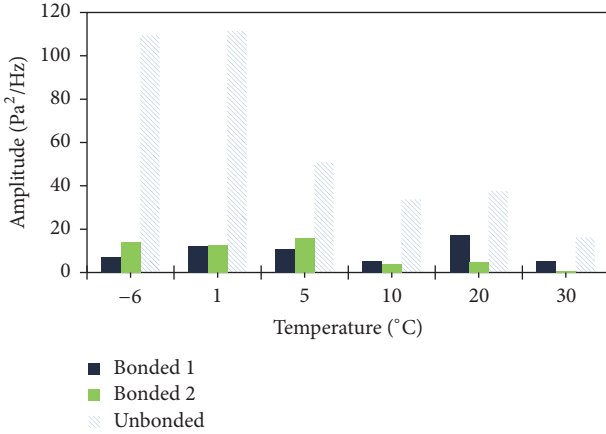


FIGURE 9: Plot of temperature versus amplitude of peak frequency at different bonding conditions.

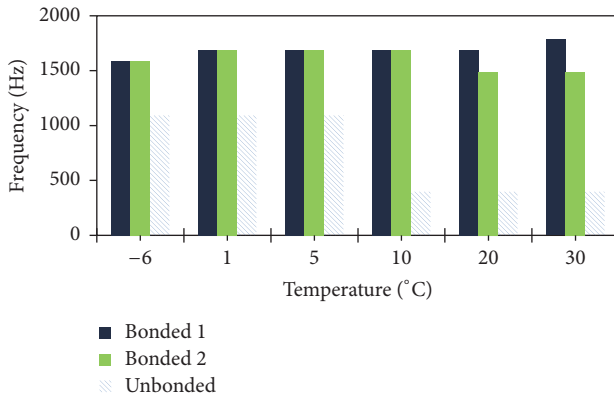


FIGURE 10: Plot of temperature versus peak frequency at different bonding conditions.

TABLE 2: Condition level description for field evaluation.

| Condition level | Description |
|-----------------|---|
| Good | Good condition, no inspected damage on the interlayer |
| Minor | Minor damage: interface of cement concrete shows scaling Cement concrete aggregates are exposed |
| Severe | Deterioration depth is greater than 25 mm Aggregates are removed from the surface Traces of moisture are remarkable |
| Heaved | Asphalt concrete is heaved and completely detached from the cement concrete |

condition and heaved sections occurred at frequency less than 500 Hz.

It was also noted that peaks occurred at similar frequencies as summarized in Table 3 wherein, at good and minor condition, peaks occurred at higher frequency value of 2,800 Hz which was not evident in severe and heaved conditions. Heaved section identified only two peaks at 389 ± 49 Hz and 682 ± 69 Hz.

TABLE 3: Observed peaks at frequency spectra for different field condition (frequency, Hz).

| Good | Minor | Severe | Heaved |
|----------------|---------------|----------------|--------------|
| 305 ± 20 | 308 ± 51 | 331 ± 56 | 389 ± 49 |
| 489 ± 9 | 501 ± 24 | 461 ± 22 | |
| 707 ± 28 | | 650 ± 68 | 682 ± 69 |
| 1098 ± 21 | 1096 ± 11 | 1088 ± 33 | |
| 1593 ± 34 | 1597 ± 21 | 1566 ± 58 | |
| 2329 ± 198 | 2272 ± 96 | 2163 ± 252 | |
| 2877 ± 21 | 2860 ± 39 | | |

8. Evaluation Matrix of the Interface Condition

Based on results presented in this study, there were significant observations in the frequency spectra of impact sounds that can distinguish interlayer condition. First, the peak frequency of interlayer condition was always different at any temperature condition and, second, the amplitude of the frequency spectra of unbonded slab specimen was always higher than that of the bonded slab specimen. From these observations, frequency versus amplitude was plotted resulting in a feature space.

The feature space of laboratory data presented in Figure 13 showed exclusive clusters between bonded and unbonded conditions. It was also observed that unbonded condition exhibited two different clusters depending on temperature condition, yet none of them coincided with bonded condition. This was a good indicator that the features, peak frequency, and its amplitude were good parameters to indicate interlayer condition and it was not affected by temperature dependence of asphalt concrete.

The feature space of the field data, on the other hand, was presented in Figure 14. In this feature space, the points from heaved section and 50% of the points of severe condition displayed consistent clustering at 500 Hz. Around 61% of the points of good condition and 76% of the points of minor condition were clustered in 1,100 Hz.

It was noted in field data that the hitting point selected for sounding test and the measurement point of deterioration after water jet may not exactly coincide with each other resulting in some error in validation. Figure 11(b) showed that rapid changes in the condition of concrete surface may cause possible error in comparing sounding test result and visual inspection.

In Figure 15, a generalized decision matrix was proposed for use in the analysis of interlayer condition. From the feature space of the laboratory and field tests, four zones identifying the different levels of interlayer condition were proposed. Each zone was bounded by significant peak frequency range observed in the laboratory and in the field tests.

As shown in Figure 15, the results of laboratory and field data were plotted in the proposed decision matrix where data points were clustered in four different zones. The data points clustered in *Zone a* were the high temperature unbonded condition of laboratory data, the points from heaved section,



FIGURE 11: Impact sounding test performed in Yanggok Bridge in South Korea before asphalt concrete overlay rehabilitation: (a) sounding test; (b) measuring delamination after water jet.

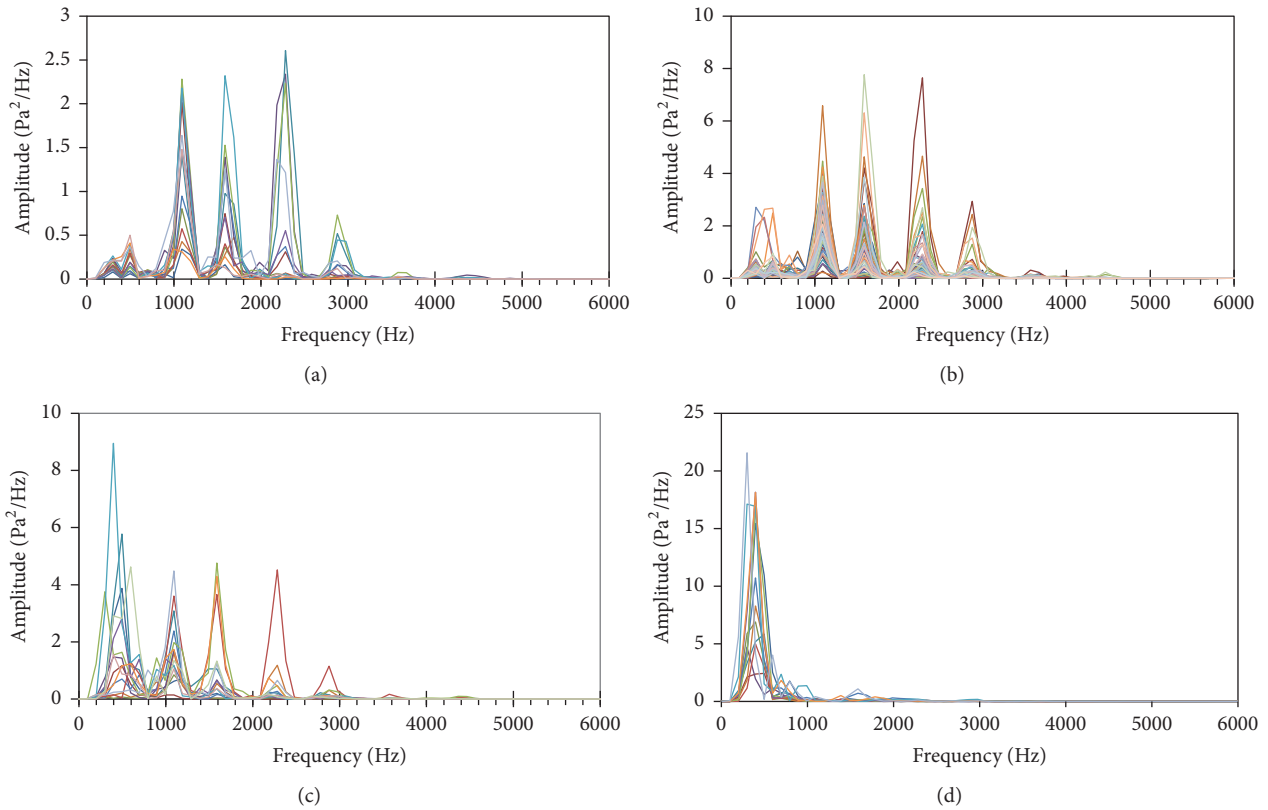


FIGURE 12: Combined frequency spectra of different points depending on condition level: (a) good condition; (b) minor condition; (c) severe damage; (d) heaved sections.

and the 50% of severe damage points in field data. In *Zone b*, points collected from low temperature unbonded condition of laboratory data were grouped. In *Zone c*, on the other hand, 61% of the data points were from good condition assessment and 76% of data points were from the minor damage in the field data condition assessment. Lastly, points in *Zone d* were data points from bonded slab data including 21% of data points from good condition and 10% of data points from minor damage condition of field data.

Table 4 summarized the description of the decision matrix as well as the interlayer conditions observed during the field test. *Zone a* data points showed severe damage condition wherein, aside from completely detached asphalt

concrete interlayer, pothole-like damage was observed from the cement concrete bridge deck. Compared with previous condition assessment presented in Table 2, the proposed *Zone a* of the decision matrix represented combined characteristics of severe damage and heaved condition as observed both in the field and in the laboratory. Thus, laboratory field test was able to simulate the field condition.

In *Zone b*, on the other hand, the interlayer condition displayed a completely detached asphalt concrete but no damage on the cement concrete layer. This characteristic of *Zone c* is inherent with minor condition assessment mentioned in Table 2. However, the data points identified in this zone were from the laboratory specimen of unbonded condition

TABLE 4: Summarized description of the proposed zonal condition level of bridge deck pavement.

| Zone | Condition | Description | |
|------|-----------|--|--|
| | | Frequency spectra | Visual inspection |
| a | Severe | Peak frequency less than 600 Hz | Deterioration depth is greater than 25 mm Asphalt concrete is heaved Traces of moisture are remarkable |
| b | Debonded | Peak frequency of 1,000 to 1,300 Hz, peak amplitude higher than 50 Pa ² /Hz | Asphalt concrete is completely detached from the concrete deck |
| c | Fair | Peak frequency of 1,000 to 1,300 Hz, peak amplitude lower than 50 Pa ² /Hz | Surface of concrete deck shows minor scaling |
| d | Good | Peak frequency higher than 1,500 Hz | Good condition, no inspected damage on the surface of concrete deck |

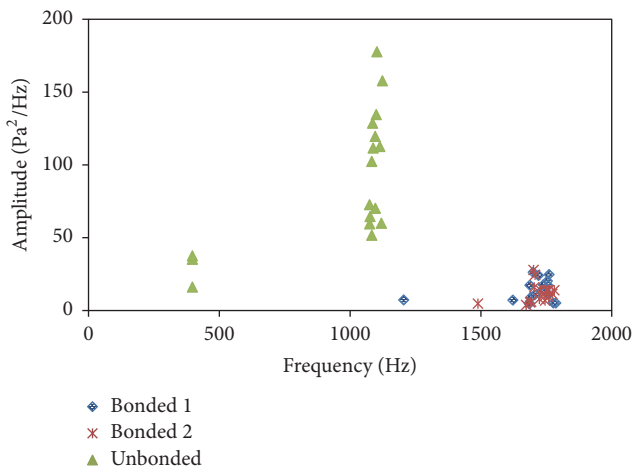


FIGURE 13: Feature space of interlayer bonding condition in the laboratory setup.

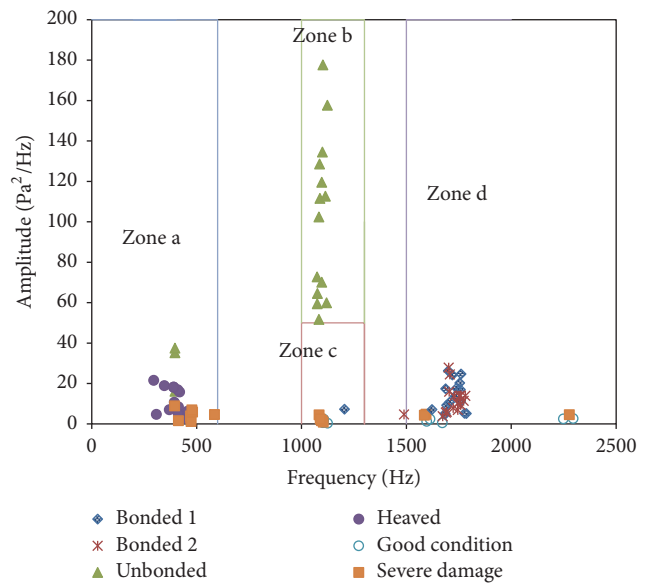


FIGURE 15: Decision matrix of interlayer condition in the laboratory and in the field.

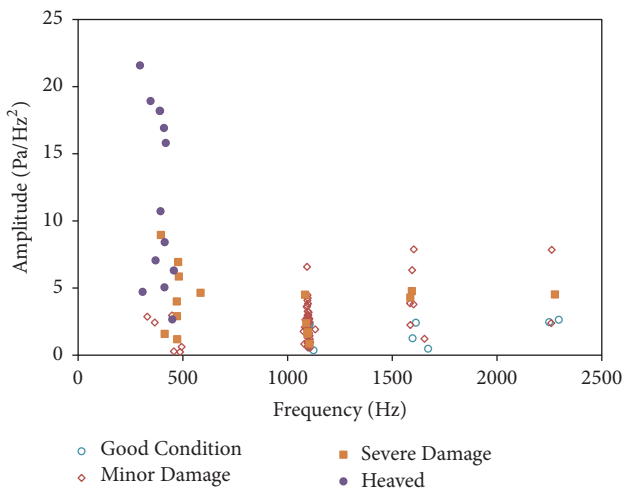


FIGURE 14: Feature space of interlayer condition in the field.

at high temperature. Thus, more field tests were needed to be performed to validate this condition. In the same way, the *Zone c* of the decision matrix was composed of both good and minor condition assessment of data points in the field. This showed that *Zone c* was a new interlayer condition identified

using sounding test method. This condition poses critical transition of interlayer condition from good to debonded condition, meaning, at this state, interlayer section started to develop debonding. Lastly, the *Zone d* of the decision matrix showed no damage on the interlayer section of the concrete bridge deck. The data points belonging to *Zone d* were points showing complete bonding and no interlayer damage. Low percentage of good condition data from the field shows that the concrete bridge deck was subjected to traffic and environmental stress and rehabilitation was really needed.

9. Summary and Conclusion

In this study, a simple and direct approach to identify the interlayer condition between concrete bridge deck and asphalt pavement using sounding tests was proposed. It was observed from an extensive laboratory and field experiments that peak amplitude and peak frequency of sounding data in frequency domain were good parameters for determining

interlayer bonding condition. These parameters were dependent such that peak amplitude and peak frequency of data points collected in the laboratory and in the field were plotted in a feature space. Consequently, a proposed generalized decision matrix approach based on the feature space was presented in this study. In this approach, overall analysis of data by clustering of points resulted in four different zones which can describe the interlayer conditions. The proposed analysis was capable of detecting intermediate conditions interlayer, which emphasized the transition of damage in interlayer section. Although the proposed decision matrix analysis of sounding test method was feasible in determining interlayer condition, further field studies are needed to validate the proposed decision matrix in this study.

Conflicts of Interest

The authors declare that they have no conflicts of interest.

Acknowledgments

This research was partially supported by a grant (17TLRP-C099510-03) from Transportation & Logistics Research Program (TLRP) funded by the Ministry of Land, Infrastructure, and Transport of Korean Government and the Seoul Metropolitan Government.

References

- [1] T. W. Kim, J. Baek, H. J. Lee, and S. Y. Lee, "Effect of pavement design parameters on the behaviour of orthotropic steel bridge deck pavements under traffic loading," *International Journal of Pavement Engineering*, vol. 15, no. 5, pp. 471–482, 2014.
- [2] B. Pouteau et al., *FABAC accelerated loading test of bond between cement overlay and asphalt layers*, in *Pavement Cracking*, CRC Press, 2008.
- [3] L. Shao, Y. Li, and L. Zhang, "Research of structural properties of asphalt pavement system on orthotropic steel bridge deck in full scale tests," in *Proceedings of the 2nd International Conference on Accelerated Pavement Testing*, p. 16, 2004.
- [4] EAPA, Asphalt pavements on bridge decks. 2013, EAPA. p. 33.
- [5] ASTM, "D4580/D4580M-12: standard practice for measuring delaminations in concrete bridge decks by sounding," in *Proceedings of the ASTM Volume 04.03 Road and Paving Materials; Vehicle Pavement Systems.*, , ASTM International, West Conshohocken, PA, USA, 2012.
- [6] ASTM, "D4788-03: Standard Test Method for Detecting Delaminations in Bridge Decks Using Infrared Thermography," in *Proceedings of the ASTM Volume 04.03 Road and Paving Materials; Vehicle Pavement Systems. 2007*, ASTM International, Conshohocken, PA, USA, 2007.
- [7] ASTM, "D6087-08: Standard Test Method for Evaluating Asphalt-Covered Concrete Bridge Decks Using Ground Penetrating Radar," in *Proceedings of the ASTM Volume 04.03 Road and Paving Materials; Vehicle Pavement Systems. 2008*, ASTM International, Conshohocken, PA, USA, 2008.
- [8] M. K. Heitzman et al., "Nondestructive Testing to Identify Delaminations Between HMA Layers," in *Transportation Research Board: 500 Fifth St*, Washington, DC, USA, 2013.
- [9] T. Saarenketo and T. Scullion, "Road evaluation with ground penetrating radar," *Journal of Applied Geophysics*, vol. 43, no. 2–4, pp. 119–138, 2000.
- [10] M. Celaya et al., "Delamination detection of HMA airport pavements with NDT devices," in *Proceedings of the FAA Worldwide Airport Technology Transfer Conference*, 2010.
- [11] D. Munoz, "Finite Element Modeling Of Non-destructive Test Methods Used For Detection of Delamination In Hot Mix Asphalt Pavements," in *The University of texas in El Paso: El Paso*, p. 67, 2009.
- [12] M. E. Henderson et al., *Acoustic inspection of concrete bridge decks*, SPIE, 1999.
- [13] Y. Lu, Y. Zhang, Y. Cao, J. Gregory McDaniel, and M. L. Wang, "A mobile acoustic subsurface sensing (MASS) system for rapid roadway assessment," *Sensors (Switzerland)*, vol. 13, no. 5, pp. 5881–5896, 2013.
- [14] T. Suda, A. Tabata, J. Kawakami, and T. Suzuki, "Development of an impact sound diagnosis system for tunnel concrete lining," *Tunnelling and Underground Space Technology*, vol. 19, no. 4–5, pp. 328–329, 2004.
- [15] G. Zhang, R. S. Harichandran, and P. Ramuhalli, "Application of noise cancelling and damage detection algorithms in NDE of concrete bridge decks using impact signals," *Journal of Nondestructive Evaluation*, vol. 30, no. 4, pp. 259–272, 2011.
- [16] MDOT, *Instruction Manual for Bridge Deck Delamination Detector*, Michigan Department of Transportation, Lansing, Mich, USA, 1977.
- [17] B. L. Giordano and S. McAdams, "Material identification of real impact sounds: Effects of size variation in steel, glass, wood, and plexiglass plates," *Journal of the Acoustical Society of America*, vol. 119, no. 2, pp. 1171–1181, 2006.
- [18] S. McAdams, A. Chaignec, and V. Roussarie, "The psychomechanics of simulated sound sources: Material properties of impacted bars," *Journal of the Acoustical Society of America*, vol. 115, no. 3, pp. 1306–1320, 2004.
- [19] A. M. Alexander et al., *Impacts as a Source of Acoustic Pulse-echo Energy for Nondestructive Testing of Concrete Structures*, U.S. Army Engineer Waterways Experiment Station, 1993.
- [20] R. B. Randall, *Frequency analysis*, Brüel & Kjaer, 1987.
- [21] F. Tong, S. K. Tso, and X. M. Xu, "Tile-wall bonding integrity inspection based on time-domain features of impact acoustics," *Sensors and Actuators, A: Physical*, vol. 132, no. 2, pp. 557–566, 2006.
- [22] S. X. Liu, F. Tong, B. L. Luk, and K. P. Liu, "Fuzzy pattern recognition of impact acoustic signals for nondestructive evaluation," *Sensors and Actuators, A: Physical*, vol. 167, no. 2, pp. 588–593, 2011.
- [23] J. S. Popovics, "Investigation of a Full-Lane Acoustic Scanning Method for Bridge Deck Nondestructive Evaluation," *Transportation Research Board*, 2010.
- [24] M. Sansalone and W. B. Streett, *Impact-echo: non-destructive evaluation of concrete and masonry*, Bullbrier Press, 1997.
- [25] M. Sansalone and N. J. Carino, "Detecting delaminations in concrete slabs with and without overlays using the impact-echo method," *ACI Materials Journal*, vol. 86, no. 2, pp. 175–184, 1989.
- [26] F. Fahy and P. Gardonio, "Sound and Structural Vibration—Radiation, Transmission and Response," *Noise Control Engineering Journal*, vol. 55, no. 3, p. 373, 2007.
- [27] J. W. S. Rayleigh and R. B. Lindsay, *The Theory of Sound*, Dover Publications, New York, NY, USA, 1945.

Research Article

A Highly Sensitive Intensity-Modulated Optical Fiber Magnetic Field Sensor Based on the Magnetic Fluid and Multimode Interference

Yi Huang, Tingyun Wang, Chuanlu Deng, Xiaobei Zhang, Fufei Pang, Xuekun Bai, Weilong Dong, Liangjiang Wang, and Zhenyi Chen

Key Laboratory of Specialty Fiber Optics and Optical Access Networks, School of Communication and Information Engineering, Shanghai University, 149 Yanchang Road, Shanghai 200072, China

Correspondence should be addressed to Tingyun Wang; tywang@shu.edu.cn

Received 5 July 2017; Accepted 27 August 2017; Published 9 October 2017

Academic Editor: Zhou Zhi

Copyright © 2017 Yi Huang et al. This is an open access article distributed under the Creative Commons Attribution License, which permits unrestricted use, distribution, and reproduction in any medium, provided the original work is properly cited.

Fiber-optic magnetic field sensing is an important method of magnetic field monitoring, which is essential for the safety of civil infrastructures, especially for power plant. We theoretically and experimentally demonstrated an optical fiber magnetic field sensor based on a single-mode-multimode-single-mode (SMS) structure immersed into the magnetic fluid (MF). The length of multimode section fiber is determined based on the self-image effect through the simulation. Due to variation characteristics of the refractive index and absorption coefficient of MF under different magnetic fields, an effective method to improve the sensitivity of SMS fiber structure is realized based on the intensity modulation method. This sensor shows a high sensitivity up to 0.097 dB/Oe and a high modulation depth up to 78% in a relatively linear range, for the no-core fiber (NCF) with the diameter of 125 μm and length of 59.8 mm as the multimode section. This optical fiber sensor possesses advantages of low cost, ease of fabrication, high sensitivity, simple structure, and compact size, with great potential applications in measuring the magnetic field.

1. Introduction

Reliable and highly sensitive magnetic field sensors are quite important for monitoring the variation of the magnetic field strength of civil infrastructure such as power plant. It is also well known that fiber-optic magnetic field sensor has the advantages of good insulation and strong antielectromagnetic interference. The multimode interference (MMI) in the single-mode-multimode-single-mode (SMS) structure is sensitive to external parameters, such as the refractive index, temperature, and axial strain. Various optical fiber devices using the SMS fiber structure have been proposed and demonstrated, such as temperature sensors [1], refractometers [2–4], bandpass filters [5, 6], wavelength tunable fiber laser [7], and chemical gas detector [8]. For the excellent SMS structure, all the above optical fiber devices have advantages such as the low cost, ease of fabrication, and compatibility with standard optical fiber devices. However this SMS structure is intrinsically immune to magnetic fields due to the low magneto-optical coefficient of silica. Therefore,

it is difficult to achieve the magnetic field sensing if only using a SMS structure. Magnetic fluid (MF), as a stable colloidal suspension of ferromagnetic nanoparticles (~ 10 nm) in certain suitable liquid carriers, owns characteristics such as the special magneto-optical property in the form of Faraday effect, changeable refractive index, birefringence, and anisotropy. And the magneto-optical performance can be tuned by applying the external magnetic field [9–11]. Therefore, fiber magneto-optical sensors combined structures through the MF and SMS have been successfully realized [12–14]. The previous wavelength-based demodulation fiber sensing systems are complicated, expensive, bulky, and time-consuming, which are not suitable for the outdoor real-time monitoring. However, the intensity demodulation method can directly detect the light intensity using a simple photoelectric conversion device and hence own the features of low cost, small size, and fast response time.

In this paper, a magnetic field sensor based on the single-mode-multimode-single-mode (SMS) structure with no-core fiber as the multimode section immersing in MF is

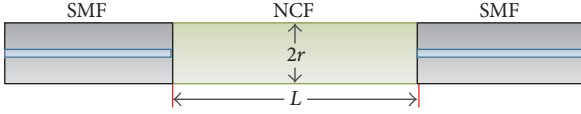


FIGURE 1: Diagram of the SNS fiber structure.

investigated theoretically and experimentally. The proposed magnetic field sensor has the features of intensity encoding and intensity multiplexing capabilities. More importantly, the magnetic field sensor has a simple structure with the potential for high sensitivity intensity-modulated magnetic field measurements. Compared with fiber magnetic sensors based on enhanced Bragg grating [15] and other optical fiber sensors based on MF, such as MF infiltrated photonic crystal fibers [16, 17], Sagnac interferometers [18], cascaded blazng gratings [19], and fiber tapers [20], the proposed scheme features low cost, easy fabrication, and high sensitivity. The proposed structure has higher sensitivity of 0.097 dB/Oe and modulation depth of 78% compared with the existing magnetic field sensors based on SMS and MF, which are mostly wavelength demodulation, such as the magnetic field sensor with sensing sensitivity of 0.01939 dB/Oe by using a square no-core fiber [12]. In addition, the proposed structure reduces the complexity of sensing demodulation, which can be realized easily without other auxiliary processes and the splice loss is smaller. Therefore, the intensity demodulation fiber-optic sensors are more practical and applicable than wavelength demodulation sensors. This structure sensor can be used for magnetic field monitoring of civil infrastructure, such as power plant.

2. Principle and Simulation

2.1. Principle of SMS. The proposed magnetic field sensor is based on the SMS structure and MF. The SMS fiber structure is fabricated by fusion splicing a specific length section of step-index multimode fiber (MMF) between two sections of standard single-mode fiber (SMF). In this paper, the multimode fiber of the SMS structure is chosen as a section of NCF. The schematic configuration of the proposed SMF-NCF-SMF (SNS) fiber structure is shown in Figure 1.

When light transfers from SMF to NCF, a series of linearly polarized modes $\{LP_{nm}\}$ of NCF are excited. Due to the circular symmetry of the SMF fundamental mode and the ideal fiber, only the symmetric mode $\{LP_{0m}\}$ can be excited. Hence, the input fundamental mode field distribution of the NCF $E(r, 0)$ can be written in terms of $\{LP_{0m}\}$ modes as follows:

$$E(r, 0) = \sum_{m=1}^M c_m \psi_m(r), \quad (1)$$

where $\psi_m(r)$ is the field distribution of $\{LP_{0m}\}$, r is the radial coordinate in the cross section of fiber, M is the number of $\{LP_{0m}\}$, and c_m is the excitation coefficient of the $\{LP_{0m}\}$

mode. c_m can be calculated by overlap integral between $E(r, 0)$ and $\psi_m(r)$, which can be expressed as

$$c_m = \frac{\int_0^\infty E(r, 0) \psi_m(r) r dr}{\int_0^\infty \psi_m(r) \psi_m(r) r dr}. \quad (2)$$

In the NCF section, the field distribution is the result of interferences of all the excited modes $\{LP_{0m}\}$ with different propagation constants, which depends on the length of NCF. Given the length of NCF as L , the field distribution $E(r, L)$ can be written as follows:

$$E(r, z) = \sum_{m=1}^M c_m \psi_m(r) \exp(i\beta_m L), \quad (3)$$

where β_m is the propagation constant of the $\{LP_{0m}\}$ mode. When the NCF length meets the relation of $\beta_m L = k\pi$ ($k = 1, 2, 3, \dots$), this is defined as the reimaging point.

When the output field distribution $E(r, L)$ from NCF transfers to the second SMF, the power coupling efficiency can be obtained through the overlap integral between $E(r, L)$ and $E(r, 0)$. The normalized output power spectrum can be calculated by

$$T = 10 \log_{10} \left[\frac{\left| \int_0^\infty E(r, L) E(r, 0) r dr \right|^2}{\int_0^\infty |E(r, L)|^2 r dr \int_0^\infty |E(r, 0)|^2 r dr} \right]. \quad (4)$$

By simplification, the normalized output power spectrum also can be expressed as

$$T = 10 \log_{10} \left[\frac{\left| \sum_{m=1}^M c_m^2 \cdot \exp(-i\beta_m L) \right|^2}{\sum_{m=1}^M c_m^2} \right]. \quad (5)$$

2.2. Simulation of the Magnetic Field Sensing. In the simulation, the SNS structure immersed into MF is designed as the magnetic field sensor, and the MF can be recognized as the cladding of NCF. The SMF has a core diameter of $9 \mu\text{m}$ and the refractive indices of core and cladding are 1.4504 and 1.4447, respectively. The NCF diameter is $125 \mu\text{m}$ and the refractive index is 1.4447. The refractive index of MF (EMG 705) is estimated to be about 1.42 [21].

Figure 2 shows the excitation coefficients for $\{LP_{0m}\}$ modes in NCF when the wavelength λ is 1550 nm. The mode excitation coefficient first increases and then decreases as mode order increases. When the mode order increases to a certain value of 18, the mode excitation coefficient is approximately 0. Moreover, the excitation coefficient distribution characteristic is different for the certain mode order under different wavelength. It means that the interference pattern of all the excited modes also is different.

For the SNS structure, the optimal length of NCF can be determined through the light propagation along NCF, as shown in Figure 3. The reimaging point R within the NCF is at a z position 60 mm. The insets display the enlarged details for the reimaging point R and the coupling point O between SMF and NCF, which indicates that the interference pattern for the two points almost is the same.

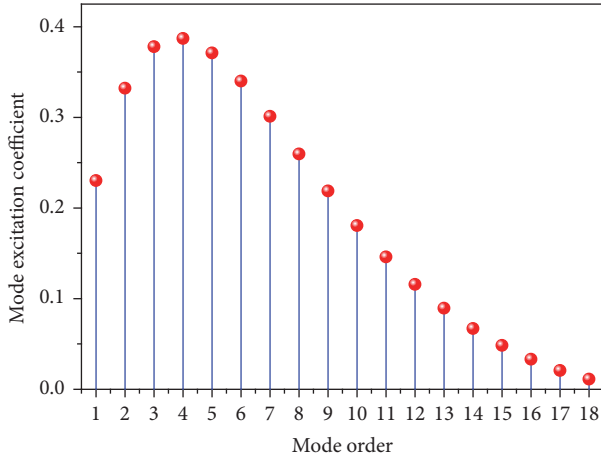


FIGURE 2: Excitation coefficient for modes with different order in NCF under a surrounding RI of 1.42.

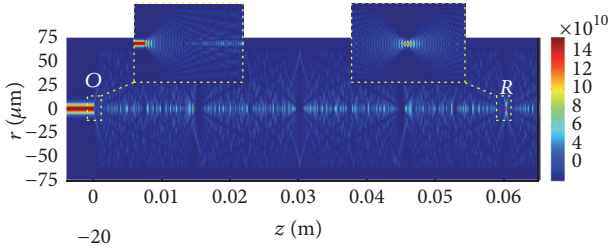


FIGURE 3: Light propagation along the NCF.

The MF is based on a commercial product of EMG 705. Under magnetic field of 0–200 Oe, the RI change of MF is approximately 0.003 [22], and the attenuation coefficient α_f changes in the order of 10^4 [23]. Due to the great absorption characteristics of MF, (5) can be amended as follows:

$$T = 10 \log_{10} \left[\frac{|\sum_{m=1}^M c_m^2 \exp(-\gamma_m L) \cdot \exp(-i\beta_m L)|^2}{\sum_{m=1}^M c_m^2} \right], \quad (6)$$

where γ_m is the evanescent absorption coefficient of the $\{LP_{0m}\}$ mode with relation to the refractive index n_f and the attenuation coefficient α_f [24, 25].

Figure 4 shows the calculated transmission spectrum of the SNS structure under different magnetic fields when the NCF length is 59.8 mm. As shown in Figure 4, there are dips (A), (B), and (D) and peak (C) (reimaging point), due to the principle of MMI. The wavelength shifts of dips (A), (B), and (D) are very small, because the RI change of MF under magnetic field varies lightly. However, in the magnetic field sensor based on SMS structure immersing in MF, the wavelength shift is large under different magnetic fields, because the smaller the NCF diameter, the larger the sensitivity of SNS structure [3]. Furthermore, the modulation depths of dips (A), (B), and (D) change greatly, which is derived from the larger change of absorption coefficients

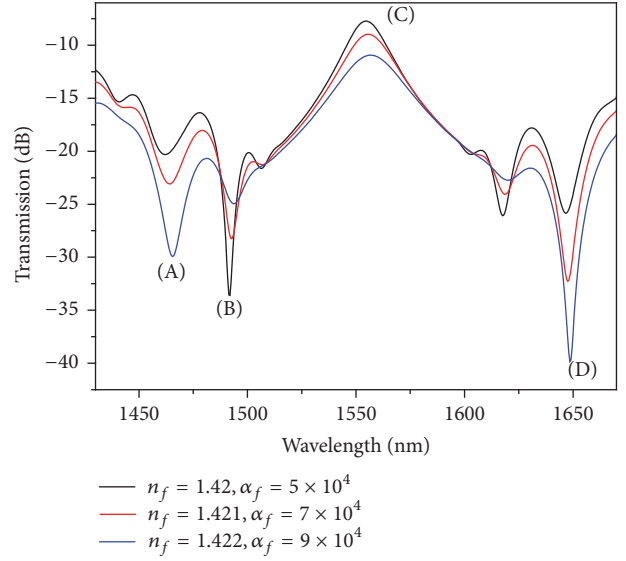


FIGURE 4: The calculated transmission spectra of the SNS structure under different magnetic fields.

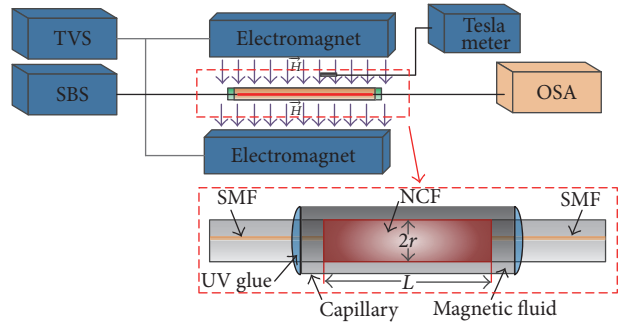


FIGURE 5: Schematic diagram of the experimental setup.

γ_m of MF under different magnetic fields. Moreover, the reimaging point (peak (C)) also shows similar changing characteristics. As the attenuation coefficient α_f increases with increasing the magnetic field, the demodulation depths of dips (A) and (D) and peak (C) are strengthened; however, the demodulation depth of dip (B) is weakened.

Therefore, the SNS structure can be designed as a magnetic field sensor based on the intensity modulation. Compared to the previous scheme adopting a combination with the wavelength shift and intensity modulation [12, 13], it can greatly reduce the complexity of sensing demodulation.

3. Experiments and Results

The experimental setup of the proposed magnetic field sensor is shown in Figure 5. It consists of a supercontinuum broadband source (SBS) (NKT, SuperK COMPACT), an optical spectrum analyzer (OSA) (Yokogawa AQ6375), a sensor head based on a MMI and the MF, two electromagnets, and a tunable voltage source (TVS). A SBS and an OSA are used to record the transmission spectrum. The sensor

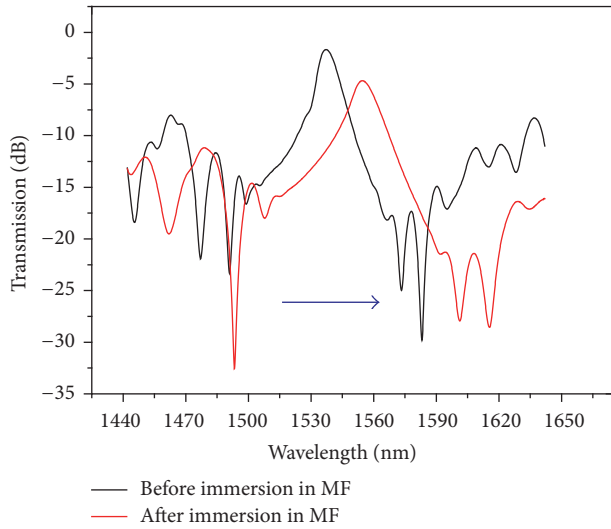


FIGURE 6: The transmission spectra of the proposed sensors with and without the immersion in MF.

head is formed by a MMI immersed in the MF. The MMI is constructed by splicing a section of NCF (Prime Optical Fiber Co. Ltd., NCF125) between two SMFs (SMF-28e, Corning, Inc.). The NCF is made of pure silica, where the radius is $r = 62.5 \mu\text{m}$, the length is $L = 59.8 \text{ mm}$, and its refractive index is 1.4446. The capillary is infiltrated with MF (EMG705, Ferrotec, Inc.). The density and saturation magnetization of the MF are 1.19 g/cm^3 (25°C) and 220 Oe, respectively. The two ends of the capillary are sealed with UV glue. The external magnetic field perpendicular to the fiber axis is generated by two electromagnets dynamically tuned by the TVS. The strength of the magnetic field is controlled by tuning the magnitude of the supply current. The magnetic field direction is perpendicular to the optical fiber axis. A Tesla meter (HT 108) with a resolution of 0.1 Oe is used to measure the magnetic field intensity along the perpendicular axis. During the experiment, the ambient temperature is kept at 25°C .

The transmission spectrum of the MMI before and after immersing into the MF is shown in Figure 6, and a red-shift to long wavelength side occurs when the MMI is immersed into the MF. By immersing the MMI section into the MF and exploiting RI tunability of the MF under varying magnetic field, a magnetic field sensor can be achieved.

Figure 7 shows the transmission characteristics of the proposed sensor by tuning the TVS to change the magnetic field strength (H) ranging from 0 to 240 Oe with a step of 15 Oe. Each curve is recorded after 5 min after specific H is applied to ensure the stabilization of the spectrum. Three distinct interference dips and a peak are observed in the wavelength range of 1450 to 1625 nm; that is, the interference dip around 1461 nm is referred to as dip (A), while around 1495 nm it is referred to as dip (B) and around 1617 nm it is referred to as dip (D), and the interference peak around 1552 nm is referred to as peak (C). peak (C) is the reimaging point. With the magnetic field increases, the depths of the interference dips (A) and (D) monotonously increase, and it is reversed for dip (B). Moreover, the interference peak

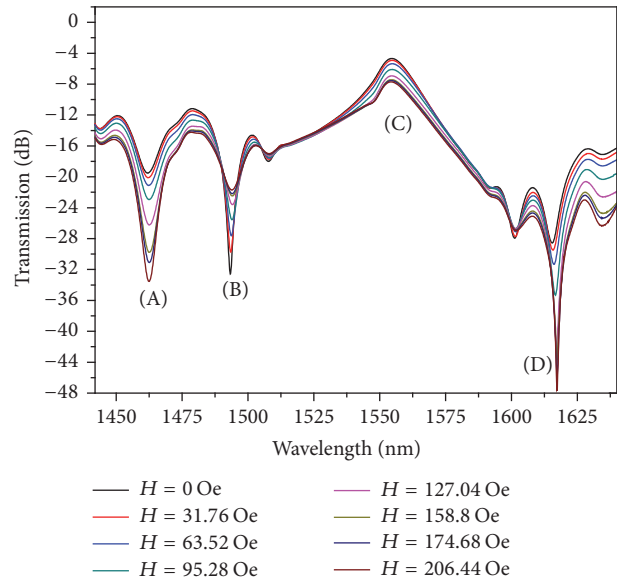


FIGURE 7: Transmission spectra of the proposed sensing structure at magnetic field strength ranging from 0 to 206.44 Oe.

(C) becomes shallower and shallower monotonously. The changing characteristics of experimental spectral response confirm well the simulation results.

The experimental results can be explained by the tunable refractive index n_f and evanescent field absorption γ_m of the MF. When an external magnetic field is applied to the MF, the magnetic particles form the agglomeration and then chain-like clusters. The chain-like cluster of particles changes the extinction coefficient of MF, which determines the attenuation coefficient α_f [23, 24]. The intensity attenuation is mainly caused by the evanescent field absorption coefficient γ_m of the MF. According to the evanescent field absorption theory in a multimode fiber [24], the change of γ_m is approximately in the order of 10^1 , and its influence on the intensity attenuation is not negligible, whereas because the change of n_f is only of the order of 10^{-3} , the wavelength shift on the transmission spectrum caused by the MMI is almost constant.

Figure 8 is an enlarged view of dip (A) and peak (C). The intensity of the interference dip (A) changes from -19.77 dB to -34.70 dB as shown in Figure 8(a) and the intensity of the interference peak (C) changes from -4.79 dB to -7.75 dB as shown in Figure 8(b) with the increase of the magnetic field strength. As in the principle simulation section, on one hand the center wavelength of dip (A) and peak (C) hardly shifts with the change of the magnetic field; on the other hand the intensities of peak (C) decrease and the intensities of dip (A) increase with an increase of the magnetic field because of the tunable RI and absorption coefficient of MF. Similarly, the intensity of dips (B) and (D) changes from -32.57 dB and -28.56 dB to -47.67 dB , respectively.

The intensity of dip (A) and peak (C) as a function of external magnetic field is shown in Figure 9(a), indicating that the intensity is linearly proportionally to magnetic field strength in the range of 63.52–142.92 Oe and 79.4–206.44 Oe,

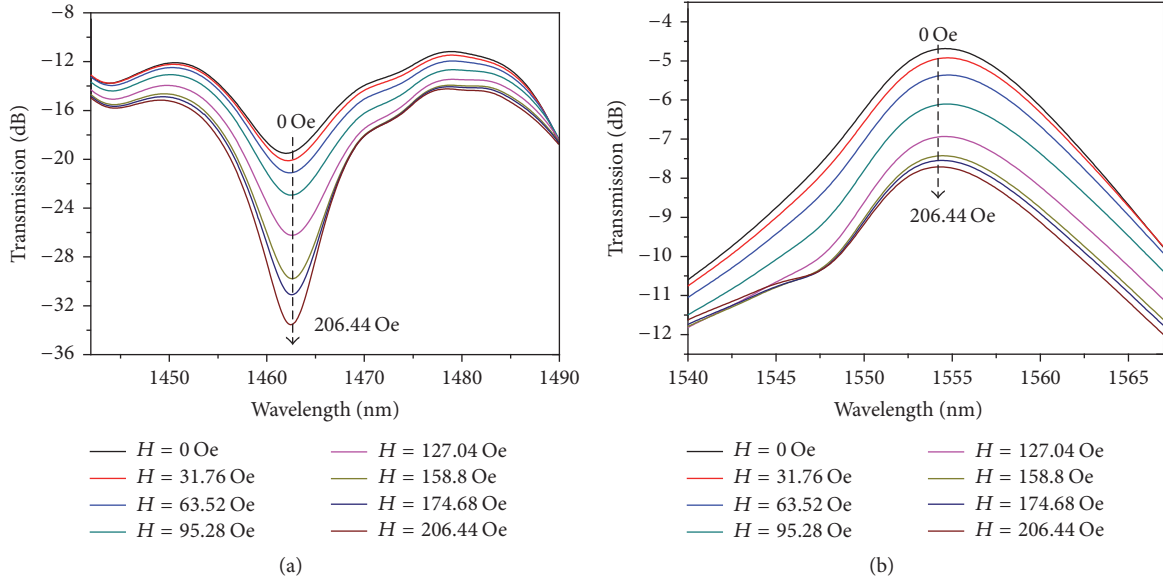


FIGURE 8: Transmission spectra of (a) dip (A) and (b) peak (C) subjected to different strengths of magnetic field.

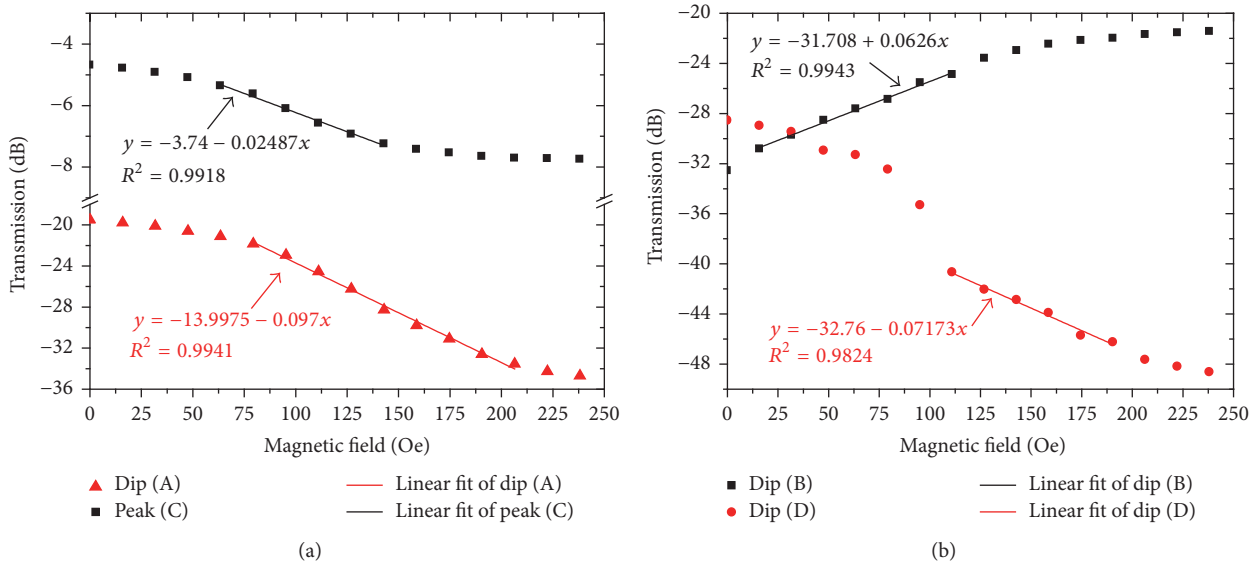


FIGURE 9: Intensities of (a) dip (A), peak (C) and (b) dip (B), dip (D) as functions of magnetic field.

respectively. Such linear relationship benefits practical sensing application [26]. By linear fitting, the maximum sensitivities of magnetic field are found to be 0.097 dB/Oe and 0.0248 dB/Oe for dip (A) and peak (C), respectively. Similarly, the linearly changing range for dipoles (B) and (D) is 15.88–111.16 Oe and 111.16–190.56 Oe, respectively, with the maximum sensitivities as 0.0626 dB/Oe and 0.071 dB/Oe, respectively, which is shown in Figure 9(b). It is made clear that the intensity of dipoles (A), (B), and (D) is larger than that of peak (C), with the sensitivity of dip (A) being the largest one.

Sensitivity is an important parameter of sensor performance. High sensitivity is usually preferable in practical application. Besides, considering the comprehensive sensing

properties of the proposed magnetic field sensor, the modulation depth (M) is defined as [26]

$$M = 1 - \frac{T_{\min}}{T_{\max}} = \frac{T_{\max} - T_{\min}}{T_{\max}}, \quad (7)$$

where T_{\max} and T_{\min} are the maximum and minimum of the intensity in transmission spectrum with the magnetic field, respectively, and M is the contrast ratio between T_{\max} and T_{\min} . The modulation depth as a function is shown in Figure 10. The modulation depth of dip (A), peak (C), dip (B), and dip (D) is 78%, 65%, 23%, and 61%, respectively, which can be used for the sensing demodulation.

From (6), the transmission of dipoles (A), (B), and (D) and peak (C) is related to the excitation coefficient c_m , the

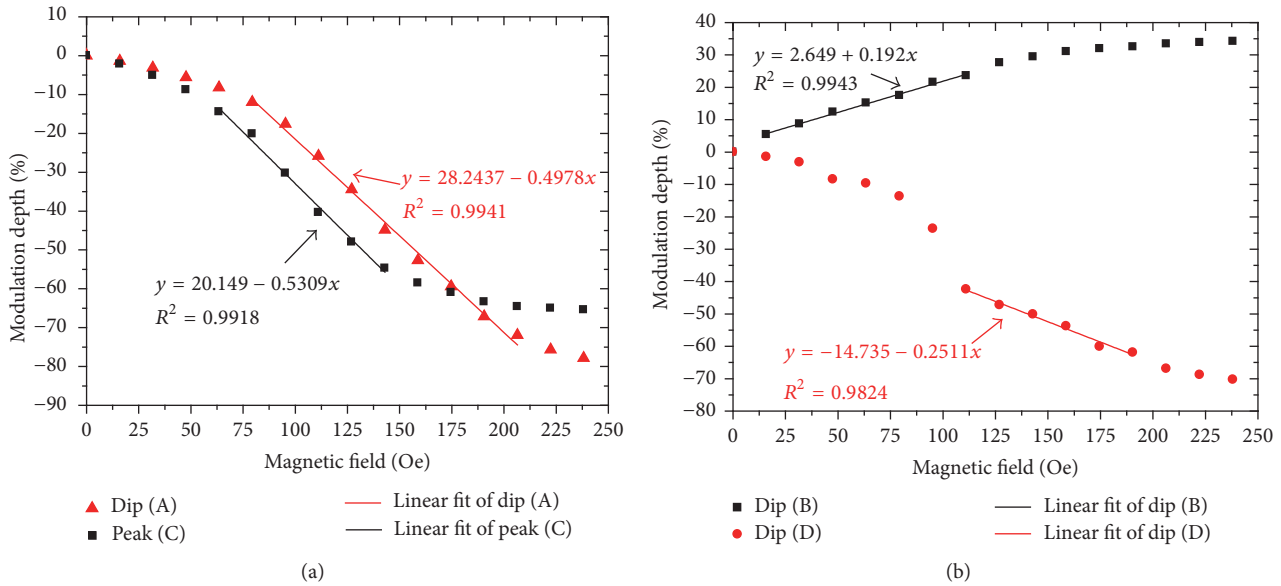


FIGURE 10: Modulation depth of (a) dip (A), peak (C) and (b) dip (B), dip (D) versus the strength of magnetic field.

evanescent absorption coefficient γ_m , and the mode phase $\beta_m L$. For peak (C), it is a self-image point and the ideal transmission is 100% if the evanescent absorption coefficient is zero. However, the intensity of peak (C) will vary a little if the evanescent absorption coefficient exists. Similarly, the intensities of dips (A), (B), and (D) will also vary if the evanescent absorption coefficient exists. However, the variations of intensities of dips (A), (B), and (D) will have larger variations because the previous values are on a much lower level, while the intensity of peak (C) is on a larger level.

Considering the sensitivity and modulation depth, dip (A) with a larger sensitivity is more suitable for practical sensing application. The sensitivity of the proposed structure is higher (0.097 dB/Oe) than that of [12] (0.01939 dB/Oe).

4. Conclusions

In conclusion, an intensity-modulated magnetic field sensor based on the combination with SNS structure and MF is investigated theoretically and experimentally. This sensor has a high sensitivity of 0.097 dB/Oe and high modulation depth of 78% in a relatively linear range. It has features including low cost, ease of fabrication, compactness, and high sensitivity, which suggests that the proposed sensor is simple and effective in the measurement of magnetic field.

Conflicts of Interest

The authors declare no conflicts of interest.

Acknowledgments

This work is supported by the National Natural Science Foundation of China (NSF) (61475096, 61520106014, 61635006, 61675126, and 61475095).

References

- [1] S. M. Tripathi, A. Kumar, R. K. Varshney, Y. B. P. Kumar, E. Marin, and J. P. Meunier, "Strain and temperature sensing characteristics of single-mode-multimode-single-mode structures," *Journal of Lightwave Technology*, vol. 27, no. 13, pp. 2348–2356, 2009.
- [2] Z. B. Liu, Z. Tan, B. Yin, Y. Bai, and S. Jian, "Refractive index sensing characterization of a singlemode-claddingless-singlemode fiber structure based fiber ring cavity laser," *Optics Express*, vol. 22, no. 5, pp. 5037–5042, 2014.
- [3] Q. Wu, Y. Semenova, P. Wang, and G. Farrell, "High sensitivity SMS fiber structure based refractometer - Analysis and experiment," *Optics Express*, vol. 19, no. 9, pp. 7937–7944, 2011.
- [4] X. Zhang, H. Shao, Y. Yang, H. Pan, F. Pang, and T. Wang, "Refractometry with a tailored sensitivity based on a single-mode-capillary-single-mode fiber structure," *IEEE Photonics Journal*, vol. 9, no. 2, pp. 1–8, 2017.
- [5] W. S. Mohammed, P. W. E. Smith, and X. Gu, "All-fiber multimode interference bandpass filter," *Optics Letters*, vol. 31, no. 17, pp. 2547–2549, 2006.
- [6] J. E. Antonio-Lopez, A. Castillo-Guzman, D. A. May-Arrijoa, R. Selvas-Aguilar, and P. Likamwa, "Tunable multimode-interference bandpass fiber filter," *Optics Letters*, vol. 35, no. 3, pp. 324–326, 2010.
- [7] A. Castillo-Guzman, J. E. Antonio-Lopez, R. Selvas-Aguilar, D. A. May-Arrijoa, J. Estudillo-Ayala, and P. LiKamWa, "Widely tunable erbium-doped fiber laser based on multimode interference effect," *Optics Express*, vol. 18, no. 2, pp. 591–597, 2010.
- [8] X. Lan, J. Huang, Q. Han et al., "Fiber ring laser interrogated zeolite-coated singlemode-multimode-singlemode structure for trace chemical detection," *Optics Letters*, vol. 37, no. 11, pp. 1998–2000, 2012.
- [9] C. Y. Hong, H. E. Horng, F. C. Kuo, S. Y. Yang, H. C. Yang, and J. M. Wu, "Evidence of multiple states of ordered structures and a phase transition in magnetic fluid films under perpendicular magnetic fields," *Applied Physics Letters*, vol. 75, no. 15, pp. 2196–2198, 1999.

- [10] S. Y. Yang, J. J. Chieh, H. E. Horng, C.-Y. Hong, and H. C. Yang, "Origin and applications of magnetically tunable refractive index of magnetic fluid films," *Applied Physics Letters*, vol. 84, no. 25, pp. 5204–5206, 2004.
- [11] J. E. Antonio-Lopez, J. J. Sanchez-Mondragon, P. LiKamWa, and D. A. May-Arrijoja, "Fiber-optic sensor for liquid level measurement," *Optics Letters*, vol. 36, no. 17, pp. 3425–3427, 2011.
- [12] W. Lin, Y. Miao, H. Zhang, B. Liu, Y. Liu, and B. Song, "Fiber-optic in-line magnetic field sensor based on the magnetic fluid and multimode interference effects," *Applied Physics Letters*, vol. 103, no. 15, Article ID 151101, 2013.
- [13] H. Wang, S. Pu, N. Wang, S. Dong, and J. Huang, "Magnetic field sensing based on singlemode-multimode-singlemode fiber structures using magnetic fluids as cladding," *Optics Letters*, vol. 38, no. 19, pp. 3765–3768, 2013.
- [14] S. Dong, S. Pu, and J. Huang, "Magnetic field sensing based on magneto-volume variation of magnetic fluids investigated by air-gap Fabry-Pérot fiber interferometers," *Applied Physics Letters*, vol. 103, no. 11, Article ID 111907, 2013.
- [15] Y. Dai, M. Yang, G. Xu, and Y. Yuan, "Magnetic field sensor based on fiber Bragg grating with a spiral microgroove ablated by femtosecond laser," *Optics Express*, vol. 21, no. 14, pp. 17386–17391, 2013.
- [16] H. V. Thakur, S. M. Nalawade, S. Gupta, R. Kitture, and S. N. Kale, "Photonic crystal fiber injected with Fe₃O₄ nanofluid for magnetic field detection," *Applied Physics Letters*, vol. 99, no. 16, Article ID 161101, 2011.
- [17] P. Zu, C. Chiu Chan, T. Gong, Y. Jin, W. Chang Wong, and X. Dong, "Magneto-optical fiber sensor based on bandgap effect of photonic crystal fiber infiltrated with magnetic fluid," *Applied Physics Letters*, vol. 101, no. 24, Article ID 241118, 2012.
- [18] P. Zu, C. C. Chan, W. S. Lew et al., "Magneto-optical fiber sensor based on magnetic fluid," *Optics Letters*, vol. 37, no. 3, pp. 398–400, 2012.
- [19] P. Childs, A. Candiani, and S. Pissadakis, "Optical fiber cladding ring magnetic field sensor," *IEEE Photonics Technology Letters*, vol. 23, no. 13, pp. 929–931, 2011.
- [20] S. Pu, X. Chen, Y. Chen et al., "Fiber-optic evanescent field modulator using a magnetic fluid as the cladding," *Journal of Applied Physics*, vol. 99, no. 9, p. 093516, 2006.
- [21] H. E. Horng, C.-Y. Hong, S. Y. Yang, and H. C. Yang, "Designing the refractive indices by using magnetic fluids," *Applied Physics Letters*, vol. 82, no. 15, pp. 2434–2436, 2003.
- [22] Y. F. Chen, S. Y. Yang, W. S. Tse, H. E. Horng, C. Y. Hong, and H. C. Yang, "Thermal effect on the field-dependent refractive index of the magnetic fluid film," *Applied Physics Letters*, vol. 82, no. 20, pp. 3481–3483, 2003.
- [23] X. Fang, Y. Xuan, and Q. Li, "Theoretical investigation of the extinction coefficient of magnetic fluid," *Journal of Nanoparticle Research*, vol. 15, no. 5, pp. 1–12, 2013.
- [24] X. Fang, Y. Xuan, and Q. Li, "Measurement of the extinction coefficients of magnetic fluids," *Nanoscale Research Letters*, vol. 6, no. 1, pp. 1–5, 2011.
- [25] V. Ruddy, B. D. MacCraith, and J. A. Murphy, "Evanescent wave absorption spectroscopy using multimode fibers," *Journal of Applied Physics*, vol. 67, no. 10, pp. 6070–6074, 1990.
- [26] J. Tang, S. Pu, S. Dong, and L. Luo, "Magnetic field sensing based on magnetic-fluid-clad multimode-singlemode-multimode fiber structures," *Sensors (Switzerland)*, vol. 14, no. 10, pp. 19086–19094, 2014.

Research Article

Experimental Verification for Cable Force Estimation Using Handheld Shooting of Smartphones

Xuefeng Zhao,¹ Kwang Ri,^{1,2} and Niannian Wang¹

¹State Key Laboratory of Coastal and Offshore Engineering, School of Civil Engineering, Dalian University of Technology, Dalian 116024, China

²School of Civil Engineering, Pyongyang University of Architecture, Pyongyang 1001, Democratic People's Republic of Korea

Correspondence should be addressed to Xuefeng Zhao; zhaoxf@dlut.edu.cn

Received 23 May 2017; Accepted 6 July 2017; Published 7 August 2017

Academic Editor: Lei Yuan

Copyright © 2017 Xuefeng Zhao et al. This is an open access article distributed under the Creative Commons Attribution License, which permits unrestricted use, distribution, and reproduction in any medium, provided the original work is properly cited.

Currently, due to the rapid development and popularization of smartphones, the usage of ubiquitous smartphones has attracted growing interest in the field of structural health monitoring (SHM). The portable and rapid cable force measurement for cable-supported structures, such as a cable-stayed bridge and a suspension bridge, has an important and practical significance in the evaluation of initial damage and the recovery of transportation networks. The extraction of dynamic characteristics (natural frequencies) of cable is considered as an essential issue in the cable force estimation. Therefore, in this study, a vision-based approach is proposed for identifying the natural frequencies of cable using handheld shooting of smartphone camera. The boundary of cable is selected as a target to be tracked in the region of interest (ROI) of video image sequence captured by smartphone camera, and the dynamic characteristics of cable are identified according to its dynamic displacement responses in frequency domain. The moving average is adopted to eliminate the noise associated with the shaking of smartphone camera during measurement. A laboratory scale cable model test and a pedestrian cable-stayed bridge test are carried out to evaluate the proposed approach. The results demonstrate the feasibility of using smartphone camera for cable force estimation.

1. Introduction

Since cables are primary elements for ensuring the overall structural integrity and safety of cable-stayed bridges, the accurate cable force measurement has very important practical significance in the bridge health monitoring [1]. The cable-stayed bridges are monitored by the continuous cable force measurements during construction, and the bridge health status is evaluated by the change in cable force resulting from the damage and degradation during service stage. In particular, the portable and rapid cable force measurement plays an extremely vital role in the evaluation of initial damage and the formulation of recovery plans for ensuring the security of transportation networks after severe events such as typhoon and earthquake.

Currently, the vibration method is widely used for the estimation of cable force because of its simplicity and speediness [2, 3]. In the vibration method, the cable force is indirectly estimated from the natural frequencies of

cable [4, 5], which are commonly extracted from the acceleration responses of cable that is measured by accelerometer sensor installed on cable. The vibration method, however, requires that each of accelerometer sensors should be connected with data acquisition system through electrical cables, and the cable installation is costly and time-consuming. Although wireless sensors have recently emerged to overcome some of these issues, additional issues are then introduced concerning the data transmission reliability, power supply, and network bandwidth [6]. Therefore, it is necessary to develop noncontact method for estimating cable force without attaching sensors to cables.

As one of the typical noncontact methods, vision-based method, which extracts dynamic characteristics of object from video images through the template matching techniques, has received increasing attention in SHM such as system identification [7–12] and damage detection [13, 14]. Although the vision-based method is largely influenced by outdoor field environmental conditions such as illumination

variation and background disturbance, it offers significant advantages such as low cost, ease of operation, and multipoint vibration measurement with a single camera. To our knowledge, only a few attempts have been made to apply vision-based methods for cable force estimation. For example, Ji and Chang [15] used a nontarget image-based technique for cable vibration measurement. An optical flow method was adopted to estimate displacement of an arbitrarily chosen ROI on the image plane. The diameter of the cable and the coordinates of the camera were adopted as references for determining the actual displacement of ROI in the 3D object space. The optical flow method considers the motion of object at pixel level according to the change in the image intensities on the image plane [16] and requires an iterative approach [17] for calculating optical flow vector that indicates the magnitude and direction of motion of the ROI in the image plane. Kim et al. [18] developed a vision-based monitoring system for measuring the dynamic characteristics of remote stay cables by means of the template matching method using the normalized cross correlation. The template matching method makes it possible for the object itself to be used as a template in the case of no target.

On the other hand, with the rapid development and popularization of smartphone in recent years, the usage of ubiquitous smartphone has attracted growing interest in the field of SHM owing to its unique feature [19]. Most smartphones have powerful operating system, large memory resource, and a variety of high-performance sensors, and such characteristics are very appropriate for the implementation of SHM. Several researchers studied the application feasibility of smartphone for extracting structural vibration responses from the accelerometer embedded in smartphone [20–24]. Particularly, the smartphone application Orion-CC developed by the authors for smartphone based cloud-SHM [25] is possible to estimate the cable force using the accelerometer embedded in smartphone as well as to upload to the data sharing platform and to share with the public [26]. Although the smartphone inner sensors have limitation in precision of measurement, they are appropriate for the cable force estimation because cable is relatively distinct in vibration rather than the other structural elements. In the previous study, the authors investigated the feasibility and validity of vision-based cable force measuring method using smartphone camera [27]. The dynamic characteristics of cable were extracted from the displacement response of a predefined black circle target attached on the cable. The laboratory cable model test demonstrated the feasibility and reliability for extracting dynamic characteristics of cable at the sampling rate (frames per second) of the current smartphone camera.

As can be seen from the previous studies, the vision-based cable force monitoring is mainly conducted by the vision system (including a digital camera installed with high-quality zoom lens, a computer for image processing, and a data storage server) mounted on the deck or tower of the cable-stayed bridge. Moreover, the dynamic characteristics (natural frequencies) of cable are extracted from the actual real-time displacement responses of cable. Meanwhile, the cable force estimation using smartphone is limited to the

smartphone inner accelerometer, and in the case of using smartphone camera, the dynamic characteristics of cable are extracted from the actual displacement responses of a predefined target attached on the cable surface, by means of smartphone mounted on tripod. The utilization of smartphone for measuring cable force would make it possible for personnel to evaluate quickly the initial damage and safety status of cable-stayed bridge, owing to its features such as ease of installation, low cost, and convenience. Although the cable force estimation based on the smartphone inner accelerometer is convenient and easy to install, it requires that the smartphones should be fixed tightly on the cables using the mobile phone jackets because the coupling between the cable and the smartphone can affect the vibration measurement, which sometimes may be either difficult or inappropriate for cable force measurement of inaccessible cable bridges. Therefore, it is necessary to develop a portable and noncontact method for estimating cable force using smartphone camera without any target and tripod.

In this study, as the update of the target vision-based cable force measurement using a smartphone, a novel nontarget approach that is appropriate for handheld shooting of smartphone camera is proposed and its feasibility and practicality are preliminarily validated through a laboratory test and a field test. The dynamic characteristics for cable force estimation are identified from the dynamic displacement responses of one side of cable boundary on the image plane. To enhance the accuracy of cable force measurement, the correction for the shaking of smartphone camera during measurement is performed by means of the moving average filter in the analysis process of cable vibration. The proposed method does not require any installation of tripod and target unlike the previous one. Furthermore, the ROI is selected on the cable boundary through the detection of it, and the cable force is estimated via smartphone application without the calibration for the actual displacement response. The comprehensive comparison tests between using smartphone built-in accelerometer and using smartphone camera, including target and nontarget method, fixed and handheld shooting, and smartphone application and MATLAB postprocessing, demonstrate the feasibility and practicality of using smartphone camera for cable force estimation.

2. Cable Force Estimation Algorithm Using Smartphone Camera

2.1. Image Processing Method

2.1.1. Hough Transform for Detecting Cable Boundary. In order to convert 2D vibration of cable on image plane to 1D vibration in accordance with the data processing performance of the current smartphone, it is necessary to define the inclination angle of cable for the rotation transform of image, which can be determined by the position of cable boundary in the image plane. The boundary of cable for identifying the inclination angle of inclined stay cable and for selecting the ROI is detected by Hough transform (HT) on the image of the first scene captured by smartphone camera.



FIGURE 1: Model of a ramp digital edge.

HT is recognized as a popular and efficient technique for detecting straight lines in images, even in the presence of noise [28–32]. The Canny edge detection algorithm based on the Gaussian low-pass filter [33, 34] is first adopted to identify all of the edges contained in the grayscale image, resulting in a binary image. By means of HT, for each chosen value of θ , the edge pixels of image are voted to a parameter space according to

$$\rho = x \cos \theta + y \sin \theta, \quad (1)$$

where ρ is the distance from the origin to the line along a vector perpendicular to the line and θ is the angle between the line's perpendicular and the horizontal axis, and then the parameters of lines are determined by identifying the highest values (i.e., peaks) in the accumulator array (ρ, θ) .

2.1.2. Measurement of Cable Boundary Location. Since the amplitude of cable vibration is relatively small compared with the distance between smartphone camera and cable, the actual motion of cable in the 3D object space and the corresponding motion on the 2D image plane are linearly correlated, and thus they have the same frequency contents obtained from Fourier transform. In addition, since only the vibration response (i.e., frequencies) of cable is required in the cable force estimation, there is no need to determine the scaling factor (units: mm/pixel) to transform the pixel coordinate vibrations into physical coordinate ones, and the dynamic characteristics of cable can be extracted according to the change in the location of the cable boundary in the chosen ROI of image. The boundary of cable in the ROI is represented as an edge between two image regions as shown in Figure 1.

Assuming an ideal negative edge profile centered in x_{edge} ,

$$\text{edge}(x) = \begin{cases} A_{\max} & \text{if } x < x_{\text{edge}} \\ A_{\min} & \text{if } x \geq x_{\text{edge}} \end{cases} \quad (2)$$

where A_{\max} and A_{\min} represent the maximum and minimum intensity values [35]. The image intensity profile $y(x)$ is obtained as the convolution of the function $\text{edge}(x)$ and a Gaussian function G with zero mean and standard deviation σ_{edge} as shown in (3b):

$$G(0, \sigma_{\text{edge}}, x) = \frac{1}{\sqrt{2\pi}} e^{-x^2/2\sigma_{\text{edge}}^2} \quad (3a)$$

$$y(x) = \int_{-\infty}^{+\infty} \text{edge}(x - \xi) \cdot G(0, \sigma_{\text{edge}}, \xi) d\xi. \quad (3b)$$

This edge can be easily detected using the first-order derivative of the image intensity profile function; namely, the

location of the cable boundary in the ROI is identified as the location of the maximum first-order finite-difference in each of the frames. The sums of the pixel intensities in the ROI are used to estimate the dynamic characteristics of cable because the pixel intensity of one point is not sufficient for the accurate location determination of the cable boundary.

2.2. Moving Average Filter. To estimate the dynamic characteristics of cable using the handheld shooting of smartphone camera without a tripod, it is necessary to reduce the noise associated with the shaking of smartphone camera during measurement. In general, the process of determining position and orientation of cameras such as SLAM (Simultaneous Localization and Mapping) or Visual Odometry requires a great deal of computational power and a high calculation cost; it would be inappropriate for the applications of the current smartphones. When the shaking of the smartphone camera is relatively weak compared to the vibration of cable, the moving average can be used to extract the movement components of smartphone from the displacement-time history. Generally, the excellent quality filter in the frequency domain could cause the worst quality in the time domain and vice versa [36]. Although the moving average is insufficient to classify one band of frequencies, it is considered as the most popular filter in Digital Signal Processor (DSP), because it not only is easy to comprehend and use but also possesses exceptionally good property in the time domain. It is commonly used to smooth out short-term variations and emphasize longer-term trends or cycles. The moving average filter controls accuracy of the dynamic characteristics by averaging a number of points from the input data to obtain each point in the output data as expressed in

$$y(i) = \frac{1}{n} \sum_{j=0}^{n-1} x(i+j), \quad (4)$$

where $[x]$ is the input data, $[y]$ is the output data, and n is the number of points in the average. The more accurate displacement-time history for extracting dynamic characteristics of cable is obtained by removing the movement components of smartphone that are smoothed out through the moving average, prior to the Fourier transform.

2.3. Summary of Algorithm. The algorithm for cable force estimation using smartphone camera is shown in Figure 2. The video file captured using smartphone camera is converted into image files. The boundary of cable is detected by means of Hough transform (HT) on the image of the first scene captured by smartphone camera, from which the inclination angle of cable is determined, and the ROI is selected and rotated around its centroid accordingly on each of images converted from video file. The sums of the pixel intensities along the longitudinal direction of cable and its first-order finite-differences are calculated to identify the location of the cable boundary in the ROI. The integer-pixel location of the cable boundary is acquired by locating the peak of the first-order finite-differences, and the more accurate location in less than one pixel is identified in a neighborhood around the

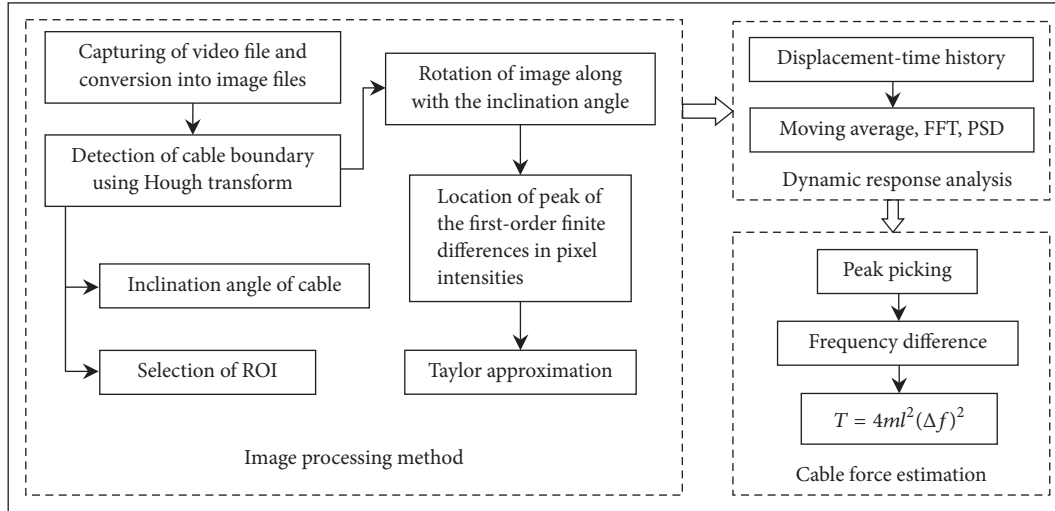


FIGURE 2: Algorithm for cable force estimation.

initial peak using the first-order Taylor series approximation. The displacement-time history of cable boundary is obtained according to the change of peak in its location and then smoothed out by means of the moving average in order to eliminate the noise generated by shaking of smartphone.

The power spectral density (PSD) is obtained from the displacement response via FFT, from which the natural frequencies in each mode are extracted using the peak picking method. The cable force is finally estimated by the relationship between the frequency difference and cable force as shown in

$$T = 4ml^2 (\Delta f)^2, \quad (5)$$

where m is the linear mass density, l is the cable length, and Δf is the frequency difference. Although several practical formulae for cable force estimation have been studied, the flat taut string theory that neglects the effect of sag and stiffness of cable is adopted to evaluate the feasibility of cable force measurement using smartphone camera, due to its simplicity and speediness. In this study, a smartphone application that is developed by Objective-C in accordance with the algorithm explained above is used to estimate the cable force by the smartphone camera.

3. Experimental Verifications

To validate the proposed cable force measurement method based on the image processing, two tests are carried out, as compared with those of using smartphone built-in accelerometer, including a laboratory scale cable model test and a field test. In each test of cable force measurement using smartphone camera, the comparison tests are conducted in three different ways, namely, the measurement using smartphone mounted on a tripod when there is an artificial target, those using smartphone mounted on a tripod when there is no any target, and those using handheld shooting

of smartphone camera without any target and tripod. As the smartphone for experiment, four iPhone 6 devices are used. The first smartphone referred to as Smartphone 1, in which a smartphone application Orion-CC is installed, is used to estimate cable force using smartphone built-in accelerometer, and its sampling rate is set to 100 Hz. The smartphone application Orion-CC is possible to not only estimate cable force from the acceleration responses of cable vibration that is extracted using accelerometer embedded in smartphone, but also upload to the data sharing platform and share with the public. Further details regarding the operation guide and cable force measurement of the smartphone application Orion-CC can be seen in [22]. The second smartphone referred to as Smartphone 2, in which a smartphone application D-Viewer is installed, is utilized for the extraction of dynamic characteristics of cable from the dynamic displacement response of a black circle target attached on cable. The maximum number of black pixels is determined in the selected ROI of the binary image, from which the centroid of target and its dynamic displacement response are extracted for cable force measurement. The sampling rate of D-Viewer is 30 Hz; namely, it is the same as the frames per second (fps) of smartphone camera. Since D-Viewer is a vision-based displacement monitoring application using smartphone camera, it requires the actual size of target and the calibration for the actual displacement response. Further details regarding the operation guide and structural displacement monitoring of the smartphone application D-Viewer can be found in [37]. The other two smartphones referred to as Smartphone 3 and Smartphone 4 are used to estimate the cable force using the proposed image processing approach, respectively. One is mounted on the tripod, while the other one is used for the handheld shooting of any participant. Table 1 summarizes the relevant parameters of iPhone 6 used in experiments [38].

To verify the accuracy and precision of the identified natural frequencies, error analysis is carried out using the

TABLE 1: Relevant parameters of iPhone 6 devices.

| Operating system | Display | Chips | Video recording |
|------------------|--|--|---|
| IOS 9 | Retina HD display 4.7-inch (diagonal) 1334-by-750-pixel resolution at 326 ppi 1400 : 1 contrast ratio (typical) | A8 chip with 64-bit architecture M8 motion coprocessor | 1080p HD video recording (30 fps or 60 fps) |

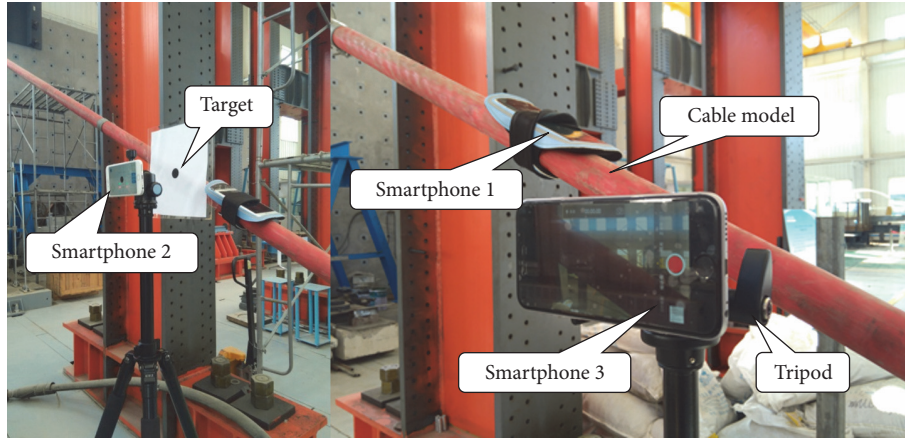


FIGURE 3: Installation of smartphones.

mean absolute deviation percent (MADP) shown in (6) and the root mean square error (RMSE) shown in (7)

$$\text{MADP} = \frac{\sum_{i=1}^n |f_b - f_s|}{\sum_{i=1}^n |f_b|}, \quad (6)$$

$$\text{RMSE} = \sqrt{\frac{\sum_{i=1}^n (f_b - f_s)^2}{n}}, \quad (7)$$

where n is the number of replicates, f_b are the natural frequencies measured by smartphone built-in accelerometer and smartphone camera mounted on the tripod and those (handheld shooting) processed by MATLAB, respectively, and f_s are the natural frequencies measured by APP D-Viewer, handheld shooting of smartphone camera, and those (handheld shooting) processed by smartphone application, respectively.

3.1. Laboratory Scale Cable Model Test

3.1.1. Overview of Experiment. The cable model is installed in the Bridge Lab of Dalian University of Technology. The model is a 15.53 m single cable, and its linear mass density is 3.95 kg/m. The Smartphone 1 installed with APP Orion-CC is fixed tightly on the cable model via mobile phone jacket, and Smartphones 2 and 3 are mounted on a tripod via double-sided adhesive tape to extract the dynamic characteristics of cable without the shaking of smartphone camera. An organic glass panel, on which there is a preprinted black circle of 2 cm in diameter, is attached to the cable model using superglue.

Smartphone 4 is used to measure the cable vibration without any tripod; that is, any participant shoots the cable vibration with it in his hand and extracts the dynamic characteristics of cable. The three smartphones except Smartphone 1 are placed at about 20 cm away from the cable, respectively, so that the field of view appropriate for the measurement is satisfied without smartphone camera zoom. The reference accelerometer is not installed on the cable because the performance of smartphone built-in accelerometer for cable force measurement has been validated through previous studies [22]. Figure 3 shows the installation of smartphones. The smartphone camera captures the cable vibration at a resolution of 1920×1080 pixels with a sampling rate of 30 fps. The participant tries to keep a stationary posture as much as possible during measurement. The test is carried out simultaneously under the artificial knocking excitation and the measuring time of the participant is set as 30 seconds taking into account his patience during measurement.

3.1.2. Test Results. The boundary of cable model detected by HT on the image of the first scene captured by smartphone camera, the selected ROI, and the rotation of image are shown in Figure 4. Figures 5–8 show the acceleration and displacement-time history responses of cable model that are measured by four smartphones, and the corresponding power spectral densities (PSD), respectively.

Figure 8(a) shows the displacement-time history of cable model that the participant measured with Smartphone 4 in his hand, in which the red curve indicates the movement contents of Smartphone 4 smoothed out in time domain

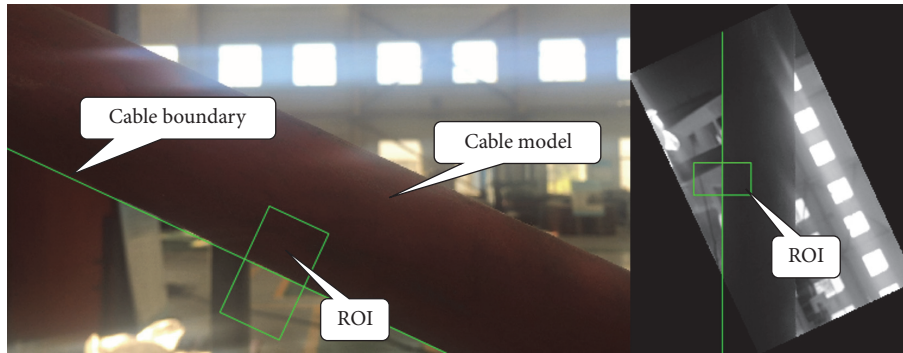


FIGURE 4: Detection of cable boundary and rotation of image.

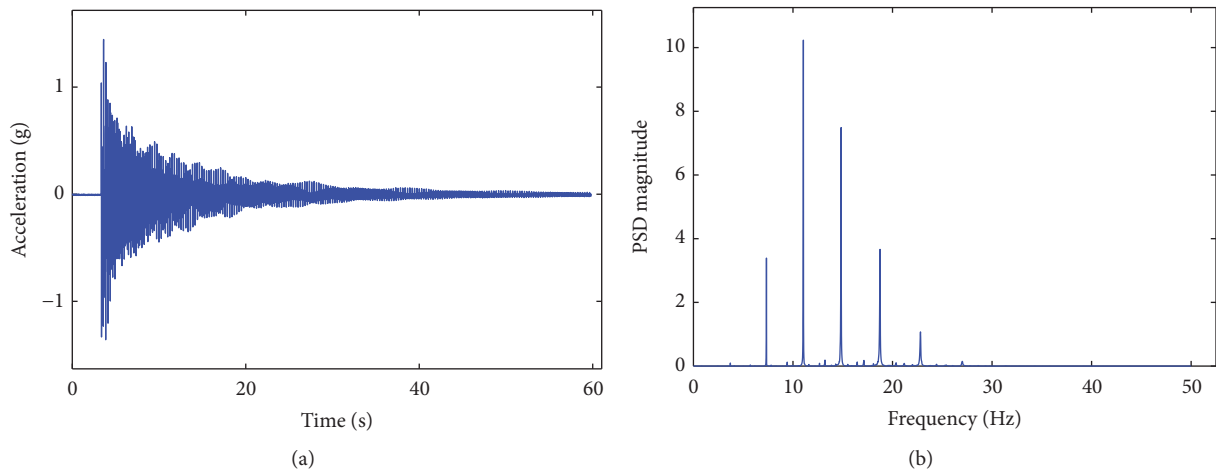


FIGURE 5: Measurement using Smartphone 1: (a) acceleration-time history; (b) corresponding PSD.

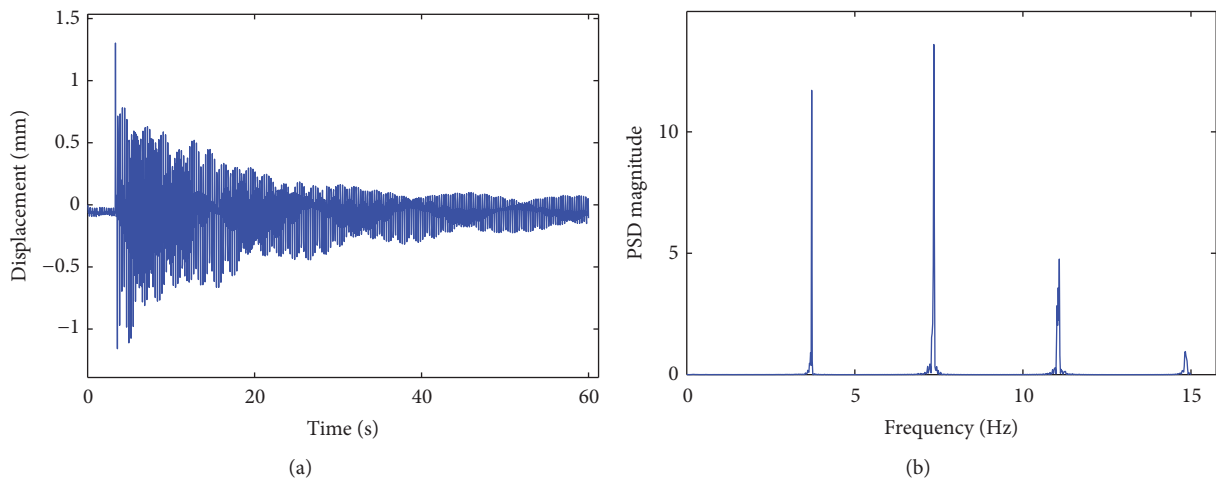


FIGURE 6: Measurement using Smartphone 2: (a) displacement-time history; (b) corresponding PSD.

by means of the moving average. The displacement-time history of cable model is obtained according to the change in the location of peak in the first-order finite-difference of sums of pixel intensities in ROI, as shown in Figure 8(c). The displacement-time history eliminated the movement

contents of smartphone and the corresponding PSD are shown in Figures 8(b) and 8(d), respectively. Figure 9 illustrates three screenshots of smartphone application for cable force measurement using handheld shooting. Table 1 compares the natural frequency values of cable model in each

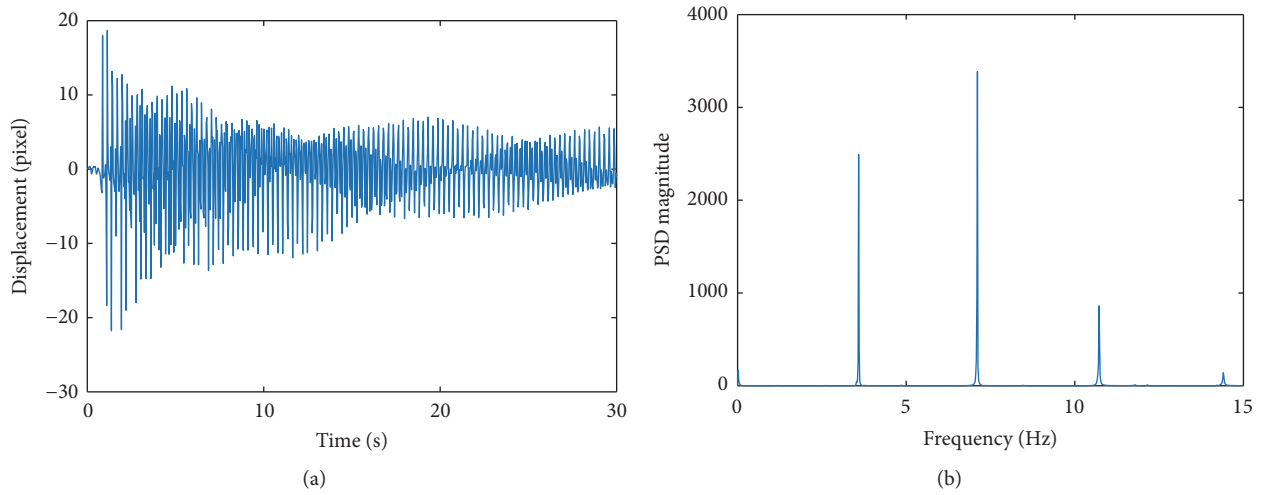


FIGURE 7: Measurement using Smartphone 3: (a) displacement-time history; (b) corresponding PSD.

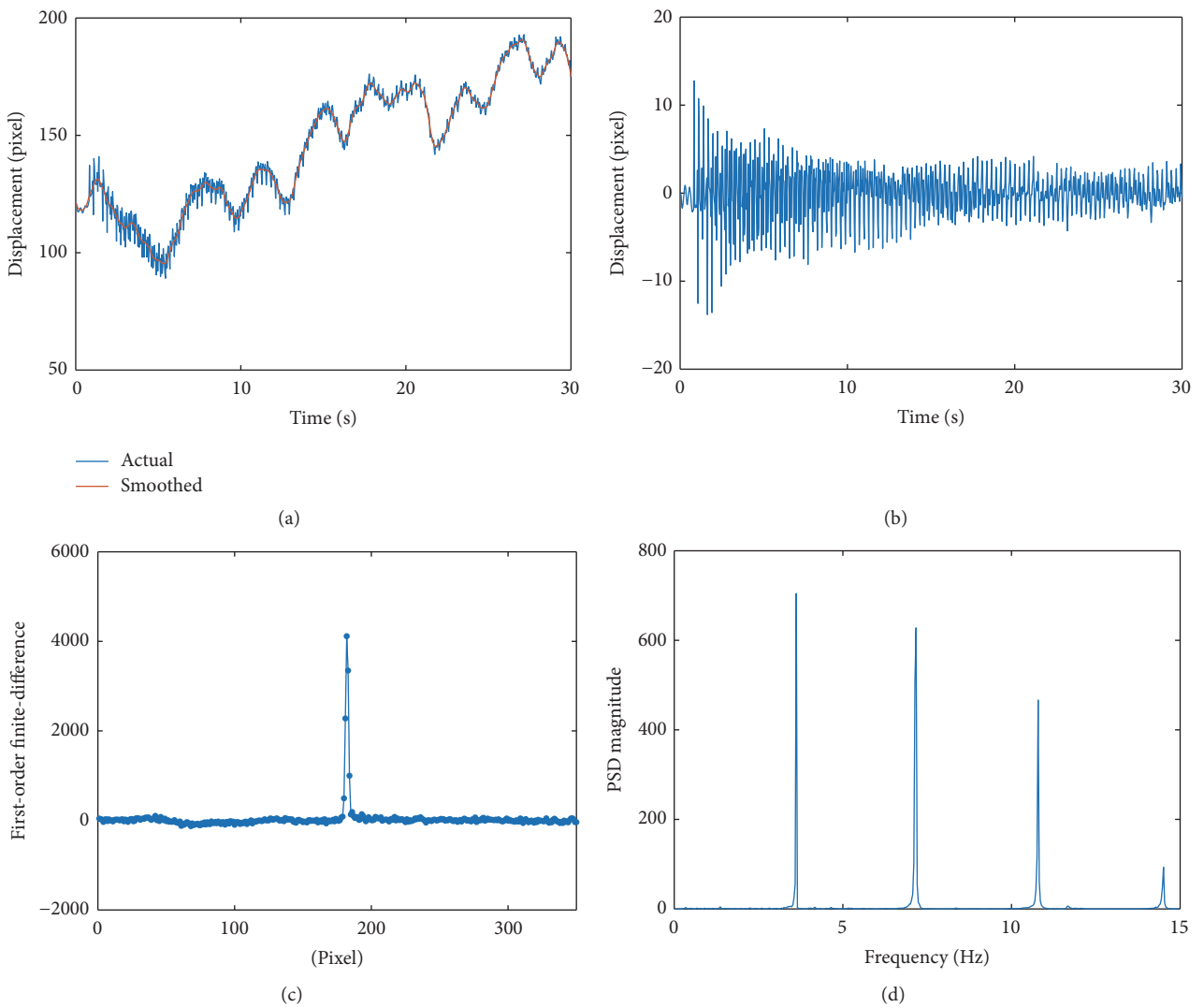


FIGURE 8: Measurement using Smartphone 4: (a) displacement-time history (before moving average); (b) displacement-time history (after moving average); (c) first-order finite-difference of sums of pixel intensities in ROI; (d) corresponding PSD of (b).

TABLE 2: Comparison of frequencies of scale cable model.

| Item | Frequency (Hz) | | | | |
|-------------------|----------------|-------|--------|--------|--------|
| | 1st | 2nd | 3rd | 4th | 5th |
| APP Orion-CC | — | 7.336 | 11.046 | 14.839 | 18.750 |
| APP D-Viewer | 3.716 | 7.350 | 11.083 | 14.833 | — |
| Tripod | 3.588 | 7.111 | 10.717 | 14.404 | — |
| Handheld shooting | 3.618 | 7.107 | 10.789 | 14.507 | — |
| Smartphone APP | 3.512 | 7.025 | 10.773 | 14.520 | — |

TABLE 3: Error analysis of identified frequencies at each mode.

| Item | MADP (%) | | | RMSD (Hz) | | |
|-------------------|----------|------|------|-----------|-------|-------|
| | 2nd | 3rd | 4th | 2nd | 3rd | 4th |
| APP D-Viewer | 0.19 | 0.20 | 0.08 | 0.015 | 0.025 | 0.015 |
| Tripod | 2.24 | 1.96 | 1.75 | 0.148 | 0.214 | 0.283 |
| Handheld shooting | 2.65 | 2.34 | 2.30 | 0.196 | 0.259 | 0.342 |
| Smartphone APP | 3.13 | 2.49 | 2.15 | 0.257 | 0.275 | 0.320 |

mode of a typical test, which are extracted from PSD by the peak picking method. The error analysis results in the replicates, for the natural frequencies that are measured in different ways using smartphone camera, are summarized in Table 2, which are compared with those using smartphone built-in accelerometer and smartphone application.

As can be seen in the figures, although the vibration amplitudes and PSD peak values are different from each other due to the differences of sampling rate, measuring position, and measuring item, it is observed that the same frequency components can be accurately obtained by the different methods as shown in Table 2. The accuracy in frequency increases as the vibration mode increases, as shown in Table 3. Although the error in frequency changes with different measurement ways, the frequency values extracted by smartphone built-in accelerometer (Smartphone 1) and smartphone camera (Smartphone 4) are highly comparable, with remarkably small error of less than 3.13%.

Furthermore, it is observed that the first natural frequency of cable model is clearly identified by the image processing method using smartphone camera. In general, it is very difficult to extract the first frequency of cable because the measuring position of smartphone is relatively low compared to the length of cable. Although it is impossible to obtain the frequencies in the higher mode owing to the low sampling rate of smartphone camera, the exact frequencies are identified in the lower vibration mode. The excellent agreement is observed between the results of Smartphones 3 and 4, demonstrating the unexceptionally good performance of the moving average for eliminating the shaking of smartphone camera during measurement.

The maximum error in the identified frequencies that are analyzed by means of MATLAB is 2.65%, while those analyzed by the smartphone application have a maximum error of 3.13%. It is observed that the proposed image processing approach is appropriate for the operating system of smartphone.

As a result, the different tests show that the dynamic characteristics of cable for cable force estimation can be accurately identified by the handheld shooting of smartphone, without any target and the information on it, despite the limitation of sampling time, sampling rate, and data processing performance of smartphone.

3.2. Field Test

3.2.1. Overview of Experiment. In order to investigate the feasibility of the vision-based cable force measurement on actual structures, a field test is conducted on a cable-stayed pedestrian bridge located in Dalian City, Liaoning Province, China, as shown in Figure 10. The longest cable is chosen for test at one side of tower. The cable is 21 m in length and 75 mm in diameter. The linear mass density of cable is 18.5 kg/m. Like the laboratory test, the same four smartphones are used to measure cable force in the different ways. To ensure the field of view appropriate for the measurement without smartphone camera zoom, the smartphone cameras shoot the cable vibration at about 30 cm away from the cable, respectively. Again, the preprinted black circle of 2 cm in diameter is used as a target to be tracked by Smartphone 2.

The smartphone camera captures the cable vibration at a resolution of 1920×1080 pixels with a sampling rate of 30 fps. The test is carried out simultaneously under the artificial knocking excitation and the measuring time of the participant is set as 30 seconds. The participant also tries to keep a stationary posture as much as possible during measurement. Figure 11 shows the installation of smartphones.

3.2.2. Test Results. Figure 12 shows the cable boundary detected by HT on the image of the first scene captured by smartphone camera, the selected ROI, and the rotation of image. Although the background of image is also very complex, the boundary of cable can be accurately detected by HT for the setting of ROI and the rotation of images.

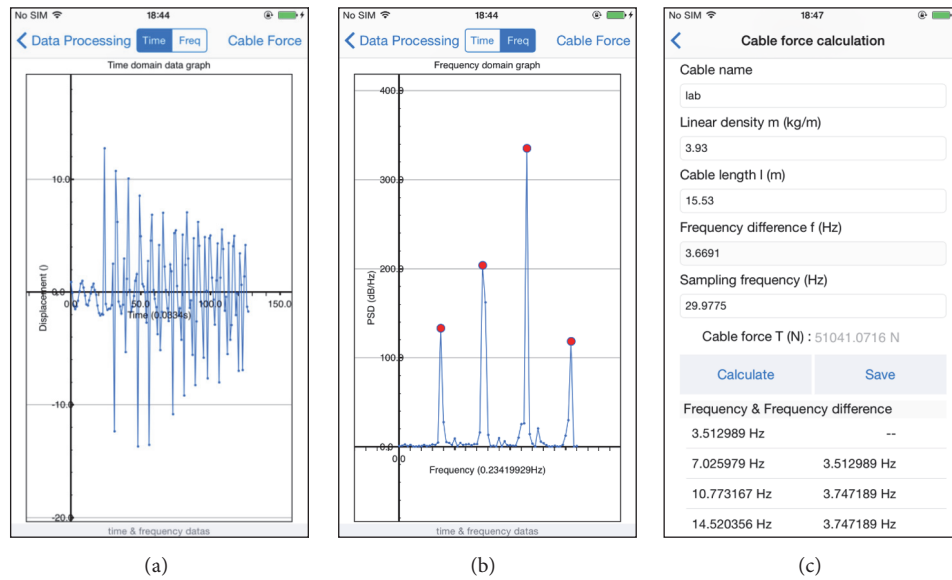


FIGURE 9: Cable force estimation using smartphone application: (a) displacement-time history (after moving average); (b) corresponding PSD. (c) Natural frequencies of cable and cable force.

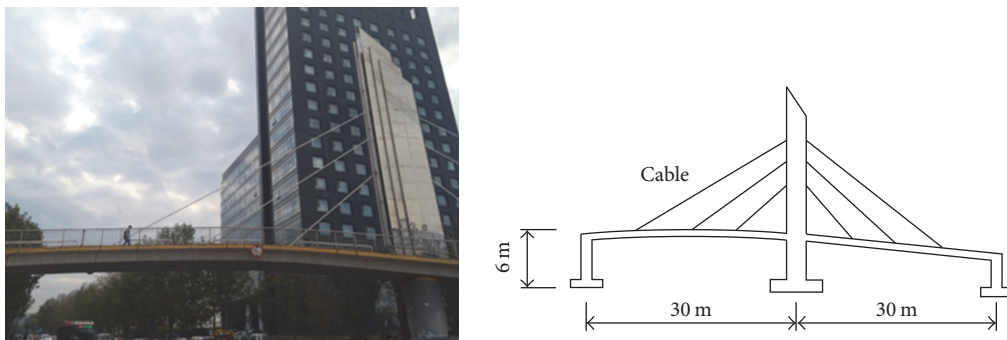


FIGURE 10: Dagong cable-stayed pedestrian bridge.

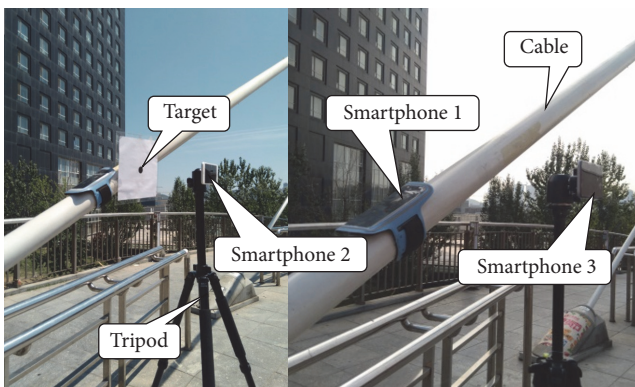


FIGURE 11: Installation of smartphones.

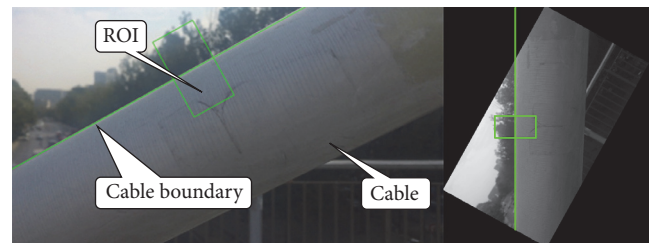


FIGURE 12: Detection of cable boundary and rotation of image.

The acceleration and displacement-time history responses of cable that are measured by four smartphones, and the corresponding PSD, are shown in Figures 13–16, respectively. Figure 16(b) is enlarged (between 5 s and 7 s) to show more

details on the moving average. Table 4 compares the natural frequencies of cable in each mode that are measured in different ways using four smartphones and the cable forces determined from (5).

Like the laboratory test, although it is impossible to obtain the frequencies in the higher mode owing to the low sampling rate of smartphone camera, the exact frequencies are identified in the lower vibration mode. Again, the satisfactory

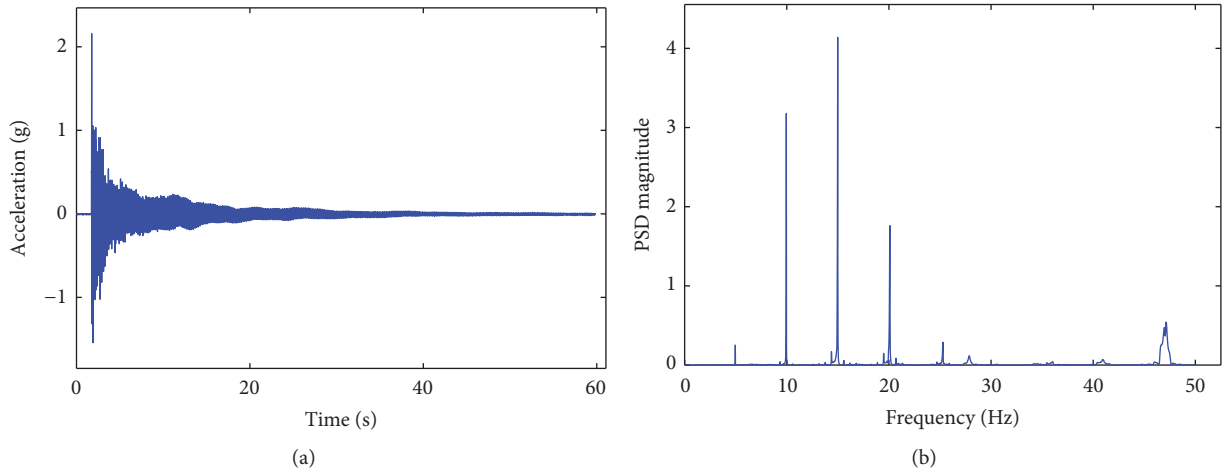


FIGURE 13: Measurement using Smartphone 1: (a) acceleration-time history; (b) corresponding PSD.

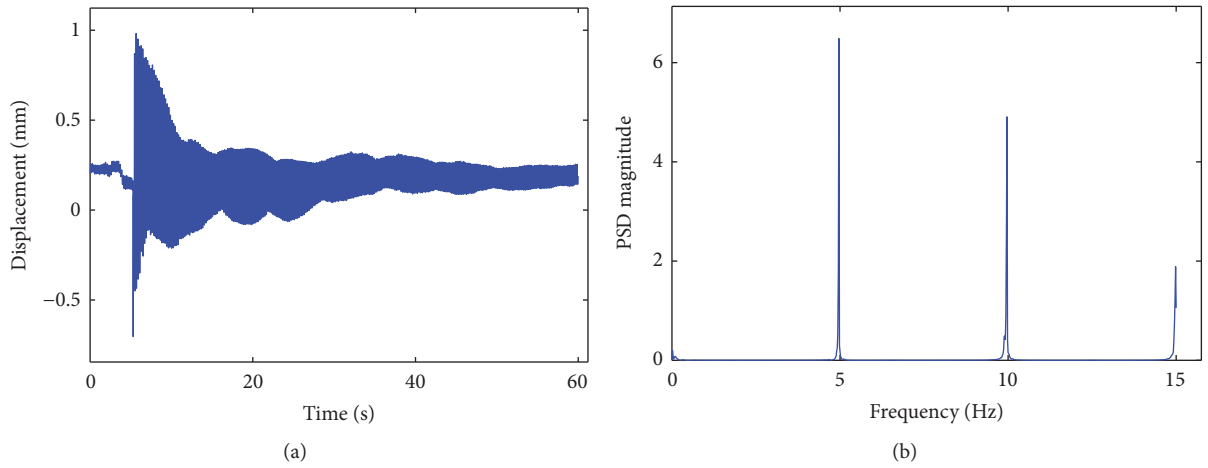


FIGURE 14: Measurement using Smartphone 2: (a) displacement-time history; (b) corresponding PSD.

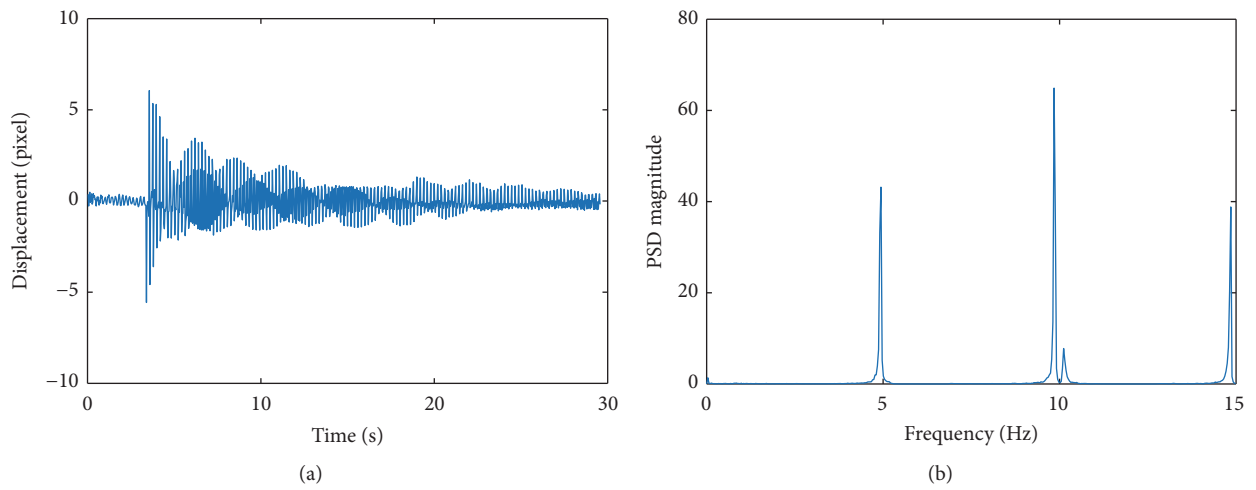


FIGURE 15: Measurement using Smartphone 3: (a) displacement-time history; (b) corresponding PSD.

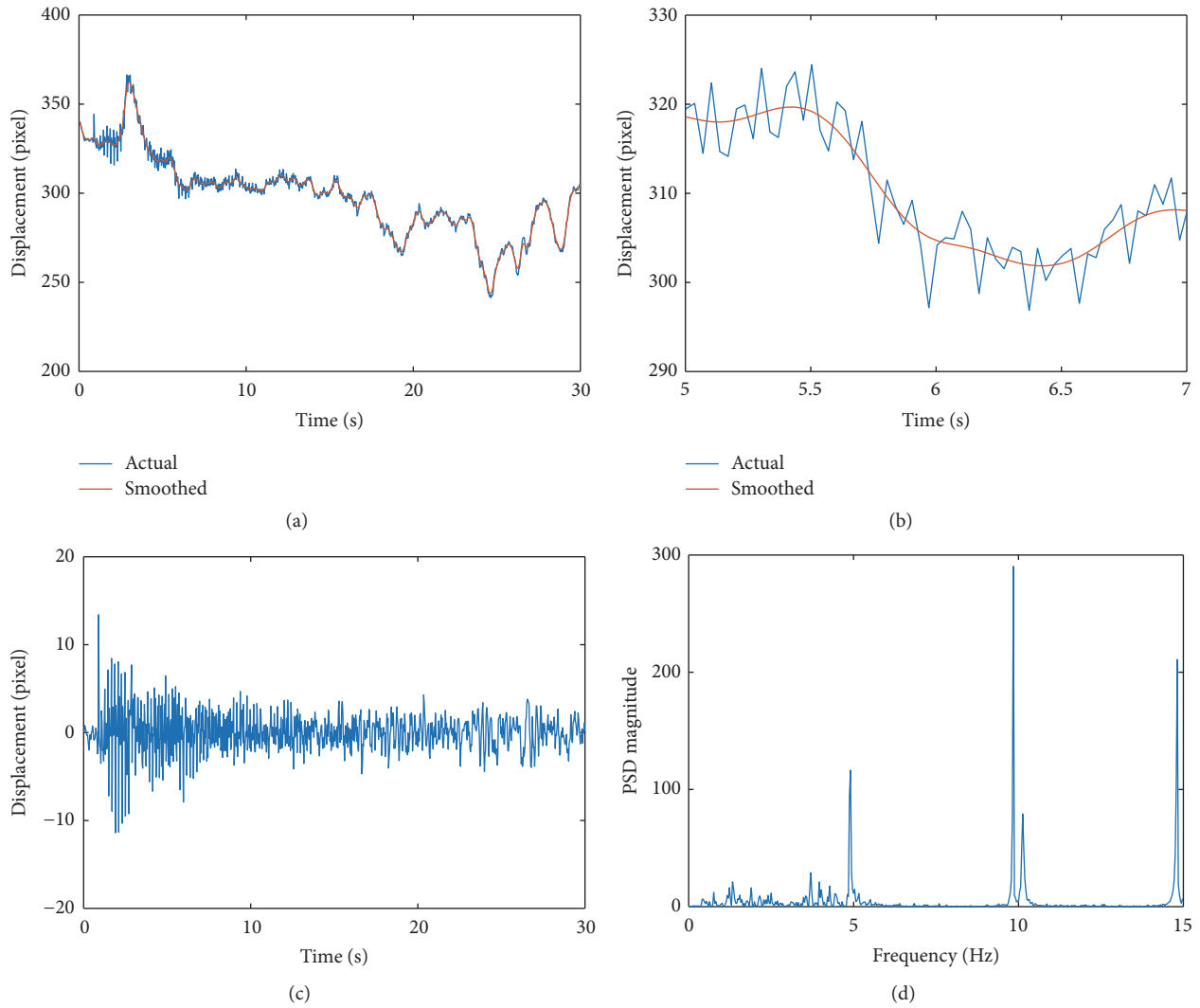


FIGURE 16: Measurement using Smartphone 4: (a) displacement-time history (before moving average); (b) enlarged displacement-time history (before moving average); (c) displacement-time history (after moving average); (d) corresponding PSD.

TABLE 4: Comparison of cable forces for pedestrian bridge.

| Item | Frequency (Hz) | | | | | Cable force (kN) | Error (%) |
|-------------------|----------------|-------|--------|--------|--------|------------------|-----------|
| | 1st | 2nd | 3rd | 4th | 5th | | |
| APP Orion-CC | 4.961 | 9.939 | 14.968 | 20.063 | 25.132 | 1542.1 | |
| APP D-Viewer | 4.966 | 9.966 | 14.983 | — | — | 1521.2 | 1.4 |
| Tripod | 4.939 | 9.844 | 14.851 | — | — | 1489.5 | 3.4 |
| Handheld shooting | 4.906 | 9.845 | 14.815 | — | — | 1485.7 | 3.7 |
| Smartphone APP | — | 8.284 | — | — | — | — | — |

agreement is obtained between the cable forces identified using Smartphones 1 and 2, with a small error of less than 1.5%.

The cable forces measured by Smartphones 3 and 4 are highly comparable, demonstrating the unexceptionally good performance of the moving average for eliminating the shaking of smartphone camera during measurement.

The error in cable force measured by handheld shooting of smartphone camera is very small (below $\pm 5\%$). Although the natural frequencies of cable are not accurately identified by the smartphone application in the case of handheld shooting because of the low amplitude of actual structure, the cable forces analyzed by MATLAB agree very well with those of using the smartphone built-in accelerometer.

4. Conclusions

In the study, a vision-based approach is proposed for cable force estimation using handheld shooting of smartphone camera. The boundary of cable is selected as a target, and the displacement-time history of cable is obtained according to the change in its location in ROI of video image sequence captured by smartphone camera. The location of the cable boundary is identified as the location of the maximum first-order finite-difference of the pixel intensity sums in ROI. The noise associated with the shaking of smartphone camera during measurement is eliminated by means of the moving average in time domain. The comprehensive comparison tests are carried out in different measurement ways, involving target and nontarget method, fixed and handheld shooting, and smartphone application and MATLAB postprocessing. The following conclusions can be drawn from this study:

- (1) In spite of the complexity of image background, the boundary of cable is accurately detected on the image of the first scene captured by smartphone camera, and the accurate dynamic characteristics of cable are rapidly identified by only one smartphone camera.
- (2) The unexceptionally good performance of the moving average for eliminating the shaking of smartphone camera is shown through the comparison with the measurement by the smartphone camera mounted on the tripod.
- (3) The comparison with the displacement monitoring application demonstrates that it is possible to estimate cable force using smartphone camera without any target and its actual size. Although it is impossible to obtain the frequencies in the higher mode owing to the low sampling rate of smartphone camera, the exact frequencies are identified in the lower vibration mode. The frame rate of smartphone camera is expected to continue to increase in the future.
- (4) The measurement error of smartphone application in the field bridge cable test shows that the higher-performance smartphone should be used in the cable force measurement.
- (5) The laboratory and field tests demonstrate the advantages over the traditional measurement methods such as convenience, ease of operation, and speediness.

It is noted that some of the issues are yet to be addressed such as the measurement by environmental and traffic-induced vibration, the remote measurement using smartphone camera zoom lens, the evaluation on shaking of smartphone camera using smartphone built-in sensors, and the application for long-span cable-stayed bridges. Nevertheless, this study demonstrates the feasibility of cable force measurement using handheld shooting of smartphone camera. Based on the preliminary efforts, the authors are exploring the more effective method for cable force estimation using smartphone camera, in accordance with the improvement of smartphone.

Conflicts of Interest

The authors declare no conflicts of interest.

Acknowledgments

The authors acknowledge the National Natural Science Foundation of China for providing the financial support (51278085, 51221961).

References

- [1] H. Wenzel, *Health Monitoring of Bridges*, John Wiley and Sons, Inc, New Jersey, NJ, USA, 2009.
- [2] Z. Fang and J.-Q. Wang, "Practical formula for cable tension estimation by vibration method," *Journal of Bridge Engineering*, vol. 17, no. 1, pp. 161–164, 2012.
- [3] S. Cho, J. Yim, S. W. Shin, H.-J. Jung, C.-B. Yun, and M. L. Wang, "Comparative field study of cable tension measurement for a cable-stayed bridge," *Journal of Bridge Engineering*, vol. 18, no. 8, pp. 748–757, 2013.
- [4] H. Zui, T. Shinke, and Y. Namita, "Practical formulas for estimation of cable tension by vibration method," *Journal of Structural Engineering*, vol. 122, no. 6, pp. 651–656, 1996.
- [5] B. H. Kim and T. Park, "Estimation of cable tension force using the frequency-based system identification method," *Journal of Sound and Vibration*, vol. 304, no. 3–5, pp. 660–676, 2007.
- [6] S.-H. Sim, J. Li, H. Jo et al., "A wireless smart sensor network for automated monitoring of cable tension," *Smart Materials and Structures*, vol. 23, no. 2, Article ID 025006, 2014.
- [7] J. J. Lee, Y. Fukuda, M. Shinozuka, S. Cho, and C.-B. Yun, "Development and application of a vision-based displacement measurement system for structural health monitoring of civil structures," *Smart Structures and Systems*, vol. 3, no. 3, pp. 373–384, 2007.
- [8] D. Zhang, J. Guo, X. Lei, and C. Zhu, "A high-speed vision-based sensor for dynamic vibration analysis using fast motion extraction algorithms," *Sensors*, vol. 16, no. 4, article no. 572, 2016.
- [9] D. Feng and M. Q. Feng, "Vision-based multipoint displacement measurement for structural health monitoring," *Structural Control and Health Monitoring*, vol. 23, no. 5, pp. 876–890, 2016.
- [10] W. Wang, J. E. Mottershead, and C. Mares, "Vibration mode shape recognition using image processing," *Journal of Sound and Vibration*, vol. 326, no. 3–5, pp. 909–938, 2009.
- [11] J. G. Chen, N. Wadhwa, Y.-J. Cha, F. Durand, W. T. Freeman, and O. Buyukozturk, "Modal identification of simple structures with high-speed video using motion magnification," *Journal of Sound and Vibration*, vol. 345, pp. 58–71, 2015.
- [12] H. Yoon, H. Elanwar, H. Choi, M. Golparvar-Fard, and B. F. Spencer, "Target-free approach for vision-based structural system identification using consumer-grade cameras," *Structural Control and Health Monitoring*, vol. 23, pp. 1405–1416, 2016.
- [13] Y.-Z. Song, C. R. Bowen, A. H. Kim, A. Nassehi, J. Padgett, and N. Gathercole, "Virtual visual sensors and their application in structural health monitoring," *Structural Health Monitoring*, vol. 13, no. 3, pp. 251–264, 2014.
- [14] Z. Dworakowski, P. Kohut, A. Gallina, K. Holak, and T. Uhl, "Vision-based algorithms for damage detection and localization in structural health monitoring," *Structural Control and Health Monitoring*, vol. 23, no. 1, pp. 35–50, 2016.

- [15] Y. F. Ji and C. C. Chang, "Nontarget image-based technique for small cable vibration measurement," *Journal of Bridge Engineering*, vol. 13, no. 1, pp. 34–42, 2008.
- [16] E. Caetano, S. Silva, and J. Bateira, "A vision system for vibration monitoring of civil engineering structures," *Experimental Techniques*, vol. 35, no. 4, pp. 74–82, 2011.
- [17] R. Jain, R. Kasturi, and B. G. Schunck, *Machine Vision*, McGraw-Hill, Inc, New York, NY, USA, 1995.
- [18] S.-W. Kim, B.-G. Jeon, N.-S. Kim, and J.-C. Park, "Vision-based monitoring system for evaluating cable tensile forces on a cable-stayed bridge," *Structural Health Monitoring*, vol. 12, no. 5-6, pp. 440–456, 2013.
- [19] Y. Yu, X. Zhao, and J. Ou, "A new idea: mobile structural health monitoring using Smart phones," in *Proceedings of the 3rd International Conference on Intelligent Control and Information Processing (ICICIP '12)*, pp. 714–716, Dalian, China, July 2012.
- [20] G. Morgenthal and H. Höpfner, "The application of smartphones to measuring transient structural displacements," *Journal of Civil Structural Health Monitoring*, vol. 2, no. 3-4, pp. 149–161, 2012.
- [21] J. Reilly, S. Dashti, M. Ervasti, J. D. Bray, S. D. Glaser, and A. M. Bayen, "Mobile phones as seismologic sensors: automating data extraction for the shake system," *IEEE Transactions on Automation Science and Engineering*, vol. 10, no. 2, pp. 242–251, 2013.
- [22] Y. Yu, R. Han, X. Zhao et al., "Initial validation of mobile-structural health monitoring method using smartphones," *International Journal of Distributed Sensor Networks*, vol. 2015, Article ID 274391, 14 pages, 2015.
- [23] M. Feng, Y. Fukuda, M. Mizuta, and E. Ozer, "Citizen sensors for SHM: use of accelerometer data from smartphones," *Sensors*, vol. 15, no. 2, pp. 2980–2998, 2015.
- [24] H. Tan and J. Chen, "Experiment verification of mobile phones for vibration measurement," in *Proceedings of the 7th International Conference on Structural Health Monitoring of Intelligent Infrastructure, International Society for Structural Health Monitoring of Intelligent Infrastructure*, Torino, Italy, 2015.
- [25] Orion-CC., <https://itunes.apple.com/cn/app/orion-cc/id951253417?mt=8>, 2015.
- [26] X. Zhao, Y. Yu, M. Li, and J. Ou, "Research on Cloud-SHM and its applications," in *Proceedings of the 7th International Conference on Structural Health Monitoring of Intelligent Infrastructure, International Society for Structural Health Monitoring of Intelligent Infrastructure*, Torino, Italy, 2015.
- [27] X. Zhao, K. Ri, R. Han, Y. Yu, M. Li, and J. Ou, "Experimental research on quick structural health monitoring technique for bridges using smartphone," *Advances in Materials Science and Engineering*, vol. 2016, pp. 1–14, 2016.
- [28] J. Matas, C. Galambos, and J. Kittler, "Robust detection of lines using the progressive probabilistic hough transform," *Computer Vision and Image Understanding*, vol. 78, no. 1, pp. 119–137, 2000.
- [29] N. Aggarwal and W. C. Karl, "Line detection in images through regularized hough transform," *IEEE Transactions on Image Processing*, vol. 15, no. 3, pp. 582–591, 2006.
- [30] J. Song and M. R. Lyu, "A Hough transform based line recognition method utilizing both parameter space and image space," *Pattern Recognition*, vol. 38, no. 4, pp. 539–552, 2005.
- [31] L. A. F. Fernandes and M. M. Oliveira, "Real-time line detection through an improved Hough transform voting scheme," *Pattern Recognition*, vol. 41, no. 1, pp. 299–314, 2008.
- [32] Y. Zhao, H. Pan, C. Du, and Y. Zheng, "Principal direction-based Hough transform for line detection," *Optical Review*, vol. 22, no. 2, pp. 224–231, 2015.
- [33] J. Canny, "A computational approach to edge detection," *IEEE Transactions on Pattern Analysis and Machine Intelligence*, vol. 8, no. 6, pp. 679–698, 1986.
- [34] O. Marques, *Practical Image and Video Processing Using MATLAB*, John Wiley and Sons, Inc, New Jersey, NJ, USA, 2011.
- [35] A. Cantatore, A. Cigada, R. Sala, and E. Zappa, "Hyperbolic tangent algorithm for periodic effect cancellation in sub-pixel resolution edge displacement measurement," *Measurement*, vol. 42, no. 8, pp. 1226–1232, 2009.
- [36] S. W. Smith, *Digital Signal Processing: A Practical Guide for Engineers And Scientists*, Elsevier Inc., 2003.
- [37] X. Zhao, H. Liu, Y. Yu et al., "Displacement monitoring technique using a smartphone based on the laser projection-sensing method," *Sensors and Actuators, A: Physical*, vol. 246, pp. 35–47, 2016.
- [38] iPhone6, <http://www.apple.com/iphone-6s/specs>, 2015.

Research Article

A Study for Optimum Survey Method of Underwater Structure Using the Dual Sonar Sensor

Youngseok Kim, Heungsu Lee, Chul Park, and Sangsik Choi

Daum Engineering Co., Ltd., Seongnam-si, Republic of Korea

Correspondence should be addressed to Youngseok Kim; youngseok21c@hanmail.net

Received 9 December 2016; Revised 14 February 2017; Accepted 8 March 2017; Published 22 May 2017

Academic Editor: Yinan Zhang

Copyright © 2017 Youngseok Kim et al. This is an open access article distributed under the Creative Commons Attribution License, which permits unrestricted use, distribution, and reproduction in any medium, provided the original work is properly cited.

We have developed dual sonar equipment and an improved operating method for improving resolution in order to solve the problems of limitations of the optical equipment and the application method of SSS (side scan sonar) in the investigation of damage of underwater structures. We analyzed the influence factors of the resolution of sonar data through the comparison of resolution and data quality in indoor test. Also we confirmed the problems about the overlapping area of the dual sonar. Depth and distance were analyzed as major influencing factors for survey angle. Specimens were scanned while adjusting distance and towfish angle according to depth change in order to verify applicability of the developed dual sonar in the field experiment. Optimal resolution was found to be 3 cm in specimen spacing, and 20 sample data items were extracted. We developed the regression model based on the multiple regression analysis and developed the RealDualSONAR-DAQ tool, the dual sonar optimum operating method program based on proposed correlation equations. We can use the developed tools to get the value of the major influencing factors for dual sonar operation and obtain high quality sonar data to analyze damage of underwater structures.

1. Introduction

In South Korea, after the collapse of the Seongsu Bridge (1994) [1], the “Special Act on Safety Management of Public Facilities” was enacted and promulgated, and the routine inspections, the detailed inspections, and the precision safety diagnosis are carried out regularly according to condition of facilities. However, the possibility of disasters in bridges and underwater structures is increasing due to the deterioration of facilities and the increase in the frequency of rainfall due to abnormal weather and scouring phenomenon around the underwater structure, scaling and exfoliation of structure’s surface, and damage and cracking due to the impact of floating materials acceleration. And there is the high possibility that the structure will collapse due to the overturn or breakage of the structure in severe cases [2].

In general, conventional methods have been used such as underwater inspections by diving personnel and depth surveying. This method uses optical equipment, so if the turbidity is not good, it is difficult to identify the damage [3, 4]. In addition, divers have safety problems due to environmental influences such as flow velocity and tidal current and securing

visibility. The research to apply “Remote-Operated-Vehicle (ROV)” or “SOund-NAvigation and Ranging (sonar)” as a solution to problems is actively underway [5]. However, since ROV is mainly used with the optical equipment, it is difficult to apply it in the Korean sea where the turbidity is high and the tide is strong [6]. Also, sonar is towing equipment and is mainly used for surveying the river/sea bed. It is not suitable for direct application to investigation of underwater structures because angle adjustment is impossible. Therefore, in this study, a development of effective equipment to investigate damage of underwater structures using sonar and an operating method to improve the resolution of sonar data were studied.

2. Applicability Analysis of Sonar Sensor

2.1. Theoretical Background of Sonar. Sonar is a device that detects azimuth and distance of a target by a sound wave. Since electromagnetic wave is transmitted faster and farther than sound wave in the air, radar (Radio Detecting and Ranging) is capable of detecting ground and marine object, and corresponding equipment for underwater use is sonar.

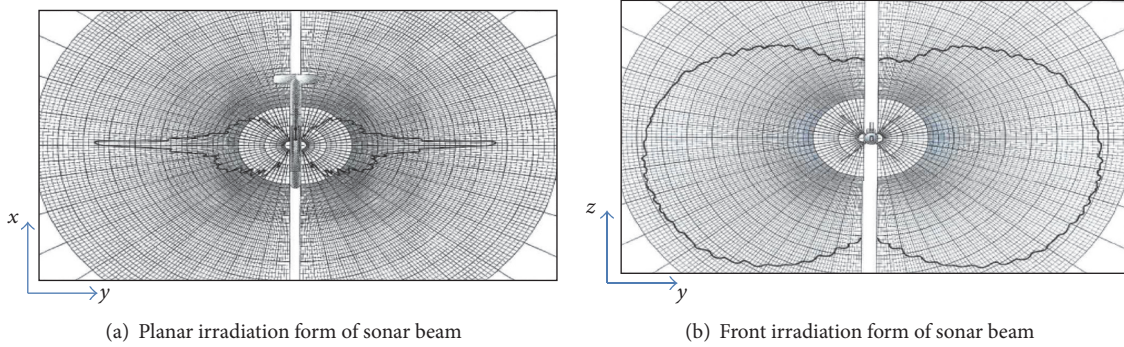


FIGURE 1: Irradiation form of sonar beam.

TABLE 1: The evaluation standard of resolution and data.

| Class | Resolution | Data rating |
|-------|---|--|
| A | Structural evaluation possible (Verification tile spacing over 90% of total area) | Excellent data accuracy (Scanning wall over 4 m) |
| B | Possible to distinguish overall (Verification tile spacing over 70% of total area) | Possible to distinguish the overall data (Scanning wall over 3 m) |
| C | Can be identified for some area (Verification tile spacing over 50% of total area) | Data can be separated for some area (Scanning wall over 2 m) |
| D | Not identifiable overall (Verification tile spacing over 30% of total area) | Poor data accuracy overall (Scanning wall over 1 m) |

The sound wave applied to sonar has a pressure wave of about 1,500 m/sec and has the property of transmitting well in water. Therefore, so far, various types of sonar have been developed and operated according to the purpose and use, as the only means of detecting targets in the water in an active or passive way [7, 8]. Side scan sonar (SSS) system is an underwater ultrasonic system that scans both sides. As a towfish (towed underwater) is towed by the traction signal cable, the towfish sends and receives ultrasound underwater from transducers on both sides. It is a system that transmits a signal through a traction signal cable and restores the shape into a two-dimensional image using a signal and an image processing apparatus [9].

2.2. Resolution Factor Analysis of Sonar Data. If you want to focus on the subject when you take pictures using a camera, you need to adjust the lens, aperture, shutter speed, sensitivity, and so forth to get a clear picture. An autofocus function has been developed that automatically captures the subject's focus as it progresses from a manual camera to a DSLR. Side scan sonar (SSS) also has factors that affect the quality of data [10]. As shown in Figure 1, x is an axial direction of the towfish, y is a perpendicular direction, and z is a vertical direction. Since the main beam and the auxiliary beam do not radiate in a regular shape, there may be a difference in resolution depending on the contact surface of the beam. Therefore, we tried to grasp influence factors for obtaining high resolution data [7].

When operating underwater imaging equipment, the resolution of data collected can vary depending on angle of the towfish and distance from the structure [8]. Therefore, we carried out various verification experiments to obtain high

quality data by operating the underwater image acquisition equipment appropriately according to the situation. Through indoor experiments, we confirmed the resolution change of the data collected at the same depth (5 m) according to angle of the towfish and distance from the structure as shown in Figures 2(a) and 2(b).

As shown in Table 1, the resolution was evaluated according to the verification of tile spacing in total area, and the data grade was evaluated with range scanned in 5 m wall. As shown in (c) to (f) of Figure 2, the resolution and the data quality were evaluated at different distances and angles. Here, the yellow line in sonar data is tile joint in the wall and the highlight in sonar data depends on sound intensity and resolution. The resolution changes according to distance and angle are summarized as the graph in Figure 3.

As shown in the above results, the resolution of sonar data is influenced by distance from the structure and angle of the towfish. The shape of the beams emitted from sonar is not linear and the intensity of sound waves is different. Therefore, it is considered that the resolution depends on angle and distance.

2.3. Overlay Analysis. The existing SSS is basically equipped with transducers on left and right sides of towfish for the purposes of survey of the seabed. This equipment needs to be improved in order to apply this equipment to underwater structures' surveys. In general, the underwater survey is carried out to assess the damage of structures and bed topography and to judge them comprehensively. Therefore, since the existing SSS is difficult to simultaneously investigate riverbed and underwater structures and work efficiency is low, two towfishes are used to investigate river and underwater

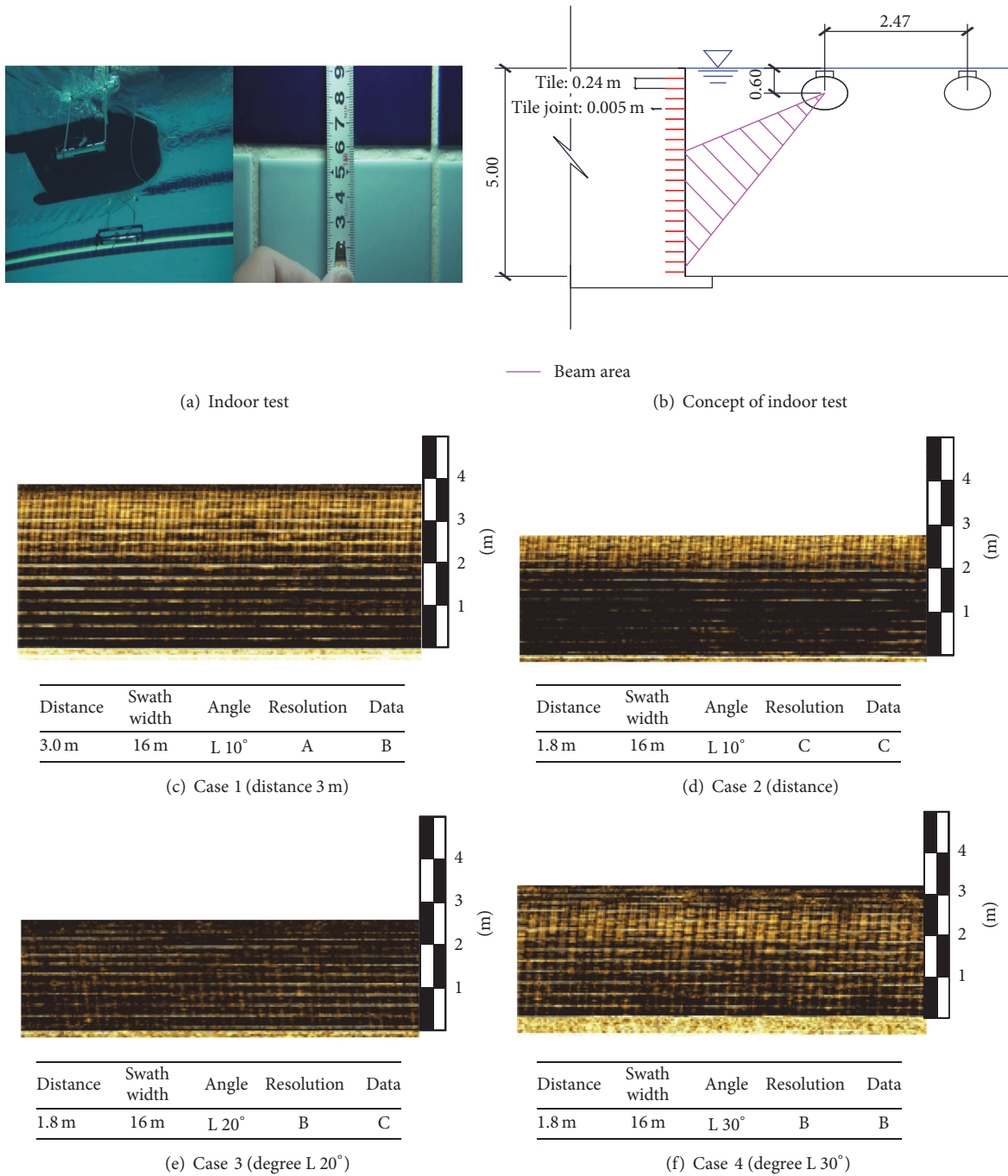


FIGURE 2: Indoor test and data.

structures, respectively. However, if two towfishes are operated, the overlapping of the sound waves occurs as shown in Figure 4, so that the interference of sound wave may occur. This was verified through laboratory experiments.

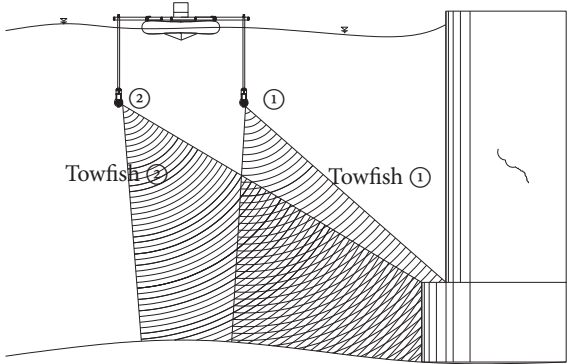
Figure 5 shows the overlapping area and nonoverlapping of sonar data. (a) in Figure 5 shows concept of indoor test and (b) is A grade of wall data to compare with overlapping area of sonar data. As shown in (c) and (d), the data of the overlapped part could not distinguish the indoor pool tile spacing due to sound wave interference, and the data quality was degraded.

If each control unit of two towfishes is used, sonar beam is not emitted at the same time. Therefore, when the radiated beam hits the surface of structure and reflects back, the interference of each signal occurs. And it was confirmed that the status cannot be surveyed by the acquired image.

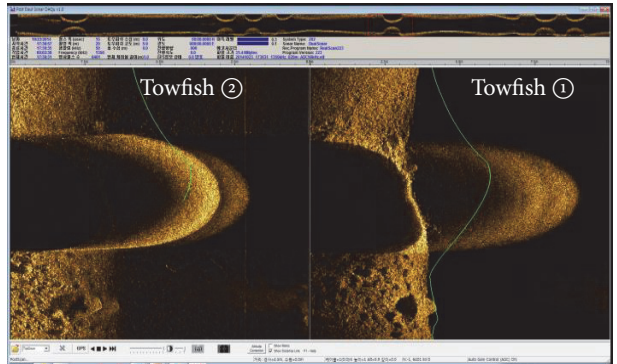
As shown (a) in Figure 6, when sonar beam is emitted at different intervals, the interference of sound waves occurred with each other and sonar data quality is deteriorated. Therefore, it is designed to be able to radiate sonar beam at the same time as shown (b) in Figure 6.

TABLE 2: Overlapping area occurs.

| Classification | Distance to the structure | Frequency | Swath width | Towfish angle | Resolution grade |
|----------------|---------------------------|-----------|-------------|---------------|------------------|
| Towfish ① | 1.50 m | 1250 kHz | 16 m | R 70° | A |
| Towfish ② | 3.80 m | 1250 kHz | 16 m | L 20° | |



(a) Concept of Case 1 (overlapping area)



(b) Case 1 sonar data

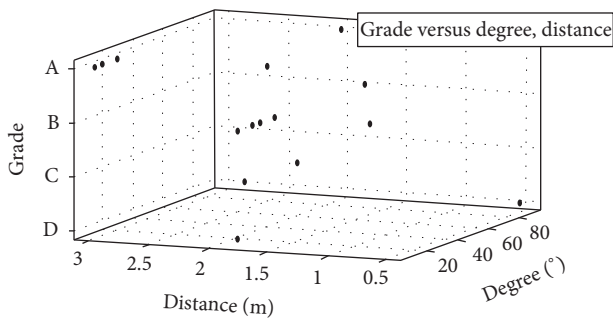


FIGURE 3: Change in resolution depending on distance and angle.

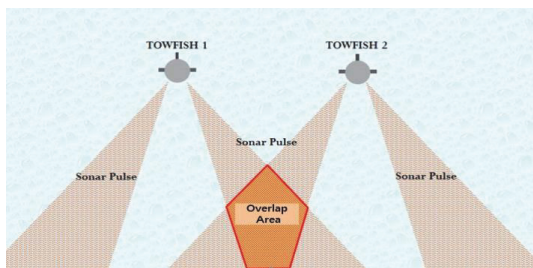


FIGURE 4: Occurrence of overlapped area due to acquisition of bidirectional underwater image.

In order to solve these problems, a controller and a dual sonar are developed as shown in Figure 6(c) so that sonar beams can be emitted simultaneously from two towfishes. The developed dual sonar is designed as shown in Figure 6(d) to control two towfishes simultaneously and to control sound wave irradiation interval of each towfishes. The beam is simultaneously radiated from the module of the transducer, thereby solving the problem that the interference of sound wave occurs.

3. Field Application Analysis and Resolution Enhancement Technique

3.1. Application of the Dual Sonar Sensor. In order to analyze the field applicability of the developed dual sonar, we measured the foundation and the lower surface of piers at towfish (right) and towfish (left) at the same frequency in the test-bed. Field test was performed with the existence of overlapping interval as a variable.

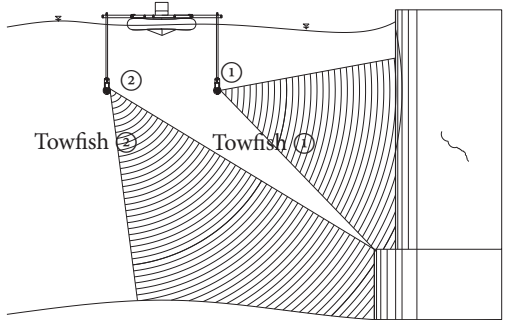
Table 2 shows the result of experiment in which overlapping sections are generated, and Table 3 shows experimental result in the case where there are no overlapping sections. The data of number 1 towfish and number 2 towfish in Table 2 show a resolution level despite the overlapping area. And there is no difference in resolution grade compared to the data in the case of no overlapping section.

As a result of comparing data that caused overlap and data that did not overlap, it was found that there was no difference in the quality and resolution of the data. So, it is considered that there is no influence of scattering and disturbance of sound waves in the overlapping section. The developed dual sonar can investigate underwater structures in addition to the surveying of river bed topography of the existing SSS. As underwater structures and river are simultaneously surveyed, the inspection period can be shortened and the inspection cost can be saved.

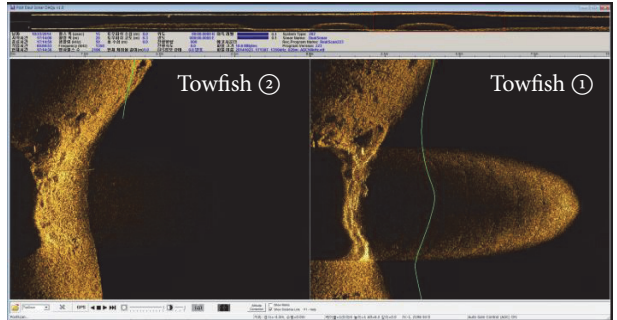
3.2. Resolution Enhancement by Multiple Regression Analysis. Through laboratory experiments, sonar data were confirmed to be influenced by distance from the structure and angle of the towfish. As the depth of field changes, angle of the towfish or distance is expected to change. In the field experiment, the prepared specimen was scanned while adjusting distance from the structure and angle of the towfish according to depth change. The specimen was scanned while adjusting the distance to the structure and angle of incidence according to the depth change. Optimal resolution was found to be 3 cm in

TABLE 3: No overlapping area exists.

| Classification | Distance to the structure | Frequency | Shooting width | Towfish angle | Resolution grade |
|----------------|---------------------------|-----------|----------------|---------------|------------------|
| Towfish (R) | 1.50 m | 1250 kHz | 16 m | R 45° | A |
| Towfish (L) | 3.80 m | 1250 kHz | 16 m | L 10° | |



(a) Concept of Case 2 (no overlapping area)



(b) Case 2 sonar data

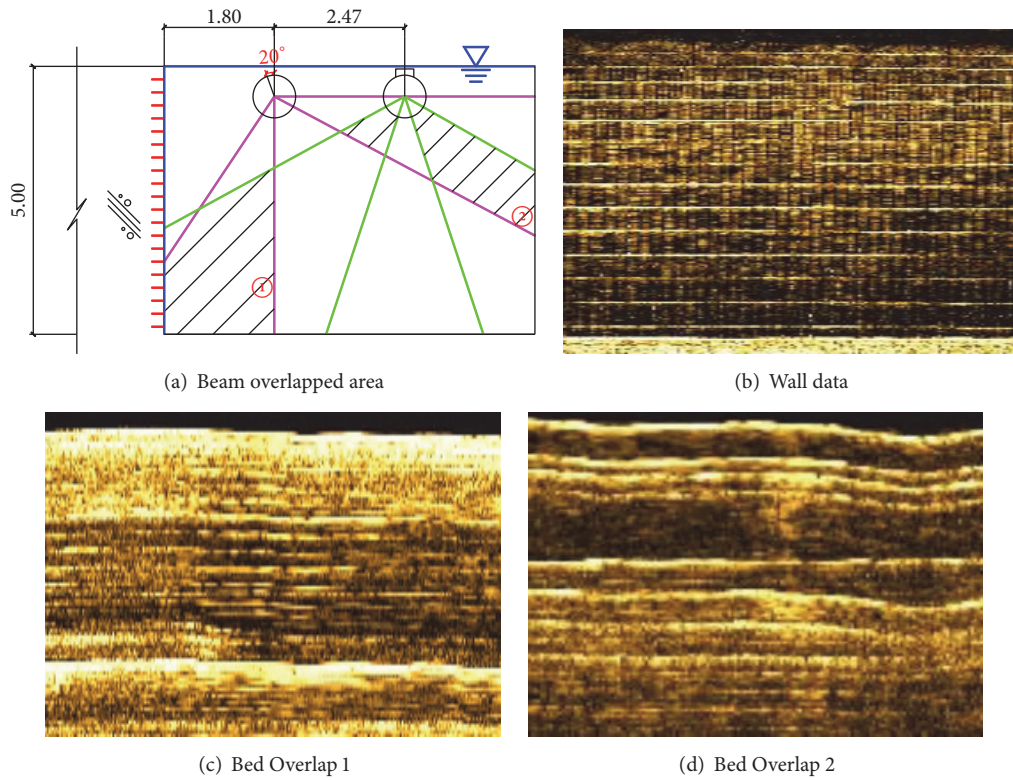


FIGURE 5: Experimental diagram and data of interference according to frequency band.

specimen spacing, and 20 sample data items were extracted as shown in Figure 7. The white box in Figures 7(c) and 7(d) is the scanned image of specimen (b).

As shown in Table 4, when surveying underwater structures and riverbed, the left and right towfish are indicated as ① + ③, and in the case of only surveying the riverbed, towfish is indicated by ② + ③.

Multiple regression analysis is regression analysis where multiple independent variables are used to indicate changes in dependent variables when dependent variables are

expected to be affected by two or more independent variables [2, 11]. When the number of independent variables is k , the regression model is as follows:

$$y_i = \beta_0 + \beta_1 x_{i1} + \beta_2 x_{i2} + \dots + \beta_k x_{ik}. \quad (1)$$

Here, y is a dependent variable, x_1, \dots, x_k are the given independent variables, and β_1, \dots, β_k are the unknown regression coefficient. In this study, we have established a second-order or higher-order curve estimation model such

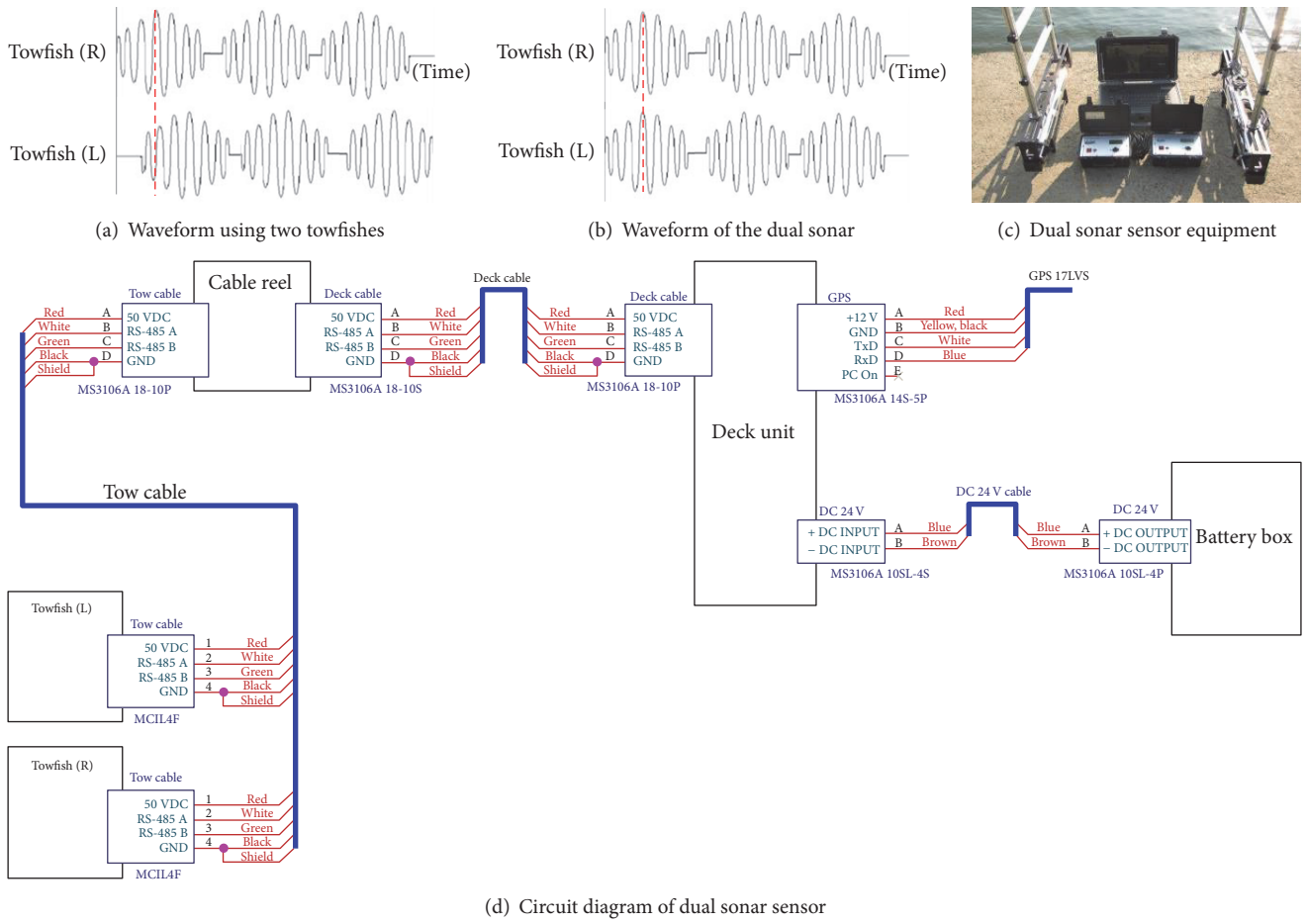


FIGURE 6: Graph of waveform and circuit diagram of the dual sonar.

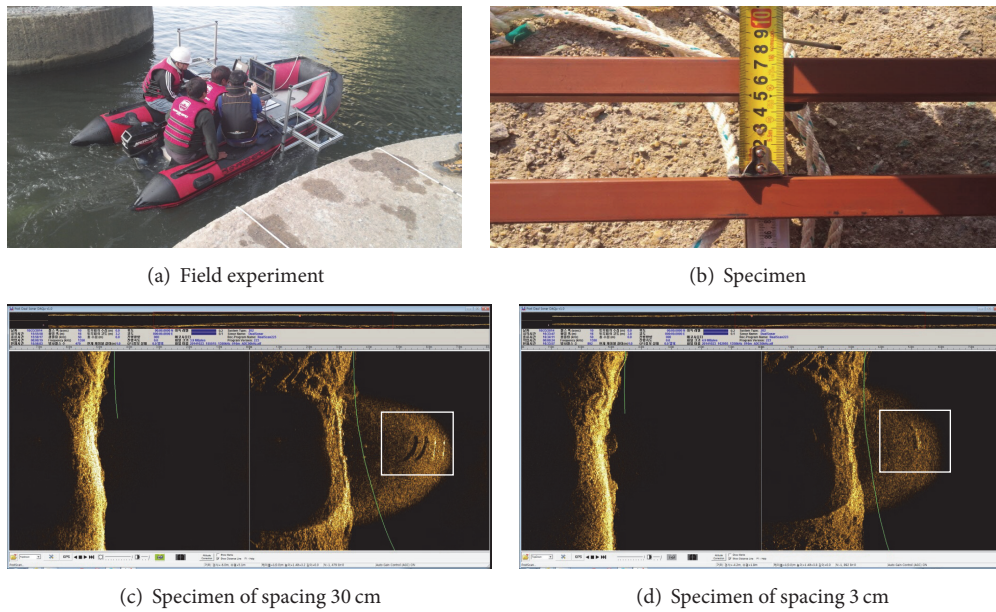


FIGURE 7: Field application experiment.

TABLE 4: Sample data.

| Number | Depth (m) | ① Towfish (L) (wall) | | ② Towfish (L) (bed) | | ③ Towfish (R) (bed) | |
|--------|-----------|----------------------|--------------|---------------------|--------------|---------------------|--------------|
| | | Angle (R) | Distance (m) | Angle (R) | Distance (m) | Angle (R) | Distance (m) |
| 1 | 4.6 | 53.6 | 1.6 | -2.7 | 14.0 | 140.0 | 3.9 |
| 2 | 3.8 | 51.2 | 1.5 | -2.4 | 13.6 | 141.0 | 3.8 |
| 3 | 3.1 | 50.6 | 1.4 | -2.1 | 13.3 | 143.0 | 3.7 |
| 4 | 9.1 | 51.3 | 1.6 | -3.1 | 16.1 | 137.0 | 3.9 |
| ⋮ | ⋮ | ⋮ | ⋮ | ⋮ | ⋮ | ⋮ | ⋮ |
| 15 | 7.3 | 50.4 | 1.3 | -3.0 | 15.2 | 138.5 | 3.6 |
| 16 | 3.9 | 51.5 | 1.2 | -3.1 | 13.6 | 139.9 | 3.5 |
| 17 | 4.8 | 51.2 | 1.2 | -2.7 | 14.0 | 139.5 | 3.5 |
| 20 | 8.2 | 50.2 | 1.4 | -3.0 | 15.7 | 138.1 | 3.7 |

as since the relationship between angle of the towfish (dependent variable) and two independent variable distributions is more than quadratic.

$$f(x, y) = \beta_{00} + \beta_{10}x + \beta_{01}y + \beta_{20}x^2 + \beta_{11}xy + \beta_{02}y^2. \quad (2)$$

The basis of multiple regression analysis is the method of least residual squares. To minimize this error, the function is differentiated for each unknown. This is a method of going back to a value whose differential value becomes zero [12]. The coefficient of correlation used in this study is coefficient of determination and adjusted R -square, and the coefficient of determination can be expressed as the square of the correlation coefficient R [13]. In addition, to prevent the correlation R_{adj}^2 from increasing because of the addition of a relatively low independent variable, the coefficient of determination after adjustment was used [14]. This is shown in the following:

$$R_{adj}^2 = 1 - \frac{(1 - R^2)(n - 1)}{n - k - 1}. \quad (3)$$

To verify the reliability of the derived multilinear regression equation, correlation coefficient, decision coefficient, correction coefficient, and error were calculated. The error was calculated using RMSE (Root Mean Square Error), and the error is shown in the following:

$$RMSE = \sqrt{\frac{1}{N} \sum_{i=1}^n (M_n - P_n)^2}. \quad (4)$$

The Matlab 2016b program was used to analyze the correlation between depth of the water and angle of the towfish, and the multiple regression model for the final towfish survey is shown in the following (5) to (7). From (2), dependent variables x , y and regression coefficients $\beta_{00}, \dots, \beta_{02}$ were obtained as follows.

$$Y_{LS} = 100.3 + 1.953x - 81.38y - 0.0128x^2 - 1.396xy + 32.98y^2 \quad (5)$$

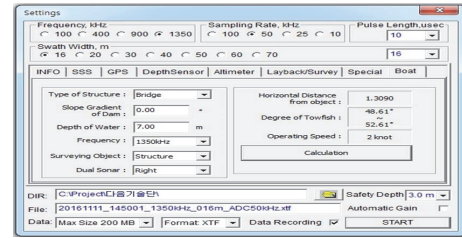


FIGURE 8: Dual sonar sensor operating program tool.

$$Y_{LB} = 941.2 + 90.93x - 168.8y + 2.151x^2 - 8.089xy + 7.537y^2 \quad (6)$$

$$Y_{RB} = 131.9 + 3.919x - 1.87y + 0.06189x^2 - 1.421xy + 1.453y^2, \quad (7)$$

where x is depth of water, y is distance from the structure, Y_{LS} is angle of the towfish (left) when surveying the underwater structure, Y_{LB} is angle of the towfish (left), and Y_{RB} is angle of the towfish (right) when surveying the bed. The regression model graphs and decision coefficients are summarized in Table 5.

R^2 (R -square), which is the adjusted coefficient of determination, is 0.65~0.93, and the effect of distance between water depth and structure on angle of the towfish is 65~93%. As shown in Table 6, the significance of the proposed regression coefficients was obtained by t -test [15]. As a result of analysis, the distance between water depth and structure showed a major influence on angle of the towfish. In this case, since the P value, which is probability of significance, indicates the degree of rejection of the null hypothesis that the independent variable affects the dependent variable, it can be judged that the smaller the P value is, the more significant it is [14, 16]. The larger value and the more independent variables affect the dependent variable because the standardization factor (β) is an indicator of the influence of each independent variable on the dependent variable [17].

The RealDualSONAR-DAQ such as that in Figure 8, a program for the operation of distance between water depth

TABLE 5: Multiple regression analysis results.

| | Graph | Classification | Value |
|-------------------------|-------|--|--------------------------------------|
| Towfish (L) (structure) | | SSE R-square Adjusted R-square RMSE | 1.589 0.8936 0.8493 0.3639 |
| Towfish (L) (bed) | | SSE R-square Adjusted R-square RMSE | 0.3823 0.7546 0.6523 0.1785 |
| Towfish (R) (bed) | | SSE R-square Adjusted R-square RMSE | 1.771 0.951 0.9306 0.384 |

TABLE 6: Coefficient of effective factors.

| | Effective factors | B | β | t | P |
|-------------------------|-------------------|--------|---------|--------|-------|
| Towfish (L) (structure) | Depth | -0.308 | -0.740 | -3.966 | 0.001 |
| | Distance | 3.708 | 0.600 | 3.215 | 0.006 |
| Towfish (L) (bed) | Depth | -1.089 | -8.099 | -2.706 | 0.016 |
| | Distance | 2.042 | 7.390 | 2.469 | 0.026 |
| Towfish (R) (bed) | Depth | -0.637 | -0.983 | -9.245 | 0.000 |
| | Distance | 1.801 | 0.187 | 1.762 | 0.098 |

and structure and angle of the towfish, was developed based on the equation derived by the above regression analysis and provides operational information of sonar by linking sonar survey distance and angle. The high resolution data can be obtained by entering type and depth of structure in the setting window before the dual sonar operation.

4. Conclusion

In this study, we developed the equipment to investigate damage of underwater structures effectively using the dual sonar and studied the operation method to improve the resolution of sonar data. Through the indoor experiment, we confirmed sound wave interference phenomenon in the overlapping section of the dual sonar operation and verified that sonar data resolution depends on the distance between water depth and structure and angle of towfish. In the dual sonar operation, the problem of sound wave interference phenomenon which occurred in the overlapped region was solved by the control part design and module development, and it was verified through the field experiment.

In addition, it was found that the optimal resolution was obtained when the interval of 3 cm specimens could be identified through the test, and 20 sample data items for each survey item were extracted. The regression model for the object of investigation was derived through multiple regression analysis. The derived regression model explains that the influence of distance between water depth and structure on angle of the towfish angle is 65~93%. The significance test was confirmed by *t*-test, and distance between water depth and structure was found to have a major influence on the survey angle. The RealDualSONAR-DAQ, the dual sonar operating program, was developed based on the derived correlation. Since this is based on empirical data of the dual sonar of 1MHz, it is necessary to verify and update the derived model through a lot of data accumulation in the future.

Through this study, it is possible to obtain the appropriate survey angle of towfish by using data of depth and distance collected from the field. Therefore, it is possible to prevent degradation of sonar data due to inexperienced operations and to obtain good sonar data to analyze damage of underwater structure. Based on the accurate sonar data, which is the result of this study, it is considered that reliable safety evaluation of underwater structures is possible.

Conflicts of Interest

The authors declare no conflicts of interest regarding the publication of this paper.

Acknowledgments

This paper is a study conducted with the support of the Korea Agency for Infrastructure Technology Advancement funded by the government (Ministry of Land, Infrastructure and Transport) in 2016 (no. 16CTAP-C097867-02).

References

- [1] Central Disaster and Safety Countermeasure Headquarter, *Disaster Annals*, 2012 (Korean).
- [2] H.-S. A. Alfredo and W. H. Tang, *Probability Concepts in Engineering: Emphasis on Applications in Civil & Environmental Engineering*, John Wiley & Sons, 2007.
- [3] D. Agdas, J. A. Rice, J. R. Martinez, and I. R. Lasa, "Comparison of visual inspection and structural-health monitoring as bridge condition assessment methods," *Journal of Performance of Constructed Facilities*, vol. 30, no. 3, 2016.
- [4] J.-H. Park, Y.-S. Park, C. Park, and J.-J. Lee, "Development of sonar sensor-based smart underwater inspection system," in *Proceedings of the Korea Institute for Structural Maintenance and Inspection Conference*, vol. 17, pp. 126–129, 2013.
- [5] V. Chandran, S. Elgar, and A. Nguyen, "Detection of mines in acoustic images using higher order spectral features," *IEEE Journal of Oceanic Engineering*, vol. 27, no. 3, pp. 610–618, 2002.
- [6] C. Park, *A study on the development of safety inspection method in underwater structures using a high resolution SONAR sensor [Ph.D. thesis]*, Hanyang University, 2015.
- [7] Y. Kim, C. Park, and S. Choi, "A study of operation methods for application of safety inspection of underwater structures using high resolution side scan SONAR sensor," *Korea Society of Coastal Disaster Prevention*, vol. 3, no. 2, pp. 67–73, 2016.
- [8] C. Park, Y. Kim, and S. Choi, "A regression analysis study of the applicability of side scan SONAR sensor based safety inspection of underwater structures," in *Proceedings of the 18th International Conference on Nondestructive Testing and Evaluation*, 2016.
- [9] F. Ollivier, P. Cervenka, and P. Alais, "Side scan SONAR using phased arrays for high resolution imaging and wide swath bathymetry," *The Institution of Electrical Engineers*, vol. 143, no. 3, pp. 163–168, 1996.
- [10] H.-N. Ho, J.-J. Lee, C. Park, and B.-W. Jo, "An efficient image enhancement algorithm for sonar sensor data," *International Journal of Latest Research in Science and Technology*, vol. 2, no. 6, pp. 38–43, 2013.
- [11] C. Petrousatou, S. Lambropoulos, and J. Pantouvakis, "Road tunnel early cost estimates using multiple regression analysis," *Operational Research*, vol. 6, no. 3, pp. 311–322, 2006.
- [12] A. Sorsa, A. Isokangas, S. Santa-Aho, M. Vippola, T. Lepistö, and K. Leiviskä, "Prediction of residual stresses using partial least squares regression on barkhausen noise signals," *Journal of Nondestructive Evaluation*, vol. 33, no. 1, pp. 43–50, 2014.
- [13] M. Kumar and V. K. Srivastava, "Pitman nearness and concentration probability comparisons of the sample coefficient of determination and its adjusted version in linear regression models," *Communications in Statistics. Theory and Methods*, vol. 33, no. 7, pp. 1629–1641, 2004.
- [14] S. Lee, D. Kim, and Y. Choi, "Development of predictive model for the number of potholes using multi regression analysis," *Journal of Korean Society of Hazard Mitigation*, vol. 14, no. 3, pp. 91–98, 2014.
- [15] K. Cha, S. Kim, J. H. Kim, M. Park, and J. S. Kong, "Development of the deterioration models for the port structures by the multiple regression analysis and markov chain," *Journal of the Computational Structural Engineering Institute of Korea*, vol. 28, no. 3, pp. 229–239, 2015.

- [16] S. C. Chelgani, B. Hart, W. C. Grady, and J. C. Hower, "Study relationship between inorganic and organic coal analysis with gross calorific value by multiple regression and ANFIS," *International Journal of Coal Preparation and Utilization*, vol. 31, no. 1, pp. 9–19, 2011.
- [17] V. Mokhtari, "Regression analysis of factors in the agricultural production cooperative success of Ilam," *Journal of Trends in Advanced Science and Engineering*, vol. 4, no. 2, pp. 100–109, 2012.